REPORT DOCUMENTATION PAGE

Form Approved OMB NO. 0704-0188

1. REPORT DATE (DD-MM-YYYY)	2. REPORT TYPE	3. DATES COVERED (From - To)
07-12-2015	Final Report	1-Oct-2010 - 30-Sep-2014

4. TITLE AND SUBTITLE

FINAL REPORT: Temporal and Spatial Distribution of Soil Moisture in Heterogeneous Vadose Zone with Moisture Barriers as Affected by Atmospheric Boundary Conditions

5a. CONTRACT NUMBER
W911NF-10-1-0501

5b. GRANT NUMBER

5c. PROGRAM ELEMENT NUMBER
622784

6. AUTHORS

Tissa Illangasekare, Kathleen M. Smits, Toshi Sakaki

5d. PROJECT NUMBER

5e. TASK NUMBER

5f. WORK UNIT NUMBER

7. PERFORMING ORGANIZATION NAMES AND ADDRESSES

Colorado School of Mines
1500 Illinois Street, Guggenheim Hall, Room 130

Golden, CO 80401 -1887

8. PERFORMING ORGANIZATION REPORT NUMBER

9. SPONSORING/MONITORING AGENCY NAME(S) AND ADDRESS (ES)

U.S. Army Research Office
P.O. Box 12211
Research Triangle Park, NC 27709-2211

10. SPONSOR/MONITOR'S ACRONYM(S)
ARO

11. SPONSOR/MONITOR'S REPORT NUMBER(S)
55120-EV.25

12. DISTRIBUTION AVAILIBILITY STATEMENT

Approved for Public Release; Distribution Unlimited

13. SUPPLEMENTARY NOTES

The views, opinions and/or findings contained in this report are those of the author(s) and should not contrued as an official Department of the Army position, policy or decision, unless so designated by other documentation.

14. ABSTRACT

This research seeks to improve our understanding of the non-isothermal, multi-phase flow processes of water, water vapor and air in the shallow subsurface by performing controlled experiments at different test scales under transient conditions using soil with accurately known hydraulic/thermal properties. Experimental data is used to test existing theories and appropriate numerical models, providing new insights into mass flux and thermal process interactions. This work provides a critical step toward refining our understanding of the non-isothermal, multi-phase flow processes of water, water vapor and air in the shallow subsurface coupled with thermal processes in order to better

15. SUBJECT TERMS

soil moisture, vadose zone, landmine detection, land atmosphere interaction, multiphase flow

16. SECURITY CLASSIFICATION OF:			17. LIMITATION OF ABSTRACT	15. NUMBER OF PAGES	19a. NAME OF RESPONSIBLE PERSON
a. REPORT	b. ABSTRACT	c. THIS PAGE			Tissa Illangasekare
UU	UU	UU	UU		19b. TELEPHONE NUMBER: 303-384-2126

Standard Form 298 (Rev 8/98)
Prescribed by ANSI Std. Z39.18

Report Title

FINAL REPORT: Temporal and Spatial Distribution of Soil Moisture in Heterogeneous Vadose Zone with Moisture Barriers as Affected by Atmospheric Boundary Conditions

ABSTRACT

This research seeks to improve our understanding of the non-isothermal, multi-phase flow processes of water, water vapor and air in the shallow subsurface by performing controlled experiments at different test scales under transient conditions using soil with accurately known hydraulic/thermal properties. Experimental data is used to test existing theories and appropriate numerical models, providing new insights into mass flux and thermal process interactions. This work provides a critical step toward refining our understanding of the non-isothermal, multi-phase flow processes of water, water vapor and air in the shallow subsurface coupled with thermal processes in order to better predict the spatial and temporal distribution of soil moisture/temperature around buried objects such as landmines. It is our hope that this data and knowledge of the fundamental processes that occur at the land/atmospheric interface will improve the comprehension and interpretation of sensor imagery and lead to the development of more robust signal processing and interpretation techniques that allow for the discrimination of real threats from anomalies that results from natural processes. In addition to landmine detection, this knowledge is critical to many engineering applications, including the efficiency of thermal remediation of contaminated soils, the flux of from soil, natural or forced ventilation, and water resource management in dry land.

Primary aims of the project were to:

- To develop a better understanding of the hydraulic and thermal characteristics of mixed or disturbed soils as well as the temperature dependence of thermal properties. The burying of landmines involves artificial mixing/disturbance of soil in natural conditions prior to burial. Knowledge of the effects of mixing/disturbance on thermal and hydraulic properties of soils will help discriminate such locations from undisturbed soils.
- Improve our fundamental understanding of the non-isothermal, multi-phase flow processes of water, water vapor and air in the shallow subsurface by performing controlled experiments under transient conditions at hierarchy of scales using soils with accurately known hydraulic/thermal properties.
- Use experimental data to test existing theories with the goal of developing appropriate numerical models that will become part of a "virtual laboratory" that could be used for the simulation of threat detection scenarios.

Enter List of papers submitted or published that acknowledge ARO support from the start of the project to the date of this printing. List the papers, including journal references, in the following categories:

(a) Papers published in peer-reviewed journals (N/A for none)

Received		Paper
08/23/2013	14	Kathleen M. Smits, Toshihiro Sakaki, Stacy E. Howington, John F. Peters, Tissa H. Illangasekare. Temperature Dependence of Thermal Properties of Sands across a Wide Range of Temperatures (30–70°C), Vadose Zone Journal, (10 2012): 0. doi: 10.2136/vzj2012.0033
08/23/2013	17	Kathleen M. Smits, Abdullah Cihan, Viet V. Ngo, Tissa H. Illangasekare. Reply to comment by Michael D. Novak on "Evaporation from soils under thermal boundary conditions: Experimental and modeling investigation to compare equilibrium and nonequilibrium based approaches", Water Resources Research, (05 2012): 0. doi: 10.1029/2011WR011609
08/23/2013	16	Kathleen M. Smits, Viet V. Ngo, Abdullah Cihan, Toshihiro Sakaki, Tissa H. Illangasekare. An evaluation of models of bare soil evaporation formulated with different land surface boundary conditions and assumptions, Water Resources Research, (12 2012): 0. doi: 10.1029/2012WR012113
08/23/2013	15	Kathleen M. Smits, Abdullah Cihan, Toshihiro Sakaki, Stacy E. Howington, John F. Peters, Tissa H. Illangasekare. Soil Moisture and Thermal Behavior in the Vicinity of Buried Objects Affecting Remote Sensing Detection: Experimental and Modeling Investigation, IEEE Transactions on Geoscience and Remote Sensing, (05 2013): 0. doi: 10.1109/TGRS.2012.2214485
09/18/2014	21	Andrew C. Trautz, Kathleen M. Smits, Paul Schulte, Tissa H. Illangasekare. Sensible Heat Balance and Heat-Pulse Method Applicability to In Situ Soil-Water Evaporation, Vadose Zone Journal, (06 2014): 0. doi: 10.2136/vzj2012.0215
09/26/2014	26	Hossein Davarzani, Kathleen Smits, Ryan M. Tolene, Tissa Illangasekare. Study of the effect of wind speed on evaporation from soil through integrated modeling of the atmospheric boundary layer and shallow subsurface, Water Resources Research, (01 2014): 0. doi: 10.1002/2013WR013952
12/06/2015	28	Kathleen M. Smits, Abdullah Cihan, Andrew C. Trautz. Continuum-scale investigation of evaporation from bare soil under different boundary and initial conditions: An evaluation of nonequilibrium phase change, Water Resources Research, (09 2015): 0. doi: 10.1002/2014WR016504
12/06/2015	29	Toshihiro Sakaki, Kathleen M. Smits. Water Retention Characteristics and Pore Structure of Binary Mixtures, Vadose Zone Journal, (01 2015): 0. doi: 10.2136/vzj2014.06.0065
12/06/2015	30	Kathleen Smits, Victoria Eagen, Andrew Trautz. Exploring the Effects of Atmospheric Forcings on Evaporation: Experimental Integration of the Atmospheric Boundary Layer and Shallow Subsurface, Journal of Visualized Experiments, (06 2015): 0. doi: 10.3791/52704
TOTAL:	**9**	

Number of Papers published in peer-reviewed journals:

(b) Papers published in non-peer-reviewed journals (N/A for none)

Received	Paper

TOTAL: **7**

Number of Papers published in non peer-reviewed journals:

(c) Presentations

Wallen, B., K.M. Smits and S.E. Howington. Thermal conductivity of binary sand mixtures evaluated through the full range of saturation. Hydrology Days. Colorado State University, Ft. Collins, CO, March, 2015. (poster)

Smits, K.M., A.C. Trautz, B. Wallen and A. Cihan. Study of the effect of soil disturbance on vapor transport through integrated modeling of the atmospheric boundary layer and shallow subsurface. American Geophysical Union Fall Meeting. San Francisco, CA, Dec 2014. (poster)

Trautz, A., K.M. Smits, T.H. Illangaseare and P. Schulte. 2014. Experimental investigation of atmospheric and soil effects on boundary layer development above the land atmosphere interface. American Geophysical Union Fall Meeting. San Francisco, CA, Dec 2014. (poster)

Wallen, B., A.C. Trautz, and K.M. Smits. 2014. Comparison of evaporative fluxes from porous surfaces resolved by remotely sensed and in-situ temperature and soil moisture data. American Geophysical Union Fall Meeting. San Francisco, CA, Dec 2014. (poster)

Trautz, A., K.M. Smits, T.H. Illangaseare and P. Schulte, 2014. Investigation of the influence of boundary layer turbulent flow on heat and mass and momentum exchange at the land-atmosphere interface. Gordon Research Conference. Bates College, ME, July 2014. (poster)

Trautz, A.C., K.M. Smits, A. Cihan. 2013. Evaporation and condensation in soils: Experimental and modeling investigation to compare non-equilibrium-based approaches under different atmospheric boundary conditions. American Geophysical Union Fall Meeting. San Francisco, CA, Dec 2013. (poster)

Davarzani, H., K.M. Smits and T.H. Illangasekare. 2013. Study of the effect of wind speed on evaporation from soil through integrated modeling of atmospheric boundary layer and shallow subsurface. European Geophysical Union, Vienna, Austria, April 2013. (poster)

Trautz, A., K.M. Smits, A. Cihan, and T.H. Illangasekare. 2013. Evaporation from soils under diurnal boundary conditions:Experimental and modeling investigation to evaluate nonequilibrium-based approaches. European Geophysical Union, Vienna, Austria, April 2013. (poster)

Davarzani, H., K.M. Smits and T.H. Illangasekare. 2012. Study of the effect of wind speed on evaporation from soil through integrated modeling of atmospheric boundary layer and shallow subsurface. American Geophysical Union Fall Meeting. San Francisco, CA, Dec 2012. (presentation)

Trautz, A., K.M. Smits, P. Schulte, A. Cihan, and T.H. Illangasekare. 2012. Integration of heat-pulse and sensible heat balance methods to estimate. American Geophysical Union Fall Meeting. San Francisco, CA, Dec 2012. (poster)

Trautz, A., K.M. Smits, and T.H. Illangasekare. 2012. Integration of heat-pulse and sensible heat balance methods to estimate. Gordon Research Conference, Les Desiblertes, Switzerland, June 2012. (poster)

Smits, K. M., V.J. Ngo, A. Cihan, and T.H. Illangasekare. 2012. Evaporation from soils subjected to natural boundary conditions at the land-atmospheric interface, European Geophysical Union, Vienna, Austria, April 2012. (poster)

Illangasekare, T.H., K. Smits, T.Sakaki and A. Cihan. 2011. Soil Moisture Processes in the Shallow Subsurface Near Land/Atmospheric Interface- Challenges and New Research Approaches, Invited speaker at “Perspectives for the Future of Hydrology in a Changing Environment. Memorial Session in Honour of Professor Jim Dooge”, European Geological Union, Annual Meeting, Vienna , April 2011. (presentation)

Illangasekare, T.H., K. Smits, V. Ngo, A. Limsuat, T.Sakaki and A. Cihan, 2011. Soil Moisture Processes in the Shallow Subsurface Near Land/Atmospheric Interface- Opportunities, Challenges and New Research Approaches, - Borland Lecturer, AGU Hydrology Days, Colorado State University, 2011. (presentation)

Smits, K. M., V.J. Ngo, A. Cihan, T. Sakaki, and T.H. Illangasekare. 2011. An experimental and modeling study of evaporation from bare soils subjected to natural boundary conditions at the land-atmospheric interface American Geophysical Union Fall Meeting, San Francisco, CA, Dec 2011. (poster)

Smits, K. M., V.J. Ngo, A. Cihan, T. Sakaki, and T.H. Illangasekare. 2011. Numerical simulation on the effect of heterogeneity on evaporation/condensation in soils under diurnal temperature fluctuations, Proceedings from MODFLOW and More, Golden, CO, June, 2011. (poster)

Illangasekare, T.H., K. Smits, A. Limsuwat and T. Sakaki. 2011. Soil moisture processes in the near surface unsaturated zone: experimental investigations in multiscale test systems. Annual Meeting of the International Society for Porous Media (Interpore 2011) Proceedings from Interpore, Bordeaux, France, March, 2011. (presentation)

Smits, K.M., T. Sakaki, and T.H. Illangasekare. 2011. Thermal conductivity of soils as affected by temperature, Proceedings from Hydrology Days. Colorado State University, Fort Collins, CO, March, 2011. (presentation)

Number of Presentations: 18.00

Non Peer-Reviewed Conference Proceeding publications (other than abstracts):

Received	Paper
08/30/2011	5 Kathleen M. Smits, , Abdullah Cihan, , Toshihiro Sakaki, , Stacy Howington, , John Peters, Tissa H. Illangasekare. The effect of heterogeneity on evaporation/condensation in soil – numerical simulation, Modflow and More . 09-MAY-11, . : ,
08/30/2011	6 Kathleen M. Smits,, Viet V. Ngo, , Abdullah Cihan, , Toshihiro Sakaki, Tissa H. Illangasekare. An experimental and modeling study of evaporation from bare soils subjected to natural boundary conditions at the land-atmospheric interface, American Geophysical Union Fall Meeting. 05-DEC-11, . : ,
TOTAL:	**2**

Number of Non Peer-Reviewed Conference Proceeding publications (other than abstracts):

Peer-Reviewed Conference Proceeding publications (other than abstracts):

Received	Paper
TOTAL:	

Number of Peer-Reviewed Conference Proceeding publications (other than abstracts):

(d) Manuscripts

Received		Paper
08/29/2012	8.00	Toshihiro Sakaki, Anuchit Limsuwat, Abdullah Cihan, Christophe C. Frippiat, Tissa H. Illangasekare. Water Retention in a Coarse Soil Pocket under Wetting and Drainage Cycles, Vadose Zone Journal (03 2011)
08/29/2012	10.00	Kathleen M Smits, Viet V. Ngo, Abdullah Cihan, Toshihiro Sakaki, Tissa Illangasekare. An evaluation of models of bare soil evaporation formulated with different land surface boundary conditions and assumptions , Water Resources Research (04 2012)
08/29/2012	9.00	Kathleen M. Smits, Abdullah Cihan, Viet V. Ngo, Tissa H. Illangasekare. Reply to comment by Michael D. Novak on ‘‘Evaporation fromsoils under thermal boundary conditions: Experimental andmodeling investigation to compare equilibrium and nonequilibriumbased approaches’’, Water Resources Research (08 2011)
08/30/2011	1.00	Toshihiro Sakaki, Anuchit Limsuwat, Tissa H. Illagasekare. A simple method for calibrating dielectric soil moisture sensors: laboratory validation in sands, Vadose Zone Journa (03 2011)
08/30/2011	2.00	Toshihiro Sakaki, Anuchit Limsuwat, Tissa H. Illangasekare. An improved air pressure measuring method and demonstrated application to drainage in heterogeneous soils, Vadose Zone Journal (05 2011)
08/30/2011	3.00	Toshihiro Sakaki, Anuchit Limsuwat, Abdullah Cihan, Christophe C. Frippiat, Tissa H. Illangasekare. Water retention in a coarse soil pocket under wetting and drainage cycles, Vadose Zone Journal (05 2011)
08/30/2011	4.00	Kathleen M. Smits,, Abdullah Cihan,, Toshihiro Sakaki,, Stacy E. Howington,, John F. Peters, Tissa H. Illangasekare. SOIL MOISTURE AND THERMAL BEHAVIOR IN THE VICINITY OF BURIED OBJECTS AFFECTING REMOTE SENSING DETECTION: EXPERIMENTAL AND MODELING INVESTIGATION , IEEE Transactions on Geoscience and Remote Sensing (08 2011)
08/30/2011	7.00	Kathleen M. Smits, Abdullah Cihan, Toshihiro Sakaki, Tissa H. Illangasekare. Evaporation from soils under thermal boundary conditions: experimental and modeling investigation to compare equilibrium and nonequilibrium based approaches, Water Resources Research (01 2011)
08/30/2012	11.00	Kathleen M. Smits, Abdullah Cihan, Toshihiro Sakaki, Stacy E. Howington, John F. Peters, Tissa H. Illangasekare. SOIL MOISTURE AND THERMAL BEHAVIOR IN THE VICINITY OF BURIED OBJECTS AFFECTING REMOTE SENSING DETECTION: EXPERIMENTAL AND MODELING INVESTIGATION , IEEE Transactions in geophysics (05 2011)
08/30/2012	12.00	Kathleen M. Smits, Toshihiro Sakaki, Stacy E. Howington , John F. Peters, Tissa H. Illangasekare. Temperature dependence of thermal properties of sands over a wide range of temperatures [30-70oC], Vadose Zone Journal (05 2012)

TOTAL: **10**

Number of Manuscripts:

Books

Received Book

TOTAL:

Received Book Chapter

TOTAL:

Patents Submitted

Patents Awarded

Awards

Illangasekare
2015 Langbein Lecture for the American Geophysical Union's Bowie Lectures
Fellow of the Soil Science Society of America
Henry Darcy Medal, 2012, European Geological Union
Shimuzu Fellow, Dept. of Civil and Environmental Engineering, Stanford University, 2012

Smits
2015 National Science Foundation CAREER Award

Graduate Students

NAME	PERCENT_SUPPORTED	Discipline
Andrew Trautz	0.50	
Benjamin Wallen	0.05	
Tiande Wu	0.05	
FTE Equivalent:	**0.60**	
Total Number:	**3**	

Names of Post Doctorates

NAME	PERCENT_SUPPORTED
FTE Equivalent:	
Total Number:	

Names of Faculty Supported

NAME	PERCENT_SUPPORTED	National Academy Member
Kathleen M Smits	0.10	
Tissa Illangasekare	0.05	
Toshi Sakaki	0.01	
FTE Equivalent:	**0.16**	
Total Number:	**3**	

Names of Under Graduate students supported

NAME	PERCENT_SUPPORTED	Discipline
Victoria Eagen	0.09	Mechanical Engineering
Kira Dickey	0.09	Geophysics
Christopher Jenkins	0.09	Mechanical Engineering
Tiande Wu	0.09	Environmental Engineering
FTE Equivalent:	**0.36**	
Total Number:	**4**	

Student Metrics

This section only applies to graduating undergraduates supported by this agreement in this reporting period

The number of undergraduates funded by this agreement who graduated during this period: 3.00

The number of undergraduates funded by this agreement who graduated during this period with a degree in science, mathematics, engineering, or technology fields:..... 3.00

The number of undergraduates funded by your agreement who graduated during this period and will continue to pursue a graduate or Ph.D. degree in science, mathematics, engineering, or technology fields:..... 1.00

Number of graduating undergraduates who achieved a 3.5 GPA to 4.0 (4.0 max scale):..... 2.00

Number of graduating undergraduates funded by a DoD funded Center of Excellence grant for Education, Research and Engineering:..... 0.00

The number of undergraduates funded by your agreement who graduated during this period and intend to work for the Department of Defense 0.00

The number of undergraduates funded by your agreement who graduated during this period and will receive scholarships or fellowships for further studies in science, mathematics, engineering or technology fields:..... 1.00

Names of Personnel receiving masters degrees

NAME
Tiande Wu
Andrew Trautz
Total Number: **2**

Names of personnel receiving PHDs

NAME
Andrew Trautz
Total Number: **1**

Names of other research staff

NAME	PERCENT_SUPPORTED
FTE Equivalent:	
Total Number:	

Sub Contractors (DD882)

Inventions (DD882)

Scientific Progress

See Attachment

Technology Transfer

See Attachment

FINAL REPORT

PROJECT NUMBER: 55120-EV

FOR PERIOD BEGINNING OCT 1, 2010 AND ENDING SEPT 30, 2014

TEMPORAL AND SPATIAL DISTRIBUTION OF SOIL MOISTURE IN HETEROGENEOUS VADOSE ZONE WITH MOISTURE BARRIERS AS AFFECTED BY ATMOSPHERIC BOUNDARY CONDITIONS

Principal Investigator: Tissa H. Illangasekare
AMAX Distinguished Chair of Environmental Science and Engineering and Professor of Civil Engineering
Director, Center for Experimental Study of Subsurface Environmental Processes (CESEP)
Colorado School of Mines, Golden CO 80401
Tel: 303 384 2126; Fax:303 273 3311; e-mail: tissa@mines.edu;
URL: cesep.mines.edu

Co-principal Investigator: Kathleen Smits
Assistant Professor
Department of Civil and Env. Engineering
Colorado School of Mines, Golden CO 80401
Tel: 303 384 2126; Fax:303 273 3311; e-mail: ksmits@mines.edu

Co-principal Investigator: Toshihiro Sakaki
Now at International Services and Projects Division
National Cooperative for the Disposal of Radioactive Waste
Wettingen, 5430, Switzerland.

Submitted to: David M. Stepp
Chief, Terrestrial Science Branch
Engineering and Environmental Sciences Division
Army Research Office
P.O. Box 12211
Research Triangle Park, NC 27709-2211

March 30, 2015

TABLE OF CONTENTS

1. Project Overview and Summary

1.1 Objectives

This research seeks to improve our understanding of the non-isothermal, multi-phase flow processes of water, water vapor and air in the shallow subsurface by performing controlled experiments at different test scales under transient conditions using soil with accurately known hydraulic/thermal properties. Experimental data is used to test existing theories and appropriate numerical models, providing new insights into mass flux and thermal process interactions**.** This work provides a critical step toward refining our understanding of the non-isothermal, multi-phase flow processes of water, water vapor and air in the shallow subsurface coupled with thermal processes in order to better predict the spatial and temporal distribution of soil moisture/temperature around buried objects such as landmines. It is our hope that this data and knowledge of the fundamental processes that occur at the land/atmospheric interface will improve the comprehension and interpretation of sensor imagery and lead to the development of more robust signal processing and interpretation techniques that allow for the discrimination of real threats from anomalies that results from natural processes. In addition to landmine detection, this knowledge is critical to many engineering applications, including the efficiency of thermal remediation of contaminated soils, the flux of CO_2 from soil, natural or forced ventilation, and water resource management in dry land.

Primary aims of the project are to:

- To develop a better understanding of the hydraulic and thermal characteristics of mixed or disturbed soils as well as the temperature dependence of thermal properties. The burying of landmines involves artificial mixing/disturbance of soil in natural conditions prior to burial. Knowledge of the effects of mixing/disturbance on thermal and hydraulic properties of soils will help discriminate such locations from undisturbed soils.
- Improve our fundamental understanding of the non-isothermal, multi-phase flow processes of water, water vapor and air in the shallow subsurface by performing controlled experiments under transient conditions at hierarchy of scales using soils with accurately known hydraulic/thermal properties.

- Use experimental data to test existing theories with the goal of developing appropriate numerical models that will become part of a “virtual laboratory” that could be used for the simulation of threat detection scenarios.

A project funded by the Air Force Office of Scientific Research (AFOSR) investigates non-isothermal multiphase flow in the shallow subsurface. Research conducted under the AFOSR study makes a comprehensive look through both experimental and modeling how the fluid flow processes in the atmosphere are coupled with the shallow subsurface water and moisture flow. The fundamental research conducted in the AFOSR study specific to land/atmospheric coupling has helped in the ARO project. Because of this close relevance, relevant findings from the AFOSR study are also presented in this final report.

1.2 Approach

Experimental simulations are performed to generate data to obtain insights on the coupled processes of heat and mass flow in soils near the land surface that are affected by natural and human activities (e.g. digging and backfilling), parameterization of these coupled processes, scale dependence of parameters that capture the critical processes, up-scaling of the parameters in heterogeneous field systems to regional and global scales and validation of models for theoretical analysis. Our approach uses various experimental setups that include small and intermediate scale cells and tanks, and modeling codes to develop comprehensive data sets and modeling tools that meet the needs of the Army.

The questions that are raised and hypotheses that are tested as part of this research can only be addressed through careful experimentation in the laboratory. Data available from field sites are incomplete and costly to obtain, and the degree of control that is needed to obtain a fundamental understanding of processes and to generate data for model validation are inadequate. Experiments for this work are performed in the Center for Experimental Study of Subsurface Environmental Processes (CESEP) using various size 2-dimensional soil tank apparatuses. Soil tanks and the atmosphere above them are equipped with an array of state of the art sensor technologies, allowing for the collection of accurate data at high temporal and spatial resolutions. Within each soil tank, soil moisture, capillary pressure, air pressure, water pressure, temperature and relative humidity distributions are monitored. In the atmosphere, air pressure, airspeed, air turbulence, temperature and relative humidity are measured at fine spatial resolutions using air pressure sensors, relative humidity and temperature sensors.

- **Characterization of the hydraulic/thermal properties of mixed/disturbed soils under different temperatures**: When a landmine or any other object is buried, the native soil conditions are often altered or disturbed due to human activity (e.g., digging and backfilling). In addition, in the case of artificial mixing of top soil with underlying soil for example, the grain size distribution and hydraulic and thermal properties of the locally mixed soil may be quite different from that of the surrounding soil; it can be bi- or multi-modal (e.g., very coarse soil is mixed with very fine soil). Although it is well known that the apparent thermal conductivity (λ) of partially wet soil is a function of water (θ) and air content, available λ–θ data is scarce, incomplete and very often limited to specific soils, select moisture content values and select temperatures partially due to difficult, laborious and error-prone experiments. As demonstrated by Smits et al. (2010 and 2012), the scarcity of experimental data reported in previous reports leads to empirical models that do not reflect the actual relationship between thermal conductivity and soil properties such as soil moisture, porosity, and temperature. This task investigates the hydraulic and thermal properties of soils as a function of water saturation, porosity (which is directly related to the degree of disturbance caused by digging/backfilling) and temperature (22 – 70^{o}C). Different sands, varying in grain size and mixture (in which the grain size distribution is not smooth) were used.

- **Experimental investigation of small-scale hydrologic and thermal patterns in the vicinity of buried anomalies:** In this task, our focus is on the effects of artificial disturbance/mixing of soil on soil moisture and temperature behavior in the shallow subsurface at an intermediate scale. We consider a mine field typically encountered in arid regions. In this investigation, we assume a specific field setting that has little surface vegetation and is covered by a somewhat coarse soil layer. The action of moving/mixing the soil to bury a mine causes surface disturbances, such as texture changes, and induces a decrease of soil phase in the layer over the mine. The mixing process alters the hydraulic/thermal properties of the soil.
  - **Model validation using data generated:** The goal of this task is to identify the conditions that create distinct differences in the spatial and temporal distribution of soil moisture around subsurface anomalies (i.e. heterogeneities to include different soil types, rocks, surrogate land mines, metal objects etc.) as a result of changes in atmospheric conditions using a fully coupled numerical model to solve the governing

equations for heat, liquid water and water vapor transport in soil. The theoretical analysis necessary for up-scaling the knowledge from the laboratory to the field is conducted using models validated using the experimental data. The code implements a non-isothermal solution that accounts for non-equilibrium liquid/gas phase change with gas phase vapor diffusion and fully couples atmospheric and subsurface flow conditions. This work expands our exploration of the effects of the soil environment on heat and mass transfer processes by investigating the influences of buried anomalies and surface conditions on evaporation/condensation processes, liquid water and water vapor flow.

1.3 Technical Significance and Army Relevance

The overall goal of this research is to improve our understanding of the non-isothermal, multi-phase flow processes of water, water vapor and air in the shallow subsurface in order to better predict the spatial and temporal distribution of soil moisture. Research findings will help in providing more spatially refined soil moisture and temperature distribution predictions, enabling the Army to better understand, model/simulate, and predict the environmental conditions that are most relevant to mine detection performance. The experimental data sets generated by the investigators at CSM provide a systematic experimental study of the effects of the near surface boundary conditions on soil moisture and temperature distributions in the shallow subsurface. Increasing our knowledge of the effects of geohydrologic/thermal properties and behaviors on the landmine signature will ultimately help to properly interpret sensor imagery. In addition, experimental results can be used to validate numerical results from the ERDC's Computational TestBed.

Results allow for a variety of scenarios to be tested that would be costly or difficult to test in the field. This knowledge is critical to many Army applications in addition to mine detection, including the efficiency of thermal remediation of contaminated soils, vapor intrusion into structures, leakage of sequestered CO_2 through the unsaturated zone, and water resource management in dry land. Benefits to the Army come from (1) cost savings from the use of CSMs unique experimental capabilities, (2) cost savings from using models that have the ability to simulate possible conditions that may be encountered in a real mine field setting 3) accurate environmental assessments and effective remedial

design (e.g. vapor intrusion into buildings and subsurface structures at DoD to facilities and bases).

1.4 Summary of the status of the project tasks

This section provides a summary of the status of the project tasks. Details on the status of each task can be found in subsequent chapters.

<u>Task 1</u>: Characterization of the hydraulic/thermal properties of the mixed/disturbed soils, and for different temperatures

This study presents a comprehensive set of soil hydraulic and thermal properties for uniform and mixed sands with different porosities for a wide range of temperatures and soil moistures. Based on our knowledge on soil mixing, we selected a mixture of two sands that is expected to show distinct effects due to mixing. A set of hydraulic conductivity tests, water characteristic curve measurements and thermal property measurements were prepared. These soils and the thermal and hydrologic data was used in experiments in intermediate scale test tanks (i.e. task #2) to obtain data to validate methods and modeling tools used for landmine detection. *Our study is novel as thermal and hydraulic properties of soils were measured in a "continuous" manner as a function of temperature, water saturation, and porosity for both homogeneous and mixed soils. In addition, we develop a new functional form to relate soil moisture and temperature to thermal conductivity. This work resulted in three peer reviewed publications over the course of this project. This work is highlighted in chapters 2 and 3.*

<u>Task 2</u>: Experimental investigation of small-scale hydrologic and thermal patterns in the vicinity of buried objects

In this task, our focus is on the effects of changes in atmospheric conditions on soil moisture and temperature behavior in the shallow subsurface at a relatively small scale. Details of this task can be found in chapter 4-5. We also performed a series of experiments that focused on equilibrium vs. nonequilibrium phase change as well as ways to properly capture evaporation processes (chapters 5 and 6). Experimental results will be presented together with numerical results as part of Task 3 (below). *This study is novel in that water retention behavior in disturbed soil embedded in an undisturbed soil has never been investigated in this manner. In addition, the upward flow or re-distribution of moisture to dry regions has not been experimentally demonstrated and therefore is not*

included in modeling efforts, prior to our study here. Because the presence of moisture in the soil greatly influences the magnitude of the maximum thermal contrast that occurs around a buried object, this knowledge is critical to accurately comprehending and interpreting sensor imagery. This work resulted in four publications over the course of this project.

Task 3: Model validation using data generated

The goal of this task was to validate existing simulation codes using the experimental data collected in Task 2 in order to gain further insight into the fundamental process of heat and liquid water and water vapor transport in the shallow subsurface. Several numerical simulations are currently being performed for various laboratory simulations. Numerical results are included in chapters 5 and 6.

In Chapter 5, we investigate five different concepts used to model phase change. Equilibrium phase change is traditionally used in hydrology. The assumption is that the change from liquid water to water vapor (and vice versa) occurs instantaneously. The more realistic, yet not commonly employed method accounts for the time associated with the phase change. In this work, we developed a new formulation to properly model non-equilibrium phase change.

Chapter 6 presents a model that is based on the coupling of Navier-Stokes free flow and Darcy flow in porous medium. Results demonstrate that the coupling concept can predict very well the different stages of drying process in porous media. Increasing the wind speed increases the evaporation rate at low velocity values; then, at high values of wind speed the evaporation rate becomes independent of flow in free fluid. *This work resulted in two peer reviewed publications over the course of this project.*

1.5 Technology Transfer:

- The PI's, Illangasekare and Smits and PhD student Wallen had a conference call with ERDC scientists to discuss findings from soil mixture work (November 2013). ERDC scientist, Stacy Howington, contributed extensively to the work and is a co-author on the manuscript on the thermal properties of soil mixtures work that is currently under review.

- The PI Smits had a conference call with ERDC scientists to discuss incorporating a field component into future research efforts (January 2014). ERDC scientists are designing an experimental plan with PI Smits and PhD student Wallen.

- March 2014 shared data and numerical model with ERDC scientists on nonequilbrium phase change to include in modeling efforts. The data and model are being used to compare with ERDC in house modeling efforts. PI Smits continues to discuss the mathematical theory with ERDC scientists monthly (April through September 2014). These discussions are on-going and will lead to collaborations/ publications between ERDC scientists and the PI's that are currently being written.

- The PI's, Illangasekare, Smits and PhD student Rice visited ERDC in August 2012 to present research results and findings to ERDC scientists. In addition, Rice stayed at ERDC for two weeks to work with ERDC scientists on both numerical modeling and experimental procedures. The meetings resulted in ERDC and the PI's providing each other with experimental ideas on sensor technologies and sampling procedures, resulting in better and more complete data sets.
- Scientists from ERDC visited Colorado School of Mines on March 5-6, 2013 to discuss research findings. The two day meeting included talks and research brainstorming on soil disturbance, land/atmospheric interaction processes and chemical detection of buried objects. The PI's provided ERDC researchers with 4 experimental data sets that they are using for their numerical modeling efforts.
- The PI, Smits, assisted two ERDC scientists throughout the year on land/atmospheric modeling concepts and how to properly couple single phase free flow with multi-phase porous media flow. These discussions are on-going and will lead to collaborations/ publications between ERDC scientists and the PI's that are currently being written.
- The PI's, Illangasekare and Smits visited ERDC in November 2011 to present research results and findings to ERDC scientists. In addition, Smits visited ERDC for one week to work with ERDC scientists on both numerical modeling and experimental procedures. The PI's provided ERDC with two-dimensional

experimental data sets on the temporal and spatial distribution of soil moisture/temperature in the vadose zone that can be used to better understand fundamental processes and validate numerical models. Experimental results can be used to validate numerical results from the ERDC's Computational TestBed.

- The PI, Smits, assisted the ERDC with implementing two concepts into their developmental code in July 2012. The proper functional form that describes the relationship between soil water content and capillary pressure under water contents lower than residual was recommended. In addition, the proper function to describe flow due to capillary flow and film flow was recommended for inclusion.
- The PI's, Illangasekare and Smits visited ERDC in July 2012 to present the research results and findings to ERDC scientist and engineers. The PI's discussed ways that the Army can include the proper coupling of Navier-Stokes free flow and Darcy flow in porous medium in their codes.
- The research team provided the ERDC with two-dimensional experimental data sets in November 2010 on the temporal and spatial distribution of soil moisture/temperature in the vadose zone that can be used to better understand fundamental processes and validate numerical models Experimental results can be used to validate numerical results from the ERDC's Computational TestBed.

- The research team assisted the ERDC with implementing two concepts into their developmental code, Pi-ADH, the Adaptive Hydrology Groundwater Model in November-December 2010. The proper functional form that that describes the relationship between thermal conductivity, water content and temperature was recommended. Water vapor flow under varying temperature gradients was applied based on a concept that allows non-equilibrium liquid/gas phase change with gas phase vapor diffusion.

- The PI, Illangasekare visited ERDC in June 2011 to present the research results and findings at a PI meeting attended by the ARO program director, other investigators funded by ARO and ERDC scientist. The PI also had separate meetings with other ERDC scientist with overlapping interests in the shallow subsurface soil moisture processes.

2.0 Water retention properties and pore structure of binary mixtures

Abstract

The mixing of different sized soil particles is known to affect soil properties such as density, porosity, hydraulic conductivity and soil water retention. To better understand how the mixing controls these properties, especially the soil water retention, a set of laboratory experiments was performed using binary mixtures with seven different mixing fractions. For each mixture, the water retention property, porosity and saturated hydraulic conductivity were obtained. To enhance the effects of mixing, coarse and fine sands with a relatively large particle size contrast were used. Results showed two distinct ranges of the volumetric fraction of fine particles where the soil behavior was controlled either by the coarse or fine particles. At equal to or above a fine fraction of 0.3, the fine particles controlled the behavior. Introducing more coarse particles to the fine particles led to rather gradual changes in the water retention property. Wall effects at the coarse-fine interfaces are largely responsible for the changes in the water retention curves. For the mixtures with a fine fraction lower than 0.3, the displacement pressure was the same or very close to that of the coarse sand due to the unfilled pores between the coarse particles. None of the obtained water retention curves for the binary mixtures showed a sign of the pore structure being dual porosity to which a superposition of the retention curves of each pore component is applicable.

2.1. Introduction

The particle size distribution (PSD) of soils varies over a wide range from relatively narrow (e.g., beach sand) to very wide, and sometimes, multi-modal (e.g., aggregated loam). PSD is oftentimes used to characterize soils, nonetheless, it does not contain all of the information necessary to define the soil's properties (*Assouline and Roualt*, 1997). To determine the hydraulic properties of the soil (e.g., hydraulic conductivity, water retention), additional knowledge, such as the packing of the soil particles and the pore size distribution is necessary. Knowledge on how the physical properties of the soils are controlled by factors such as mineral composition, particle size distribution, or compaction conditions is important in various applications, for example, when soil materials with certain hydraulic or thermal characteristics are needed in the fabrication of synthetic soil liners for landfills (e.g., *Jones*, 1954; *Holtz and Lowitz*, 1957; *Garga and Madureira*, 1985; *Fragasy et al.* 1990; *Shelly and Daniel*, 1993), backfill for soil borehole thermal energy storage systems (e.g. *Ohga and Mikoda*, 2001; *High-Combi*, 2008), and agricultural soils affecting productivity (e.g., *Moroizumi and Horino*, 2002).

It is well known that the porosity of a two component mixture (i.e. binary mixture) is dependent on the volumetric fraction of each particle size and the ratio of the particle diameters. Two granular materials of uniform but different sizes represented as spheres, when mixed, can produce a lower mixture porosity under certain packing conditions; the porosity of the mixture is always less than the linear combination of the porosities of the two materials. In addition, a porosity minimum is always observed for some combination of the two materials in the mixture. A large number of studies have come out from the ceramic and powder industries related to particle packing and controlling density (e.g., *Westman and Hugill*, 1930; *Westman*, 1936; *Ouchiyama and Tanaka*, 1984; *Stovall et al.*,

1986). *Westman and Hugill* (1930) performed a series of experiments on binary mixtures generated by mixing a set of coarse particles (hereinafter referred to as C, with the mean diameter of *D*) with a set of fine particles (hereinafter referred to as F, with the mean diameter of *d*). They tested mixtures with different diameter ratios, *D*/*d*, ranging from 50.5 to 6.3. For all *D*/*d* combinations tested, a minimum porosity was achieved for mixtures containing 30% by volume of fine particles (i.e., C:F ratio was 7:3). Other researchers followed this early study for applications in soil sciences. *Holts and Lowitz* (1957), *Garga and Madureira* (1985), and *Fragaszy et al.* (1990) studied compaction behavior of gravelly soils and reported that the maximum density was achieved at about 70% gravel content, consistent with the findings in the ceramic studies mentioned above. In addition, *Westman and Hugill* (1930) stated that significant reduction in porosity (or increase in bulk density) was observed for $D/d \geq \sim 7$. *Koltermann and Gorelick* (1995) generalized that when the volume fraction of fine material equals the porosity of the coarse-grained material, the fine material completely fills the pores of the coarser grains (hereinafter, referred to as the primary pore) and a minimum porosity is achieved. This fraction of the fine material is referred to as the critical fine fraction (f_{crit}). As will be described in the latter sections, when the fine fraction is above this critical volume fraction, the fine material controls the behavior of the soil while below the critical fraction, the dominant mode of the coarse material controls the sample's behavior.

The difference in the particle packing is oftentimes referred to as coarse or fine packing (*Clarke*, 1979). In the coarse packing, smaller particles are contained within the pore space created by coarse particles that carry the load through grain contacts (also known as grain supported). In the fine packing, coarser particles are dispersed and/or floated in a fine-grained matrix (also known as matrix supported) (*Clarke*, 1979). The minimum porosity occurs when the small particles completely fill the voids of the load-

bearing, larger particles which corresponds to, as noted above, a fine fraction of ~30%. The porosity reduction is typically on the order of a factor of ~2. Quantitative relationships have been developed for the porosity of a mixture of coarse and fine particles and will be discussed later.

Unlike the small changes in porosity that result from small changes in fine content, the permeability of binary mixtures, varies by orders of magnitude with small changes of fine content (e.g., *Hazen*, 1911; *Krumbein and Monk*, 1942; *Collins*, 1961; *Koltermann and Gorelick*, 1995; *Milczarek et al.*, 2006; *Kamann et al.*, 2007; *Zhang*, 2011). When the fraction of fine particles is less than the critical value (~30% by volume, i.e., coarse-packing), some primary pores between the large particles remain unfilled. Such unfilled pores form connected paths, leading to a significant increase in hydraulic conductivity; i.e., the permeability is controlled by the coarse particles. For mixtures with a fine fraction larger than the critical value (i.e., fine-packing), the variation is generally not as significant, demonstrating a more gradual change. Changes in the hydraulic conductivity for various D/d ratios are described, for example, in *Zhang* (2011). Other studies such as those by *Tyc et al*. (1988); *Knoll and Knight* (1994); *Robinson and Freidman* (2001) focus on the effect of particle mixing on the dielectric permittivity.

Retention of water in soils, typically described by the relationship between the capillary pressure or matric potential (P_c) and water content (θ), or equivalently saturation (S), hereinafter, referred to as the water retention curve, WRC, is controlled by capillarity that is largely determined by soil pore size distribution. The pore size distribution is, in turn, determined by a combined effects of soil texture (particle-size distribution), and soil structure (arrangement of the particles) (e.g., *Haverkamp et al.*, 2002). Despite a large body of literature on estimating the WRC from particle (or pore) size distribution for a wide range of soils (e.g. *Gupta and Larson*, 1979; *Arya and Paris*, 1981; *Saxton et al.*,

1986; *Haverkamp and Parlange*, 1986; *Wu et al.*, 1990; *Smettem and Gregory*, 1996; *Assouine et al.*, 1998; *Schaap et al.*, 1998), and on how density or porosity is affected by mixing two or more soils with different grain sizes (e.g., *Westman and Hugill*, 1930; *Westman*, 1936; *Ouchiyama and Tanaka*, 1984; *Stovall et al.*, 1986), our survey of hydrology and soil science literature on how the WRC is affected by mixing two sets of particles with different particle sizes showed extremely limited study.

Dunner (1994) investigated some water retention data for soils that were not well represented by a sigmoidal shape that can be defined, e.g., by the parametric model proposed by *van Genuchten* (1980). In loamy soils, aggregates can form and potentially affect the pore size distribution in its intermediate range (e.g., *Dunner*, 1994). Biological processes such as plant growth or animal activities can also result in pores that are even larger than those induced by aggregation processes (e.g., *Dunner*, 1994). The secondary pore system that is different than that of the original soil result in a dual-porosity system for which the water retention curves do not exhibit a typical sigmoidal shape but a bimodal or multimodal shape. *Dunner* (1994) also states that such bimodal/multimodal water retention curve can be observed for soils with a specific particle size distribution. For these soils, a flexible water retention model (where two unimodal retention curves were superimposed) was shown to better represent the non-sigmoidal shape. However, it is unknown to what extent binary mixtures exhibit WRCs that can be described by the superposition of WRC of each particle set.

In this study, using two uniform sands with different particle sizes (i.e., coarse and fine), we generated a set of binary mixture samples with different mixing fractions. Each of the sand samples has a narrow particle size distribution and, thus, exhibits a highly unimodal water retention curve. For each binary mixture, the WRC was measured. By changing the mixing fraction in a systematic manner, we investigated how binary mixing

affects the water retention curves, in particular, whether or not binary mixing results in a retention curve with a non-sigmoidal or bi-modal shape. The retention curves were obtained only for the primary drainage cycle under tightly compacted conditions. Porosity and hydraulic conductivity were also obtained for each binary mixture to verify findings in literature and support that the mixture samples are well prepared (mixed).

2.2. Material and methods

This section will first discuss the test sands and mixtures, followed by a description of the experimental setup and procedure.

2.2.1 Test sands and binary mixtures

The two sand samples, coarse (C) and fine (F), selected to investigate how the C:F ratios influence the water retention curves, are as follows. The coarse sand was Accusand #12/20 (mean grain size D = 1.04 mm, uniformity coefficient = 1.2, Unimin Co., Ottawa, MN) whereas the fine sand was Ottawa sand #110 (mean size d = 0.12 mm, uniformity coefficient = 1.7, U.S. Silica Co., Ottawa, MN). The grain size distributions of the two sands are shown in **Figure 1**. When tightly packed, both sand samples have a porosity of 0.33 and bulk dry density of 1.78 g/cm^3. These two sand samples with a sufficiently large particle size contrast (D/d = 8.7) were selected to enhance the effect of different C:F mixing ratios according to the finding of, e.g., *Westman and Hugill* (1930).

The two sands were mixed at seven different C:F ratios; 10:0, 9:1, 8:2, 7:3, 5:5, 2:8 and 0:10, respectively. These samples are referred to as C10F0, C9F1, C8F2, C7F3, C5F5, C2F8 and C0F10, respectively. Selected properties are provided in **Table 1**.

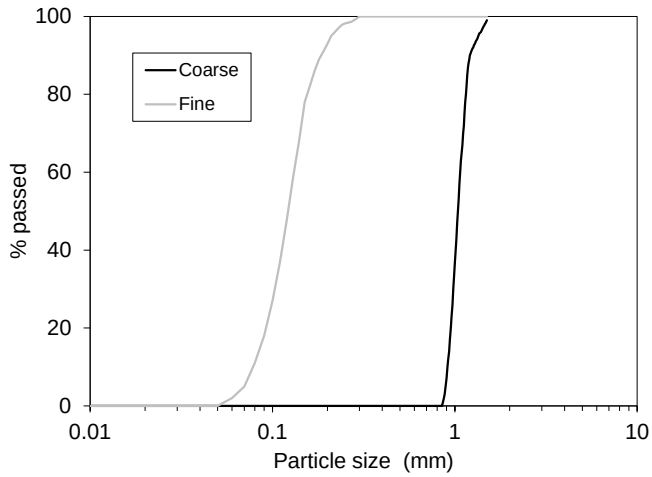

Figure 1. Grain size distribution of the coarse and fine sand.

Table 1. Selected properties of the mixtures. Porosity and dry density values are for the samples used to measure the WRC. Saturated hydraulic conductivity was measured using separate mixture samples.

mixtures	dry density (g/cm^3)	porosity	saturated hydraulic conductivity* Ks (cm/s)	displacement pressure** Pd (kPa)	remark
C10F0	1.77	0.336	0.38	0.78	coarse only
C9F1	1.95	0.264	0.080	0.78	
C8F2	2.05	0.227	0.016	0.99	
C7F3	2.15	0.190	0.0036	6.0	critical mixture
C5F5	1.96	0.260	0.0036	6.3	
C2F8	1.87	0.294	0.0044	7.6	
C0F10	1.74	0.342	0.0050	7.8	fine only
* corrected to 20 ^{o}C, constant-head method					
** estimated using a method described in Corey and Brooks (1997)					

The measured porosity values of the seven sand samples are shown in **Figure 2** demonstrating how they relate to the zero mixing, ideal (*Clarke*, 1979) and partial mixing models (*Zhang*, 2011). The three models summarized in *Zhang* (2011) were selected to define the upper, lower and intermediate bounds. The upper bound was defined by assuming no mixing between the two materials, the lower bound by assuming full/ideal mixing where fine particles fill the void spaces of the pore spaces between the coarse particles (*Clarke*, 1979). The intermediate porosities due to partial mixing that are more realistic (*Zhang*, 2011) in which a mixing coefficient that takes a value between 0 (no mixing) and 1 (full mixing) was introduced to describe the degree of partial mixing. In the study of *Zhang* (2011) using binary mixtures with a wide range of D/d, the mixing coefficient used in the partial mixing model was found to be a function of the fine fraction, the average value (i.e., averaged over the whole fine fraction range) was fitted to be 0.0363 (D/d) + 0.2326 for $D/d < 21$. Our binary mixtures had a D/d value of 8.7 which led to the mixing coefficient of 0.548. For the prediction shown in **Figure 2**, this value was used. More details of the three models can be found in *Zhang* (2011).

It can be observed in **Figure 2** that the seven different mixtures of our samples roughly agreed with the porosity values predicted based on the partial mixing theory. The coarse sand has a porosity of about 0.33 (i.e., primary pore as defined earlier). If extremely fine particles (with a porosity of 0.33) are used to fill the pores, the remaining pore space available will be 33% of the primary pores, i.e., 0.11 (hereinafter, referred to as the secondary pore) of the total volume. The combination of the two sands with $D/d = 8.7$ perhaps did not lead to a "perfect" filling of the primary pores, thus, the C7F3 mixture resulted in a porosity of 0.19 which is somewhat larger than 0.11. The best-fit empirical

equation proposed by *Zhang* (2011) to estimate the mixing coefficient also suggests that the mixing coefficient increases as D/d increases (i.e., smaller particles become finer). This implies that as D/d increases, mixing conditions approach the perfect mixing. The empirical equation by *Zhang* (2011) yields a mixing coefficient of 1 (i.e., perfect mixing) when $D/d = 21$; this perhaps indicates that the binary mixture will practically be perfectly mixed when D/d is 21 or larger (unless other factors such as aggregation becomes dominant as observed in one of the silt mixture dealt by *Zhang* (2011)). In this study, however, identifying the optimal mixing coefficient for our mixture samples or validating the equation by *Zhang* (2011) were not the main scope, no further fine tuning/fitting of the mixing coefficient was performed. Nonetheless, the porosity data strongly suggest that the mixing of these samples is well described by the partial mixing theory by *Zhang* (2011).

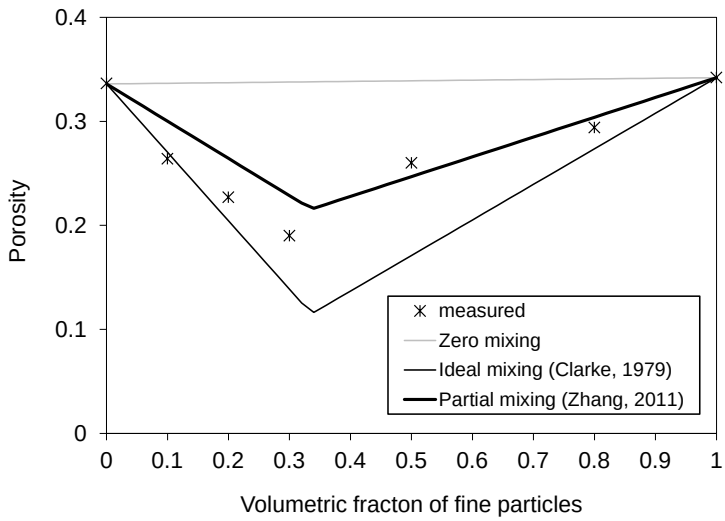

Figure 2. A comparison of the porosity of the measured data with predictions made using the zero, ideal and partial mixing models

Figure 3 shows the saturated hydraulic conductivity (K_s) values obtained for the seven sand mixtures with different C:F ratios. The mixtures were separately prepared for the permeability tests using a constant-head column apparatus. As our focus in this study was on the water retention property of binary mixtures, the permeability tests were

performed only to confirm the findings that K_s is controlled by the coarse particles below f_{crit} and by the fine particles above f_{crit}, respectively, as reported in past studies (e.g., *Marion et al*, 1992; *Shakoor and Cook* 1990; *Zhang* 2011).

The results in **Figure 3** show that the K_s values show a bi-log-linear behavior that is distinctly separated at f_{crit} (= 0.3). For fine contents greater than the critical value f_{crit} (C7F3, C5F5, C8F2 and C0F10 mixtures), data show that the K_s is essentially that of the fine grained component (i.e., fine-controlled) and not much affected by the fraction of the fine particles. This was also shown in other studies (e.g., *Marion et al.,* 1992; *Shakoor and Cook*, 1990, *Zhang*, 2011). As described by *Koltermann and Gorelick* (1995), the behavior of K_s with fines can be explained by the geometry and size distribution of the pores that control the fluid flow.

Starting with the fine grained sand (C0F10) in **Figure 3**, some coarse particles are added to the fine grained sand (e.g., C2F8). The coarse grains displace some of the fines, and the porosity somewhat decreases but the pore structure is still fine controlled. The presence of coarse particles distributed over the domain reduces the effective cross sectional area for the flow to occur. This explains the observation that K_s is slightly lower for the mixtures C7F3, C5F5 and C8F2 with coarse particles as compared to that of the fine particles only (C0F10). Nonetheless, K_s is practically that of the fine grained sand. As more coarse grains are added to the mixture, the percentage of the fines decreases until the fraction of the fines reaches f_{crit} (i.e., C7F3) and then becomes less than f_{crit} (i.e., C8F2, C9F1). At this point, there are enough coarse particles in contact with one another to form a load-bearing skeleton. Due to the insufficient amount of fine particles to fill all of the primary pores, more primary pores become free of and/or partially filled with the fines. The measured K_s is then reflecting that of the coarse particles (i.e., coarse-controlled) and increases rapidly as the fine fraction decreases. Finally, when there are no fines left, the K_s

is that of the coarse particles. These observations are generally consistent with the findings for binary mixtures with a relatively large *D*/*d* ratio reported in the past study, e.g., by *Zhang* (2011).

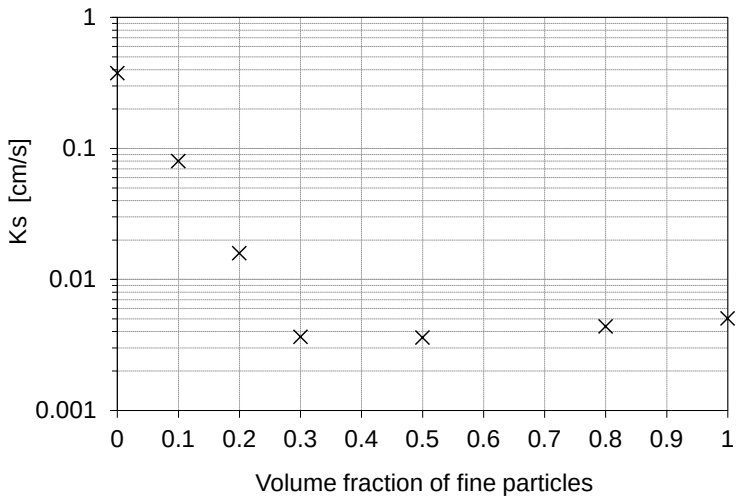

Figure 3. Measured saturated hydraulic conductivity obtained for binary mixtures with various C:F ratios (*D*/*d*=8.7). Data were obtained using the constant-head method and corrected to 20^{o} C.

2.2.2 Experimental setup and procedures for WRC measurement

The experimental setup used in this study for measuring the WRC is shown in **Figure 4**. The cell was equipped with a soil moisture sensor (EC-5, Decagon Devices, Inc. Pullman, WA) and a tensiometer (porous cup with a diameter = 0.64 cm, length = 2 cm, air entry pressure = 51kPa, PN 0652X03-B0.5M2, Soilmoisture Equipment Co., Santa Barbara, CA). Another large porous cup (diameter = 1 cm, original length = 10 cm and cut to 6.5 cm, air entry pressure = 51 kPa, high flow, PN 0652X04-B0.5M2, Soilmoisture Equipment Co., Santa Barbara, CA) was installed about 1.5 cm above the cell bottom as a drain port. This was used instead of a porous plate (that is typically used for a Tempe cell type setup) and was connected to a 2 m-long water reservoir. Each mixture was thoroughly mixed, wet-packed in the cell shown in **Figure 4** and compacted by tapping the cell and

sand sample as much as possible. The porosity (shown in **Table 1** and **Figure 2**) was calculated from the known particle density (= 2.65 g/cm^3) and height of the sample at the end of tapping.

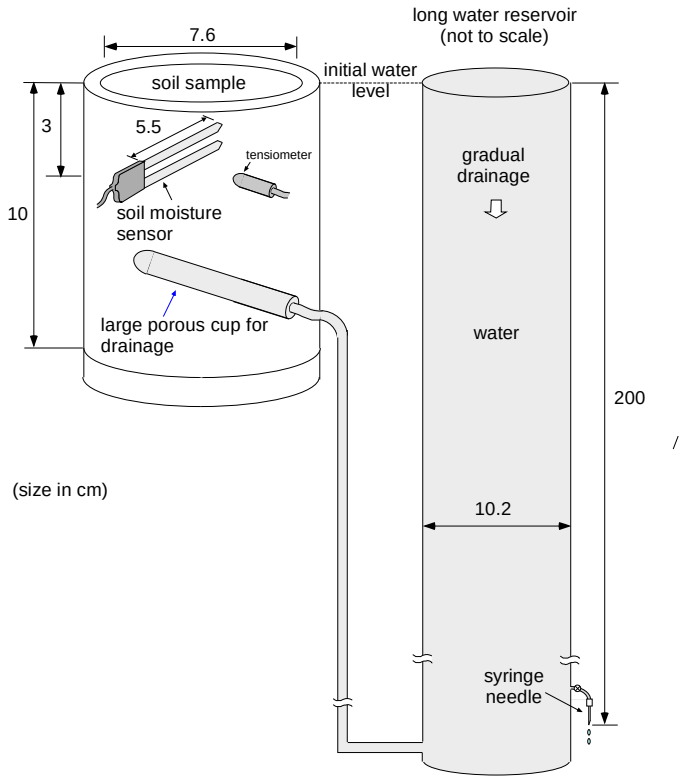

Figure 4. Experimental setup for measuring the WRC. The water reservoir is not to scale.

The water level in the soil was initially set to the surface of the soil sample. Drainage of water from the soil sample was induced by lowering the water level in the water reservoir through a syringe needle attached near the bottom of the water reservoir to induce a gradual and continuous drainage. An appropriate needle gauge was chosen for each mixture sample to achieve a reasonable drainage rate (roughly 0.1–0.5 kPa/hour for the mixtures C10F0, C9F1, C8F2, C7F3, C5F5, C2F8 and, 2.6 kPa/hour for C0F10). Slow drainage rates were selected such that it would be fair to assume that the effect of dynamic capillary pressure as described by, for example, *Hassanizadeh et al.*, 1990, *Sakaki et al.*, 2010 and *Camps-Roach et al.*, 2010 could be neglected. The soil moisture sensor was

calibrated in accordance with the method developed by Sakaki *et al.* (2008; 2010). The soil water pressure captured by the tensiometer was measured using a precision pressure transducer (P55D, Validyne Engineering Corp., Northridge, CA, accuracy ±0.25% full scale). The water saturation and water pressure in the soil were recorded every one minute.

2.3. Results and discussion

2.3.1 Water retention curves

The measured WRC as defined in this study as the P_c-θ relationships for the seven sand mixtures with different C:F ratios are presented in **Figure 5**. Displacement pressure (P_d) was also evaluated for each curve (*Corey and Brooks*, 1997) and plotted in **Figure 6**. In these figures, the water retention properties are distinctly different depending on the C:F ratio. As observed for the hydraulic conductivity, the WRC and P_d values can be divided into two groups; fine- and coarse-controlled for the mixtures with the fine fraction higher or lower than f_{crit}, respectively. The results for each group were analyzed closely and the findings are provided below.

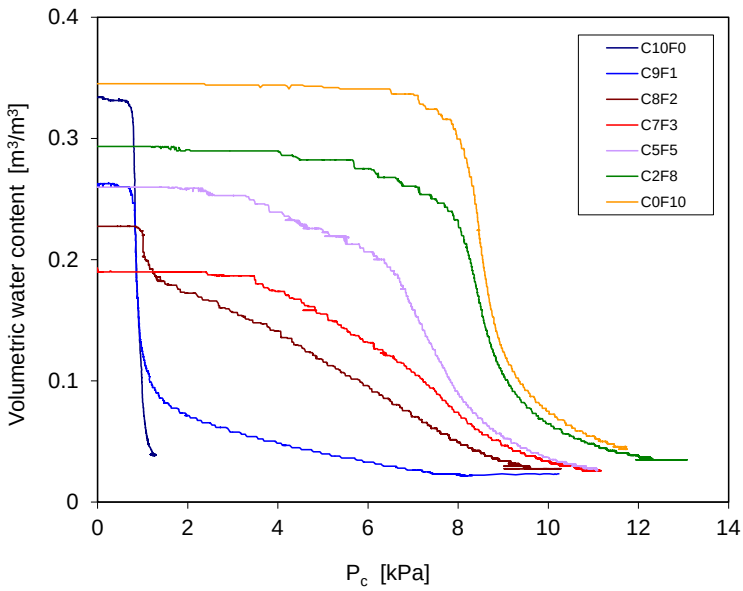

Figure 5. WRCs (P_c-θ relationships) obtained for the binary mixtures with various C:F ratios (primary drainage cycle, D/d=8.7).

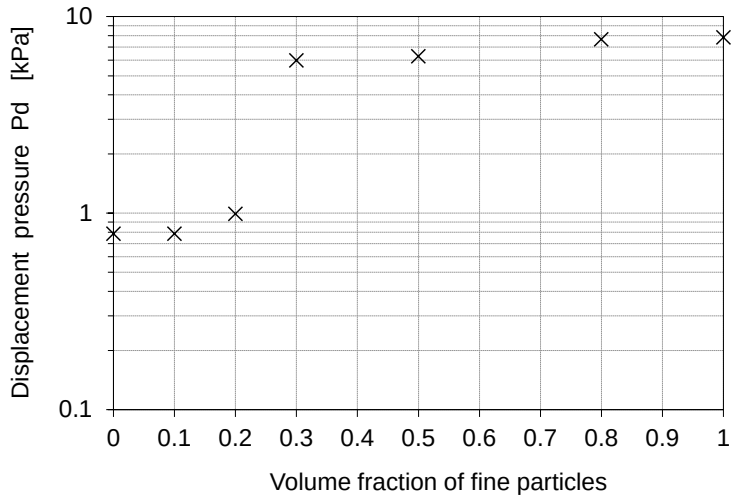

Figure 6. Displacement pressure obtained for the binary mixtures with various C:F ratios (primary drainage cycle, D/d=8.7). The method described in *Corey and Brooks* (1997) was used.

Fine-controlled mixtures:

The water retention property of the C0F10, C2F8, C5F5 and C7F3 mixtures are largely controlled by the fine particles. The C0F10 exhibits the water retention property consistent with other published data (e.g., *Sakaki and Illangasekare*, 2007). As the fraction of fine particles decreases, the general trend is that for the same water content, P_c decreases gradually. The reduction of porosity resulting from mixing of coarse and fine particles described in **Figure 2** also affects the shape of the WRCs. The P_d values decrease gradually as the fine fraction decreases. This gradual change results from introducing large particles (significantly larger than the fine particles) leading to an increase in the pore size due to the following two possible reasons. First, at all of the surfaces of the coarse particles, fine particles are forced to align along the surfaces, leading to the pore size between the fine particles along the surface of the coarse particles being somewhat larger than that of the randomly packed fine particles. Secondly, some large pores between the coarse particles remain due to imperfections in the soil mixing.

Because of these effects (for the fine-controlled mixture, the former is expected to be more dominant), distributed within the mixture samples, the macroscopic water retention behavior results in somewhat lower displacement pressure as more coarse particles are introduced. Note that for C5F5 and C7F3 mixtures, the retention curves exhibit a slight kink roughly at P_c = 7 kPa, resulting in non-sigmoidal WRCs. For these samples, P_d gradually decreased as the coarse fraction increased as noted above. After a certain P_c is reached in these curves, retention of water is more dominantly controlled by the pores of the fine particles rather than the pores at the interface between the coarse and fine particles.

Coarse-controlled mixtures:

The retention property of C8F2, C9F1 and C10F0 are quite different than those for the fine-controlled mixtures. Results showed a displacement pressure equal or close to that of the coarse sand followed by a rapid drainage, resulting in a flat portion in the retention curves. Those with smaller fine fractions showed a longer flat portion on the P_c-θ curves. For the mixtures with a fine fraction less than f_{crit}, the amount of fine particles is insufficient to fill the primary pores between the coarse particles. Ideally, if the two sands are perfectly mixed, the pores between the coarse particles are filled with the fines uniformly as in **Figure 7a**. Under these conditions, every primary pore between the coarse particles has a somewhat similar pore size and the displacement pressure would show a stronger dependence on the fine fraction as observed in the hydraulic conductivity. This would result in a mirrored behavior of **Figure 3** rather than what is observed in **Figure 6**.

In reality, however, mixing is not as ideal or uniform, and some pores are filled more with the fines and other are filled less or even not filled at all as illustrated in **Figure 7b**. Under such conditions, the less-filled or unfilled primary pores will drain early, resulting in a P_d that is the same or close to that of the coarse sand. Therefore, the

retention behavior of the binary mixtures with fine fractions less than that of C7F3 is strongly "coarse-controlled". After the large pores drain and the suction continues to increase, rather rapid drainage proceeds. As soon as the effect of the fines starts taking control, the timing of which is controlled by the amount of fines, the water retention curve becomes steeper. This behavior was well pronounced for the C1F9 sample in **Figure 6**. Inhomogeneity effects due to the somewhat uneven distribution of the small particles to the large particles on a macroscale in the mixing seem to affect the water retention property more than the hydraulic conductivity presented in **Figure 3.** This is because drainage occurs at a lower P_c which is clearly observed in the P_c-θ curves whereas the hydraulic conductivity is an averaged behavior of all of the filled, partially-filled and unfilled pores (i.e., a combined effect of the unmixed and well-mixed parts).

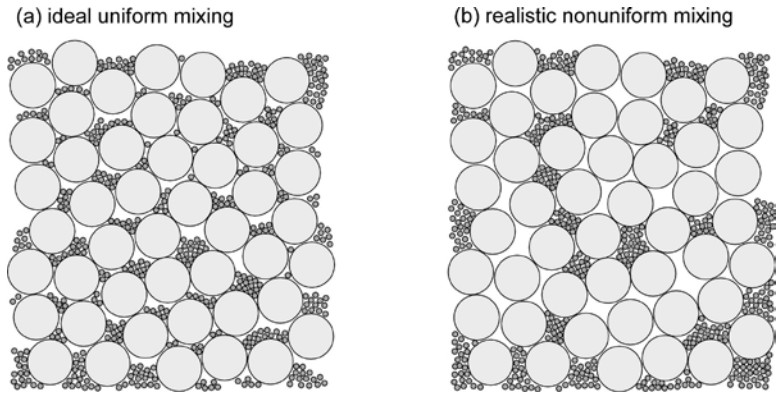

Figure 7. Schematic illustration of particle packing conditions, left) ideal mixing where all primary pores are uniformly filled, right) actual mixing where some of the primary pores remain unfilled.

It has to be noted here that none of the WRCs for the intermediate mixtures (i.e., C9F1, C8F2, C7F3, C5F5 and C2F8) can be well described by a simple superposition of two WRCs (e.g., *Dunner*, 1994 proposed for a dual porosity system for which the WRCs for both pore systems are known) of the coarse only (C10F0) and fine only (C0F10) sample. For example, although the curve is not shown, superposition of C0F10 and C10F0

curves at a 1:1 ratio leads to a sharp step in the curve at half the porosity and does not show any similarity with the C5F5 curves observed in **Figure 5**. This suggests that mixing of two sets of uniform particles result in a pore system that is different than the typical dual porosity system. In the next section, an attempt was made to better understand the effect of mixing on the pore structure.

2.3.2 Estimation of pore structure

To verify the interpretation described in section 3.1 and to better understand the pore structure of the binary mixtures, water retention data were further analyzed. First, the water retention curves were differentiated (i.e., $d\theta/dP_c$, specific capacity, **Figure 8** left column). The shape of this curve implies at what P_c values the release of water is significant. Knowing that the release of water is a function of pore size, the derivatives were then related to pore size (**Figure 8** right column). The values of P_c were converted into the effective pore diameter (d_e) which is obtained simply by re-writing an equation for water rise in a capillary tube as follows;

$$d_e = \frac{4\gamma \cos\delta}{\rho_w g P_d} \tag{1}$$

where, γ is the surface tension force, δ is the contact angle, ρ_w is the water density (= 1000 kg/m^3), and g is the gravitational force (=9.8 m/s^2). This analysis provides a visual indication of the distribution of pore size.

In **Figure 8**, the derivative for the C0F10 mixture showed a sharp peak at around P_c = 8 kPa which corresponds to the P_d of this material. It distributes roughly over 6 < P_c < 12 kPa. The corresponding d_e is roughly from 0.025 to 0.05 mm with the peak observed

at around 0.033 mm, which is roughly 30% of the particle diameter. The past studies by *Kamiya et al*. (1996) and *Takahashi et al*. (2008) suggested that for uniform materials, the mean pore size is about 30 % of the particle size. Our results agreed closely with their findings.

For the C2F8 mixture, the peaks are less distinct but seen at the same P_c (i.e., d_e) and spread slightly toward lower P_c. This implies that the water retention property is very close to that of the C0F10 sample. Adding 20% of coarse particles to fine particles generate a mixture where the coarse particles are somewhat sparsely distributed and floating in the fine particles. Under such conditions, the water retention property is not affected significantly. Slight spread of the derivative toward the smaller P_c (i.e., larger d_e) is probably due to, as mentioned earlier, the surface of the coarse particles force the fine particles to align which leads to somewhat larger pore size. It is presumed that such pores caused some of the pore water to be released at a lower P_c.

In the results of C5F5 sample, the peaks became even less distinct compared to those for the C2F8 mixture. Also noteworthy is that the peaks were observed at around P_c of ~7 kPa and effective pore diameter of 0.04 mm. Mixing two sets of particles with a distinct D/d at a 1:1 ratio, results in a mean pore size which is only slightly larger than that of the fine particle only sample; this is mainly due to the wall effect mentioned above. Nevertheless, at this mixing ratio, the retention property is still dominantly controlled by the fine particle because the coarse particles are still "floating" in the fine particles.

For the C7F3 mixture, $d\theta/dP_c$ further spreads over $3 < P_c < 10$ kPa corresponding to 0.03 to 0.09 mm. Although the peaks are only slightly detectable, they still appear at P_c of 7.5 kPa and d_e of 0.04 mm. At this mixing fraction, the amount of the fine particle just fills the void spaces between the coarse particles. Therefore, the void spaces are still determined largely by those between the fine particles and those at the large-fine particle

interfaces. The data does not show any evidence of unfilled pores between the large particles.

The mixtures with the fine fraction less than 30%, however, started to show quite different behavior. The C8F2 mixture showed a similar spectrum of P_c and d_e as C7F3 except it extended to a lower P_c (larger effective pore diameter) and showed a peak at P_c of ~1 kPa and d_e of 0.3 mm. This indicates that the main pore structure is somewhat similar to C7F3 but some of the primary pores between the coarse particles now remain unfilled. This is because the C8F2 mixture, again, does not have a sufficient amount of fine particles to fill all the void spaces between the coarse particles. The peak observed at the d_e of ~0.3 mm is roughly 30% of the diameter of the coarse particles. This justifies that the unfilled pores range from partially filled to fully unfilled as illustrated in **Figure 7**. If the unfilled pores are uniformly unfilled as in **Figure 7a**, the peak would have been observed at somewhat higher P_c (smaller d_e) that reflects the size of the uniformly unfilled pores. In the C9F1 mixture, this behavior is more distinct. Due to a fine fraction of only 10%, the pores controlled by the fine particles are disappearing. Instead, the peak in the P_c and effective pore diameter is more distinct. Just like the C8F2 mixture, the unfilled pores between the coarse particles indicate the non-uniform filling as those not filled with the fine particles are controlling the drainage of water. Finally, in results for the C10F0 sample (coarse only), none of the wide spectrum in the P_c and effective pore diameter is observed indicating the results reflects solely the effect of the pores between the coarse particles.

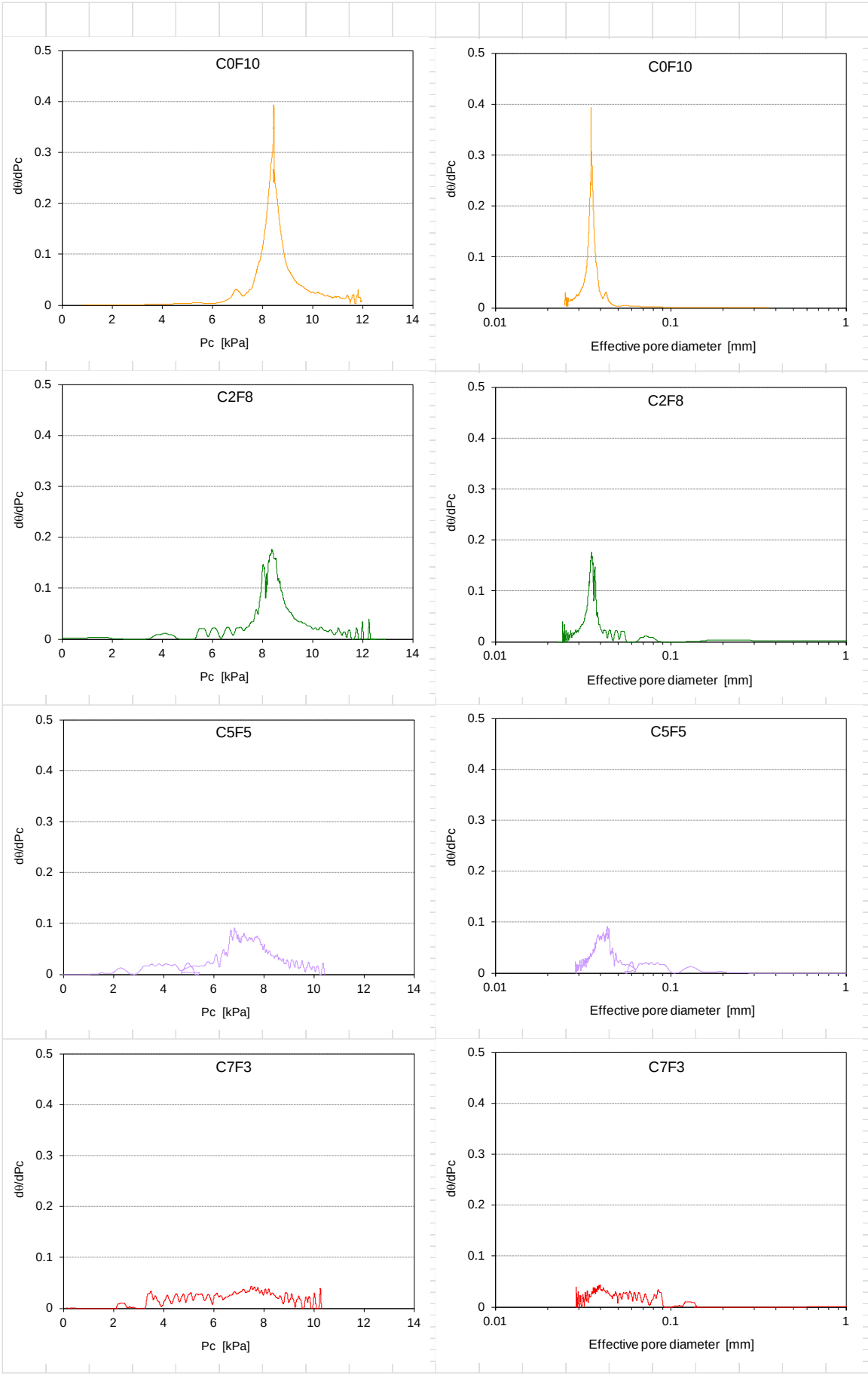
C0F10
dθ/dPc
Pc [kPa]
C0F10
dθ/dPc
Effective pore diameter [mm]
C2F8
dθ/dPc
Pc [kPa]
C2F8
dθ/dPc
Effective pore diameter [mm]
C5F5
dθ/dPc
Pc [kPa]
C5F5
dθ/dPc
Effective pore diameter [mm]
C7F3
dθ/dPc
Pc [kPa]
C7F3
dθ/dPc
Effective pore diameter [mm]

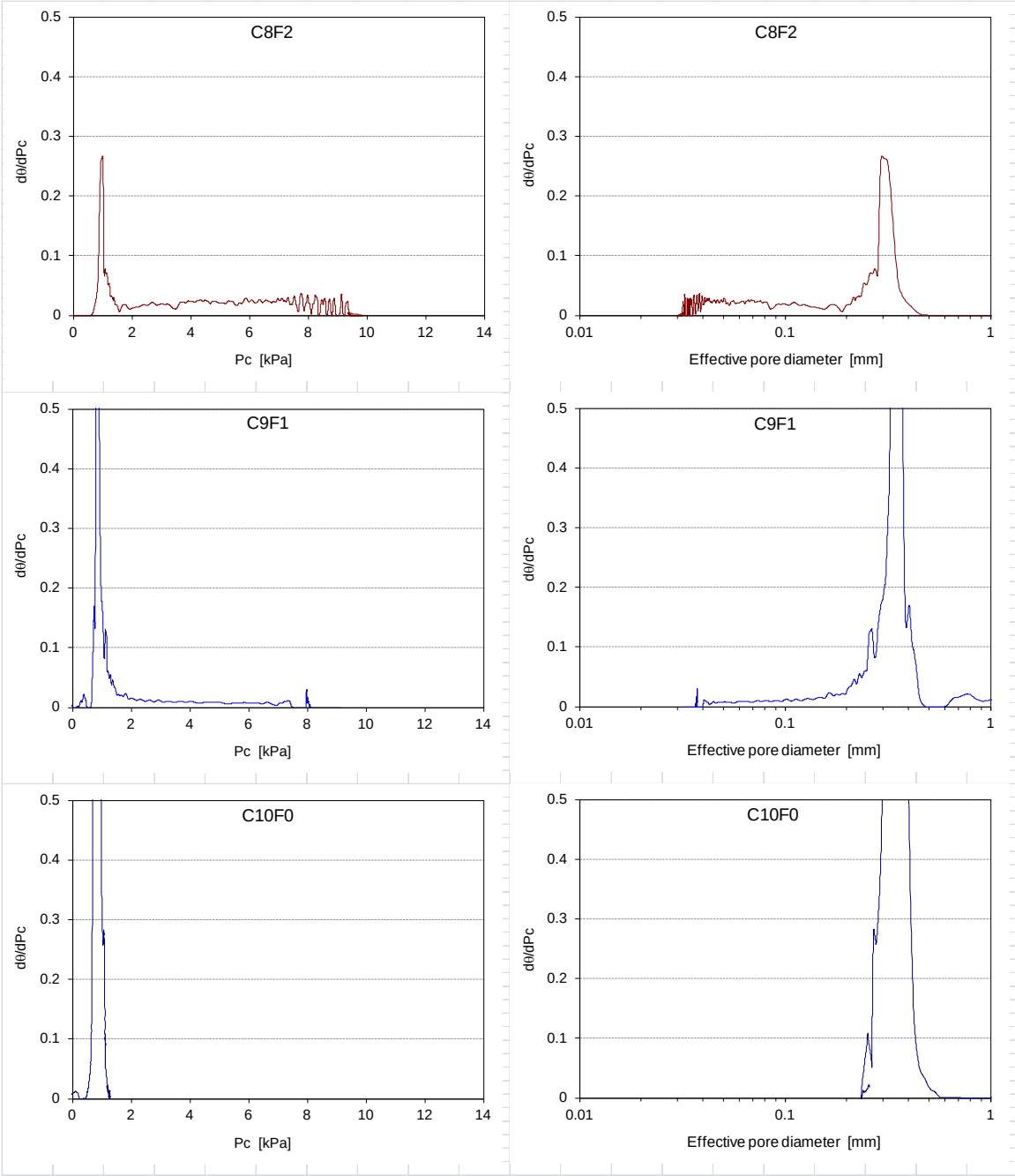

Figure 8. Left) 1st derivative $d\theta/dP_c$ of the water retention curves, Right) Estimated pore size distribution based on capillary rise equation.

An additional analysis was made for the behavior of the fine-controlled materials where the coarse particles are distributed (or "floating" as defined by *Koltermann and Gorelick*, 1995) in the fine particles. In the above interpretation, the effect of a coarse-fine interface was introduced. This is known as the *wall effect* which typically results in cyclic

porosity distribution as shown in **Figure 9**. The wall effect is typically discussed for cases where a set of particles are filled in a container with a known diameter. As the particles are forced to align at the container wall, the porosity at the wall is locally higher than the mean porosity. *Suzuki et al*. (2008) performed a series of packing tests under various conditions and proposed a mathematical model to approximate the porosity profile as a function of the distance from the wall (normalized to the particle diameter). Their results showed that if the container is significantly larger than the particle size, the porosity profile takes its highest value at the wall and reaches the average porosity only after 1~2 particle sizes away from the wall (black line in the figure). If the container size is smaller, the cyclic behavior is observed over a longer distance (grey line in the figure).

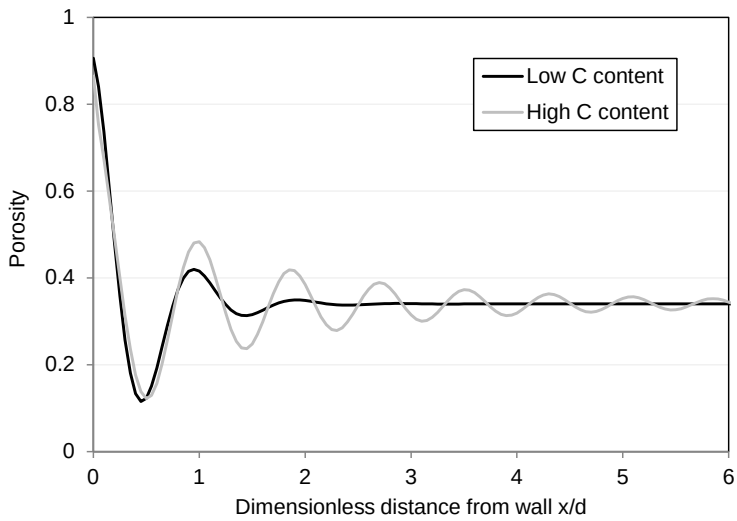

Figure 9. Porosity distributions with different levels of wall effect. The approximation proposed by *Suzuki et al*. (2008) was used to show the key features of the wall effect in the context of binary mixtures with a large *D*/*d* ratio. An average porosity of 0.34 was used based on our materials. The small particle diameter was 0.1 mm, and the container size was 10 mm for the black line and 1 mm for the grey line

For our fine-controlled mixtures, this explains the behavior observed in **Figure 8**. For C2F8 where only a relatively small amount of coarse particles are introduced,

assuming that the coarse particles are well distributed, at the surface of one of the coarse particles, the fine particles are aligned but the next coarse particle is sufficiently far. This is analogous to the case where particles are packed in a large container (black line in the figure). As more coarse particles are introduced (e.g., C5F5 and C7F3), the average distance between the coarse particles becomes smaller. This is analogous to a case where particles are filled in a small container. Therefore, the fines between the coarse particles start to exhibit the wall effect similar to the grey line in the figure. Because the cyclic behavior in **Figure 8** over a longer distance also infers that the porosity values are not only the maximum at the wall and the average value but also take more intermediate values in between (i.e., peaks in the grey line). We believe that this explains that the pore analysis for C2F8 in **Figure 8** showed a distinct generation of a small amount of pores at ~0.08 mm, and that for C5F5 and C7F3 more pores between 0.09 and 0.035 mm were generated. For the other small peak observed in C5F5 and C7F3 at ~0.14 mm, a possible cause could be uneven mixing, leading to a small amount of pores between the coarse particles that are not fully filled with fine particles.

As described in the material and methods section, the mixtures were prepared by mixing two uniform sand samples with different particle sizes, each of which has a distinct water retention curve. The above analysis suggests that the mixtures are categorized into two types; coarse-controlled (C10F0, C9F1 and C8F2) and fine controlled (C7F3, C5F5, C2F8 and C0F10). The fine-controlled mixtures resulted in pores that ranged from those of the fine particles (~0.035 mm) up to 0.09 mm. This upper limit reflects the pores induced at the fine-coarse interface where the fine particles are forced to align along the surface of the coarse particles. The C7F3 mixture is a special case where the fine particles almost perfectly filled the pores between the coarse particles. Estimated d_e values exhibited no peaks, suggesting that neither of the fine or coarse particles dominated the

pore structure. For all the coarse-controlled mixtures, on the other hand, the pore structure showed a peak only at the size that reflected that of the coarse particles. In summary, none of the binary mixture samples examined in this study showed two peaks in the estimated d_e spectrum indicating that the pore structure not being dual porosity. Although the two sands result in different pore sizes when packed separately, the mixture of these at any fractions did not lead to a binary pore structure (dual porosity) whose water retention curve is well described by the superimposing model developed by *Dunner* (1994) for soils with dual porosity.

2.4. Conclusions

The purpose of this work was to determine the effect of soil mixing on soil water retention behavior. Using two uniform sands with a relatively large particle size contrast D/d = 8.7, we created a set of binary mixtures with different C:F ratios. The WRC was measured for each mixture using a Tempe cell-based apparatus under a slow drainage. The obtained WRCs were quite different depending on the volumetric fraction of the fine particles and can be divided into two categories; fine- and coarse-controlled. Mixtures with a fine fraction equal or higher than f_{crit}, the water retention behavior as well as hydraulic conductivity were largely controlled by the fine particles. The fine only sample retained water against the highest suction. As the fraction of coarse particles increased, the mixture released water at somewhat lower suctions. This suggests that the larger particles, even when distributed in the fine particles as in C2F8 and C5F5 mixtures, contributed to increase the pore size via the wall effect. Also what is noteworthy is that the variation in porosity (or equivalently, the maximum water content) decreased by a factor of two between the C0F10 and C7F3 mixtures, consistent with, e.g., *Zhang* (2011).

For those mixtures with a fine fraction lower than f_{crit}, (i.e. coarse controlled) the displacement pressure was the same as or close to that of the coarse only sample. The hydraulic conductivity showed high sensitivity to the fraction of fine particles for coarse controlled samples. This suggests that the large pores between the coarse particles that remain partially filled or unfilled with the fine particles start to control the drainage behavior, but the hydraulic conductivity is more representative of the average behavior (i.e., a combined effect of the unmixed and well-mixed parts). These unfilled pores result from imperfections in the soil mixing during soil packing. The effect of the fine particles became noticeable as the drainage proceeded until the large unfilled pores drained. From this time on, the shape of the retention curve was controlled by the amount of the fine particles. The inflection point on the WRC appears earlier for mixtures with higher fine contents.

The obtained water retention curves for the binary mixtures did not show any sign of pore structure consisting of two pore sizes (i.e. dual porosity). For the soils with a dual porosity pore structure, as *Dunner* (1994) studied, superposition of the retention curves of each pore component described that of the whole system relatively well. However, it was found in this study that mixing two sets of particles with two different *particle* sizes generated mixtures that did not lead to a pore structure where the two different *pore* sizes were retained. Binary mixing did not necessarily exhibit dual porosity type of pore structure to which the superposition proposed by *Dunner* (1994) is applicable.

In this study, only a single value of D/d was tested. Future work studying soils with a variety of D/d values for a more detailed understanding on how binary mixing affects the hydraulic properties is needed. Furthermore, a mathematical model to predict the water retention properties of binary mixtures needs to be developed in order to properly incorporate the effects of binary mixing. Such a model should be able to

reconstruct the retention curve (shape, displacement pressure, maximum saturation or porosity, and perhaps uncertainty resulting from imperfection in mixing) when the *D*/*d* value, C:F ratio, and water retention curve of each material are provided.

Acknowledgments

This research was partly funded by the U. S. Army Research Office Award W911NF-04-1-0169. The authors acknowledge Russell S. Harmon, David Stepp and the Army Research Office for financial support and John F. Peters and Stacy E. Howington from the U.S. Army Engineer Research and Development Center (ERDC) for their technical contributions. The saturated conductivity values of the sand samples were partly measured by Anuchit Limsuwat.

References

Arya, L.M. and J. F. Paris (1981), A physicoempirical model to predict the soil moisture characteristic from particle-size distribution and bulk density data, *Soil Sci. Soc. Am. J.*, 45, 1023–1030.

Assouline, S. and Y. Rouault (1997), Modeling the relationship between particle and pore size distributions in a multicomponent sphere pack: Application to the water retention curve. *Colloid and Surfaces A*, 127: 201-209.

Assouline, S., D. Tessier, and A. Bruand (1998), A conceptual model of the soil water retention curve, *Water Resour. Res.*, 34(2), 223–231, doi:10.1029/97WR03039.

Assouline, S. (2006), Modeling the relationship between soil bulk density and the water retention curve, *Vadose Zone Journal*, 5:554-563.

Camps-Roach, G., D. M. O'Carroll, T. A. Newson, T. Sakaki, and T. H. Illangasekare (2010), Experimental investigation of dynamic effects in capillary pressure: Grain size dependency and upscaling, *Water Resour. Res.*, 46, W08544, doi:10.1029/2009WR008881.

Clarke, R. 1979. Reservoir properties of conglomerates and conglomeratic sandstones. AAPG Bull. 63:799–809.

Collins, R . E. (1961), Flow of Fluids Through Porous Materials, Reinhold, New York.

Corey, A. T. and Brooks (1997), The Brooks-Corey relationship, Proceedings of the International Workshop on Characterization and measurement of the hydraulic properties of unsaturated porous media, Part 1, Eds., M. Th. Van Genuchten, F. J. Leij and L. Wu, pp 13-18, October 22-24, Riverside California, 1997.

Durner, W. (1994), Hydraulic conductivity estimation for soils with heterogeneous pore structure, Water Resour. Res., 30(2), 211–223, doi:10.1029/93WR02676.

Fragaszy, R. J., Weizhi, S., and Siddiqi, F. H. (1990), Effects of oversize particles on the density of clean granular soils, *Geotech. Test. J.*, 13(2), 106-114.

Garga, V. K., and Madureira, C. J. (1985), Compaction characteristics of river terrace gravel, *J. Geotech. Engrg.*, ASCE, 111(8), 987-1007.

Gupta, S. C. and W. E. Larson (1979), Estimating soil water retention characteristic from particle size distribution, organic matter percent, and bulk density, *Water Resour. Res.*, 15, 1633–1635.

Hassanizadeh, S.M., and W.G. Gray (1990), Mechanics and thermodynamics of multiphase flow in porous media including interphase boundaries, *Adv. Water Resour.*, 13:169–186.

Haverkamp, R. and J. Y. Parlange (1986), Predicting the water-retention curve from a particle-size distribution: 1 Sandy soils without organic matter, *Soil Sci.*, 142, 325–339.

Hazen, A. (1911), Discussion of "Dams on sand foundations" by A. C. Koenig, *Trans. Am. Soc. Civ. Eng*., 73, 199.

High-Combi (2008), High solar fraction heating and cooling systems with combination of innovative components and methods, Report STREP, European Union.

Holtz, W. G., and Lowitz, C. W. (1957), Compaction characteristics of gravelly soils, Special Technical Publication No. 232, ASTM, Philadelphia, PA, 70-83.

Jones, C. W. (1954), The permeability and settlement of laboratory specimens of sand and sand-gravel mixtures, Special Technical Publication No. 163, ASTM, Philadelphia, PA, 68-78.

Kamann, P. J., R. W. Ritzi, D. F. Dominic, and C. M. Conrad (2007), Porosity and permeability in sediment mixtures, *Ground Water*, 45:429–438.

Kamiya, K., T. Uno and T. Matsushima (1996), Measurement of the distribution of sandy soil void diameter by air intrusion method, *Journal of Japan Society of Civil Engineers*, No. 541/III-35, 189-198 (in Japanese).

Keller, J. (1970), Sprinkler intensity and soil tilth. Trans. ASAE, 136: 118-125.

Koltermann, C. E. and S. M. Gorelick (1995), Fractional packing model for hydraulic conductivity derived from sediment mixtures, *Water Resources Research*, 31(12), 3283-3297.

Krumbein, W.C. and Monk, G.D. (1942), Permeability as a function of the size parameters of unconsolidated sand. *Technical Publs. American Ins. Mining Metallurgical Engineers, 1492-1503.*

Milczarek, M.A., D. Zyl, S. Peng, and R.C. Rice (2006), Saturated and unsaturated

hydraulic properties characterization at mine facilities: Are we doing it right? p. 1273–1286. In Int. Conf. on Acid Rock Drainage, 7th, St. Louis, MO. 26–30 Mar. 2006. *Am. Soc. Min. Reclam.*, Lexington, KY.

Marion, D., A. Nur, H. Yin, and D. Han (1992), Compressional velocity and porosity in sand-clay mixtures, *Geophysics*, 57(4), 554-563.

Moroizumi, T. and H. Horino (2002), The effects of tillage on soil temperature and soil water, *Soil Science*, 167: 548-559.

Ohga, H. and K. Mikoda (2001), Energy performance of borehole thermal energy storage systems. *Seventh Int. IBPSA Conference*. Rio De Janeiro, Brazil. August 13-15, 2001.

Or, D. (1996), Wetting-induced soil structural changes: The theory of liquid phase sintering. *Water Resour. Res*. 32:3041-3049.

Or, D., F. J. Leij, Snyder, V. and T. A. Ghezzehei (2000), Stochastic model for post tillage soil pore space evolution, *Water Resour. Res*. 36:1641-1652.

Ouchiyama, N. and T. Tanaka (1984), Porosity estimation for random packings of spherical particles, *Ind. Eng. Chem. Fundam*., 23, 490-493.

Sakaki, T., and T. H. Illangasekare (2007), Comparison of height-averaged and point-measured capillary pressure - saturation relations for sands using a modified Tempe cell, *Water Resources Research*, 43, W12502, doi:10.1029/2006WR005814.

Sakaki, T., A. Limsuwat, K. M. Smits, T. H. Illangasekare (2008), Empirical two-point α-mixing model for calibrating ECH$_2$O EC-5 soil moisture sensor, *Water Resources Research*, 44, W00D08, doi:10.1029/2008WR006870.

Sakaki, T., D. M. O'Carroll, and T. H. Illangasekare (2010), Direct quantification of dynamic effects in capillary pressure for drainage-wetting cycles, *Vadose Zone Journal*, 9:424-437, doi: 10.2136/vzj2009.0105.

Sakaki, T., A. Limsuwat, and T. H. Illangasekare (2011), A simple method for calibrating dielectric soil moisture sensors: Laboratory validation in sands, *Vadose Zone Journal*, 10:526-531, doi:10.2136/vzj2010.0036.

Saxton, K. E., W. J. Rawls, J. S. Romberger and R. I. Papendick (1986), Estimating gerenralized soil-water characteristics from texture, *Soil Sci. Soc. Am. J.*, 50, 1031–1036.

Schaap, M. G., F. J. Leij, M. Th. van Genuchten (1998), Neural network analysis for hierarchical prediction of soil water retention and saturated hydraulic conductivity, *Soil Sci. Soc. Am. J.*, 62, 847–855.

Shakoor, A. and Cook, B.D. (1990), The effect of stone content, size, and shape on the engineering properties of a compacted silty clay: *Assoc. Eng. Geol. Bull*., v. XXVII, pp. 245-253.

Smettem, K. R. J. and P. J. Gregory (1996), The relation between soil water retention and particle-size distribution parameters for some predominantly sandy Western Australian soils, *Aust. J. Soil Res.*, 34, pp. 695–708.

Smits, K. M., T. Sakaki, A. Limsuwat, and T. H. Illangasekare (2010), Thermal conductivity of sands under varying moisture and porosity in drainage-wetting cycles, Vadose Zone Journal, 9:172-180, doi:10.2136/vzj2009.0095.

Smits, K.M., A. Cihan, T. Sakaki, S.E. Howington, J.F. Peters, and T. H. Illangasekare (2013). Experimental and modeling investigation of soil moisture and thermal behavior in the vicinity of buried objects. IEEE Trans. in Geosci. Remote Sens., 10.1109/TGRS.2012.2214485.

Suzuki, M., T. Shinmura, K. Iimura and M. Hirota (2008), Study of the wall effect on particle packing structure using X-ray micro computed tomography, *Advanced Powder Technology*, 19, 183-195.

Stovall, T., F. De Larrard and M. Buil (1986), Linar packing density model of grain mixtures, *Powder Technology*, 48, 1-12.

Takahashi, M., Y. Urushimaru and H. Hirai (2008), Challenge for quantification of pore structure in rock ~ An experimental approach to glass beads by micro focus X-ray CT, *Proceedings of 12th Japan Symposium on Rock Mechanics*, 541-546.

Westman, A. E. R., and H. R. Hugill (1930), The packing of particles, *J. Am. Ceramic Soc*., Vol. 13, No. 10, 767-779.

Westman, A. E. R. (1936), The packing of particles: Empirical equations for intermediate diameter ratios, *J. Am. Ceramic Soc*., Vol. 19, 127-129.

Wu, L., J. A. Vomocil, S. W. Childs (1990), Pore size, particle size, aggregate size, and water retention, *Soil Sci. Soc. Am. J.*, 54, 952–956

Zhang, Z. F., A. L. Ward, J. M. Keller (2011) Determining the porosity and saturated hydraulic conductivity of binary mixtures, *Vadose Zone Journal*, 10:313–321 doi:10.2136/vzj2009.0138.

3.Thermal conductivity of binary sand mixtures evaluated through the full range of saturation

Abstract

Mixing of different sized soil particles affects soil physical and hydraulic properties however little is known on its effect on soil thermal properties. To better understand how soil mixing controls soil thermal properties, especially thermal conductivity, a set of laboratory experiments was performed using binary mixtures of two uniform sands with seven different mixing fractions over the full range of saturation. For each binary mixture, thermal conductivity, capillary pressure and water content were measured. For each sample, the effect of packing on thermal conductivity was isolated as a function of porosity. The apparent thermal conductivity, λ, to saturation, S, relationship exhibited distinct characteristics based upon the percentage of fine grained sand. The critical fraction of fines causing a shift between coarse and fine controlled mixtures occurred at a fine fraction of 0.3, with fine particles controlling the thermal behavior above 0.3. Coarse-controlled mixtures were characteristic of more abrupt, rapidly decreasing λ from saturated to residual conditions. Fine-controlled mixtures portrayed more gradual decreases in λ. Changes in rate of decrease for binary mixtures are correlated with the four saturation regimes (i.e. hydration, pendular, funicular and capillary). Measured λ-S properties were then compared with independent estimates from five models. Results show good agreement for the Campbell et al. (1994) and Lu and Dong (2014) models. A comparison between the experimental results and model predictions highlight the importance of understanding the impact of packing conditions on the thermal conductivity

of soils and the need for accurate experimental data sets to improve modeling.

3.1. Introduction

Soil thermal properties have been a focus of study to understand the impact of heat transfer on the distribution, circulation and evaporation of soil moisture. Heat transfer within soil influences micrometeorological phenomena (Philip, 1957; Hanks et al., 1967), engineering efforts such as cooling electronic devices with heat pipes and insulating buildings (Bussing and Bart, 1997; Sakaguchi et al., 2009), and agricultural production (Al Nakshabandi and Kohnke, 1964; Usowicz et al., 1996; Lipiec et al., 2007). The ability to model soil thermal properties, specifically thermal conductivity, is essential to understand heat transfer across a wide spectrum of disciplines. Previous studies provide insight on the effect of soil moisture, temperature and soil physical properties on soil thermal properties (e.g., de Vries, 1963; Johansen, 1975, Hopmans and Dane, 1986; Ochsner et al., 2001; Tarnawski and Gori, 2002); however, none of the studies to date, including the aforementioned studies, specifically focus on soil mixtures. Soil mixtures are important to understand as they better represent naturally occurring sediment than uniform or non-mixed soils; nonetheless, their thermal and hydraulic properties oftentimes vary from the individual constituents (Kamann et al., 2007; Esselburn et al., 2010; Sakaki and Smits, 2014). In addition, it is unclear if existing models of thermal conductivity and soil water content based on easily-measurable soil parameters are able to capture the behavior of soil mixtures. By using binary mixtures of the sands, combined with an understanding of the moisture regimes, we can isolate the effects of the packing condition on thermal conductivity.

Thermal conductivity is affected by a number of factors including porosity (Terzaghi, 1952; Skaggs and Smith, 1968), soil water content (Yadav and Saxena, 1977; Tarnawski and Leong, 2000), soil type (Van Rooyen and Winterkorn, 1959; Adivarahan et

al., 1962; Haigh, 2012), pore size/soil grain distribution (Sepaskhah and Boersma, 1979; Tavman, 1996; Midttømme and Roaldset, 1998), and temperature (Campbell et al., 1994; Hiraiwa and Kasubuchi, 2000; Sakaguchi et al., 2007). Increasing the contact between soil grains lowers the porosity (i.e. more mineral volume and less air volume) enabling higher heat transfer through the grain lattice structure and a higher thermal conductivity (Yadav and Saxena, 1977; Midttømme et al., 1998; Smits et al., 2010; Tarnawski et al., 2013). Past studies focused on the effect of porosity on thermal conductivity for specific field locations or unimodal soils rather than soil mixtures.

Volumetric water content, θ, has a direct impact on the apparent thermal conductivity of soil, λ (Philip and de Vries, 1957; de Vries, 1963, Al Nakshabandi and Kohnke, 1965; Lu and Likos, 2004; Smits et al., 2010; Lu and Dong, 2014). In general, λ increases with an increase in θ. Thermal conductivity of soil is considered "apparent" thermal conductivity because sand is a granular material where heat transfer processes are more complex than those in solid material. Heat is transferred by three mechanisms—conduction, radiation, and convection. Under such conditions, thermal conductivity is referred to as an apparent thermal conductivity. Grain size also affects the thermal properties of soil where larger grained materials often maintain a higher λ; however, to a smaller degree compared to changes in moisture contact and soil packing conditions (Al Nakshabandi and Kohnke, 1965; Côté and Konrad, 2009).

The mixing of different sized soil particles affects soil properties such as density, ϕ, hydraulic conductivity and soil water retention. Soil mixtures with two components, (i.e. binary mixtures), are often described by the volume fraction of each particle size and the ratio of the particle diameters. Smaller particles or soil grains have the potential to fit within and fill the voids created by the larger grains, thus producing a lower mixture ϕ.

The difference in the particle packing is oftentimes referred to as coarse or fine packing (Clarke, 1979). The packing in a soil mixture passes from coarse- to fine-dominated at a critical volume fraction of fines (Koltermann and Gorelick, 1995). The critical volume fraction of fines, f_{crit}, denotes the transition between coarse controlled and fine controlled mixtures which occurs near 30% fines as shown by Koltermann and Gorelick (1995) and Sakaki and Smits (2014). Coarse-controlled mixtures exist as long as coarse grains make up the load-bearing skeleton. As more fine grained materials are added to the mixture, the percentage of fines increases until the coarse material no longer comprises the load-bearing skeleton. When the volume fraction of fines is equal to the porosity of the coarse-grained component, the fines completely fill the voids in the coarser grains (Koltermann and Gorelick, 1995). The fundamental changes to soil properties as a result of mixing (i.e. changes in the hydraulic conductivity, soil water retention curve (SWRC), grain size distribution, density, and ϕ) oftentimes cannot be accounted for using a dual porosity model such as those developed by Gerke and van Genuchten (1993), Zimmerman et al. (1993), and Larsson and Jarvis (1999). Sakaki and Smits (2014) discuss that knowing the properties of each soil independently will not always allow an understanding of the properties of the mixture.

Although much effort has been invested in the development of λ-θ models based on easily measurable soil parameters (e.g., de Vries, 1963; Johansen, 1975; McCumber and Pielke, 1981; Campbell, 1985; Campbell et al., 1994; Tarnawski et al., 2000; Lu et al., 2007; Côté and Konrad, 2005, 2009), none of the models address the applicability to soil mixtures, specifically the effect of mixing fractions. Empirical, semi-empirical, and analytical models developed to predict λ based on measurable soil properties have not been tested to compare experimental results from binary mixtures. Previous data used for comparison with models oftentimes used homogeneous or manufactured sands or natural

soils with a range of unknown grain sizes. Through this work, which tests various binary mixtures, we can better understand the coupling of soil packing conditions and θ on λ with the potential to broaden the range of application for the models or identify points for improvement.

The motivation of this work is to systematically evaluate the effect of soil packing on soil thermal conductivity. In this study, using two uniform sands with different particle sizes (i.e., coarse and fine), we generated a set of binary mixture samples with different mixing fractions. For each binary mixture, the thermal conductivity and soil water retention curve was measured. By changing the mixing fraction in a systematic manner, we investigated how binary mixing impacts the λ-saturation, *S*, relationship and evaluate the ability of several models to predict λ-θ relationship based on measurable soil properties for the entire suite of mixtures from coarse to fine controlled.

3.2. Material and Methods

This section will first discuss the experimental setup and procedure followed by a discussion of the sands and mixtures used in testing.

3.2.1 Experimental Apparatus

A Tempe cell consisting of a network of sampling ports that was hydraulically connected to a long water column was used in this study (Fig. 1). The cell and water column were constructed out of 0.4 cm thick acrylic (specific heat = 1464 J kg^{-1} K^{-1}, λ = 0.2 W m^{-1} K^{-1}, and density = 1150 kg m^{-3}).

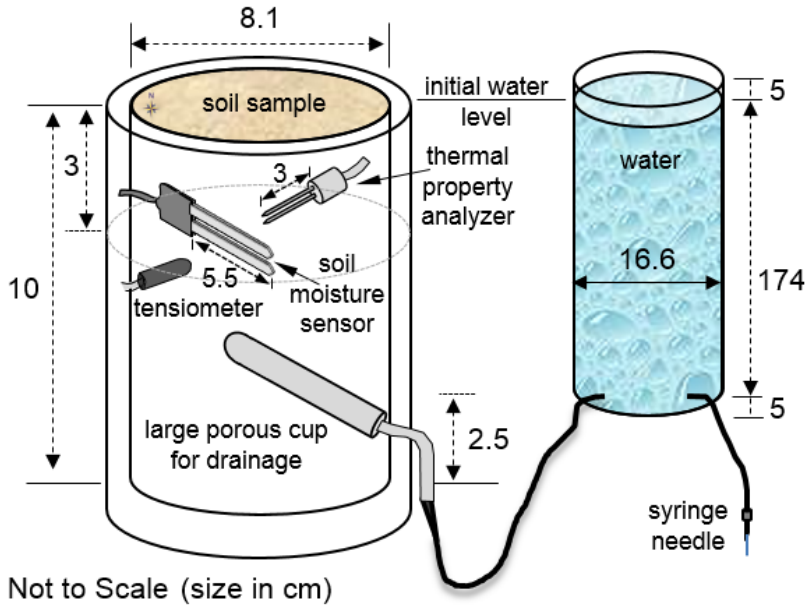

Fig. 1. Schematic of the Tempe cell and interconnected water reservoir used in experiments (not to scale). Inside volume of cell excluding sensors and porous cup for drainage is 510 cm^3.

The cell was outfitted with three sensors for measuring soil moisture, thermal properties, and capillary pressure. Soil moisture was continuously monitored using an ECH_2O EC-5 dielectric soil moisture sensor (Decagon Devices, Inc., Pullman, WA; sensor length = 5.5 cm, measurement frequency = 70 MHz, accuracy ± 3%) at 1 minute intervals; the moisture sensor was connected to an Em50 data logger (Decagon Devices, Inc., Pullman, WA). The EC-5 sensor measured the dielectric permittivity of the soil which was converted into an analog-to-digital converter number (ADC count). ADC counts were then used to determine the θ (m^3 m^{-3}) based upon the empirical two-point α-mixing model developed by Sakaki et al. (2008).

A thermal property SH-1 sensor (Decagon Devices, Pullman, WA; dual needle, length = 3 cm, spacing = 6 mm, ± 10% accuracy from 0.2 to 2 W m^{-1} K^{-1} for λ, ± 0.001 ºC for temperature) connected to a KD2 Pro™ thermal property analyzer was used to measure

λ (W m^{-1} K^{-1}). Soil thermal measurements were made at 15 minute intervals to allow thermal gradients to dissipate, per the manufacturer recommendation. The SH-1 sensor consists of two needles containing a thermistor in one needle and a heating element in the other. A current was passed through the heating element in one needle while the time dependent temperature response was monitored over time in the second needle. A dual needle algorithm (Abramowitz and Stegun, 1972) based on the line heat source analysis described in Carslaw and Jaeger (1959) and Kluitenberg et al. (1993) along with the temperature measurements and knowledge of the heat generated during heating and cooling cycles was used to calculate the λ of the soil. For further discussion see the KD2 Pro Operator's Manual (Decagon Devices, 2014).

Capillary pressure was continuously monitored using a tensiometer. The tensiometer included a small porous cup (Soilmoisture Equipment Corp., Goleta, CA; diameter = 0.64 cm, length = 2 cm, air-entry value = 51 kPa) connected to a differential pressure transducer (Validyne Engineering Corp., Northridge, CA; Model P55D, range $\pm$ 0.08 psi to $\pm$ 3200 psi). Measurements were made every one minute. To control the water pressure, a large porous cup (Soilmoisture Equipment Corp., Goleta, CA; diameter = 1.0 cm, length = 7.2 cm, air-entry value = 51 kPa) located near the bottom of the Tempe cell was used for drainage and connected to a 174 cm long water reservoir. The water level was lowered gradually via drainage through a syringe needle (21G1½ PrecisionGlide® Needle) connected at the outlet of the reservoir near the bottom of the water column (Fig. 1).

3.2.2. Sand Materials

Two different sands were used in the experiments to include a fine (Ottawa sand #110, US Silica Co., Ottawa, MN; uniformity coefficient = 1.7, mean diameter = 0.12 mm,

dry bulk density = 1.79 g cm^{-3}), and coarse grained sand (Accusand #12/20, Accusands, Unimin Corps., Ottowa, MN; uniformity coefficient = 1.2, mean diameter = 1.04 mm, dry bulk density = 1.81 g cm^{-3}). Both sands have a specific gravity of 2.65 g cm^{-3} and mineralogical composition of 99.8% quartz as provided by the manufacturer.

In addition to testing the fine and coarse grained sands separately, mixtures of the two sands were created based upon a weighted fraction of each component. The two sands were mixed at seven different coarse to fine (C:F) ratios; 10:0, 9:1, 8:2, 7:3, 5:5, 2:8 and 0:10, respectively, similar to those evaluated by Sakaki and Smits (2014). These samples are referred to as C10F0, C9F1, C8F2, C7F3, C5F5, C2F8 and C0F10, respectively. Samples were well mixed to ensure homogeneity of the binary mixture. Select properties of the binary mixtures tested here within are provided in Table 1. The van Genuchten model parameters, although not used in this current study, are needed for numerical modeling purposes and therefore included in this work.

Table 1. Properties of component sands and binary mixtures.

Binary Mixture	Porosity ϕ (-)	Air Entry Pressure h_c (cm H_2O)	Residual Water Content θ_r (m^3 m^{-3})	Thermal Conductivity		van Genuchten Model Parameters*	
				Dry	Saturated		
				λ_{dry} (W m^{-1} K^{-1})	λ_{sat} (W m^{-1} K^{-1})	α (cm^{-1})	n (-)
#12/20 (C10F0)	0.318	10.8	0.004	0.287	3.383	0.0806	12.69
C9F1	0.261	10.7	0.013	0.427	4.396	0.0750	4.50
C8F2	0.212	10.5	0.015	0.558	4.833	0.0210	4.00
C7F3	0.190	52.1	0.006	0.529	5.010	0.0175	4.45
C5F5	0.237	72.0	0.007	0.419	4.815	0.0127	6.95
C2F8	0.298	78.0	0.062	0.332	3.947	0.0118	14.50
#110 (C0F10)	0.337	72.8	0.009	0.282	3.241	0.0112	9.00

*Parameters determined as a function of experiments conducted for this paper.

Fig. 2 shows a *comparison of the porosity of the measured data with values obtained by Sakaki and Smits (2014) and with predictions made using the partial mixing model developed by Kamann et al., (2007).* Consistent with previous findings (Westman and Hugill, 1930; Holts and Lowitz, 1957; Garga and Madureira, 1985; and Fragaszy et al., 1990; *Koltermann and Gorelick, 1995)*, the minimum ϕ occurred near the C7F3 mixture (ϕ = 0.190). The minimum ϕ occurs when the small particles completely fill the voids of the load-bearing, larger particles, corresponding to a fine fraction of ~30%. Although not the focus of this work, the partial mixing model described by Kamann et al. (2007) well describes the data.

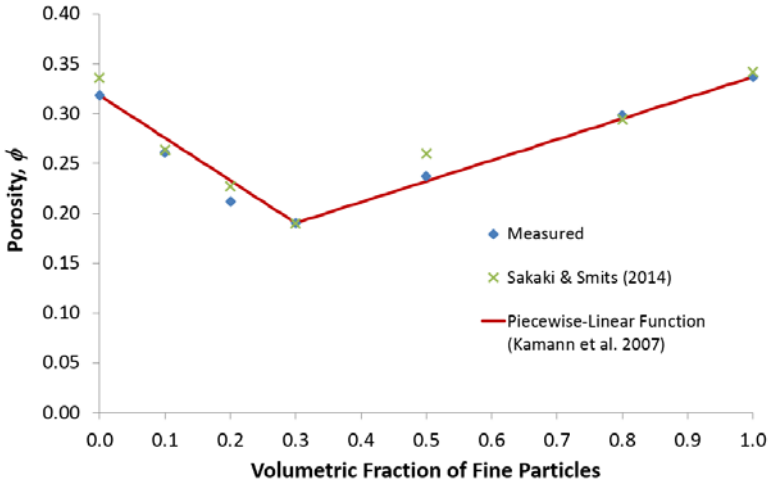

Fig. 2. *Comparison of the porosity of the measured data with values obtained by Sakai and Smits (2014) and predictions made using the partial mixing model developed by Kamann et al., (2007).*

The associated SWRC for each of the mixtures is shown in Fig. 3. For simplicity, the SWRC for each sample by Sakaki and Smits (2014) is not plotted; however, when overlain with the data shown here, the data are very similar, demonstrating the consistency and repeatability of the data. As seen in Fig. 3, the water retention properties are distinctly different depending on the C:F ratio. The SWRC can be divided based on if the mixture is fine- or coarse-controlled with the fine fraction higher or lower than f_{crit}, respectively. The water retention property of the C0F10, C2F8, C5F5 and C7F3 mixtures are largely controlled by the fine particles. As the fraction of fine particles decreases, for the same water content, P_c and P_d values decrease gradually. This gradual change results from introducing large particles (significantly larger than the fine particles) leading to an increase in the pore size. The retention property of C8F2, C9F1 and C10F0 are controlled by the coarse particles. Results for the coarse controlled samples show a displacement pressure equal or close to that of the coarse sand followed by a rapid drainage, resulting in a flat portion in the retention curves.

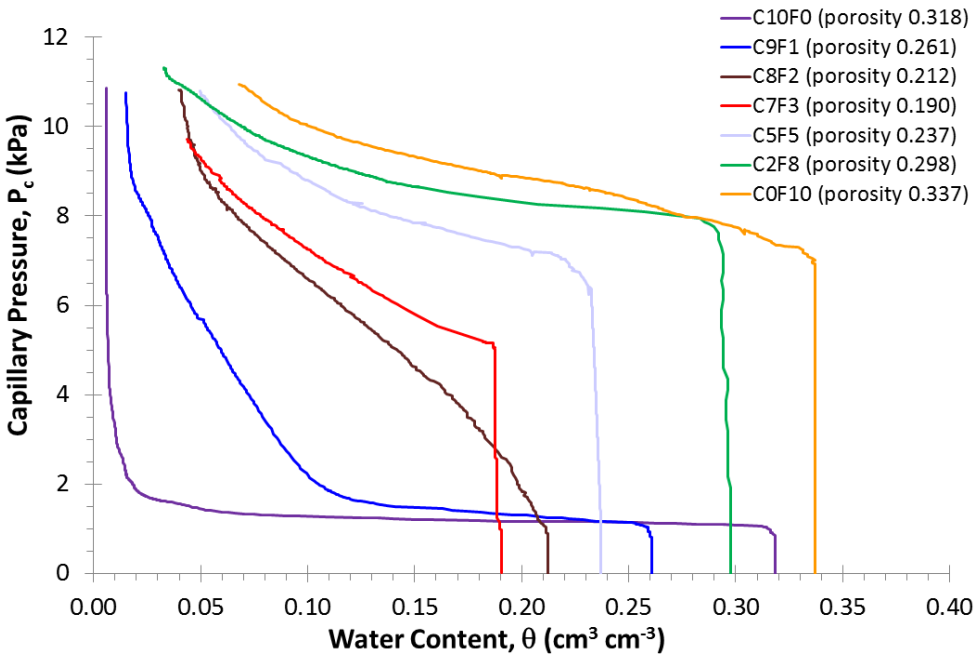

Fig. 3. Soil water retention curves (P_c-θ relationships) for each mixture (primary drainage cycle).

3.2.3 Experimental Procedure

Each sand sample (C10F0 through C0F10) was first tightly packed into the Tempe cell with dry sand to obtain residual soil moisture and thermal property values. The sand was then removed and subsequently repacked using a wet-packed method similar to Smits et al., (2010) using degassed-deionized water. Sand was poured into the cell in 2.5 cm lifts. After emplacement, each lift was tamped down followed by tapping the cell wall to achieve maximum compaction and contact with the sensors (e.g., Sakaki and Illangasekare, 2007). This was done until the surface of the sand was even with the top of the cell. With the sample fully saturated, the mixture was allowed to slowly drain over a period of seven to ten days to achieve residual water contents in each sample.

3.3. Experimental Results

Results of the seven experiments are discussed in this section. The λ-S and λ-t relationships are shown. Then, the changes in observed behavior for the data is related to associated reduction in water content over time using the framework of four regimes from fully saturated to residual conditions.

3.3.1 Apparent Thermal Conductivity of Binary Mixtures

The impact of the change in ϕ associated with each binary mixture is shown through considering the relationship of λ and S, (Fig. 4) and the change in λ over time (Fig. 5). Fig. 4 shows that for each mixture as S decreases, λ also decreases. There is initially a constant λ maintained near full saturation. This is due to at high θ values, the water phase is continuous and heat is mainly transmitted through the grain and water phases and contacts between grains, resulting in higher λ values than at lower saturations (Smits et al., 2010). The value of λ then decreases gradually with saturation until about mid-saturation values at which time the rate of decline increases slightly more. Consistent with previous findings (e.g. ., de Vries, 1963; Horton and Wierenga, 1984; Hopmans and Dane, 1986), as saturation approaches residual, λ decreases significantly. The points of inflection in the rate of λ decrease with respect to S can be explained through considering the four primary regimes that exist from fully saturated to dry conditions as the hydration, pendular, funicular, and capillary regimes (Lu and Likos, 2004; Dong et al., 2014). A discussion regarding each regime follows.

As seen in Fig. 4, a lower ϕ results in a higher λ, which can best be seen at full saturation. This is especially apparent from full S to approximately the residual S (S range from 1.0 to 0.1). For example, the lowest ϕ mixture (i.e. C7F3 ϕ = 0.190) at full S has a λ

value approximately 2 W m^{-1} K^{-1} higher than that of the highest ϕ mixture (i.e. C0F10 ϕ = 0.337). Near and below the residual saturation, the effect of ϕ on the λ becomes less apparent. At values of *S* near and below 0.1, the data does not follow the same trend due to, in part, grain to sensor contact differences and the number of grain-water pathways available for heat flow. In this regime, the water is disconnected and does not form continuous grain-water paths. Therefore, heat conduction occurs predominantly through grain-air paths and grain to grain contacts and only partly though the few grain-water paths. This results in few thermally conductive channels between soil grains and hence the very large and abrupt decrease in λ. A difference of a few tortuous grain-water pathways between samples due to packing considerations could result in differences in thermal conductivity values.

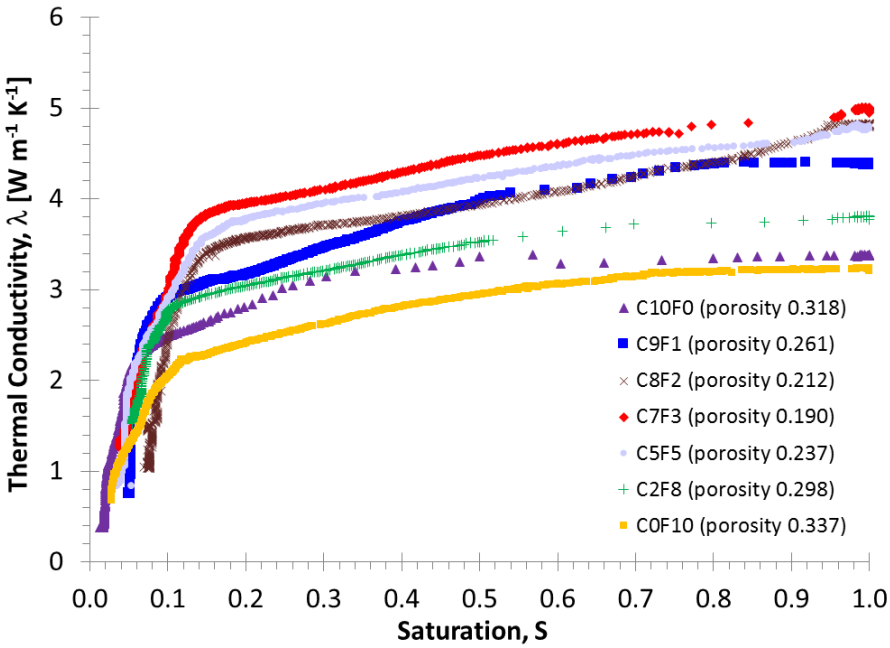

Fig. 4. λ of each binary mixture as a function of *S*.

The change in λ over time as shown in Fig. 5 enables differentiation between coarse-controlled and fine-controlled binary mixtures. The reduction in water content due to drainage during the experiments provides a means to associate a time dependence for

λ of fine verses coarse control; this is not a demonstration of the transience in the thermal behavior. The coarse-controlled mixtures (C10F0, C9F1, and C8F2) exhibit a decrease in λ within the first day of drainage followed by a more dramatic decrease prior to rapidly approaching a residual λ. The fine-controlled mixtures, including the critical fraction (C7F3, C5F5, C2F8, and C0F10), portray a longer time period maintaining saturated λ (1.5 to 2.5 days) followed by a more gradual decline in λ than with the coarse controlled mixtures. This is due to the drainage occurring more rapidly and earlier in coarse controlled mixtures compared to fine controlled. Fine-controlled binary mixtures portray a slower, more gradual rate of decrease in λ due to buffering by more tortuous water pathways resulting from a decrease in large interconnected pore spaces as compared to coarse-controlled mixtures. With these differences in mind, all samples display the same relationship over time (albeit on a different time scale). Each starts out at the saturated λ with ϕ serving as the primary influence regarding the magnitude. The rate of decrease begins and then tappers prior to reaching a maximum rate of decrease. This higher rate of decrease in λ then transitions to a slower or almost no rate of decrease as λ approaches a residual value, corresponding with the residual saturation.

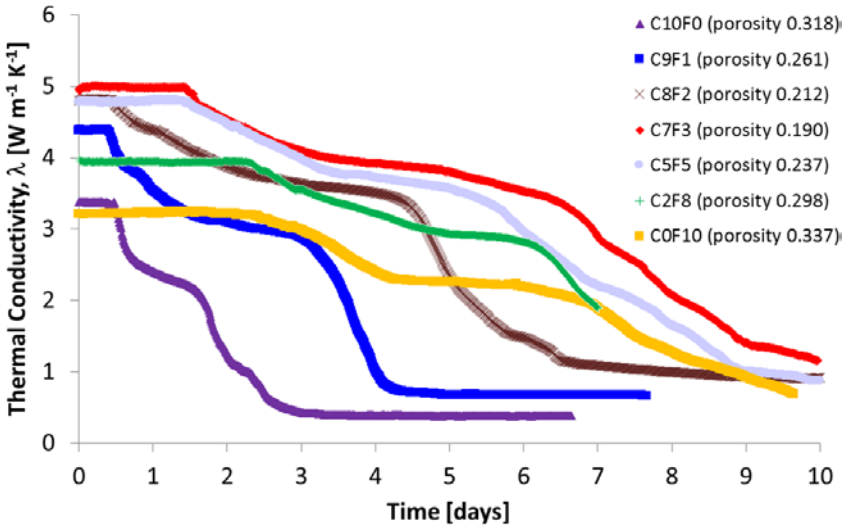

Fig. 5. Binary soil mixture impact on λ evaluated over time.

The points of inflection in the rate of λ decrease with respect to saturation and time (Figs. 4 and 5) can be explained through considering the four primary saturation regimes (i.e. hydration, pendular, funicular and capillary). The four regimes and their points of transition are conceptualized in Fig. 6. This figure portrays the correlation of the regimes between the SWRC and the relative saturation in a soil profile. Point (a) represents initial saturated conditions where S is equal to 1 corresponding to θ equal to ϕ. Point (b) is the transition between the capillary (fully saturated yet under negative pore water pressure) and funicular (hydraulic connection to the soil surface) regimes. This transition occurs as the matric suction approaches the air entry pressure. Point (b*) is the actual air entry pressure with point (b) serving as the projection of (b*) onto the SWRC as shown in the Fig. inset. At point (b), the largest pores within the soil experience breakthrough of air resulting in the initiation of significant decrease in water content during small increases in matric suction, ψ. Point (c) denotes the transition between the funicular and pendular (pore water existing in pockets or thin films) regimes where water flow reduces to water lens connectivity. The physical point on the SWRC is the point of inflection. Within the

pendular regime, there is a lack of hydraulic connection from the water table to the soil surface which results in pore water transport occurring primarily by vapor transport mechanisms (Lu and Likos, 2004). Although there is no flow of water, between different soil grains, water may connect two or more grains with these connections referred to as water bridges in nearly dry soil (Sakaguchi et al., 2007). Point (d) is the transition point between the pendular and hydration regime (structural ordering of water molecules as a function of properties of the minerals at the soil surface). At point (d), ψ increases significantly with very little decrease in S. Point (e) represents the residual saturated conditions where S remains almost constant and ψ reaches its peak.

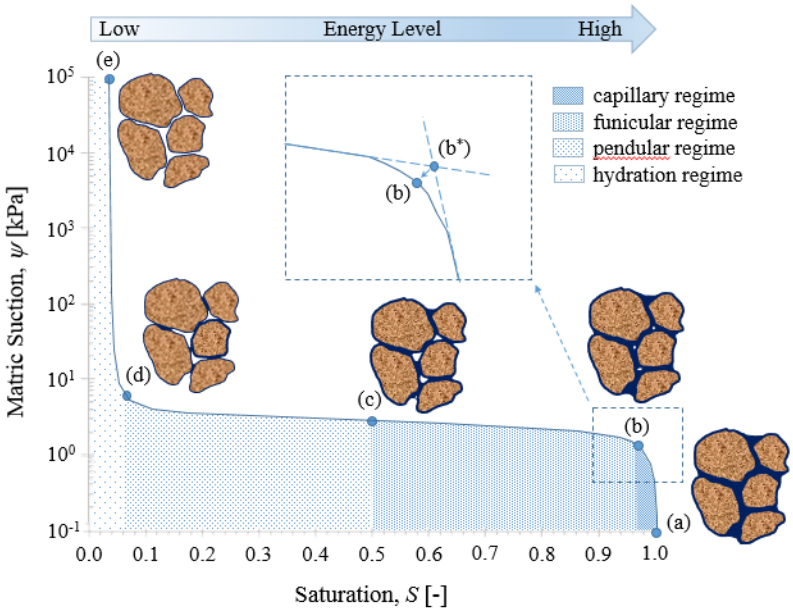

Fig. 6. Representative SWRC for a well sorted sand depicting four regimes associated with saturation, the boundary and transition points between the regimes, the associated soil saturation at each point, and the relative water energy level spectrum (amended based on Lu and Likos, 2004).

The λ–S and λ-t relationships for a representative sample under primary drainage and drying conditions is shown in Figs. 7a and b, respectively. The five points of inflection (a through e) are noted at the top of both figures to mark the transitions between regimes. These transitions are apparent due to the change in slope between the λ-S and λ-t relationships. In the capillary regime, λ is relatively constant due to the interconnection between soil grains via direct contact or water interfaces. At high S values, the water phase is continuous and heat is therefore transferred primarily through the grain and water phases and contacts between grains, resulting in high and relatively constant λ values. The λ value of water and air are typically 0.58 W m^{-1} K^{-1} (at 20^{o}C) and 0.024 W m^{-1} K^{-1} (at 20^{o}C), respectively, demonstrating that the water pathways are more conductive than the air pathways. Within the funicular regime bound by points (b) and (c), λ decreases gradually at an even rate. The small change in λ indicates that air begins to displace the water in a few of the larger pores. The rate of decrease in λ increases at point (c) and continues to decrease while in the pendular regime (between points c and d). In the pendular regime, the grain-water paths become less continuous and more tortuous. This results in heat flow through less and longer thermally conductive grain-water pathways and therefore λ decreases. Thermal conductivity significantly decreases within the hydration regime approaching a residual value after water content decreases to residual conditions as discussed by Smits et al. (2010). In the hydration regime, the water is disconnected and can no longer form continuous grain-water paths. Heat conduction occurs predominately through grain-air pathways and grain to grain contacts and only partly though long tortuous grain-water paths, resulting in very few thermally conductive pathways and hence a pronounced decrease in θ. This behavior is the same for coarse and fine controlled binary mixtures based upon experiments conducted.

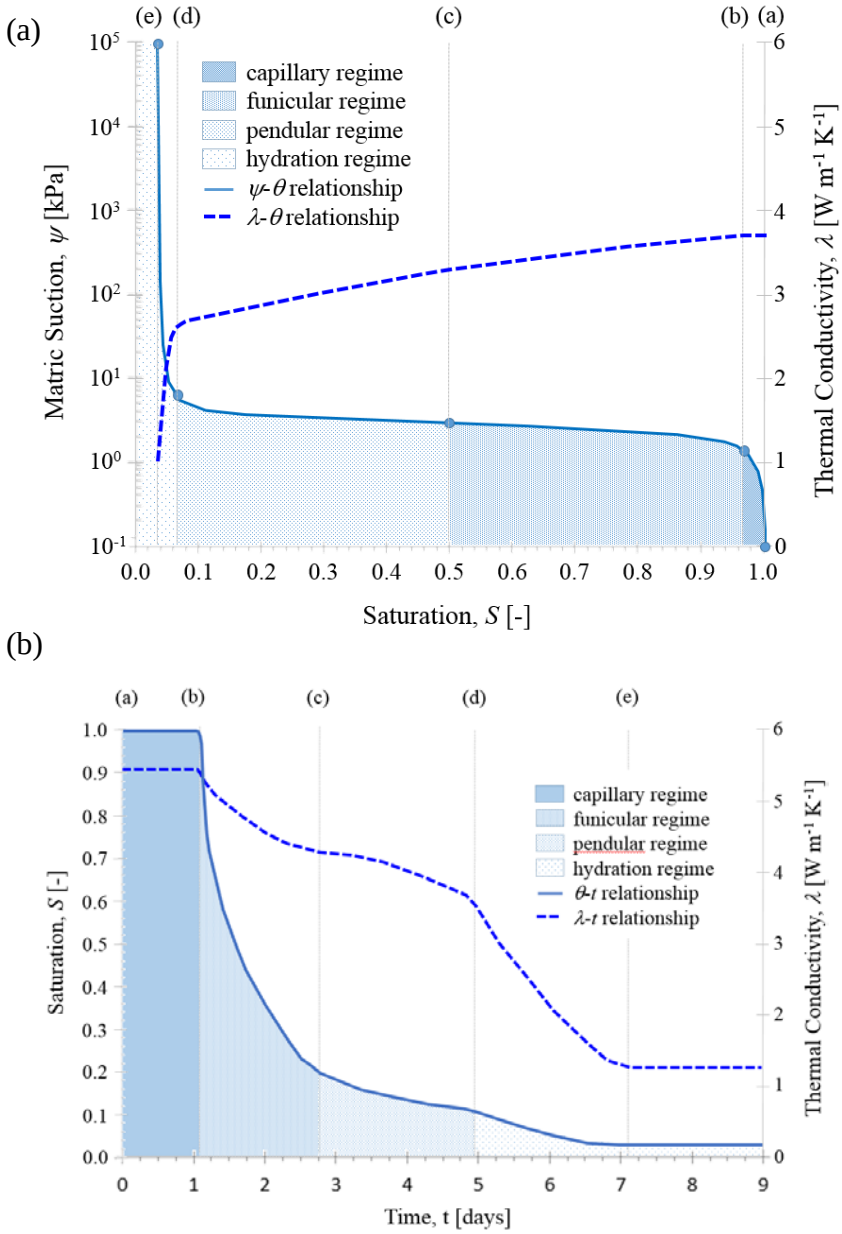

Fig. 7. Comparative relationship between θ and λ regarding (a) SWRC and λ and (b) θ and λ as a function of time for a representative soil.

The changes with respect to S and λ as a function of time are shown in Fig. 7b, demonstrating the same behavior as Fig. 7a, however with respect to time. The relationships shown in Fig. 7b more closely match coarse controlled binary mixtures. As a

mixture transitions from coarse controlled to fine controlled, the length of time associated with each transition point increases and the rate of decrease in λ becomes more gradual.

3.4. Applicability of λ–S Models to Binary Mixtures

In this study, by changing the mixing fraction in a systematic manner, we were able to investigate if soil mixing results in predictable thermal behavior using existing λ–S models. There are a variety of λ–S models available (e.g., empirical models: Lu et al., 2007; Chen, 2008 / semi-empirical models: Campbell et al., 1994; Lu and Dong, 2014 / analytical model: Haigh, 2012). The five aforementioned models are examined here for their applicability to binary mixtures. These models were selected as they were either recently derived or amended from previous models (e.g. Lu et al., 2007) or oftentimes implemented in numerical models of heat and mass transfer (e.g. Campbell et al., 1994). This section will first briefly describe each model followed by a discussion of the degree of agreement between observations and simulated results.

The Lu et al. (2007) empirical model is evaluated using Eq. [1]:

$$\lambda = \left(\left(\left(\lambda_q^q \lambda_o^{1-q}\right)^{1-\phi} \lambda_w^{\phi}\right) - \left(b - a\phi\right)\right)\exp\left\{\alpha\left[1 - S^{(\alpha-1.33)}\right]\right\} + \left(b - a\phi\right) \qquad [1]$$

where q is the quartz content of the total solids, λ_q is the thermal conductivity of quartz (= 7.7 W m^{-1} K^{-1}), λ_o is the thermal conductivity of other minerals (= 2.0 W m^{-1} K^{-1} for soils with $q > 0.2$ and = 3.0 W m^{-1} K^{-1} for soils with $q \leq 0.2$), a and b are empirical parameters, α is a soil texture dependent parameter (0.96 for coarse-textured soils and 0.27 for fine-textured soils), and 1.33 is a shape parameter. Lu et al. (2007) calculated values of 0.56 and 0.51 in their study for a and b, respectively.

The Chen (2008) empirical model incorporates the use of Eq. [2]:

$$\lambda = \lambda_w^{\phi} \lambda_q^{1-\phi} \left[\left(1 - 0.0022\right)S + 0.0022\right]^{0.78\phi} \qquad [2]$$

where λ_w is the thermal conductivity of water (= 6.096 W m^{-1} K^{-1}) and other variables previously defined.

The semi-empirical Campbell et al. (1994) model is based upon the de Vries (1963) model and posits that λ of soil can be determined from a volume-weighted sum of the λ of the mixture components:

$$\lambda = \frac{k_w x_w \lambda_w + k_a x_a \lambda_a + k_m x_m \lambda_m}{k_w x_w + k_a x_a + k_m x_m} \quad [3]$$

where the mixture components of water, gas, and mineral are denoted by subscripts *w*, *a*, and *m*, respectively, *k* is the weighting factor, and *x* is the volume fractions of each component. The model incorporates four fitting parameters to determine λ which include λ of the mineral fraction (λ_m), the cutoff water content for water recirculation or water content at which water starts to affect λ (x_{wo}), the power for the recirculation function (q_o), and a shape factor (g_a). Refer to Campbell et al. (1994) for an in depth discussion of the 20 equations required to arrive at the calculated λ.

A new semi-empirical model with application across a variety of 27 soils from saturated to dry for ambient conditions from 20-25 ^oC was developed by Lu and Dong (2014):

$$\lambda = \lambda_{sat} - \left[1 + \left(\frac{\theta}{\theta_f}\right)^m\right]^{(1/m)-1} \left(\lambda_{sat} - \lambda_{dry}\right) \quad [4]$$

where *m* is the pore fluid network connectivity parameter related to the pore-size parameter *n* in the van Genuchten (1980) model, and θ_f is the onset of funicular water content corresponding to the highest rate of change in water content between points (d) and (e) in Figs. 6 and 7. Both *m* and θ_f are fitting parameters with all other variables

defined previously. Lu and Dong (2014) state the range for the parameters for sandy soils include m between 1.4 and 2.9 and θ_f between 0.01 and 0.06; however, the best fit functional relationship for both parameters was presented using Eqs. [5] and [6].

$$\theta_f = 1.84\theta_r \quad [5]$$

$$m = 3.0 - 0.2n \quad [6]$$

where θ_r is the residual water content corresponding to the residual saturation shown as point (e) in Figs. 6 and 7, and n is the van Genutchen (1980) n.

The Lu and Dong (2014) model was demonstrated to more accurately predict λ for the 27 soils ranging from clay to silt to sand with an average R^2 value of 0.98 as compared to the Lu et al. (2007) model with an average R^2 value of 0.95 and the Coté and Konrad (2005) model with an average R^2 value of 0.94.

One recent analytical model, derived from simplified geometrical idealization of microstructure in soils (Haigh 2012), assessed one-dimensional heat flow between two equally sized spherical soil particles. The overall thermal conductivity of the soil is:

$$\lambda = \left[2(1+\xi)^2 \left\{ \frac{\alpha_w}{(1-\alpha_w)^2} \ln\left[\frac{(1+\xi)+(\alpha_w-1)x}{\xi+\alpha_w} \right] + \frac{\alpha_a}{(1-\alpha_a)^2} \ln\left[\frac{(1+\xi)}{(1+\xi)+(\alpha_a-1)x} \right] \right\} + \frac{2(1+\xi)}{(1-\alpha_w)(1-\alpha_a)} \left[(\alpha_w-\alpha_a)x - (1-\alpha_a)\alpha_w \right] \right] \lambda_q \quad [7]$$

where α_w and α_a are the thermal conductivities, normalized by that of the soil solids (λ_q = 7.69 W m^{-1} K^{-1}), of water (λ_w = 0.6096 W m^{-1} K^{-1}) and air (λ_a = 0.0219 W m^{-1} K^{-1}) respectively. ξ is a geometric parameter specific to the soil based upon the voids ratio, e, and x is a parameter defined as the root of a saturation ratio between the volume of water

and volume of void. Refer to Haigh (2012) for an in depth discussion of the 5 equations required to arrive at the calculated λ.

The Haigh (2012) model was shown to provide better prediction of λ compared to nine other models for over 120 data points evaluated with each model for quartz sands. The best fit, linear regression for the Haigh (2012) model yielded an R^2 value of 0.86 with the next closest models as Chen (2008) and Lu et al. (2007) represented by R^2 values of 0.85 and 0.78, respectively.

3.5. Comparison of Selected Models to Experimental Results

This section provides a summary of the five abovementioned models compared to experimental results. A discussion regarding each model, the applicability of the model to binary mixtures, and its ability to accurately predict the λ–S relationship follows.

Experimental data for each of the seven soil mixtures were compared with the five selected models as shown in Fig. 8. The R^2 and *NRMSE* values, quantifying the level of agreement between experimental data and model prediction, are shown in Table 2. The R^2 values provide a measure of how well the model approximates the experimental data with a number approaching 1 from 0 providing a better fit. A perfect fit between model and experimental data yields an R^2 value of 1.0. Normalized root-mean-square-error (*NRMSE*) quantifies the deviation in the model from experimental data with a smaller number providing a better fit. A perfect fit would result in a value of 0.0. The reason both are shown is to enable ease of comparison with previous and future research efforts. As seen in Fig. 8 as well as Table 2, in five out of seven data sets, the Campbell et al. (1994) model provides the highest level of agreement. The two soil mixtures with the highest percentage of fines (i.e. C2F8 and C0F10) were better modeled with the Lu et al. (2007) and Lu and

Dong (2014) models. When considering the *NRMSE* comparison, the Lu and Dong (2014) model provides a higher level of agreement compared to the Lu et al. (2007) model in five of the seven models.

(a) C10F0

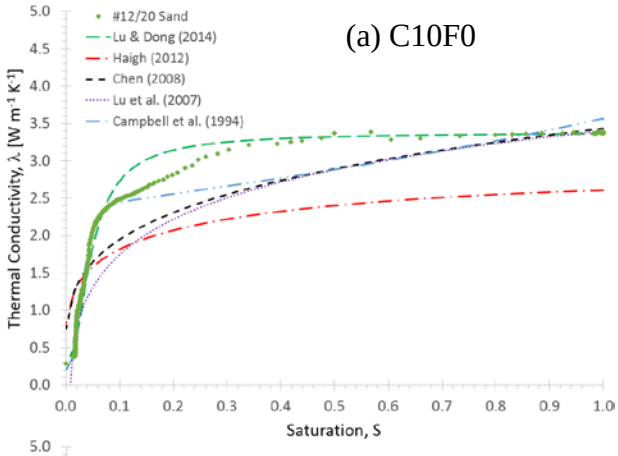

(b) C0F10

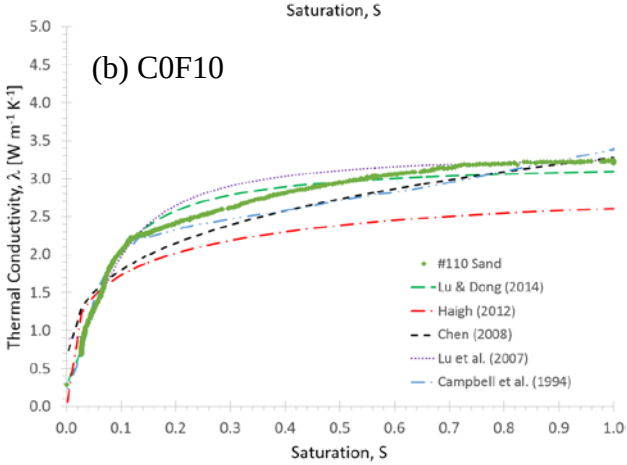

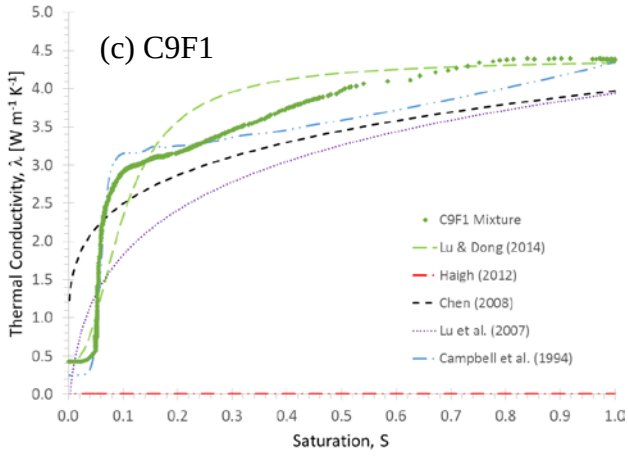
(c) C9F1
Thermal Conductivity, λ [W m⁻¹ K⁻¹]
Saturation, S
C9F1 Mixture
Lu & Dong (2014)
Haigh (2012)
Chen (2008)
Lu et al. (2007)
Campbell et al. (1994)

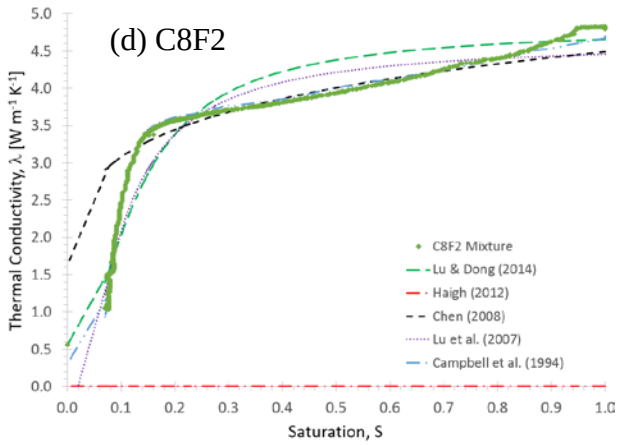
(d) C8F2
Thermal Conductivity, λ [W m⁻¹ K⁻¹]
Saturation, S
C8F2 Mixture
Lu & Dong (2014)
Haigh (2012)
Chen (2008)
Lu et al. (2007)
Campbell et al. (1994)

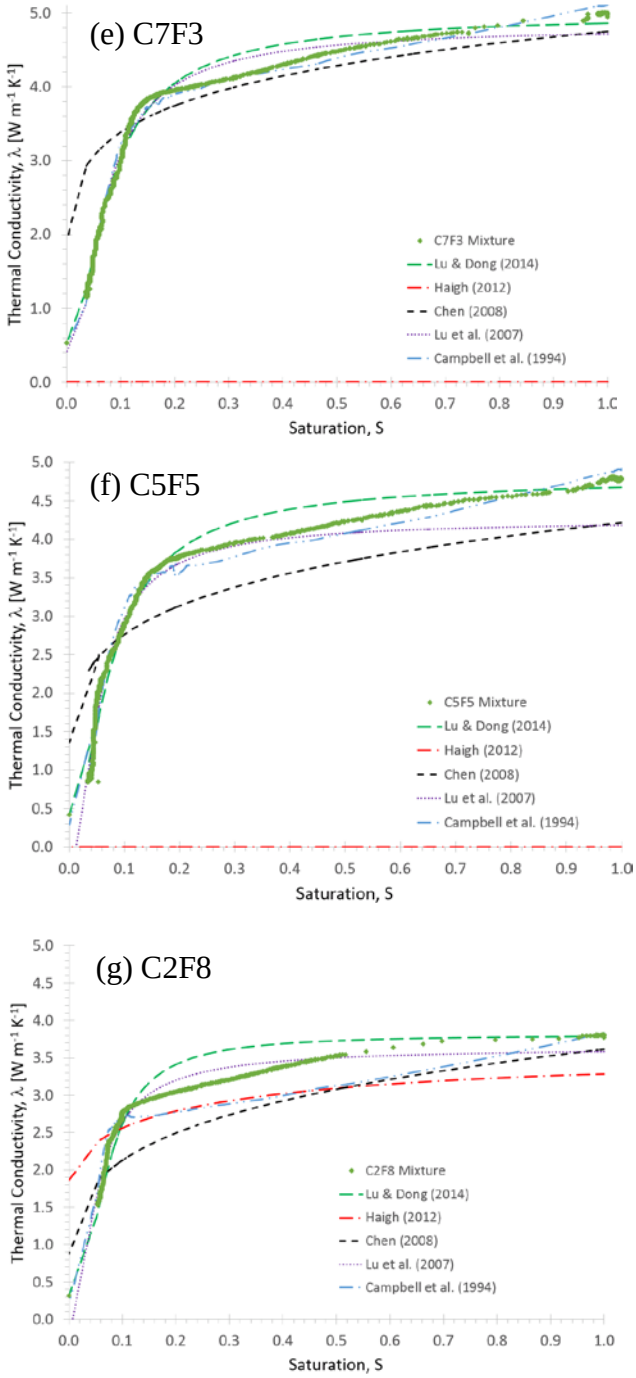

Fig. 8. Comparison of each sand mixture with the five selected models.

Table 2. Quantifying the level of agreement between experimental data and model prediction

	R^2					*NRMSE*				
Soil	Eq. (7) Haigh* (2012)	Eq. (2) Chen (2008)	Eq. (1) Lu et al. (2007)	Eq. (4) Lu and Dong (2014)	Eq. (3) Campbell et al. (1994)	Eq. (7) Haigh* (2012)	Eq. (2) Chen (2008)	Eq. (1) Lu et al. (2007)	Eq. (4) Lu and Dong (2014)	Eq. (3) Campbell et al. (1994)
#12/20 (C10F0)	0.885	0.807	0.875	0.982	**0.988**	0.2427	0.2256	0.1360	0.0477	**0.0381**
C9F1	----	0.805	0.832	0.915	**0.983**	----	0.2579	0.1727	0.0976	**0.0427**
C8F2	----	0.843	0.954	0.933	**0.993**	----	0.2196	0.0639	0.0776	**0.0245**
C7F3	----	0.847	0.983	0.983	**0.992**	----	0.1494	0.0348	0.0331	**0.0242**
C5F5	----	0.864	0.982	0.982	**0.988**	----	0.1761	0.0634	0.0423	**0.0339**
C2F8	0.836	0.797	**0.943**	0.933	0.867	0.0974	0.1444	**0.0362**	0.0617	0.0670
#110 (C0F10)	0.968	0.904	0.987	**0.989**	0.978	0.1547	0.0875	0.0345	**0.0304**	0.0419

* The experiments with dashed lines versus values entered for R^2 and *NRMSE* is a result of model failure to predict thermal conductivity. The Haigh (2012) model was not able to predict λ for soil mixtures with ϕ values lower than 0.276. The bold values correspond to the model predicting λ with the highest level of agreement to the experimental λ.

Neither the Haigh (2012) nor the Chen (2008) models make use of fitting parameters (Eqs. [2] and [7]). As a result, they are bound entirely by sample characteristics including ϕ, λ_w, λ_a, and λ_q. The Haigh (2012) analytical model was not able to predict λ for soil mixtures with low ϕ (e.g., C9F1, C8F2, C7F3, and C5F5). Due to tetrahedral packing providing the tightest packing for uniform spherical grains, the model is geometrically restricted for ϕ less than 0.276. However for binary mixtures and natural soils, the pore space between larger particles is filled with soil grains of finer material

resulting in lower values of ϕ, (i.e. < 0.276). Therefore, the Haigh (2012) model failed to capture the behavior of the binary mixtures.

The Chen (2008) empirical model under predicts λ for each of the experimental samples regardless of fine or coarse controlled binary mixtures for saturations between points (d) to (a) as shown in Fig. 6 and 7. The model over predicts λ near residual saturation (between points (d) and (e) in Fig. 6 and 7).

The Lu et al. (2007) empirical model (Eq. [1]) provided a better fit to experimental data than the Haigh (2012) or Chen (2008) models. This model includes three parameters (a, b and alpha); λ increases with a decrease in *a*, increase in *b*, and increase in α. With α as the physically based parameter, the model adjusts based on a maximum λ, λ_{max}, predicted by the model. For each of the binary mixtures, λ_{max} was under predicted compared to λ_{sat} (Fig. 8). The model under predicted λ within the hydration regime for the coarse controlled mixtures; however, for the fine controlled mixtures the model vs. experimental data provided a better fit. The discrepancy between the model and experimental data in the capillary and funicular regime is discussed below.

All parameters associated with the Lu and Dong (2014) model (Eq. [4]) are physically based whereas only one of the three parameters for the Lu et al. (2007) model are based upon the soil. Therefore, the Lu and Dong (2014) model was able to better match experimental data when compared with the other models, except for the Campbell et al. (1994) model. There was good agreement between the base sands and fine controlled mixtures within the hydration regime. However, the model was not able to capture the transition between the funicular and hydration regimes (point d shown in Fig. 6 and 7). Review of Fig. 8, portrays overestimation of λ in the funicular regime for all experimental

trials. This model to experimental data discrepancy was acknowledged as a point for future model improvement by Lu and Dong (2014).

The Campbell et al. (1994) model (Eq. [3]) incorporates four physically based parameters (g_a, q_o, l_m, and x_{wo}) and requires inputs of S and temperature, thus resulting in the highest level of model to experimental data agreement when compared against all models. The four physically based parameters provide the means for the model to effectively portray the transition point between funicular and hydration regime which the Lu and Dong (2014) model is not able to capture. The Campbell et al. (1994) model transitioned at various locations along the λ profile depending upon the parameter of interest. Two of the transition points include λ_{min} and λ_{max} which closely mirror λ_{dry} and λ_{sat}; however, they are not always the same depending on the experiment of concern. The other transition point is based upon point (d) in Fig. 6 and 7 with a slightly shift to a higher S where the rate of change is constant within the funicular regime. Increase in the λ profile occurs with an increase in λ_{max} transitioning from λ_{min} and occurs with a decrease in x_{wo} as transition points occur at both λ_{min} and λ_{max}. The λ profile experiences a more drastic or gradual transition between λ_{min} and the shifted point (d) based upon an increase or decrease in q_o, respectively. Adjustment of parameter g_a has an inverse parabolic effect on the λ profile around a value of 0.333. An increase in g_a or decrease in g_a below a value of 0.333 results in an increase in the λ profile.

For all binary mixtures, the Campbell et al. (1994) model matched the hydration regime experimental data. Within the funicular regime, the model provided a closer fit for all experiments compared with the four other models. However, within the pendular and capillary regimes, the overall best fit varied between the Campbell et al. (1994) model for C8F2, C7F3 and C5F5 mixtures and the Lu and Dong (2014) model for the C10F0, C9F1,

C2F8, and C0F10 mixtures. Therefore, depending on the focus for specific research interests regarding the various regimes of saturation, either the Campbell et al. (1994) or Lu and Dong (2014) model may provide a better choice for λ prediction.

The parameters used to enable the highest level of agreement between modeled and experimental data are provided in Table 3. The model parameters determined to provide the best fit for the Lu et al. (2007) model did not match those previously reported. The reported values include a = 0.56, b = 0.51, and α = 0.96 (coarse-textured soil) or = 0.27 (fine-textured soil). However, there was not a range provided for the various parameters other than the bounds for coarse or fine soils. The range determined for a and b was set between 0.102 and 2.8. Without applying these bounds, a typically would be set at 0 and b would be over 100 to provide the best model to experimental data fit for the coarse-controlled binary mixtures. The average soil texture parameter for coarse-controlled mixtures was 0.78 and fine-controlled mixtures was 0.024. The coarse-textured soil α was comparable to the previously reported value; however, the fine-textured soil α is smaller by an order of magnitude.

Table 3. Model parameters for the Lu et al., (2007), Lu and Dong (2014), and Campbell et al. (1994) models. Parameter values correspond to Eqs. [1], [4], and [3], respectively.

	Lu et al. (2007)			Lu and Dong (2014)*			
	a	b	α	θ_f	θ_f	m	m
Soil	best fit	best fit	best fit	best fit	Eq. [5]	best fit	Eq. [6]
#12/20 (C10F0)	2.8000	0.1020	1.1754	0.0116	0.0106	2.4912	0.10
C9F1	2.8000	0.1020	1.1425	0.0206	0.0248	2.6394	2.10
C8F2	2.8000	0.1020	0.0349	0.0205	0.0300	2.3560	2.20
C7F3	0.5970	0.5215	0.0246	0.0106	0.0135	2.1819	2.11

C5F5	2.8000	0.1020	0.0151	0.0134	0.0151	2.1850	1.61
C2F8	2.7167	0.5673	0.0144	0.0173	0.0317	2.7321	0.40
#110 (C0F10)	0.4936	1.0471	0.0419	0.0145	0.0172	1.9576	1.20

Campbell et al. (1994)

Soil	g_a [-]	q_o [-]	λ_m [W m^{-1} K^{-1}]	x_{wo} [-]
#12/20 (C10F0)	0.2788	3.5189	18.8255	0.0109
C9F1	0.3333	9.2105	20.5168	0.0163
C8F2	0.3333	5.9853	14.1977	0.0209
C7F3	0.1614	2.9813	10.0731	0.0162
C5F5	0.2577	3.2549	19.2324	0.0154
C2F8	0.3333	6.6593	20.8055	0.0158
#110 (C0F10)	0.2480	2.3785	15.7777	0.0179

*For the Lu and Dong (2014) parameters, the difference between θ_f best fit and θ_f Eq. [5] and m best fit and m Eq. [6] relates to the best fit values determined as fitting parameters and the latter of both being calculated based upon equations presented previously.

The model parameters determined for all experimental trials for the Lu and Dong (2014) model fell within the reported range for θ_f between 0.1 to 0.6 and m between 1.4 and 2.9. Application of Eq. [5] provided a comparable fit of the model to experimental data in almost all cases with the most disparity occurring for C8F2 and C2F8 soil mixtures. Therefore, Eq. [5] remains the recommended method to determine θ_f based upon θ_r. Eq. [6] did not provide as high an agreement compared with θ_f between best fit and calculated

values of *m*. However, there was more agreement for coarse-controlled binary mixtures with increased agreement as the mixtures approached the critical fraction from coarse toward fine controlled mixtures. A potential point for improvement in the Lu and Dong (2014) model includes adjustment of Eq. [6] to enable the model to better predict the best fit *m* values.

The model parameters associated with the Campbell et al. (1994) model were not reported in the literature with an appropriate range for each. However, a review of Table 4 identifies similarities for some of the parameters. In three of the seven mixtures, g_a was 0.333 and for five of the seven mixtures, the average g_a value enabling agreement between model and experimental data is 0.3. Throughout all binary mixtures, x_{wo} is fairly consistent with a mean and median value matching that of the critical fraction (C7F3) at 0.0162 and a standard deviation of 0.003. The two variables with the largest range impacting the fit of the model to experimental data are q_o and λ_m.

3.6. Conclusions

The purpose of this work was to investigate the impact of binary sand mixtures on thermal conductivity for the full range of saturation as well as determine the applicability of existing models in predicting λ based upon those mixtures. *We created a set of binary mixtures with different C:F ratios, using two sands with* relatively large particle size contras*ts. The λ-S and Pc relationships were measured for each mixture.* The mineral thermal conductivities of the coarse and fine sand grains was very similar as was the grain shape for the two sands. With moisture retention curves known and moisture regimes understood, the use of binary mixtures of the sands enabled isolation of the effect of packing on thermal conductivity (primarily through ϕ).

The obtained λ-S relationships were quite different depending on the volume fraction of the fine particles and can be divided into two categories; fine- and coarse-controlled. The change in ϕ due to the fine fraction or percentage of fines associated with each mixture was shown to affect λ. Binary mixtures with less than 30% fines exhibited coarse-controlled characteristics with a rapid rate of decrease in λ with a decrease in *S*. Fine-controlled binary mixtures (percent fines $\geq$ 30%) portrayed a slower, more gradual rate of decrease in λ with a decrease in *S* due to buffering capacity by more tortuous water pathways resulting from a decrease in large interconnected pore spaces as compared to coarse-controlled mixtures. The difference in rate of change in λ with respect to *S* resulted from transitions between the four primary saturation regimes (i.e. hydration, pendular, funicular and capillary). Within the capillary regime, the soils remains fully saturated and λ remained constant for all mixtures. Transition to the funicular regime occurs upon reaching the air entry pressure. During this regime, soils remain hydraulically connected to the surface with larger pore spaces draining of water replaced by air (occurs more rapidly in coarse-controlled binary mixtures) and λ begins to decrease. In the pendular regime, the grain-water paths become less continuous and more tortuous resulting in heat flow through less and longer thermally conductive grain-water pathways and therefore a more abrupt decrease in λ. The hydration regime is characteristic of no hydraulic connection between soil grains. Heat conduction occurs predominately through grain-air pathways and grain to grain contacts and only partly though long tortuous grain-water paths, resulting in very few thermally conductive pathways and hence a pronounced decrease in θ.

Five λ-*S* models including two empirical models (Lu et al., 2007; Chen, 2008), two semi-empirical models (Campbell et al., 1994; Lu and Dong, 2014), and one analytical model (Haigh, 2012) were used to determine model applicability for prediction of λ in

binary mixtures. The Haigh (2012) model does not apply to binary mixtures due to geometric restrictions for ϕ less than 0.276; however, there is a slightly better fit for fine-grained soils than coarse grained. The Chen (2008) model provided an 85% to 90% model-to-experimental-data fit for predicted λ for fine-controlled binary mixtures. This was only slightly better than the 80% fit for the coarse-controlled binary mixtures. The Lu et al. (2007) empirical model provided more consistent, higher degree of agreement for fine-controlled mixtures at around 98%.

The Lu and Dong (2014) model compared with the aforementioned models enables overall better fit with experimental data for the majority of the binary mixtures from residual saturation through almost the entire hydration regime as well as during the period of water film and water bridge growth in the capillary and funicular regimes. The model does over predict λ during the transition between the hydration and pendular regimes. A potential cause for this relates to the model's inability to depict an abrupt transition resulting from a well sorted soil.

The Campbell et al. (1994) model provides the highest level of agreement between model and experimental data in five of the seven experimental data sets. The model provides a slightly better fit for the coarse-controlled binary mixtures with the highest agreement near the critical fraction (Table 2). As both Campbell et al. (1994) and Lu and Dong (2014) models provide the most consistent best fit for the binary mixtures evaluated in this study. The selection over which model to use in future modeling efforts will be based upon desired degree of accuracy and focus of fit per saturated regime.

Future work studying the effect of binary mixtures with more grain sizes is required to validate the applicability of the models for additional soils. Albeit each model was able to capture the behavior for different soils, no one model was able to capture all

the behavior. Therefore, a model based on the specific transition points between each of the four saturation regimes given information on the soil hydraulic properties and limited thermal properties needs to be developed.

3.7. Acknowledgements

This research was funded by the U. S. Army Research Office Award W911NF-04-1-0169 the Engineering Research and Development Center (ERDC). The authors wish to thank John Peters from ERDC, Yi Dong, Ning Lu and Toshihiro Sakaki for conversations that improved this research. We also acknowledge Tiande (Jack) Wu for his support and technical contributions.

3.8. References

Abramowitz, M., and I.A. Stegun. 1972. Handbook of mathematical functions. Dover Publications, Inc., New York.

Adivarahan, P., D. Kunli, and J.M. Smith. 1962. Heat transfer in porous rocks through which single phase fluids are flowing. Soc. Pet. Eng. J. 2(3):290-296. doi:10.2118/368-PA

Al Nakshabandi, G., and H. Kohnke. 1965. Thermal conductivity and diffusivity of soils as related to moisture tension and other physical properties. Agric. Meteorol. 2(4):271-279. doi:10.1016/0002-1571(65)90013-0

Bussing, W., and H.J. Bart. 1997. Thermal conductivity of unsaturated packed beds – comparison of experimental results and estimation methods. Chem. Eng. Process. 36(2):119-132. doi:10.1016/S0255-2701(96)04176-1

Campbell, G.S., 1985, Soil physics with BASIC. Elsevier, New York.

Campbell, G.S., J.D. Jungbauer, W.R. Bidlake, and R.D. Hungerford. 1994. Predicting the effect of temperature on soil thermal conductivity. Soil Sci. 158(5):307-313. doi:10.1097/00010694-199411000-00001

Carslaw, H.S., and J.C. Jaeger. 1959. Conduction of heat in soils. 2nd ed. Oxford Univ. Press, London.

Chen, S.X. 2008 Thermal conductivity of sands. Heat Mass Trans. 44(10):1241-1246. doi:10.1007/s00231-007-0357-1

Clarke, R.H. 1979. Reservoir properties of conglomerates and conglomeratic sandstones. AAPG bull. 63(5):799-803.

Côté, J., and J.M. Konrad. 2005. A generalized thermal conductivity model for soils and construction materials. Can. Geotech. J. 42(2):443-458. doi:10.1139/t04-106

Côté, J., and J.M. Konrad. 2009. Assessment of structure effects on the thermal conductivity of two-phase porous geomaterials. Int. J. Heat Mass Trans. 52(3-4):769-804. doi:10.1016/j.ijheatmasstransfer.2008.07.037

Decagon Devices. 2014. KD2 Pro thermal properties analyzer operator's manual, version 20 June 2014 – 09:11:40. Decagon Devices, Inc., Pullman, WA.

de Vries, D.A. 1963. Thermal properties of soils. In: W.R. van Wijk, editor, Physics of plant environment. North-Holland Publ. Co., Amsterdam. p. 210-235.

Dong, Y., J.S. McCartney, and N. Lu. 2014. Critical review of thermal conductivity models for unsaturated soils. Geotech. and Geolog. Eng., Submitted for Review.

Esselburn, J.D., R.W. Ritzi Jr., and D.F. Dominic. 2010. Porosity and permeability in ternary sediment mixtures. Groundwater, 49(3):393-402. doi:10.1111/j.1745-6584.2010.00744.x

Fragaszy, R.J., W. Su, and F.H. Siddiqi. 1990. Effects of oversize particles on the density of clean granular soils. Geotech. Test. J., 13(2):106-114. doi:10.1520/GTJ10701J

Garga, V.K., and C.J. Madureira. 1985. Compaction characteristics of river terrace gravel. J. Geotech. Eng. 111(8):987-1007. doi:10.1061/(ASCE)0733-9410(1985)111:8(987)

Gerke, H.H., and M.T. van Genuchten. 1993. A dual-porosity model for simulating the preferential movement of water and solutes in structured porous media. Water Resour. Res. 29(2):305-319. doi:10.1029/92WR02339

Haigh, S.K. 2012. Thermal conductivity of sands. Géotech. 62(7):617-625. doi:10.1680/geot.11.P.043

Hanks, R.J., H.R. Gardner, and M.L. Fairbourn. 1967. Evaporation of water from soils as influenced by drying with wind or radiation. Soil Sci. Soc. Am. Proc. 31(5):593-598. doi:10.2136/sssaj1967.03615995003100050001x

Hiraiwa, Y., and T. Kasubuchi. 2000. Temperature dependence of thermal conductivity of soil over a wide range of temperature (5-75ºC). Eur. J. Soil Sci. 51(2):211-218. doi:10.1046/j.1365-2389.2000.00301.x

Holtz, W.G., and C.W. Lowitz. 1957. Compaction characteristics of gravelly soils. Special Tech. Pub. No. 232, ASTM, Philadelphia, PA, 70-83.

Hopmans, J.W., and J.H. Dane. 1986. Thermal conductivity of two porous media as a function of water content, temperature, and density. Soil Sci. 143:187-195. doi:10.1097/00010694-198610000-00001

Horton, R., and P.J. Wierenga. 1984. The effect of column wetting on soil thermal conductivity. Soil Sci. 138(2):102-108.

Johansen, O. 1975. Thermal conductivity of soils. Ph.D. diss. Norwegian Univ. of Science and Technol., Trondheim (CRREL Draft Transl. 637, 1977).

Kaman, P.J., R.W. Ritzi, D.F. Dominic, and C.M. Conrad. 2007. Porosity and permeability in sediment mixtures. Groundwater. 45(4):429-438. doi:10.1111/j.1745-6584.2007.00313.x

Kluitenberg, G.J., J.M. Ham, and K.L. Bristow. 1993. Error analysis of the heat pulse method for measuring soil volumetric heat capacity. Soil Sci. Soc. Am. J. 57(6):1444-1451. doi:10.2136/sssaj1993.03615995005700060008x

Koltermann, C.E., and S.M. Gorelick. 1995. Fractional packing model for hydraulic conductivity derived from sediment mixtures. Water Resour. Res. 31(12):3283-3297. doi:10.1029/95WR02020

Larsson, M.H., and N.J. Jarvis. 1999. Evaluation of a dual-porosity model to predict field-scale solute transport in a macroporous soil. J. Hydrol. 215(1-4):153-171. doi:10.1016/S0022-1694(98)00267-4

Lipiec, J., B. Usowicz, and A. Ferrero. 2007. Impact of soil compaction and wetness on thermal properties of sloping vineyard soil. Int. J. Heat Mass Trans. 50(19-20):3837-3847. doi:10.1016/j.ijheatmasstransfer.2007.02.008

Lu, N., and Y. Dong. 2014. A universal equation for thermal conductivity of unsaturated soil at room temperature. Geotech. and Geolog. Eng., Submitted for Review.

Lu, N., and W.J. Likos. 2004. Unsaturated soil mechanics. John Wiley & Sons, Inc., Hoboken. p. 429-431.

Lu, S., T. Ren, Y. Gong, and R. Horton. 2007. An improved model for predicting soil thermal conductivity from water content at room temperature. Soil Sci. Soc. Am. J. 71(1):8-14. doi:10.2136/sssaj2006.0041

McCumber, M.C., and R.A. Pielke. 1981. Simulation of the effects of surface fluxes of heat and moisture in a mesoscale numerical model. J. Geophys. Res. 86:9929-9938. doi:10.1029/JC086iC10p09929

Midttømme, K., and E. Roaldset. 1998. The effect of grain size on thermal conductivity of quartz sands and silts. Pet. Geosci. 4(2):165-172. doi:10.1144/petgeo.4.2.165

Ochsner, T.E., R. Horton, and T. Ren. 2001. A new perspective on soil thermal properties. Soil Sci. Soc. Am. J. 65(6):1641-1647. doi:10.2136/sssaj2001.1641

Philip, J.R. 1957. Evaporation, and moisture and heat fields in the soil. J. Meteorol. 14(4):354-366. doi:10.1175/1520-0469(1957)014<0354:EAMAHF>2.0.CO;2

Philip, J.R., and D.A. de Vries. 1957. Moisture movement in porous materials under temperature gradients. Trans. Am. Geophy. Union. 38(2):222-232. doi:10.1029/TR038i002p00222

Sakaguchi, I., T. Momose, and T. Kasubuchi. 2007. Decrease in thermal conductivity with increasing temperature in nearly dry sandy soil. Eur. J. Soil Sci. 58(1):92-97. doi:10.1111/j.1365-2389.2006.00803.x

Sakaguchi, I., T. Momose, H. Mochizuki, and T. Kasubuchi. 2009. Heat pipe phenomenon in soil under reduced air pressure. Eur. J. Soil Sci. 60(1):110-115. doi:10.1111/j.1365-2389.2008.01095.x

Sakaki, T., and T.H. Illangasekare. 2007. Comparison of height-averaged and point-measured capillary pressure-saturation relations for sands using a modified Tempe cell. Water Resour. Res. 43(12):W12502. doi:10.1029/2006WR005814.

Sakaki, T., A. Limsuwat, K.M. Smits, and T.H. Illangasekare. 2008. Empirical two-point α-mixing model for calibrating the ECH2O EC-5 soil moisture sensor in sands. Water Resour. Res. 44(4):W00D08. doi:10.1029/2008WR006870

Sakaki, T., and K.M. Smits. 2014. Water retention properties of binary mixtures as affected by mixing fractions. Vadose Zone J. Submitted for Review.

Sepaskhah, A.R., and L. Boersma. 1979. Thermal conductivity of soils as a function of temperature and water content. Soil Sci. Soc. Am. J. 43(3):439-444. doi:10.2136/sssaj1979.03615995004300030003x

Skaggs, R.W., and E.M. Smith. 1968. Apparent thermal conductivity of soil as related to soil porosity. Soil Sci. Soc. Am. Proc. 38:504-507. doi:10.13031/2013.39451

Smits, K.M., T. Sakaki, A. Limsuwat, and T.H. Illangasekare. 2010. Thermal conductivity of sands under varying moisture and porosity in drainage-wetting cycles. Vadose Zone J. 9(1):172-180. doi:10.2136/vzj2009.0095

Tarnawski, V.R., and F. Gori. 2002. Enhancement of the cubic cell soil thermal conductivity model. Int. J. Energy Res. 26(2):143-157. doi:10.1002/er.772

Tarnawski, V.R., and W.H. Leong. 2000. Thermal conductivity of soils at very low moisture content and moderate temperatures. Transp. Porous Media. 41(2):137-147.

Tarnawski, V.R., W.H. Leong, and K.L. Bristow. 2000. Developing a temperature-dependent Kersten function for soil thermal conductivity. Int. J. Energy Res. 24(15):1335-1350. doi:10.1002/1099-114X(200012)24:15<1335::AID-ER652>3.0.CO;2-X

Tarnawski, V.R., M.L. McCombie, T. Momose, I. Sakaguchi, and W.H. Leong. 2013. Thermal conductivity of standard sands. Part III. Full range of saturation. Int. J. of Thermophys. 34(6):1130-1147. doi:10.1007/s10765-013-1455-6

Tavman, I.H. 1996. Effective thermal conductivity of granular porous materials. Int. Commun. Heat Mass Transfer. 23(2):169-176. doi:10.1016/0735-1933(96)00003-6

Terzaghi, K. 1952. Permafrost. J. Boston Soc. Civil Eng. 39:1-50.

Usowicz, B., J. Kossowski, and P. Baranowski. 1996. Spatial variability of soil thermal properties in cultivated fields. Soil Tillage Res. 39(1-2):85-100. doi:10.1016/S0167-1987(96)01038-0

van Genuchten, M.T. 1980. A closed-form equation for predicting the hydraulic conductivity of unsaturated soils. Soil Sci. Soc. Am. J. 44(5):892-897.

Van Rooyen, M., and H.F. Winterkorn. 1959. Structural and textural influences on thermal conductivity of soils. High Res. Board Proc. 39:576-621.

Westman, A.E.R., and H.R. Hugill. 1930. The packing of particles. J. Am. Ceramic Soc. 13(10):767-779. doi:10.1111/j.1151-2916.1930.tb16222.x

Yadav, M.R., and G.S. Saxena. 1977. Thermal characteristics of the soils in relation to their physical parameters and moisture content. J. Indian Soc. Soil Sci. 25:1-6.

Zimmerman, R.W., G. Chen, T. Hadgu, and G.S. Bodvarsson. 1993. A numerical dual-porosity model with semianalytical treatment of fracture/matrix flow. Water Resour. Res. 29(7):2127-2137. doi:10.1029/93WR00749

4. The effect of soil disturbance on vapor transport under dry and wet conditions

4.1.0 Introduction

Soil-water evaporation is one of the governing processes responsible for controlling water and energy exchanges between the land and atmosphere. It is a complicated multiphase phenomenon that involves pore-scale mass and energy transfer, phase change, and liquid-vapor interfacial displacement [*Shokri et al.,* 2010] which is affected by the strongly coupled interactions of the soil's properties (i.e., thermal, hydraulic), internal transport mechanisms (e.g., vapor diffusivity), and atmospheric demand (e.g., humidity, temperature, air flow, radiation) [Van Brakel, 1980; *Prat,* 2002]. The sensitivity of water distributions and flux predictions to the hydraulic and thermal properties of homogeneous soils has been significantly studied both experimentally at laboratory and watershed scales (e.g., *Penman*, 1948; *van de Griend and Owe,* 1994; *Yamanaka et al*., 1999; *Blight,* 2002; *Prat,* 2002; *Shokri et al.,* 2009; *Sakai et al.,* 2011; *Smits et al.,* 2011). Much less work has been performed in the area of water distribution and fluxes from heterogeneous soil profiles. Literature available on evaporation from heterogeneous media is often in reference to mulch layers and other barriers to manage water loss (e.g. *Papendick et al*., 1972; *Chung and Horton,* 1987; *Yuan et al.,* 2009) and layered porous media (e.g. *Willis,* 1960; *Unger*, 1971; *Modaihsh et al.,* 1985; *Yamanaka et al*., 2004; *Shokri et al*., 2008; *Pillai et al*., 2009; *Shokri et al.,* 2010; *Huang et al.,* 2012). In addition to horizontal heterogeneity, soil thermal and hydraulic properties may vary in the vertical direction, creating textural contrasts between adjacent soils and hence heterogeneous porous surfaces. The study of evaporation from heterogenous porous surfaces is relevant to natural sedimentary environments [*Press and Siever*, 1986], manmade locations where soil is disturbed or loosened due to soil tillage practices or wheel-track compaction (e.g. *Reicosky et al*., 1980; *Hammel et al.,* 1981), locations where soil is disturbed due to the placement of a buried object such as a landmine [*Hendrickx et al.,* 2003; *van Dam et al.*, 2005; *Smits et al.,* 2013], fire burn environments [*Massman et al.,* 2008], pore size distribution due to structural cracks and root development and decay, textural layering [*Mohanty et al.*, 1994] and engineered soils designed to prevent water loss or vapor intrusion (e.g., mulch layers, waste isolation) [*Shokri et al.*, 2010]. Despite its wide relevance, there are very few studies of evaporation from heterogenous porous

surfaces (e.g. *Mohanty and Zhu*, 2007; *Lehmann and Or*, 2009; *Shahraeeni and Or*, 2010; *Nachshon et al*., 2011a, b).

In literature, evaporation is often defined according to different stages, defined by differences in evaporation rates, location of the drying front, and dominant transport mechanisms [*Lemon*, 1956; *Shokri et al.*, 2010], referred to as stage 1 and stage 2 evaporation. Stage 1 evaporation is often defined by high and relatively constant evaporation rates and the formation of a receding drying front, i.e. the interface between the water-saturated and partially air-filled region [*Lehmann et al.*, 2008; *Shokri et al.*, 2010]. Capillary flow along the hydraulically connected flow paths through the unsaturated zone above the drying front (oftentimes referred to as the "film region") sustain the high evaporation rates [*Yiotis et al.*, 2003; *Lehmann and Or*, 2009]. Nonetheless, experimental evidence suggests that Stage-1 evaporation may not always be high and constant but rather drop from the onset of the drying process. This drop is often associated with high wind velocities with a thin boundary layer and large soil pores [Shahraeeni et al., 2012]. During Stage 1, the evaporation rate is usually limited by atmospheric conditions. *Shokri et al*., [2008,9 and 10] showed that during stage 1, the liquid menisci in the fine pores at the soil surface remained coupled with the atmosphere, drawing water from the porous media to supply the high evaporative demand at the soil surface. Stage 1 evaporation continues as long as the hydraulic connection within the film flow region is maintained.

When the drying front reaches a certain depth, the downward gravity and viscous forces overcome the upward capillary forces and the hydraulic connection at the soil surface is severed [*Lehmann et al*., 2008]. Water starts to recede from the soil surface and a dry surface layer begins to form, marking the onset of Stage 2 evaporation. This is oftentimes called the "falling rate period" in which stage 1 evaporation transitions into vapor diffusion limited stage 2 evaporation [*van Brakel*, 1980; *Yiotis et al*., 2004; *Lehmann et al.*, 2008]. Stage 2 evaporation is marked by the formation of an internal vaporization plane and hence a receding drying front [*Fisher*, 1923]. The transition between stage 1 and stage 2 evaporation is difficult to determine. *Shokri and Or* [2011] experimentally demonstrated that the transition is affected predominantly by the porous media properties rather than the surface boundary conditions. Like stage 1 evaporation, stage 2 evaporation is also dependent on capillarity; large capillary pressures suppress evaporation rates by

lowering the equilibrium vapor pressure and the water energy available according to the Kelvin equation [*Ho*, 2006].

Evaporation from heterogeneous porous surfaces introduces additional processes occurring between the texturally different media. Recently, *Lehmann and Or* [2009] and *Shahraeeni and Or* [2010] studied evaporation in heterogeneous soils with vertical textural contrasts (i.e. a sharp interface perpendicular to the evaporation front). *Lehmann and Or* [2009] demonstrated that the observed drying front pattern in the heterogeneous soil column was larger than the evaporation rate predicted from the single porous media properties alone. They found that initially, the evaporation rate from the coarse and fine saturated surfaces is uniform. This was followed by a drying front forming in the coarse domain and capillary driven lateral flow from the coarse domain to the fine domain, thus enhancing the evaporation rate from the fine domain [*Lehmann and Or*, 2009]. The capillary water flows from the coarse domain to the fine domain are due to the capillary pressure gradient (i.e. the difference between the air entry value of the coarse domain and the minimum capillary pressure in the fine domain). This process is referred to as capillary pumping [*Yotis et al.*, 2001 and *Lehmann and Or*, 2009]. Mathematically, the horizontal flow component from the coarse soil to the fine soil is defined by calculating the driving capillary pressure gradient [*Lehmann et al*., 2008]. The fine domain remains saturated (i.e. stage 1 evaporation) until the drying front depth in the coarse material equals the difference between the air entry values of the two materials. *Lehmann and Or* [2009] also introduce a characteristic length (L_{cap}) to determine the transition between stage 1 and 2 evaporation for each media. L_{cap} can be calculated based on properties of the liquid (e.g. surface tension and density) and the largest and smallest capillary radii. Calculation of this value requires knowledge of the representative pore radius of the medium, a value that is not easily determined and often used as a fitting parameter. Once L_{cap} is exceeded, water is transported primarily by diffusion.

As *Shahraeeni and Or* [2010] point out, the resulting evaporation rate variability from the coarse and fine regions will also result in variability in surface temperature. Shahraeeni and Or (2010) inverted infrared thermography (IRT) data from experiments involving heterogeneous porous surfaces to obtain evaporation flux values compared to those from direct weighting of the samples. Experiments were conducted under ambient conditions (26^{o} C +_2 ^{o}C). Results showed good agreement between observed and inverted data, demonstrating the applicability of the method for ambient conditions.

Nachshon et al., [2011] conducted a study on the effects of salt precipitation on evaporation from heterogeneous porous surfaces with results in agreement with *Lehmann and Or* [2009], most of the evaporation occurred from the fine sand region.

In this study, to better understand the effect of heterogenous porous surfaces on the coupled water-vapor-heat flow processes in the shallow subsurface, we modified a theory previously developed by *Smits et al.,* [2011,2012] and *Davarzani et al.,* [2014] that allows for coupling single-phase (gas), two-component (air and water vapor) transfer in the atmosphere and two-phase (gas, liquid), two-component (air and water vapor) flow in porous media at the REV scale under non-isothermal, non-equilibrium conditions to better account for the hydraulic and thermal interactions within the media. The only input parameters needed for this model are the soil thermo-physical properties, the initial conditions in the soil and atmospheric systems and the mean wind velocity and temperature. To test the numerical formulations and codes, we performed a series of laboratory experiments under varying hydraulic and thermal boundary conditions using bench scale physical models and a unique low velocity porous media/wind tunnel, allowing for better control and gathering of accurate data at scales of interest not feasible in the field.

4.2.0 Numerical Model Formulation

The model described in *Davarzani et al*., [2014] that allows for coupling single-phase (gas), two-component (air and water vapor) transfer in the atmosphere and two-phase (gas, liquid), two-component (air and water vapor) flow in porous media at the REV scale under non-isothermal, non-equilibrium conditions was amended to better account for hydraulic and thermal interactions within the media. The reader is referred to *Davarzani et al.,* [2014] for the full model description, however, the governing equations for macroscopic flow and mass and energy balance equations for water, air, and water vapor in the porous media as well as the gas (air and water vapor) above the porous media are presented here.

4.2.1 Governing free flow medium transport equations

In the free flow domain, we assume non-isothermal, single-phase gas flow where the gas, identified with the subscript "*g*", is composed of two components: water vapor (*v*) and air (*a*). We consider that the density and viscosity of the moist air depends on the

temperature and mass fraction of water vapor. The four equations that are solved in the free flow regime include the continuity and Navier-Stokes equations and the component and energy mass balance equations. The continuity and Navier-Stokes equations, which assume an incompressible fluid, with no thermal and solute expansion, are given respectively by [*Bird et al.*, 2002]

$$\nabla.\mathbf{v}_g = 0\,, \tag{1}$$

$$\rho_g\left(\frac{\partial \mathbf{v}_g}{\partial t} + \mathbf{v}_g.\nabla\mathbf{v}_g\right) = -\nabla p_g + \mu_g\nabla.\left(\nabla\mathbf{v}_g\right) + \rho_g\mathbf{g} \tag{2}$$

Where ρ_g is the total mass density of the gas phase [kg/m3], $\boldsymbol{v}_g$ is the average velocity of the gas-phase [m/s], p_g is the pressure of the gas phase (Pa), μ_g is the dynamic viscosity for the gas phase [Pa.s], and $\boldsymbol{g}$ is the acceleration due to gravity (m^2s^{-1}). Because of the low wind velocities in this work in the free flow regime, we assume Stokes equation for the flow of motion in the free flow region (Reynolds number, Re<1), assuming a laminar, Poiseuille flow between two parallel plates and consequently, negligible vapor transfer by turbulent diffusion. Nonetheless, as discussed by *Davarzani et al.*, [2014], surface turbulence can affect the vapor transport just beneath the soil surface [*Ishihara et al.*, 1992] and will be addressed in the future works.

The energy transfer in the free flow region is described by [*Kaviany*, 2001]

$$\left(\rho c_p\right)_g\frac{\partial T}{\partial t} + \left(\rho c_p\right)_g\nabla.\left(T\,\mathbf{v}_g\right) = \nabla.\left(\mathbf{\Lambda}_g.\nabla T\right), \tag{3}$$

Where c_p is the constant pressure heat capacity ($JkgK^{-1}$), T is the moist air temperature (K), and $\mathbf{\Lambda}_g$ is the thermal dispersion tensor of moist air.

The component mass conservation for the free fluid domain can be defined as [*Bird et al.*, 2002]

$$\frac{\partial \rho_g w_v}{\partial t} + \nabla.\left(\rho_g w_v\mathbf{v}_g\right) = \nabla.\left(\mathbf{D}_v.\nabla\left(\rho_g w_v\right)\right), \tag{4}$$

where w_v is the mass fraction of water vapor component in the gas-phase in free flow domain and $\mathbf{D}_v$ (m^2s^{-1}) is the Taylor dispersion tensor of water vapor in air.

The longitudinal Taylor dispersion coefficients of equations (3) and (4) in a stratified media can be calculated as [*Wooding*, 1960]

$$\frac{\left(\Lambda_g\right)_{xx}}{\lambda_g} = 1 + \frac{Pe_T^2}{210} \tag{5}$$

$$\frac{\left(\mathrm{D}_v\right)_{xx}}{\mathscr{D}_v} = 1 + \frac{Pe_C^2}{210} \tag{6}$$

We define the thermal and solutal Péclet numbers as

$$\mathrm{P}e_T = \frac{uH}{\lambda_g \big/ \left(\rho c_p\right)_g}, \text{ and } \mathrm{P}e_C = \frac{uH}{\mathscr{D}_v} \tag{7}$$

respectively, where H is the height of free flow region, λ_g is the thermal conductivity of air-vapor binary mixture (or moist air thermal conductivity), u is the velocity field in x-direction and $\mathscr{D}_v$ is the binary diffusion coefficient of water vapor in dry air which is a function of temperature [**Campbell, 1985**].

4.2.2 Governing porous medium transport equations

4.2.2.1 **NonIsothermal Multiphase Flow**

The flow of two non-compressible immiscible fluids in a rigid porous medium can be described on the basis of Darcy's law [*Bear*, 1972]

$$\phi \frac{dS_\ell}{dp_c} \frac{\partial \rho_\ell \left(p_g - p_\ell\right)}{\partial t} + \nabla.\left(\rho_\ell \mathbf{v}_\ell\right) = -\dot{m} \tag{8}$$

$$\phi \frac{dS_g}{dp_c} \frac{\partial \rho_g \left(p_g - p_\ell\right)}{\partial t} + \nabla.\left(\rho_g \mathbf{v}_g\right) = +\dot{m} \tag{9}$$

where the subscripts l and g represent the liquid (wetting) and gas (non-wetting) phases, respectively. S is the saturation, p is the pressure (Pa), v is the average velocity within the wetting and nonwetting fluids (m s^{-1}), ρ is the total mass density for the α-phase (kg m^{-3}) and $\dot{m}$ is the phase change rate (kg m^{-3} s^{-1}). In this study, we assumed that the phase change rate, $\dot{m}$, is proportional to the difference between the equilibrium density of vapor and its actual density through a coefficient [*Eames et al.*, 1997]:

$$\dot{m} = \epsilon(p_{vs} - p_v)\left(\frac{M_w}{2\pi RT}\right)^{0.5} \quad (10)$$

where $\dot{m}$ (kg m^{-2} s^{-1}) is the interfacial mass flux, ϵ (m s^{-1}) is the evaporation coefficient, p_{vs} (Pa) is the saturation pressure, p_v (Pa) is the vapor pressure in the gas phase, M_w (kg mol^{-1}) is the molecular weight of water, R (Pa m^3 K^{-1} mol^{-1}) is the universal gas constant and T (K) is the temperature. Equations (8) and (9) can be solved simultaneously for the unknown pressures p_g and p_ℓ.

Wetting and non-wetting pressures are coupled by the macroscopic capillary pressure (p_c) saturation relationship $p_c(S_l)=p_g-p_l$. To compute the saturation and relative permeability of the wetting and non-wetting phases, several empirical models such as those by *van Genuchten* [1980] and *Brooks and Corey* [1966] are often used. Nonetheless, they commonly fail to capture the water retention behavior lower than the residual water content and therefore are oftentimes not the best options for evaporation studies. Various models have been developed to extend the van Genuchten or Brooks and Corey analytical models to dry soils (e.g. *Fredlung and Xing*, 1994; *Rossi and Nimmo*, 1994; *Fayer and Simmons*, 1995; *Webb*, 2000; *Groenevelt and Grant*, 2004; *Khlosi et al*., 2006). In this work, to compute the saturation of the gas and water phases from p_c, the *Fayer and Simmons* [1995] model was used. This model accounts for the adsorption of water vapor on the solid phase under dry conditions by modifying the residual water content. This allows for the avoidance of the common practice of using the residual water content as a fitting parameter [*Groenevelt and Grant*, 2004]. Under dry soil conditions, liquid film flow can significantly enhance the drying rate (e.g. *Laurindo and Prat*, 1998; *Yiotis et al*., 2003), thus playing an important role in evaporation from soils. This work considers both the contributions due to capillary flow and film flow to the hydraulic conductivity for the full range of saturation [*Zhang*, 2010]. The *van Genuchten* [1980] model is used to describe hydraulic conductivity due to the capillary flow while the model develop by *Tokunaga* [2009] was implemented to describe the portion due to film flow.

4.2.2.2 Heat transfer

The governing equation for the movement of heat in a variably saturated porous medium, is defined as

$$C_w \frac{\partial T}{\partial t} + \rho_w C_w u_w \nabla T - \rho_a C_a u_a \nabla T - \nabla \cdot (\lambda \nabla T) = Q + L\,\dot{m}$$

(11)

where T is the temperature (K), C_{eq} is the effective heat capacity per unit volume of soil (J m^{-3} K^{-1}), C_w and C_a are the specific heat capacities of water and gas, respectively (J m^{-3} K^{-1}), u_w and u_a are the mean pore velocities of the water and gas, respectively, λ is the effective thermal conductivity (W m^{-1} K^{-1}) [*Campbell et al.,* 1994], Q is the heat loss term (W m^{-3}) and L is the latent heat of vaporization of liquid water (J kg^{-1}) [*Monteith and Unworth,* 1990]. $L\,\dot{m}$ is the latent heat due to phase change in the soil (W m^{-3}). Equation 8 considers the sensible heat by convection of liquid water and water vapor, conduction of sensible heat as described by Fourier's law and the latent heat by vapor flow (i.e. due to phase change). The local-scale thermal equilibrium assumption is used in this work. This assumption is acceptable because the characteristic time associated with thermal equilibrium is much lower than the characteristic time associated with mass transfer. The method proposed by *Campbell* [1994] to account for the effect of temperature on thermal conductivity was used for this work. The model assumes that the thermal conductivity of any soil comprised of water (*w*), gas (*a*) and mineral (*m*) can be calculated based on the volume-weighted sum of the thermal conductivities of the components of the mixture [*Campbell et al*., 1994];

$$\lambda = \frac{k_w x_w \lambda_w + k_a x_a \lambda_a + k_m x_m \lambda_m}{k_w x_w + k_a x_a + k_m x_m}$$

(12)

where k_w, k_a and k_m are weighting factors and x_w, x_a and x_m are the volume fractions of the water, gas and mineral, respectively. The thermal conductivity of the gas phase (λ_a) is the sum of the direct heat conduction through air and the latent heat transfer across pores in the soil, where the latent heat is the main factor responsible for the variation of thermal conductivity with temperature [*Campbell et al.,* 1994].

4.2.2.3 Water vapor transport

The transport of water vapor in the gas phase is given as [*Bear,* 1972]

$$\phi \frac{\partial(\rho_g S_g w_v)}{\partial t} + \nabla.(\rho_g w_v \mathbf{v}_g - \mathrm{D}_v^* \nabla(\rho_g w_v)) = \dot{m} \tag{13}$$

Where D_v^* (m2/s) is the effective vapor diffusion coefficient and expressed as

$$\mathrm{D}_v^* = \tau \phi S_g \mathscr{D}_v \tag{4}$$

Where τ is the tortuosity, ϕ is the porosity, and $\mathscr{D}_v$ is the binary diffusion coefficient of water vapor in air (m^2s^{-1}). The tortuosity τ can be estimated using the *Penman* [1940] model ($\tau = 0.66\theta_g$). Because of slow flow velocities in porous media and high diffusion coefficients, dispersion can be neglected in the gas phase.

4.2.3 Interface boundary conditions

To couple the two domains, boundary conditions applied at the interface between the porous medium and free flow medium are required. The coupling conditions are motivated by thermodynamic equilibrium and mirror those of a simple interface. The reasoning behind the boundary conditions can be found in *Mosthaf et al*., [2011].

The continuity of the normal mass fluxes for the gas-phase (pressure jump boundary condition in the gas-phase) can be expressed as

$$\left[(\rho_g \mathbf{v}_g)\mathbf{n}\right]_{ff} = -\left[(\rho_g \mathbf{v}_g)\mathbf{n}\right]_{pm}, \text{ on } \Gamma \tag{15}$$

Where the subscripts *ff* and *pm* represent the free flow and porous medium flow, respectively, **n** is the unit normal vector and Γ represents the interface between the free flow and porous medium subdomains. The flux of the liquid phase equals zero at the interface. To express a condition for the tangential component of the velocity in the free flow regime, the Beavers-Joseph-Saffman slip boundary condition was used [*Beavers and Joseph*, 1967; *Layton et al*., 2002]:

$$\mathbf{v}_g.\mathbf{t}_\mathrm{j} = \frac{\sqrt{\mathrm{K}}}{\alpha_{BJ}} \mathbf{t}_\mathrm{j}.\nabla \mathbf{v}_g, \text{ on } \Gamma \tag{16}$$

where $\mathbf{t}_\mathrm{j}$ (j=1, …, n-1) are linear independent unit tangential vectors to the boundary Γ, and α_{BJ} is a dimensionless slip coefficient. In this study, the surface roughness of the

porous medium appears as a coefficient in the surface slip boundary condition. Oftentimes, in models that are uncoupled, aerodynamic and soil surface resistances for water vapor transfer are needed. In this model, these terms are not necessary due to the coupling conditions. The parameter α_{BJ} is empirical and depends on flow conditions, interface location, surface microstructure and porosity. The slip coefficient can be estimated using an equation proposed by *Neale and Nader*, [1974], known as the Brinkman equation. Because the Brinkman equation contains Laplacian terms and is of the same order as Stokes equation, through the use of Brinkman equation at the interface and in the bulk of porous matrix, the boundary conditions in both Stokes and Darcy equations become compatible. In this study, we used a constant slip coefficient of 0.01 based on the only measurement data available in [*Kim et al.*, 1994] which has similar porous medium properties to our experimental study.

Local thermal equilibrium at the interface was used for the continuity boundary condition for temperature at the porous medium-free medium interface.

$$[T]_{ff} = [T]_{pm}, \text{ on } \Gamma \tag{17}$$

Where the continuity of the heat fluxes is

$$\left[\mathbf{n}.\left(\left(\rho c_p\right)_\ell \mathbf{v}_\ell T + \left(\rho c_p\right)_g \mathbf{v}_g T - \Lambda^* \nabla T\right)\right]_{pm} = -\left[\mathbf{n}.\left(\left(\rho c_p\right)_g \left(T_g \mathbf{v}_g\right) - \Lambda_g \nabla T_g\right)\right]_{ff}, \text{ on } \Gamma \tag{18}$$

We also assume the continuity of the component mass fluxes across the interface. This equilibrium is considered as

$$[w_v]_{ff} = [w_v]_{pm}, \text{ on } \Gamma \tag{19}$$

Where the continuity of the component fluxes across the interface is

$$\left[\mathbf{n}.\left(\rho_g w_v \mathbf{v}_g - \mathrm{D}_v^* \nabla\left(\rho_g w_v\right)\right)\right]_{pm} = -\left[\mathbf{n}.\left(\rho_g w_v \mathbf{v}_g - \mathrm{D}_v \nabla\left(\rho_g w_v\right)\right)\right]_{ff}, \text{ on } \Gamma \tag{20}$$

After the implementation of the initial and boundary conditions, the system of partial differential equations for the model in a two-dimensional domain was simultaneously solved using the COMSOL Multiphysics software that is based on the Finite Element

Method. The free flow subdomain equations to be solved include equations 1 through 4 and equations 5, 6, 8, and 10 (renumber at the end) in the porous medium subdomain.

4.3. Materials and Methods

The numerical heat and mass transfer model discussed in the preceding section was evaluated using experimental data obtained from a two-dimensional soil tank interfaced, along its centerline, to a small wind tunnel (Figure 1). The soil tank was equipped with a sensor network, summarized in Table 1, for the continuous measurement of time-dependent subsurface and free-flow properties. A series of four experiments were performed under varying atmospheric and initial conditions, using a well characterized test sand. This soil tank-wind tunnel experimental apparatus was specifically used to generate precision soil moisture, soil and air temperature, relative humidity, air velocity, and weight measurements. In this section, the experimental materials, methods, and protocols are discussed.

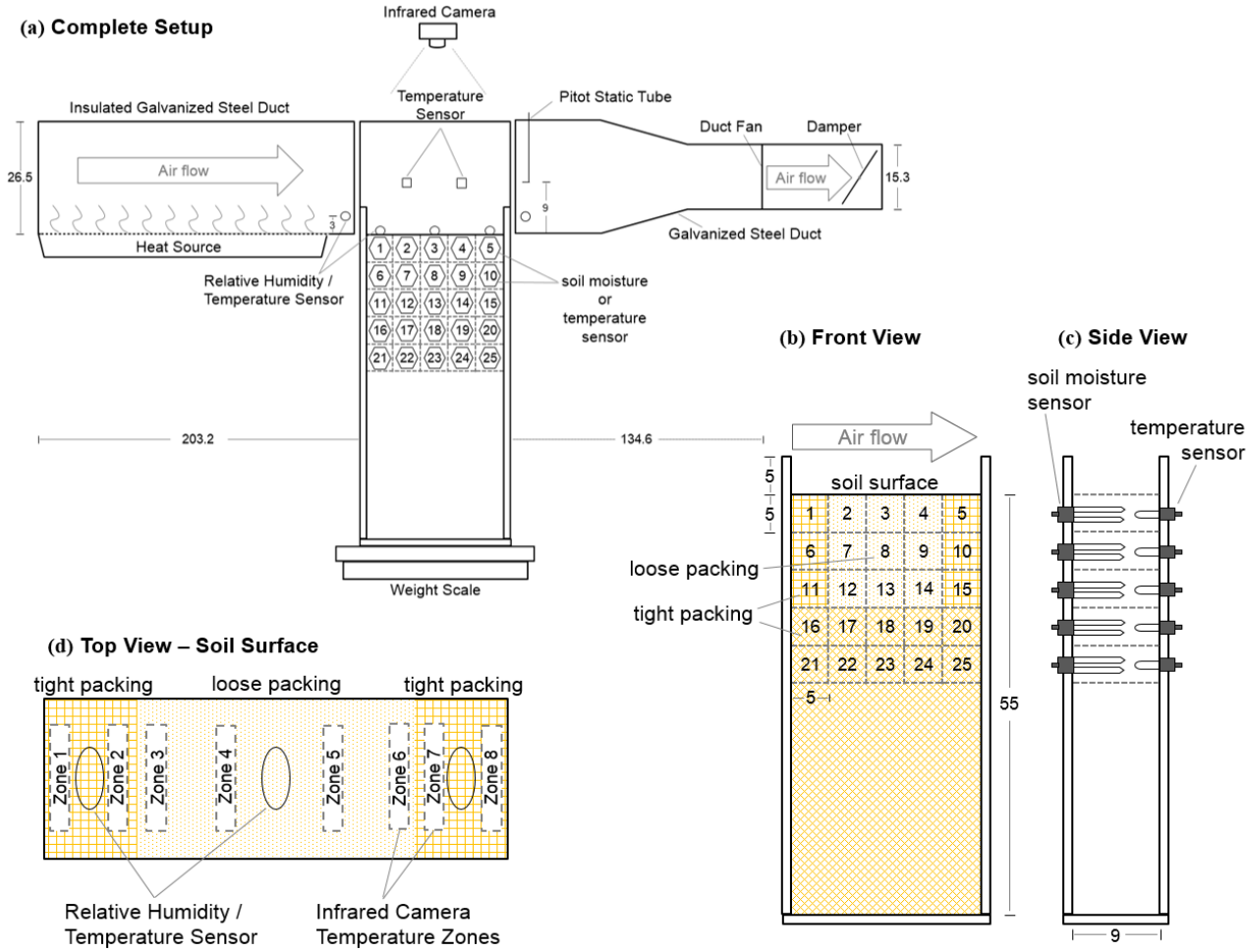

Figure 1. Schematic of experimental setup (a) complete setup including tank and ductwork (b) front view depicting tight packing (fence pattern) and loose packing (10% dotted pattern) (c) side view of tank and sensors below the surface and (d) planar view noting infrared zones established and sensors in contact with the soil surface (all dimensions are in centimeters – not drawn to scale).

Table 1. Summary of sensors used in experimental portion of present study.

Sensor	Sensor Measurements	Number of Sensors Employed in Experimental Apparatus	Sensor Sampling Frequency (min)
EC-5	Soil moisture	25	10
ECT	Soil/air temperature	19	10
SH-1	Thermal properties	1	10
EHT	Relative humidity/temperature	5	10
Infrared camera	Surface temperature/evaporation	1	1
Digital camera	Visualization of drying front	1	60
Pitot static tube	Wind velocity	1	10
Weighting scale	Cumulative evaporation/evaporation rate	1	10

4.3.1 Experimental apparatus

A two-dimensional soil tank (Figure 1), was constructed out of 1.2 cm thick acrylic (specific heat, 1464 J kg^{-1} K^{-1}; thermal conductivity, 0.2 W m^{-1} K^{-1}; density, 1150 kg m^{-3}) with an internal length of 25 cm length, internal width of 9.1 cm, and height of 55 cm. The top 25 cm of the tank contained a grid consisting of 5 cm by 5 cm squares on both sides offering the potential for a total of 50 sensors to be installed. The small wind tunnel that the soil tank was interfaced with was constructed out of galvanized steel ducts with an upstream length of 2.2 m and a downstream length of 1.6 m. A VS200 variable speed controller (Suncourt, Inc.; USA) was connected to a 15.2 cm diameter Pro DB6GTP in-line duct fan (Suncourt, Inc.; USA) located downstream of the soil tank (Figure 1) to induce and control wind velocity. A 15.2 cm diameter galvanized steel duct damper was also used to help control wind velocity. The free-stream wind velocity was monitored immediately downstream of the soil tank (Figure 1) at 10 minute intervals using a 167-12 stainless steel pitot-static tube (Dwyer Instruments, Inc.; USA) that has an accuracy of $\pm$ 5%. The dynamic pressure was physically measured by a PX653-0.1D5V pressure transducer (Omega Engineering, Inc.; USA) which was then converted to a velocity via Bernouilli's equation in a LabVIEW code (National Instruments Corp.; USA). The air temperature within the experimental apparatus was maintained at constant temperatures using five Infrared Salamander Model FTE 500-240 ceramic radiative heaters (Mor Electric Heating Assoc., Inc.; USA) installed in series along the upstream duct work, Figure 1. The heaters were controlled by a 2104 temperature control system (Chromalox; USA) regulated by an infrared temperature sensor (Exergen Corporation; USA).

4.3.2. Packing configuration and soil material

The tank was wet-packed using deionized water in the configuration presented in Figure 1 using the same sand. Packing regions are identified by their average porosity (tight packing average porosity 0.318; loose packing average porosity 0.440). The purpose for packing with two distinct regions was to portray undisturbed soil (tight packing) and disturbed soil (loose packing) enabling an understanding of the interaction between the two regions. The bottom tightly packed region was 0.4 m deep and 0.25 m wide. The top 0.15 m of soil was divided into two 0.05 m wide tightly packed regions located on either side (i.e. upstream and downstream) of a 0.15 m wide loose packing, see Figure 1. For the tight packing, sand was poured evenly across the length and width of the tank at 2.5 cm

increments. Following emplacement, each lift was tamped and the walls of the tank were tapped with a rubber mallet; refer to *Sakaki and Illangasekare* [2007] for a detailed explanation of this packing procedure. Tamping and tapping was not employed for the loose sand packing in order to prevent settling and compaction. Baffles were used to prevent mixing across the boundaries of the tight and loose packing regions (Figure 1). Once the sand surface was even with the top of the tank, the baffles were removed and the surface sensors were installed.

Accusand #30/40 (Accusands, Unimin Corps.; USA), a silica sand with mean grain size ranging from 0.420 to 0.595 mm, was used for all experiments. The manufacturer provided technical sheet identifies this sand's uniformity coefficient as approximately 1.2, grain density as 2.65 g cm^{-3}, grain shape as rounded, and mineralogical composition as 99.8% quartz. Other select properties of the #30/40 test sand are provided in Table 2. The soil water retention curves for tight and loose packed conditions are shown in Figure 2.

Table 2. Sand properties as characterized by *Smits and Limsuwat* [2009].

Packing Conditions	Dry Bulk Density (g cm^{-3})	Air Entry Pressure (cm H_2O)	Residual Water Content (m^3 m^{-3})	Van Genuchten Model Parameters*	
				α (cm^{-1})	n (–)
Tight	1.79	16.1 / 22.5	0.028	0.04	20.53
Loose	1.54	9.6 / 15.75	0.024	0.06	20.00

*Parameters determined using RETC based upon experimental data

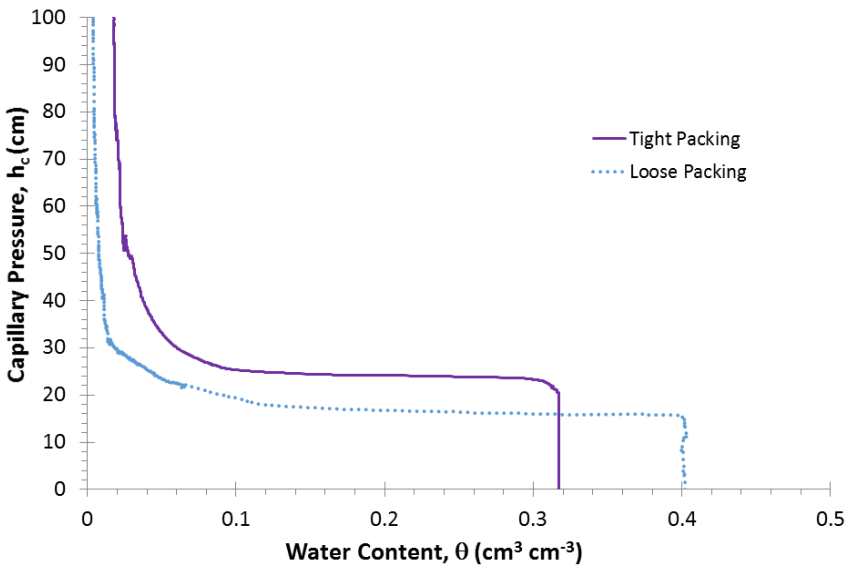

Figure 2. Soil water retention curves for #30/40 sand under tight and loose packing conditions.

4.3.3. Sensor technologies employed

Soil moisture distributions within the tank were continuously monitored at 10 minute intervals using a total of 25 ECH$_2$O EC-5 dielectric soil moisture sensors (Decagon Devices, Inc.; USA; sampling volume – 2.5 cm) installed horizontally at 5 cm increments between the depths of 2.5 and 22.5 cm (Figure 1). The EC-5 sensors with an accuracy of $\pm$ 3% measure the dielectric permittivity of the surrounding porous medium in terms of an analog-to-digital converter number (ADC count). The ADC counts were converted to volumetric water content using the two-point α-mixing model developed by *Sakaki et al*. [2008]. *Assouline et al.* [2010] showed that care must be taken when interpreting "subtle" changes in the apparent dielectric permittivity under conditions where temperature fluctuations are significant; i.e., locations close to the soil surface exposed to diurnal temperature fluctuations. The effects of temperature were taken into account through a multiple regression analysis developed by *Cobos and Campbell* [2007]. Data generated by these sensors were stored on five channel Em50 data loggers (Decagon Devices, Inc.; USA).

A total of 19 3-mm long ECT temperature sensors (Decagon Devices, Inc.; USA) were installed horizontally at 5 cm increments between the depths of 2.5 and 22.5 cm (Figure 1), to monitor the subsurface temperature distributions. An additional two ECT sensors were placed at a height of 8.5 cm above the soil surface for measuring the temperature of the air flowing above the soil surface. All of these sensors operated at a 10 minute sampling frequency. These sensors contain thermistors that measure temperature-sensitive resistance in response to an excitation voltage. The measured resistance is then converted to a temperature value with a ± 0.5 °C accuracy within the temperature range of 5 and 40°C and ±1 °C between 40 and 40°C using the Steinhart-Hart equation [*Steinhart and Hart*, 1968]:

$$\frac{1}{T} = A + B\ln(R) + C[\ln(R)]^3$$

where *A*, *B*, and C are Steinhart-Hart parameters determined for each device specifically, *R* (Ω) is the thermistor resistance, and *T* (K) is the temperature. The same five channel Em50 data loggers (Decagon Devices, Inc.; USA) used to collect EC-5 data were also used to record the temperature data.

A dual needle thermal property SH-1 sensor (Decagon Devices, Inc.; USA) was used to measure the time-dependent changes in soil thermal properties at a depth of 2.5

(Figure 1) cm due to soil drying. This sensor applies a current through a resistive heating element in one 3 cm long needle while simultaneously measuring the temperature response in a second needle 6 mm away. The SH-1 was interfaced with a KD2 Pro thermal property analyzer (Decagon Devices, Inc.; USA) which stored raw data and performed the calculations based on instantaneous heat release from an infinite line source [*Carslaw and Jaqeger,* 1959; *Kluitenberg et al.*, 1993] to calculate the thermal properties during each 30 minute heating and cooling cycle. The SH-1 and KD2 Pro specifically measured temperature (± 0.001 ^{o}C accuracy), thermal conductivity (± 10% accuracy between thermal conductivities of 0.2 and 2 W m^{-1} K^{-1}), volumetric heat capacity (± 10% accuracy for conductivities greater than 0.1 W m^{-1} K^{-1}), and thermal diffusivity (± 10% accuracy for conductivities greater than 0.1 W m^{-1} K^{-1}).

Five EHT sensors (Decagon Devices, Inc.; USA)) were used to simultaneously measure relative humidity (RH) and temperature measurements directly at the soil surface and in the atmosphere every 10 minutes (Figure 1); data was stored on Em50 data loggers (Decagon Devices, Inc.; USA). Relative humidity was measured by the EHT with a film capacitor ceramic substrate coated in a dielectric sensitive polymer that absorbs or releases water proportional to the moisture present in the air. The sorption/desorption of water changes the dielectric constant of the ceramic which in turn is correlated to a relative humidity value [*Chen and Lu*, 2005]. According to manufacturer specifications, the accuracy of the relative humidity measurements for this sensor is ± 3% between 5 and 100% RH. Identical thermistors to those employed in the ECT temperature sensors discussed above allow temperature measurements. The three EHT sensors used to measure the surface relative humidity and temperature conditions (Figure 1) were placed in firm contact with the soil grains so as to better reflect the conditions immediately at the soil-atmosphere interface. The two remaining sensors were installed immediately upstream and downstream of the soil tank.

Surface temperature was also measured remotely using a Model 7320 infrared camera (Infrared Cameras, Inc. (ICI); USA) mounted above the soil tank. The camera measures the thermal infrared radiation emitted by surfaces in the spectral range of 7-14 μm with a thermal sensitivity of 38 mK and accuracy of ±1 ^{o}C. Emissivity, reflection, and transmission corrections were applied to the radiometric temperatures automatically by the IR Flash software (ICI; USA) used to communicate with the camera. Each pixel (320x240 resolution) of the image captured by the infrared camera corresponds to a single

temperature measurement. Therefore, the soil surface was divided into eight distinct zones (Figure 1); two in each tight packing region, and four total in the loose packing region. This allowed average temperatures to be determined for use in a surface energy balance (SEB) model to determine hourly evaporation rates; refer to Section 4.1.6 for an in depth discussion.

In addition to infrared camera, evaporation was also determined by placing the soil tank on a 65 kg $\pm$1 g Model 11209-95 strain-gauge type weighting scale (Sartorius Corp.; USA). Automatic weight measurements (i.e. water loss) were made every 10 minutes and directly written to file through a LabVIEW software interface (National Instruments Corp.; USA). The location of the drying front was visually tracked with the use of a PowerShot Se IS digital camera (Canon; USA). Digital images were taken on an hourly basis and saved directly on a dedicated computer using CameraWindow software (Canon; USA).

4.3.4 Experimental summary

A total of four experiments were conducted under varying boundary conditions (e.g. air temperature, relative humidity, wind velocity) and initial conditions (i.e., saturation) as summarized in Tables 3 and 4. The first experiment (EX-1) was run under ambient conditions; the average temperature and relative humidity in the headspace above the soil surface was 22 ^{o}C and 0.19 respectively. The incoming air was continuously heated, using the temperature control system described in Section 3.1, in the second experiment (EX-2); the average headspace temperature and relative humidity was 57.5 ^{o}C and 0.10 respectively. Temperature was maintained with a range of approximately ± 5.63 ^{o}C of the mean value. The third experiment (EX-3) simulated diurnal conditions by cycling the heating control system between two set temperatures (24 and 50 °C) at 12 hour time increments. These first three experiments were initially fully saturated throughout the entire soil tank; evaporation was then allowed to occur freely throughout the duration of each experiment. In the fourth experiment (EX-4) however, a constant water table was maintained at a depth of 20.6 cm using a constant head device. The headspace temperature was maintained at approximately constant value of 66.1 ^{o}C and relative humidity of 0.01. Each experiment was run for 20 days. EX-4, the lowered water table experiment, followed the above procedures except that upon completion of the packing process, a constant head

device attached to the tank was lowered to a depth of 20.6 cm. This allowed free drainage from the tank, establishing the final constant water table conditions.

Table 3. Average characteristics and conditions of Experiments 1-4

Experiment	Average Headspace Temperature (°C)	Average Headspace Relative Humidity (%)	Average Surface Temperature (°C)	Average Wind Velocity ($m\ s^{-1}$)	Initial Water Table Depth (cm)
EX-1	22.9	19	22.3	0.755	0
EX-2	57.5	10	32.5	1.094	0
EX-3*	50.2 / 24.0	2 / 12	29.8 / 22.5	0.986 / 0.710	0
EX-4	66.1	1	28.5	1.0532	20.6

***** Diurnal heating cycle on / off

Table 4. Summary of final soil porosities.

	Porosity		
Experiment	Loose Packing[1]	Tight Packing (Sides)[2]	Tight Packing (Bottom)[3]
EX-1	0.440	0.319	0.319
EX-2	0.417	0.320	0.321
EX-3	0.449	0.318	0.315
EX-4	0.452	0.314	0.317

[1]Denoted by 10% dotted shading in Figure 1
[2]Denoted by horizontal fence pattern shading in Figure 1
[3]Denoted by diagonal fence pattern shading in Figure 1

4.4. Results and Discussion

In this section, we present a demonstration of experimental results (Section 4.1) for EX-1. Results from this experimental run (ambient conditions above the soil surface) are presented including graphs and summary tables of measured relative humidity and temperature, as well as calculated saturation from measured soil water content. Evaporation rates are compared as determined from weight loss and IR data. Data from EX-1 are used as a base case for comparison with the remaining experimental runs. Observed trends as well as differences between experiments are noted. Then, the experimental results are compared with those obtained from numerical simulations.

4.4.1 Experimental results demonstration and discussion

The primary focus of the study was to improve our current understanding of the characteristics associated with and the effects of soil disturbances on evaporation behavior

at both soil-soil and soil-atmospheric interfaces. The following in depth discussion of the experimental results of EX-1 provides an overview of the datasets generated for this study in terms of: cumulative evaporation, evaporation rate, soil moisture, subsurface temperature, relative humidity, and surface temperature. This section also provides a baseline for the discussion that will follow in Section 4.2 on the complex processes occurring within the soil (loose and tight packed regions) and atmosphere and at their interfaces (subsurface packing conditions and soil-atmosphere).

4.4.1.1. Evaporation based on weight data

Total cumulative evaporation (Figure 2a) and total evaporation rate (Figure 2b) were determined from the continuous weight measurements made using the weighting scale described earlier in Section 3.1. Weight measurements did not allow cumulative evaporation and evaporation rate from each of the differently packed regions to be determined; for this, a SEB model was employed as will be discussed later in Section 4.2. Stage I evaporation lasted approximately 5.5 days and can be identified by the constant slope of the cumulative evaporation curve (Figure 2a). The evaporation rate curve in Figure 2b similarly shows the high and relatively constant rate associated with Stage I evaporation. The high evaporation rates are sustained by flow driven by high atmospheric demand [*Yiotis et al.*, 2003; *Lehmann and Or*, 2009]. The observed decrease in evaporation rate between Day 4 and 5.5 (Figure 2b) was the result of fluctuations in weight measurements (Figure 2a). These oscillations in evaporation rate become more pronounced at later times as the frequency and amplitude of the weight measurement oscillations grew (Figure 2b). These weight fluctuations may be due to changes in atmospheric pressure within the laboratory where the experiments were performed.

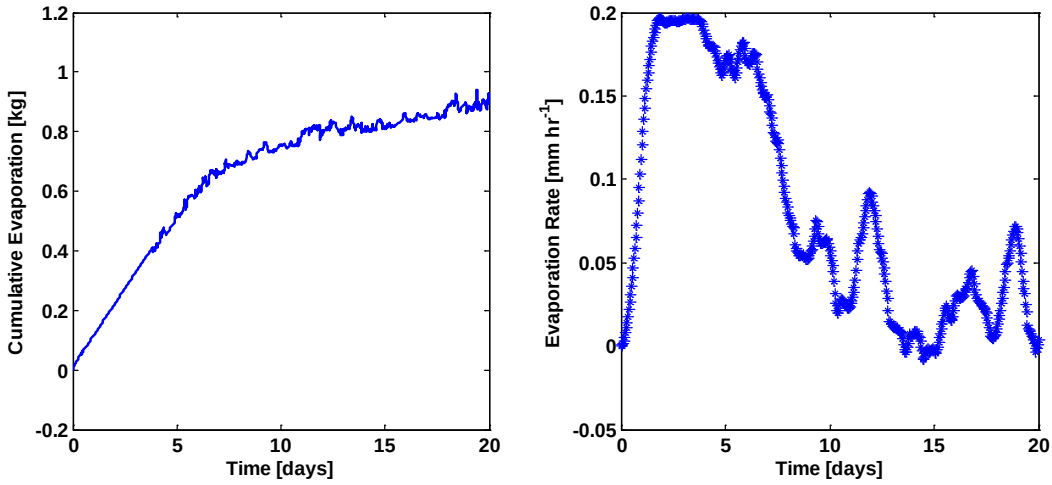

Figure 2. Cumulative water loss from sand tank with continuously heated airspace above soil surface.

Stage IIa evaporation occurred between day 5.4 and 10.9. During this period, often referred to the falling-rate stage, the evaporation rate quickly decreases as the drying front retreats beneath the soil surface, severing the hydraulic connection. This causes evaporation to become vapor diffusion limited [*van Brakel*, 1980; *Yiotis et al.*, 2004; *Lehmann et al.*, 2008]. Stage IIa is best seen in the evaporation rate curve (Figure 2b) by the rapid decrease in evaporation rate from approximately 0.175 mm hr^{-1} to about 0.025 mm hr^{-1}. Stage IIa evaporation can also be identified in the cumulative evaporation curve as the portion where the water loss as a function of time is no longer linear. From approximately Day 10.9 until the termination of EX-1, the average evaporation rate was approximately 0.0175 mm hr^{-1} (Figure 2b). This low, relatively constant rate is characteristic of vapor diffusion limited Stage IIb evaporation. The cumulative evaporation curve at this point again becomes linear (Figure 2a) if one ignores the fluctuations due to scale variability. 4.1.2. Drying front visualization

The drying front marks the plane (when idealized) or interface that separates the fully saturated and partially saturated regions. The drying front can be used as a rough way of determining what stage of evaporation may be occurring [*Lehmann et al.*, 2008; *Shokri et al.*, 2010] Figure 3 enables visualization of the drying front propagation over the 20-day experiment as observed from the digital photographs taken of the soil tank on an hourly basis. The rate at which the drying front retreats throughout the tank is dependent on the

soil packing conditions (i.e. loose or tight packing). In EX-1, the water table was initially located at the soil surface; therefore the drying front was initially at the soil surface. The depth of the drying front increased rapidly in the loose packed region through day 10 with very little change after. The drying front depth in the tight packed region on the other hand showed a relatively constant retreat throughout the 20 day duration of the experiment.

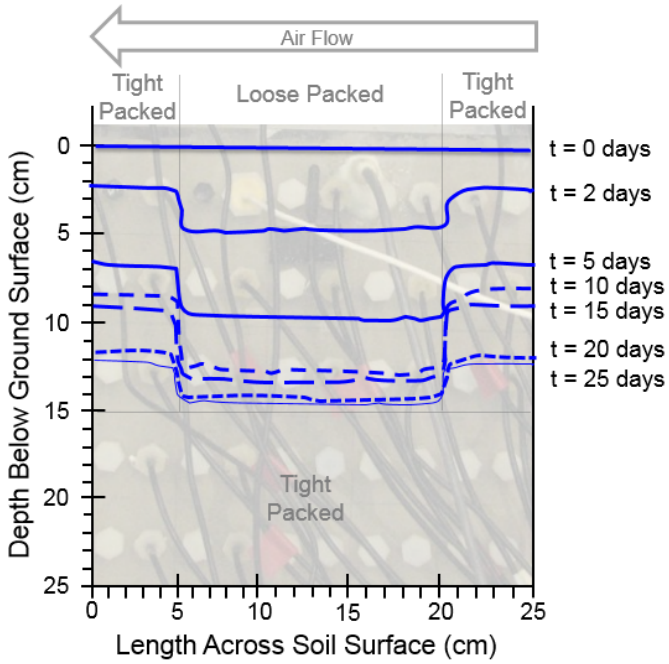

Figure 3. Evaporative front propagation within a heterogeneously packed sand tank under ambient conditions.

The change in the rate of drying front propagation can be used to roughly determine the change in the evaporative stage. The front propagation (Figure 3) correlates with the cumulative evaporation and evaporation rate curves seen in Figure 2. The decrease in weight during stage 1 evaporation for the first 5.5 days (Figure 2) corresponds to the rapid water loss, especially from the center loose packed region, which can be visualized in terms of the drying fronts in Figure 3. The slower rate of the drying front's propagation in the loosely packed sand region after day 5.5 is the result of both vapor diffusion limited stage IIa and IIb evaporation and the lateral movement of liquid water from the loosely packed region to the tightly packed regions via capillary pressure gradients, Section 1 (Figure #). This lateral movement of liquid water from the loosely packed region to the tightly packed regions helps explain why the rate of retreat of the drying fronts in the tightly packed regions appear to be constant.

4.4.1.3. Theory of evaporation analysis based surface energy balance (SEB)

As discussed earlier, total cumulative evaporation and total evaporation rate were determined using a mass balance approach, i.e. weight measurements. This is a very accurate method for determining total losses but reveals nothing about the respective evaporation from each of the three soil regions. Therefore, a SEB was applied to model evaporation rate, and cumulative evaporation, from each region. Temperature data collected remotely by the infrared camera (Section 3.3) was used in a SEB based on one derived in *Shahraeeni and Or* [2010]. Whereas the SEB of *Shahraeeni and Or* [2010] was determined for cylindrical coordinates, the SEB used in the present study was re-derived in Cartesian coordinates to match the present experimental set-up (Section 3.1, Figure 1b). A further modification of the *Shahraeeni and Or* [2010] model was the incorporation of the temperature dependency of fluid properties (Table 5) and the change in effective thermal conductivity with soil moisture.

The surface energy balance model modified from *Shahraeeni and Or* [2010] for the present study is based on the classical formulation [*Penman*, 1948]:

$$LE + G = R_n - H \tag{1}$$

in which LE is the latent heat flux, G is the soil heat flux, R_n is the net radiation flux, and H is the sensible heat flux. Equation (1) can be rewritten in infinitesimal element form taking into account heat losses/gains due to evaporation and condensation (LE), conduction and time-dependent heat storage (G), long wave radiation (R_n), and forced convection (H) [*Shahraeeni and Or*, 2010]:

$$\frac{\rho_w L_w \dot{e}}{\Delta h} + \left(\lambda_{eff} \nabla^2 T_s + \rho_w C_p \frac{DT_s}{Dt} \right) = \frac{\sigma \varepsilon (T_\infty^4 - T_s^4)}{\Delta h} + \frac{h_a (T_\infty - T_s)}{\Delta h} \tag{2}$$

where ρ_w (kg m^{-3}) is temperature dependent water density, L_w (J kg^{-1}) is temperature dependent latent heat of vaporization of water, $\dot{e}$ (m s^{-1}) is the evaporation rate, Δh (m) is the thermal decay depth, σ (5.67 × 10^{-8} W m^{-2} K^{-4}) is the Stefan-Boltzmann constant, ε (–) is surface emissivity, T_∞ (K) is the ambient temperature, T_s (K) is the surface skin temperature, h_a (W m^{-2} K^{-1}) is the convective heat transfer coefficient, λ_{eff} (W m^{-1} K^{-1}) is the effective thermal conductivity, C_p (J kg^{-1}) is the soil heat capacity, and t (s) is time. A summary of the functions that relate temperature and the temperature dependent fluid properties above and to come can be found in Table 5.

Shahraeeni and Or [2010] showed that the ratio of radiation and convection coefficients is equal to the radiation-convection tern ratio (i.e. $\sigma\varepsilon T_\infty^3 / h_a$), thereby allowing the radiation term to be dropped out of the equation. Furthermore, the heat storage term can also be neglected if steady-state conditions are assumed. This allows the final form of the surface energy balance to be written for the packing configuration used in the present study as:

$$\dot{e}_{upstream,tight} = \frac{h_a}{\rho_w L_w}\left(T_\infty - \overline{T}_{upstream,tight}\right) - \frac{\lambda_{eff}\Delta h}{\rho_w L_w w}\left(\left.\frac{\partial T_s}{\partial x}\right|_{X\,23}\right) \tag{3a}$$

$$\dot{e}_{middle,loose} = \frac{h_a}{\rho_w L_w}\left(T_\infty - \overline{T}_{middle,loose}\right) - \frac{\lambda_{eff}\Delta h}{\rho_w L_w w}\left(\left.\frac{\partial T_s}{\partial x}\right|_{X\,32} + \left.\frac{\partial T_s}{\partial x}\right|_{X\,67}\right) \tag{3b}$$

$$\dot{e}_{downstream,tight} = \frac{h_a}{\rho_w L_w}\left(T_\infty - \overline{T}_{downstream,tight}\right) - \frac{\lambda_{eff}\Delta h}{\rho_w L_w w}\left(\left.\frac{\partial T_s}{\partial x}\right|_{X\,76}\right) \tag{3c}$$

where w (m) is the width of the tank, $\overline{T}_{Sand}$ (K) corresponds to the average surface temperature of a given packing and the temperature gradient is determined between to infrared zones on either side of a given interface (Figure 1d).

Convection is one of the dominant forms of heat loss from the experimental apparatus described above in Section 3.1.; the constant air flow maintained above the soil surface means that these losses are due primarily to forced convection. The convective heat transfer coefficient h_a was calculated as [*Incropera and DeWitt,* 2001]:

$$\overline{Nu} = \frac{h_a x_{tot}}{\lambda_a} = 0.664\,\mathrm{Re}^{1/2}\,\mathrm{Pr}^{1/3} \tag{4}$$

where $\overline{Nu}$ is the dimensionless Nusselt number, λ_a (W m^{-1} K^{-1}) is temperature dependent thermal conductivity of air, and x_{tot} (m) is the total tank length (i.e. 25 cm), *Re* is the dimensionless Reynolds number, *Pr* is the dimensionless Prandtl number:

$$\mathrm{Pr} = \frac{C_{p_a}\mu_a}{K_a} \tag{5}$$

C_{pa} (J kg^{-1} K^{-1}) is the heat capacity of air and μ_a (Pa s) is the dynamic viscosity of air, both of which are temperature dependent. Equation (4) is applicable for flow over a flat plate and values of $Re \leq 10^5$ and $Pr \geq 0.6$. The use of a flat plate formulation is a simplification of the more complex duct flow of the present study, but is applicable because the *Re* and *Pr* flow conditions are met. A modified Reynolds number was used in the calculation of h_a in Equation (4) to account for the air flow occurring in a small rectangular duct:

$$\mathrm{Re} = \frac{\bar{u}\rho_a D_h \phi^*(w,H)}{\mu_a} \tag{6}$$

In the above equation, $\bar{u}$ (m s^{-1}) is the average free-stream air velocity measured by the pitot static tube, ρ_a (kg m^{-3}) is the air density which varies with temperature and relative humidity, D_h (m) is the hydraulic diameter and $\phi^*(w,H)$ is a shape function to correct for aperture [*Jones*, 1976]:

$$\phi^*(w,H) = \frac{2}{3} + \frac{11H}{24w}\left(2 - \frac{H}{w}\right) \tag{7}$$

where w (m) is the duct/tank width, and H (m) is the duct height.

In the work of *Shahraeeni and Or* [2010], the authors assume a constant thermal conductivity value throughout both Stage I and Stage II evaporation. Soil thermal conductivity can change by an order of magnitude between fully saturated and completely dry conditions. This can change the conductive heat losses/gains from one soil packing throughout time which is why in the present study, thermal conductivity was allowed to vary with soil moisture according to [*Lu and Dong*, 2014]:

$$\lambda_{eff} = \lambda_{sat} - \left(\lambda_{sat} - \lambda_{dry}\right)\left[1 + \left(\frac{\theta_w}{\theta_f}\right)^m\right]^{\left(1/m\right)-1} \tag{8}$$

where λ_{sat} (W m^{-1} K^{-1}) and λ_{dry} (W m^{-1} K^{-1}) are saturated and dry thermal conductivities of the soil respectively, θ_ω (m^3 m^{-3}) is the volumetric water content measured by an EC-5 soil moisture sensor at a depth of 2.5 cm, θ_f (m^3 m^{-3}) is the point marking the onset of funicular soil moisture, and m (–) is the pore fluid network connectivity parameter. The radius of influence of the EC-5 sensor is 2.5 cm, meaning that measurements are representative of the soil moisture conditions close to the soil-atmosphere interface. Subsequent sensitivity analysis of the surface energy balance model showed that conductive heat losses/gains were negligible compared to those from convection.

The thermal conductivity values are used to calculate the thermal decay depth (Δh), also known as the penetrating depth of radiation. Δh is defined as the depth at which the temperature reaches an ambient subsurface value, typically on the order of 2 to 3 cm [*Gardner and Hanks*, 1966]. To calculate this parameter, Fourier's law can be simply applied:

$$q_{evap} = \dot{e}_{Exp}\rho_w L_w = \lambda_{eff}\frac{T_\infty - T_{amb,sub}}{\Delta h} \quad (9)$$

where $\dot{e}_{Exp}$ (m s^{-1}) is the experimental evaporation rate (determined from weight measurements), and $T_{amb,sub}$ (K) is the ambient subsurface temperature.

Table 5. Other fluid properties applied in surface energy balance (SEB)

Variable	Equation	Reference
Density of Water	$\rho_w = 658.2 + 2.509T_s - 4.6x10^{-3}T_s^2$	*Campbell* [1985]
Latent Heat of Vaporization	$L_w = \frac{2.495x10^9 - 2.247x10^6(T_s - 273.15)}{\rho_w}$	*Forsyth* [1964]
Density of Air	$\rho_a = \frac{pM_a}{RT_\infty} - 0.611\left(\frac{M_a}{M_w} - 1\right)\exp\left(17.27\frac{T_\infty - 273.15}{T_\infty - 36}\right)\frac{M_w(RH)}{RT_\infty}$	*Lu and Likos* [2004]
Dynamic Viscosity of Water	$\mu_a = 1.458x10^{-6}\left(\frac{T_\infty^{1.5}}{T_\infty + 110.4}\right)$	*Andreas* [2005]
Thermal Conductivity of Air	$\lambda_a = 0.024 + 7.73x10^{-5}(T_\infty - 273.15) - 2.6x10^{-8}(T_\infty - 273.15)^2$	*Campbell et al.* [1994]
Heat Capacity of Air	$C_{pa} = 1005.6 + 0.017211(T_\infty - 273.15) + 3.92x10^{-4}(T_\infty - 273.15)^2$	*Andreas* [2005]

T_s (K): Surface temperature T_∞ (K): Ambient temperature

***p* (Pa): Air pressure**

***M*$_a$ (kg mol^{-1}): Molecular weight of air**

***M*$_w$ (kg mol^{-1}): Molecular weight of water**

***R* (Pa m^3 K^{-1} mol^{-1}): Ideal gas constant**

RH (–): Experimental relative humidity

4.4.1.4. Evaporation based upon surface and air temperature measurements as inputs for the sensible heat balance

The evaporation rate was determined for each packed region using both the described surface energy balance (Figure 4a). Total cumulative evaporation was determined by summing the water loss from each region (Figure 4a). This in turn was used to determine a total evaporation rate (Figure 4b). Based on the evaporation rate curves for the three packings and the total evaporation rate curve, transition from Stage I into Stage IIa is controlled by the tight packing.

(a)

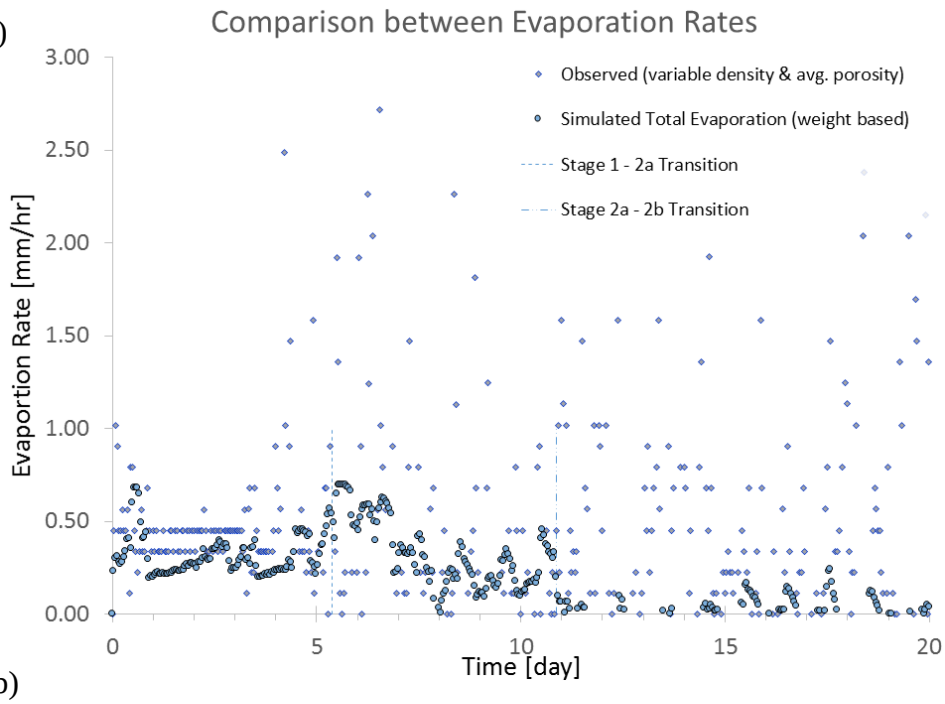

(b)

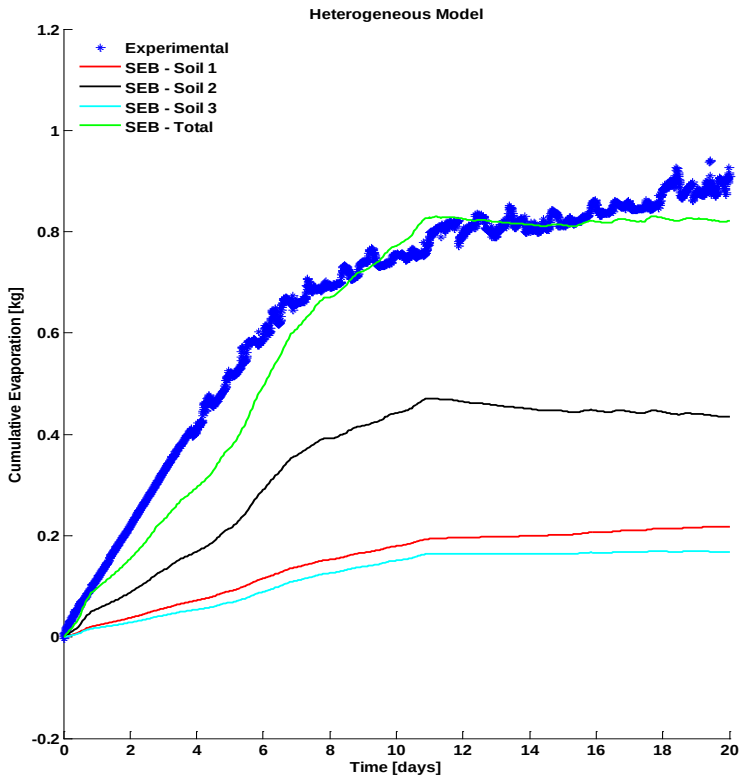

Figure 4. Cumulative water loss (Figure 4a) and evaporation rate (Figure 4b) comparison between observed and simulated values per packed region based upon sensible heat balance under ambient conditions.

Comparison between observed and simulated cumulative evaporation curves show good agreement ($r^2 = 0.987$). Simulation results show that evaporation from the loose sand packing contributes the greatest, followed by the upstream tight packing, to overall cumulative evaporation (Figure 4a). Looking at cumulative evaporation is relative however, a greater cumulative evaporation from the loose packing during Stage I evaporation would be expected given the larger surface area (3:5 ratio). Due to the heterogeneous nature of the packing configuration (tight and loose packed regions), similar height of capillary rise (16.1 cm for tight packed region and 9.6 cm for loose packed region), and difference in size of the regions (the tightly packed region surface area was 136.5 cm^2 while the loose was 91 cm^2), more evaporation was attributed to the loosely packed region. This was also seen numerically which will be discussed in section x. x. y.

One of the primary reasons for the difference in evaporation between the tight and loosely packed regions is due to the difference in capillary pressure of the two regions and subsurface water flow. The porosity of the tight and loose packed regions was 0.319 and 0.440, respectively. The higher porosity of the loosely packed center region corresponds to larger void space between soil grains, enabling more rapid evaporation. The lower porosity in the tight packed regions corresponds to smaller void space between soil grains resulting in higher capillarity (AEV = 16.1 cm) compared to the loose center. Therefore, water is retained longer in the lower porosity regions.

The loose packed center experienced the effect of evaporation of water through the larger pores as well as the transfer of water from the center to the tight packed outer cells due to capillary flow. As explained earlier, Stage I evaporation occurs at the soil-atmospheric interface or from a shallow drying front as long as the liquid water necessary to meet atmospheric demand can be supplied via capillary action [*Shokri et al.,* 2010]. These two factors caused an increased reduction in saturation for the center as would be expected for a homogeneous packing with the same porosity across the entire length of the surface. *Shahraeeni and Or* [2012] and *Assouline et al.* [2010] showed pore size plays an important role in determining evaporation rates; a fine grained soil (i.e. small pore size) will have a higher evaporation rate than that of a coarse grained soil (large pore size). A similar analogy can be extended to a tight and loose packing of the same sand. If one starts with the assumption that all of the soil grains are the same size and are perfectly spherical, the problem can be easily conceptualized. In the best case scenario, a loosely packed soil would resemble a cubic packing configuration (Figure 5a) and a tightly packed soil would

resemble a rhombohedral packing configuration (Figure 5b). This would yield porosities of approximately 0.48 for the cubic packing and 0.26 for the rhombohedral packing. Figure 5 shows that the loose packing has a much larger pore size than the tight packing, just as in the case of a coarse and fine soil. Therefore as *Shahraeeni et al.* [2012] explain, the smaller wetted surface area leads to a reduction in evaporation rate.

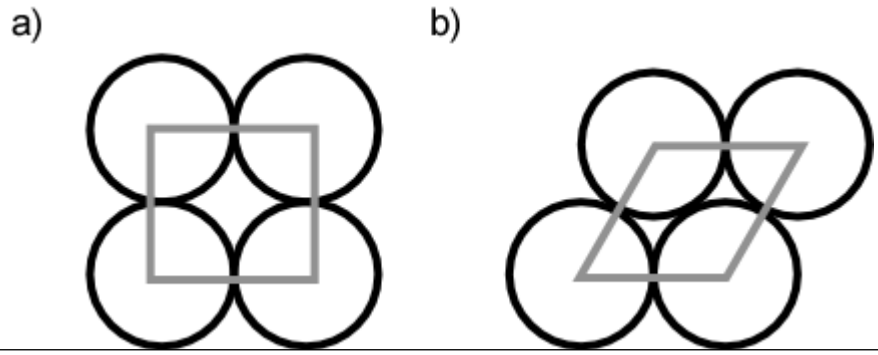

Figure 5. An idealized conceptualization of (a) a loosely packed soil as a cubic packing, and (b) a tightly packed soil as a rhombohedral packing.

The impact of the tight and loose packing resulted in water flow in similar fashion to that described by *Shahraeeni and Or* [2010]. Their research dealt with two different tightly packed sands, a fine and a coarse sand with porosity of 0.35 and 0.33 and AEV of 33.5 cm and 20 cm, respectively. The similar porosities associated with two different sands provide a correlation to the use of the same sand with two different porosities where "fine sand" corresponds to the tightly packed regions and "coarse sand" corresponds to the loosely packed region. There was a more significant difference in AEV by *Shahraeeni and Or* [2010] compared to the experimental data established for this research. Therefore, the use of the same sand under differently packed conditions did not enable a direct correlation between previous research and the current research. The previous research demonstrated that more evaporation occurred in the fine sand (tight packed region) with the coarse sand (loose packed region) contributing less to cumulative evaporation. The opposite is shown in Figure 4.

4.4.1.5. Surface temperature

The surface energy balance model employed in this study uses time-dependent surface temperature measurements made along the length of the soil surface and the headspace temperature (Figure 5). The air and surface temperatures fluctuated in

conjunction with the room temperature due to the laboratory's climate control system. Figure 5 shows that the temperature within the laboratory was very stable, varying by approximately ± 1°C the mean temperature throughout the duration of the experiment. The average surface temperatures for the differently packed regions were similar, straying less than 0.5°C from each other. As shown earlier in Figure 4, these temperature measurements lead to higher evaporation rates in the tight packing than in the loose packing, suggesting that the larger contribution of the loose packing to cumulative evaporation is the result of its larger surface area. The initially cool surface temperature, approximately 2°C lower than the ambient headspace temperature, is the result of evaporative cooling associated with Stage I evaporation when this process occurs from the drying front located at or near the soil surface. As the drying front retreats, the temperature of the soil surface will increase due to the absence of evaporative cooling associated with the phase change close to the surface [*Yiotis*, 2007]. This increase in temperature coincides with the same time identified by the evaporation curves (Figure 2, Figure 4).

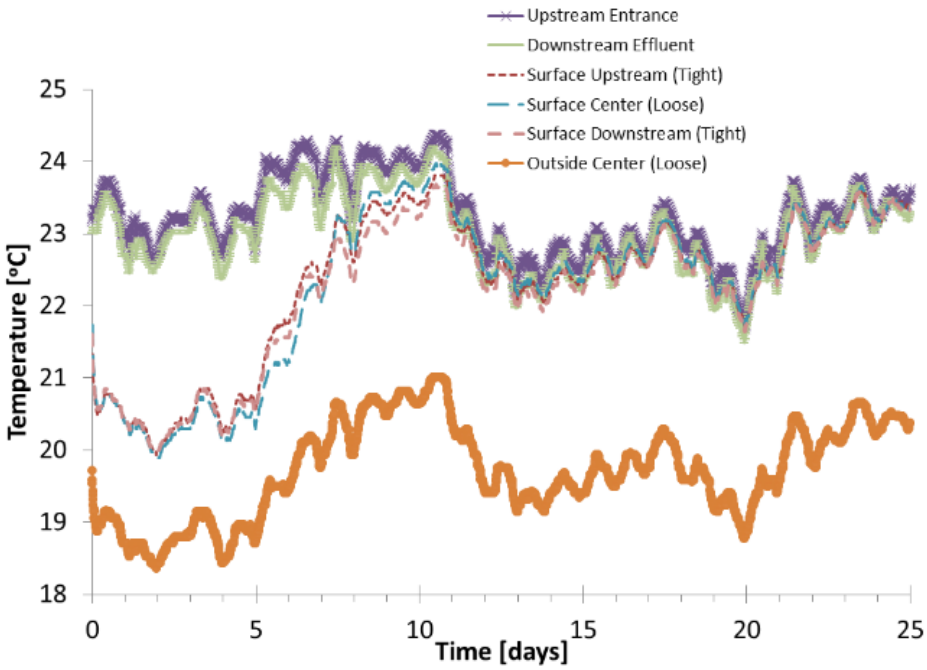

Figure 5. Temperature profiles across the surface length, head space, influent and effluent air upstream and downstream of the soil surface, and outside on the front of the tank.

4.4.1.6. Humidity

The relative humidity data collected from sensors located in the headspace (Figure 1) contributed directly to air density calculations in the SEB model and used as inputs to the numerical heat and mass transfer model. The relative humidity sensors located on the soil surface itself were used to verify the proper coupling of the porous medium and the free flow domains in terms of mass transfer across the interface (i.e. vapor concentration). Figure 6 portrays the humidity of the three soil packings and headspace upstream and downstream of the tank. RH remains similar between the loose and tight regions until day 8 at about 100%. This corresponds to the Stage IIa evaporation. The loose packed center exhibited a steep rate of decrease in RH from day 8 to 10.9 reaching a final, residual RH of about 45% at day 20. The downstream tight packed region exhibited a gradual, relatively constant rate of decrease starting near the transition to Stage IIb evaporation with the upstream tight packed region following approximately four days later. The preferential subsurface water flow from the loose center to the upstream tight packed region is evident due to the RH decreasing in the upstream tight packed region later than the downstream tight packed region. The reason for this preferential flow relates to the direction of flow of

air above the soil surface. The upstream soil was exposed to a larger evaporative demand than the downstream soil in terms of both temperature and RH. This then enhanced the evaporation rate from the upstream soil lowering the demand downstream which is only amplified by the large loose packing. This larger demand upstream is shown in Figure 4.

Figure 6:

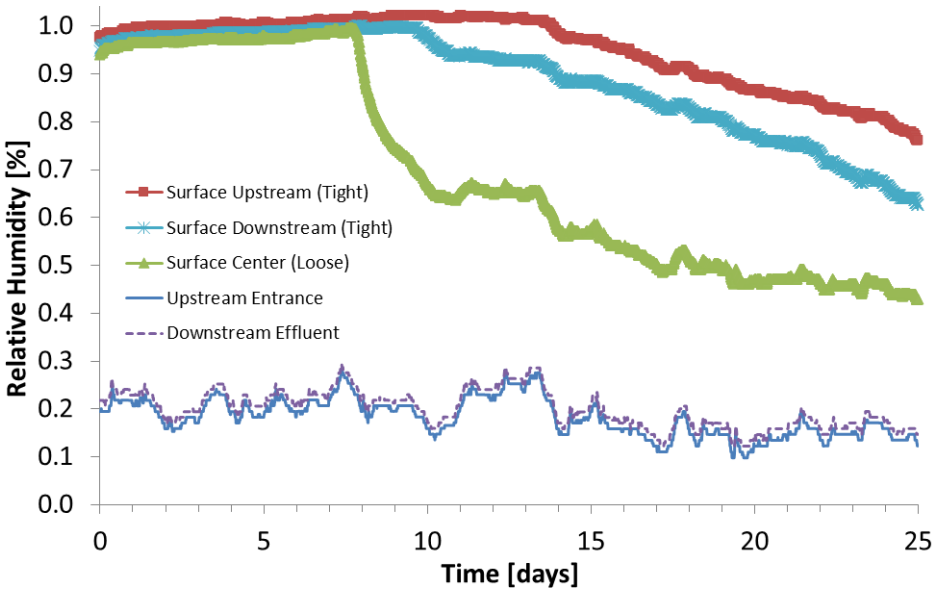

Figure 6. Relative humidity at the surface and in the headspace for EX-1.

4.4.1.7. Saturation

EX-1 started under fully saturated conditions which was then allowed to evaporate freely. As the experiment progressed, saturation decreased from full saturation by varying degrees and rates based on depth and sand packing. Figure 7 portrays saturation as a function of time within each soil packing at the depths of 2.5, 7.5, and 12.5 cm. The loosely packed center experienced a faster desaturation than the tightly packed boundaries in agreement with the other data presented above (Figure 4). Residual saturation was reached in both the tight and loose packed regions by the completion of the experiment at 2.5 cm below the surface. The lowest saturation reached by the soils increases with depth because of incomplete drying by the end of the experiment.

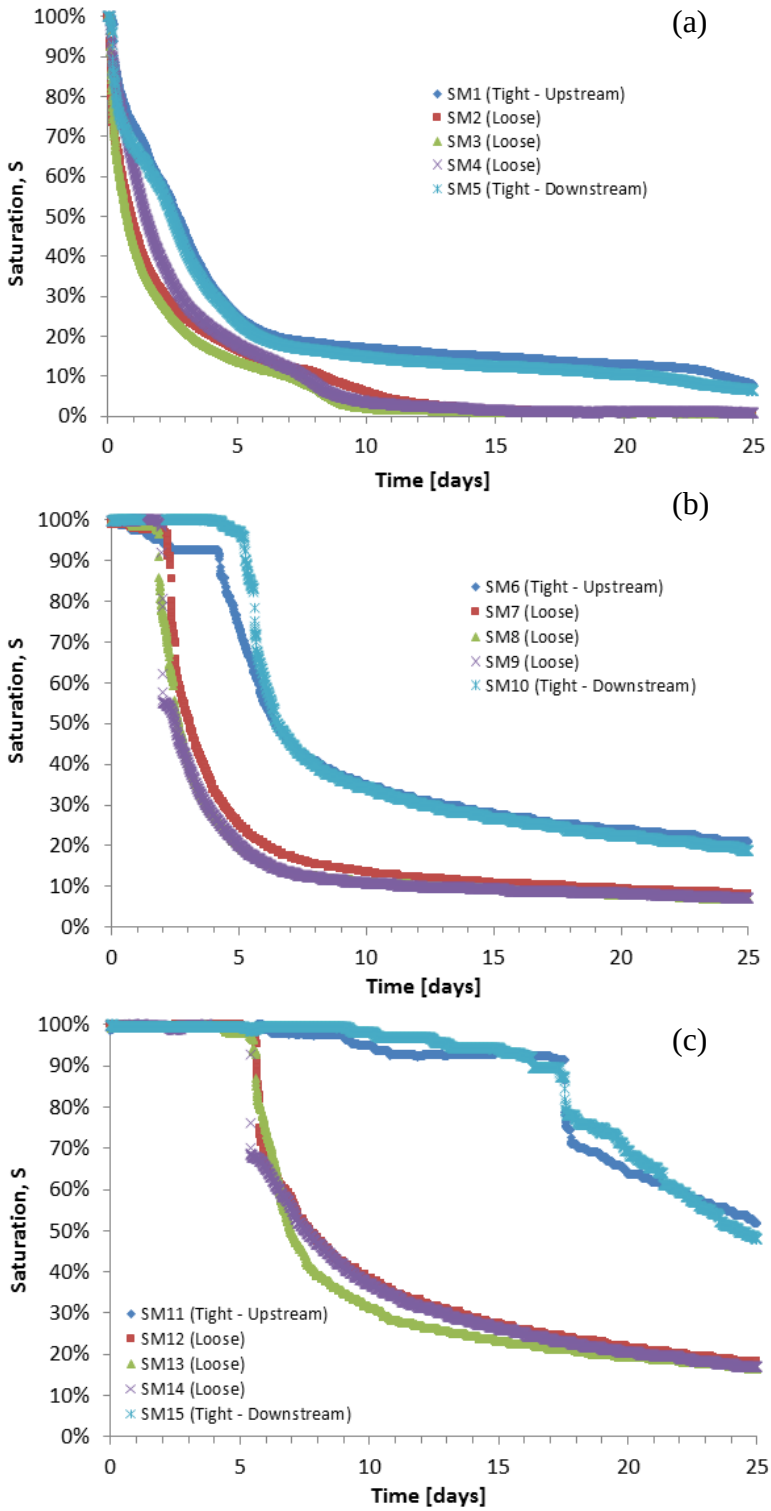

Figure 7. Soil moisture profiles across the length of the soil tank at varying depths within the heterogeneous packed region at (a) 2.5 cm bgs, (b) 7.5 cm bgs, and (c) 12.5 cm bgs.

The relatively constant saturation level maintained at 100% shown clearly in Figure 7b and 7c corresponds to Stage I evaporation at the surface. Evaporation effects

below the surface occurs after the evaporative front passes.. The lack of the constant saturation in Figure 7a denotes that the surface and top 2.5 cm bgs of the soil system experience evaporation and the soil drying at the onset of the experiment. The steep decline in saturation clearly identified throughout the depth of the sand tank corresponds to Stage I evaporation. The continued decrease at the smoother gradient corresponds to Stage IIb evaporation. As the saturation approaches a zero slope, Stage IIb is dominant. The transition between stage 2a and 2b evaporation becomes less clearly defined with an increase in depth. The movement/location of the drying front for the tight packed regions correspond to the same time period for the loose packed region one sensor level further below the surface.

4.4.1.8. Subsurface temperature

Monitoring subsurface temperature enabled further understanding of the interaction throughout the sand tank. Vertical and horizontal time-dependent temperature data were measured across the length and depth of the tank and are shown in Figure 8. The temperature data within the same packed region throughout the depth of heterogeneous packing exhibit specific characteristics associated with each stage of evaporation.

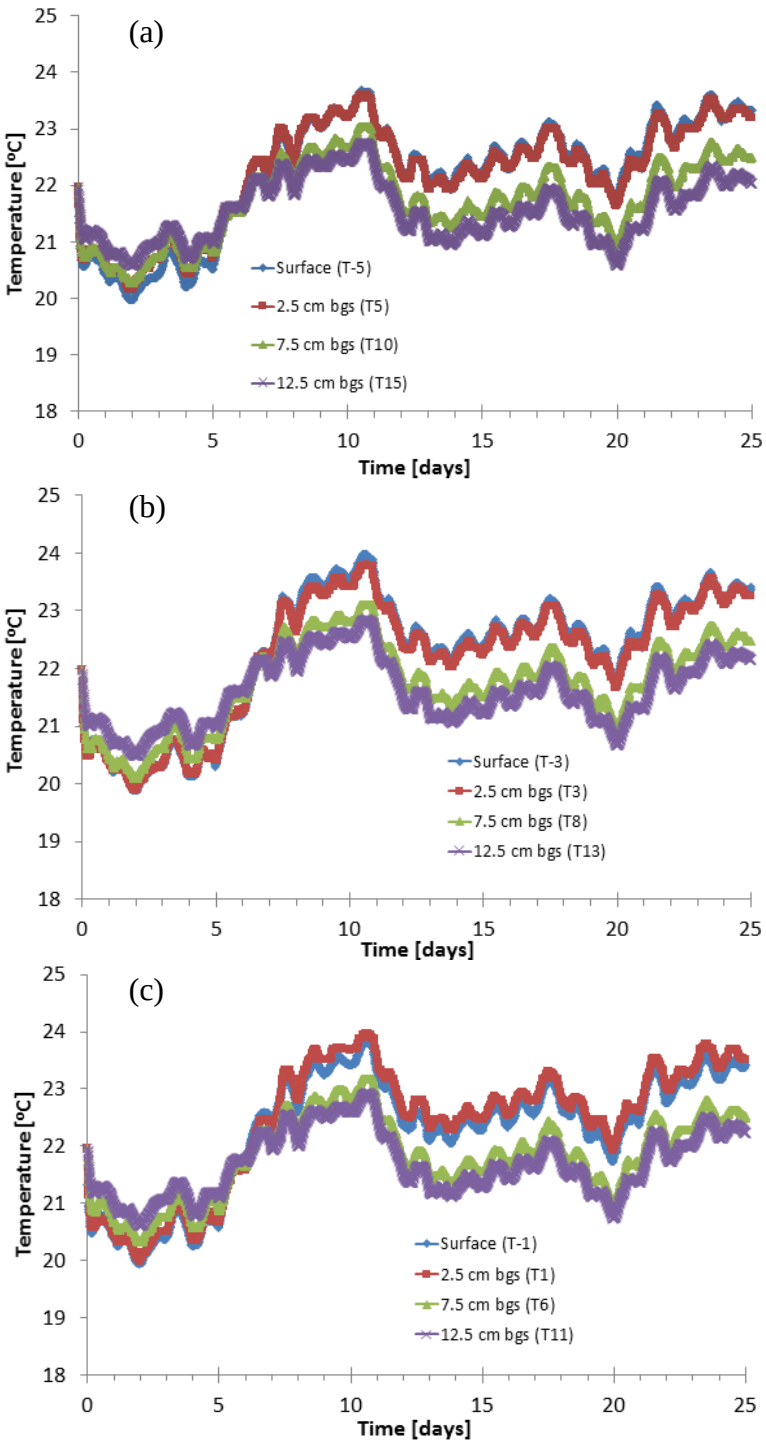

Figure 8. Measured temperature as a function of time for different packing regions within the soil tank for EX-1. Each graph (a-c) is associated with a column of sensors: (a) downstream tight packed region downstream, (b) center loose packed region, and (c) upstream tight packed region.

During the early part of the experiment (0-5 days), temperature throughout the depth and across the length of the tank remain relatively constant (±1°C). The observed

differences in temperature between sensors with depth are well within the accuracy of the sensors. As the soil dried, the temperature increased in response to moist air being a poorer thermal conductor and having a lower heat storage capacity than liquid water [Ref].

Temperatures across the length of the tank at the same depths remained almost identical while during Stage I evaporation. As the drying front retreated quickly in the loosely packed center, there was a corresponding increase in temperature sooner than the one observed in the tightly packed boundaries.

4.4.2. Experimental results comparison with EX-2, EX-3, and EX-4

The following section provides a comparison between EX-1 as the baseline condition and EX-2, EX-3, and EX-4 to highlight the differences due to the variation in boundary conditions. The focus for the discussion remains centered on the disturbed soil boundaries between the tight packed and loose packed regions. As in Section 4.1., the parameters evaluated between the four experiments conducted include evaporation rates, surface and subsurface temperature profiles, relative humidity, water flow and saturation.

4.4.2.1. Evaporation analysis comparison based upon weight analysis

The cumulative water loss based upon the environmental conditions associated with each of the four experiments is compared in Figure 9. The rate of cumulative water loss for the first three experiments transitioned from a higher rate of loss during stage 1 evaporation to a more gradual rate of loss during stage 2b evaporation. EX-1 started with a lower evaporation rate compared to EX-2 and EX-3 and then transitioned to a reduced evaporation rate at a later time due to temperature and humidity effect on evaporation. This is consistent with that shown in *Trautz et al.* [2013].

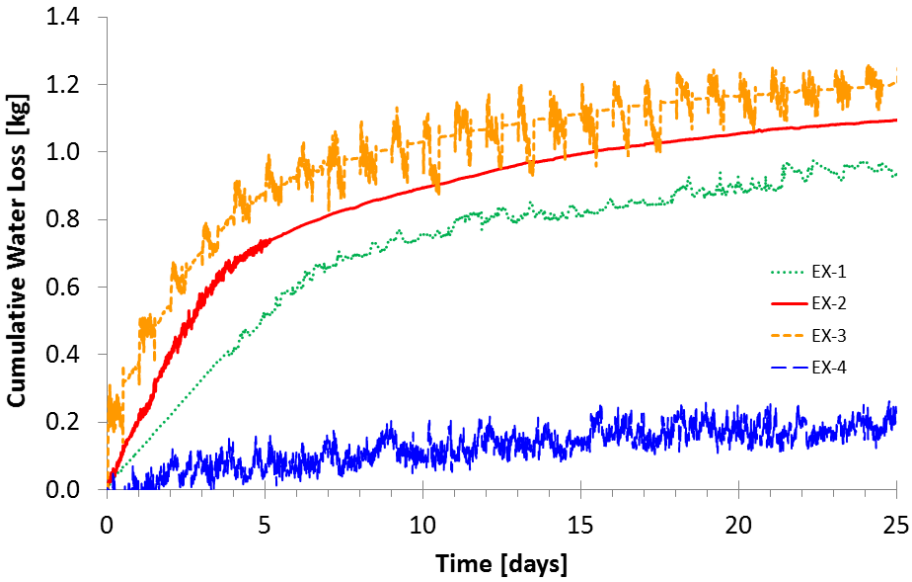

Figure 9. Cumulative water loss comparison between different environmental conditions associated with all four experiments.

EX-2 and EX-3 have similar time periods associated with the transition between stage 1, 2a, and 2b evaporation; however, the fluctuation in water loss is greatest in EX-3. The cumulative water loss evaluated from the change in weight fluctuated by a factor of 10% due to the induced increase in evaporation during the heating cycle and recovery of the system when the heater was turned off. The scale registered a different weight and continued to fluctuate while the heater was on and then stabilized during the off cycle. EX-4 does not display a similar relationship due to the effect of the constant water table. The gradual increase in cumulative water loss denotes that EX-4 began in stage 2a evaporation and transitioned to stage 2b evaporation around day 2 and maintained a constant rate of water loss throughout the experimental duration. EX-4 contained much variability regarding evaporation rate throughout the experiment as a function of the constant water table and heated air.

4.4.2.2. Evaporation front visualization comparison

Visualization of the evaporative front propagation for the other experiments is provided in Figure 10 (a), (b), and (c) for EX-2, EX-3, and EX-4, respectively. All experiments showed a relatively significant decrease in front propagation from day 0 through to the time associated with the transition to stage 2b evaporation depicted in Figure 9 where the rate of cumulative water loss decreases significantly. Front propagation continued to decrease at a much slower rate to the time associated with saturation reaching

residual saturation in the tight packed region at 2.5-cm bgs as shown in Figure 13a below. After that point, the front was essentially constant.

Figure 10:

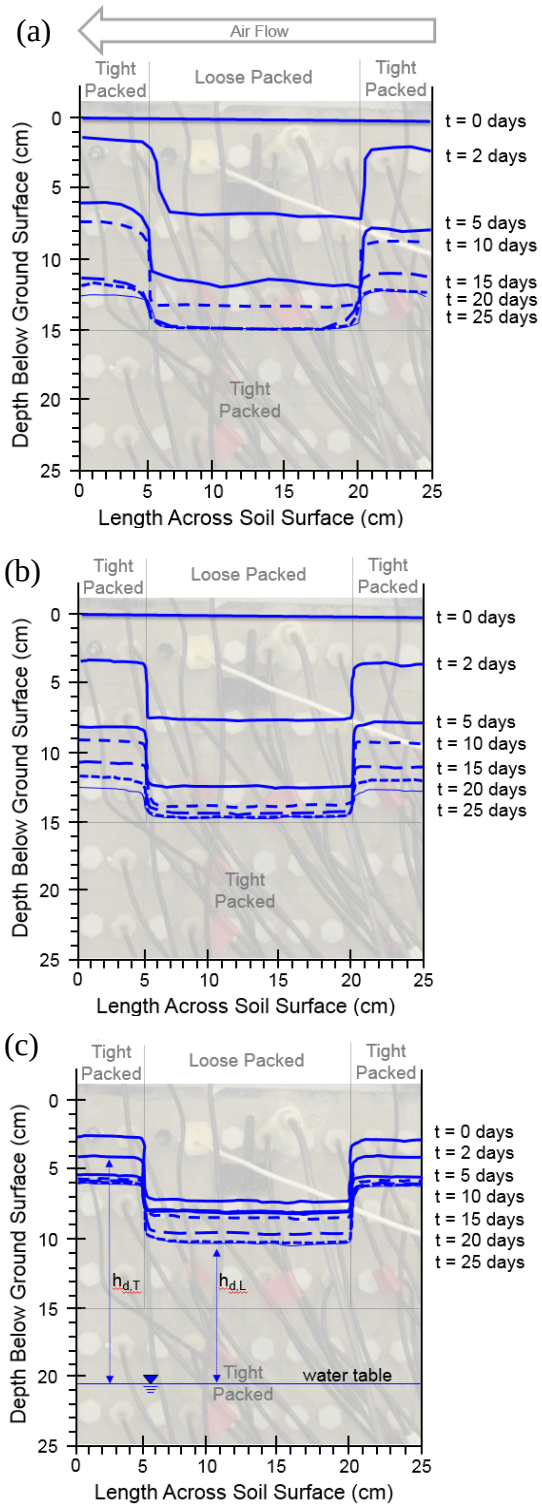

Figure 10. Evaporation front visualization across the length and throughout the depth of the sand tank over the duration of the experiments for EX-2 (a), EX-3 (b), EX-4 (c). The constant water table and air entry head, h_d, for the tight (T) and loose (L) packed regions are shown in (c).

The front propagation under ambient conditions in Figure 3 are slower than those in EX-2. The time to transition to stage two evaporation occurred later due to the lack of continuously heated air above the soil surface. Comparison between Figure 10a and Figure 10b show that the evaporative front is very similar throughout the depth and over time. The one primary exception is that the movement of the front under diurnal conditions was very consistent from day 5 through to the end of the experiment.

For EX-2, after 2 days, the water table level in the loosely packed region was 5-cm lower than that in the tightly packed region. This trend continued throughout the duration of the experiment. After day 15, the water table level in the loosely packed region reached the interface between the tight and loose packing and remained constant. The water table level in the tight packed region decreased marginally between day 15 to day 20, remaining about 2.5-cm above the level of the water table level in the loosely packed region. These relationships were observed for EX-3 as well.

The constant water table maintained in EX-4 resulted in a smaller reduction in evaporation front over the experimental duration as shown in Figure 10c. The decrease from day 0 to day 5 was a result of the method of packing and transition to maintaining the constant water table at 20.6-cm bgs. Due to the system being wet packed, the water table was maintained at 0-cm bgs. Upon beginning the experiment, the constant head device was lowered to maintain a constant water table. As a result, there was water remaining below the surface and above the capillary fringe associated with the air entry head for the various packed regions. This is evident as the water level decreases instead of remaining constant and the resulting cumulative water loss increases slightly over time due to an initial amount of water available for evaporation above that sustained by the constant head. An observation specifically shown in Figure 10c corresponds to the height of capillary rise for both the tight and loose packed regions denoted as $h_{d,T}$ and $h_{d,L}$ respectively. The air entry pressure measured as cm of water noted in Table 2 is in good agreement with the height of capillary rise above the water table in both regions. The variation between the height of rise and the air entry pressure is a function of the difference in porosities associated with the specific experiments. The $h_{d,L}$ was not influenced by the underlying tight packed region regarding the ultimate height of the capillary fringe in the loose packed center. Therefore, the limiting factor regarding the height of capillary rise is the associated air entry pressure of the material in contact with capillary fringe at the boundary layer between fully saturated and unsaturated regions in the vadose zone.

4.4.2.3. Evaporation analysis based upon surface temperature measurements comparison

The sensible heat balance conducted for EX-1 was conducted for each of the other experiments using the same method explained in Section 4.1.3. The change in environmental conditions associated with the other three experiments caused the method used for EX-1 to fail in enabling the simulated total evaporation as cumulative water loss to match the observed cumulative water loss for EX-2, EX-3, and EX-4. The total simulated cumulative water loss was over predicted for each of the experiments. The primary reason for the sensible heat balance failure was due to the continuously elevated air temperature in the head space that heated the surface. This resulted in a larger difference in temperatures between the air and the surface causing over prediction of evaporation rates. Although the method used did not adequately predict the cumulative water loss, a number of poignant observations are possible through comparing the observed and simulated cumulative water loss per region for each of the experiments as shown in Figure 11.

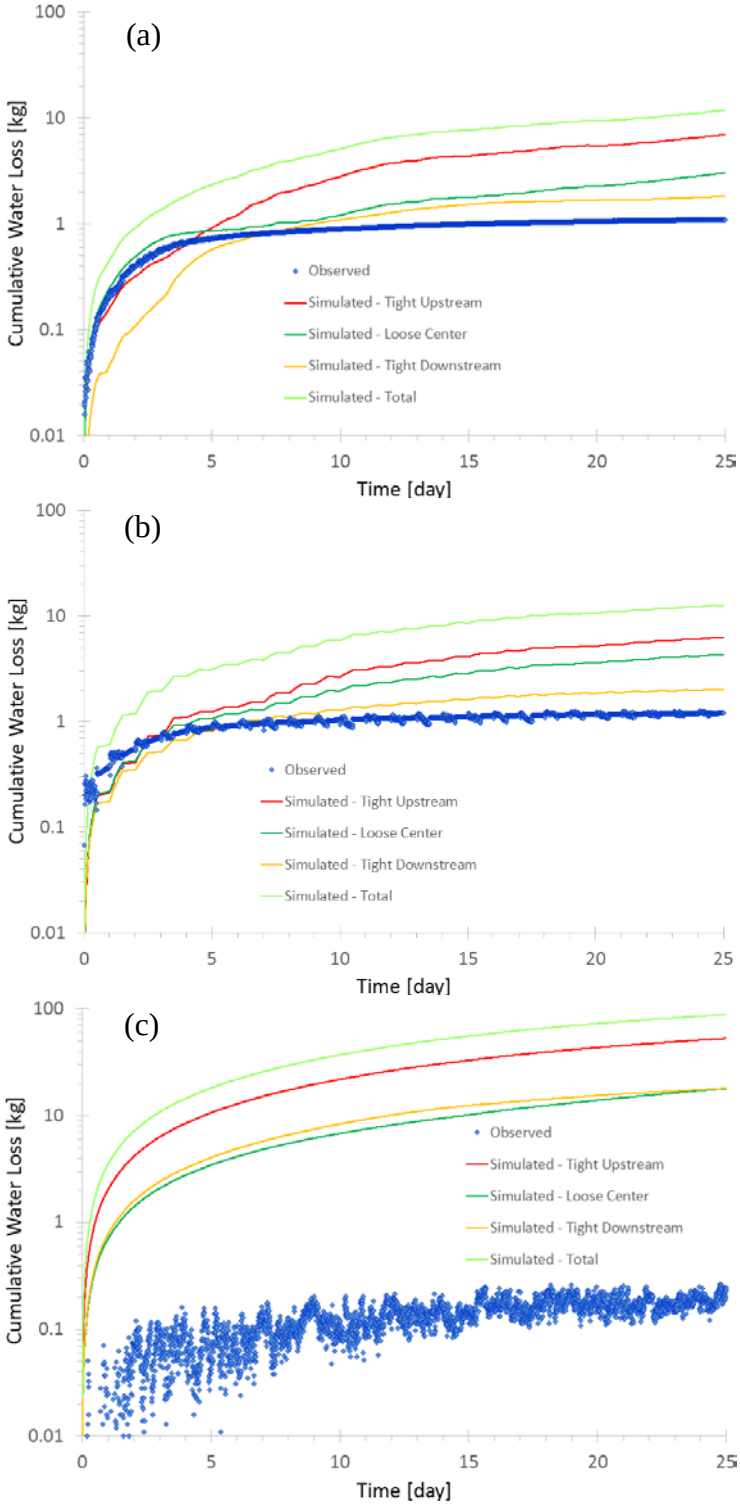

Figure 11. Comparison between observed and simulated evaporation rates across the soil surface for the different packed regions for EX-2, EX-3, and EX-4 shown in (a), (b), and (c), respectively.

The graphs are plotted on a log scale with respect to cumulative water loss to better highlight the behavior of each experiment. The period of sharp increase in observed and

simulated water loss corresponds to stage 1 evaporation. The subsequent gradual increase corresponds to stage 2a followed by stage 2b evaporation. The time period associated with the transition between the stages of evaporation are generally in good agreement with the best fit observed from the loose packed region.

The primary contributor to the total evaporation was the loose packed region during stage 1 evaporation for EX-2. The loose packed region contributes more toward total evaporation compared to the downstream tight packed region for EX-2 and EX-3. This is counter to EX-1 results and the expected relationship discussed by *Shahraeeni and Or* [2010] that would predict the tight packed regions contributing the most to evaporation. In all experiments, the upstream tight packed region contributed the most to evaporation. This was a result of the proximity to the source of the heated air, preferential subsurface water flow from the loose to the upstream tight packed region, and resulting gradient between surface and air temperature measurements. The fluctuation of EX-3 shown in Figure 11b was a result of the diurnal conditions of the experiment. When the heater was on, the evaporation rates increased. When the heater was off, the evaporation rates were close to zero as the system returned to ambient condition.

The conditions associated with EX-4 discussed in the previous section caused a continued cooling of the surface and provided a constant supply of water to the subsurface. Under these environmental conditions, the evaporation rate and resulting cumulative water loss were over predicted by two order of magnitude. However, the expected contribution to total evaporation from the tight packed regions was portrayed with preferential subsurface water flow to the upstream tight packed region.

4.4.2.4. Surface temperature comparison

Temperature profiles across the surface as shown in Figure 5 were created for each experiment. A similar trend in all experiments was observed which highlighted the temperature in the center loose packed region was typically higher than the temperatures associated with the tight packed regions upon entering stage 2a evaporation and continued to experiment completion. The surface temperature measured for the first three experiments mirrored the same relationships displayed in Figure 5. Measured temperatures across the surface remain relatively constant through stage 1 evaporation. During stage 2a evaporation, the surface temperatures increased. Throughout stage 2b evaporation, the surface temperature remained relatively constant. The fluctuations in surface temperature mirrored the fluctuations in temperature as measured outside the tank denoting the

laboratory condition changes due to the climate control system. EX-2 exhibited a temperature from initial average temperatures during stage 1 evaporation around 24 ºC to an average of 28 ºC during stage 2b evaporation. The diurnal conditions of EX-3 caused the surface temperatures to vary less (~ 15 ºC) during heating while in stage 1 evaporation and vary about 20 ºC during heating while in stage 2b evaporation. Due to the constant water table and heated air above the surface in EX-4, the temperature remained relatively constant for the duration of the experiment with fluctuations in temperature resulting from laboratory climate control systems.

4.4.2.5. Humidity comparison

The relative humidity (RH) associated with the tight and loose packed regions are compared in Figure 12. The darker set of lines (solid or dashed) correspond to the tight packed regions and the lighter set of lines relate to the loose packed regions from the four experiments. Each pair of lines per experiment includes the line with a higher RH corresponding to tight packed regions and a lower RH corresponding to the loose packed region. The average of the upstream and downstream tight packed regions was plotted for each experiment to simplify the graph for comparison purposes between the four experiments.

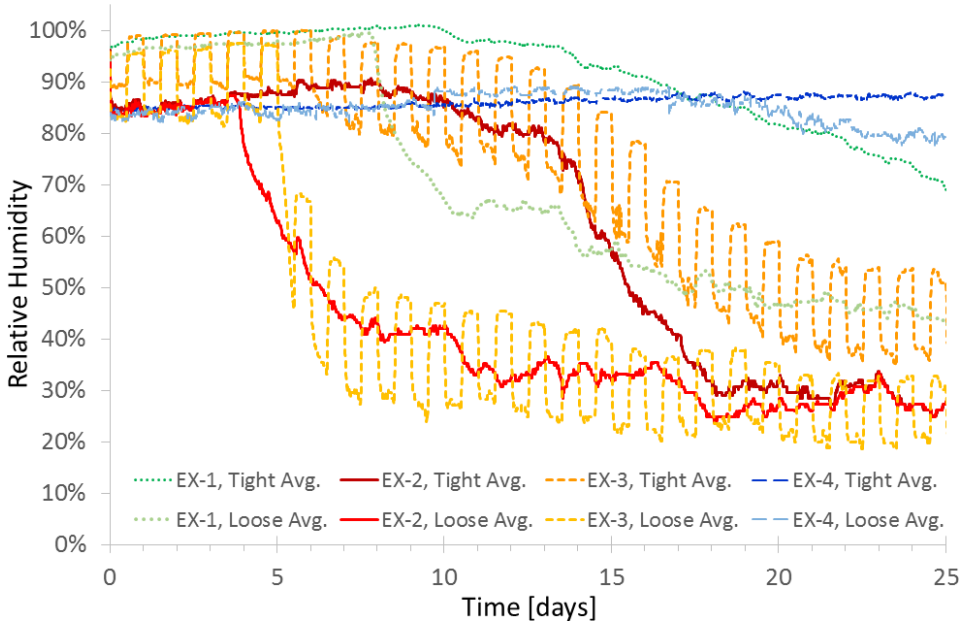

Figure 12. Surface relative humidity profile comparisons between differently packed regions between all four experiments.

Although not graphed, the same relationship as shown in Figure 6 for EX-1 held true for EX-2 and EX-3 with the upstream tight packed region exhibiting a reduction in RH shortly after the downstream tight packed region. This supports the finding that the

subsurface water flowed preferentially from the loose packed region to the upstream tight packed region more than the amount of flow from the loose packed region to the downstream tight packed region. Due to the constant water table in EX-4, the upstream and downstream tight packed region maintained the same RH for the duration of the experiment due to capillary rise and water vapor flow to the surface.

All experiments exhibit similar characteristics with the loose packed region decreasing in humidity prior to the tight packed regions. The specific time for the decrease in tight and loose packing varied between each experiment corresponding to the environmental conditions. At the point where the rate of change in average surface temperature across the differently packed regions matched the rate of change in the downstream air space temperature, the RH in the tight packed regions began to significantly decrease. For EX-1, EX-2 and EX-3, the time associated with the decrease in RH of the loose regions occurred during stage 2a evaporation. The ambient conditions of EX-1 displayed an expected trend of humidity in each region decreasing at a later time period and to a lesser extend as compared to EX-2 due to the absence of the continuously heated air above the surface. EX-3 results fluctuated between EX-1 and EX-2 due to the diurnal conditions corresponding to a fluctuation of about 10% corresponding to the fluctuation in cumulative water loss shown in Figure 11b. The drop in RH for both the tight and the loose packed regions matched EX-2 results more closely than EX-1 as the periods of heated surface air significantly contributed to the rate of evaporation. Under diurnal conditions, the heating and cooling cycles caused a more gradual decline in RH of the tight packed regions compared to EX-2 as captured by the steady decrease in evaporative front shown in Figure 10b. EX-4 maintained a relatively constant RH level as expected due to maintaining a constant water table with the loose packed region exhibiting a very gradual decrease in RH starting around day 19.

4.4.2.6. Saturation and water flow comparison

The saturation levels in the tight packed and loose packed regions at each depth are almost the same as shown in Figure 7. For comparison with the other experiments, the average saturation for each of the regions is provided in Figure 13. The line style used in Figure 12 to identify the tight and loose packed regions for each experiment was followed for Figure 13. The saturation as a function of packed region per experiment is shown for 2.5 cm bgs, 7.5 cm bgs, and 12.5 cm bgs in Figure 13a, 13b, and 13c, respectively. As with relative humidity in Figure 12, each pair of lines per experiment includes the line with a

higher saturation corresponding to tight packed conditions and a lower saturation corresponding to loose packed conditions.

Figure 13:

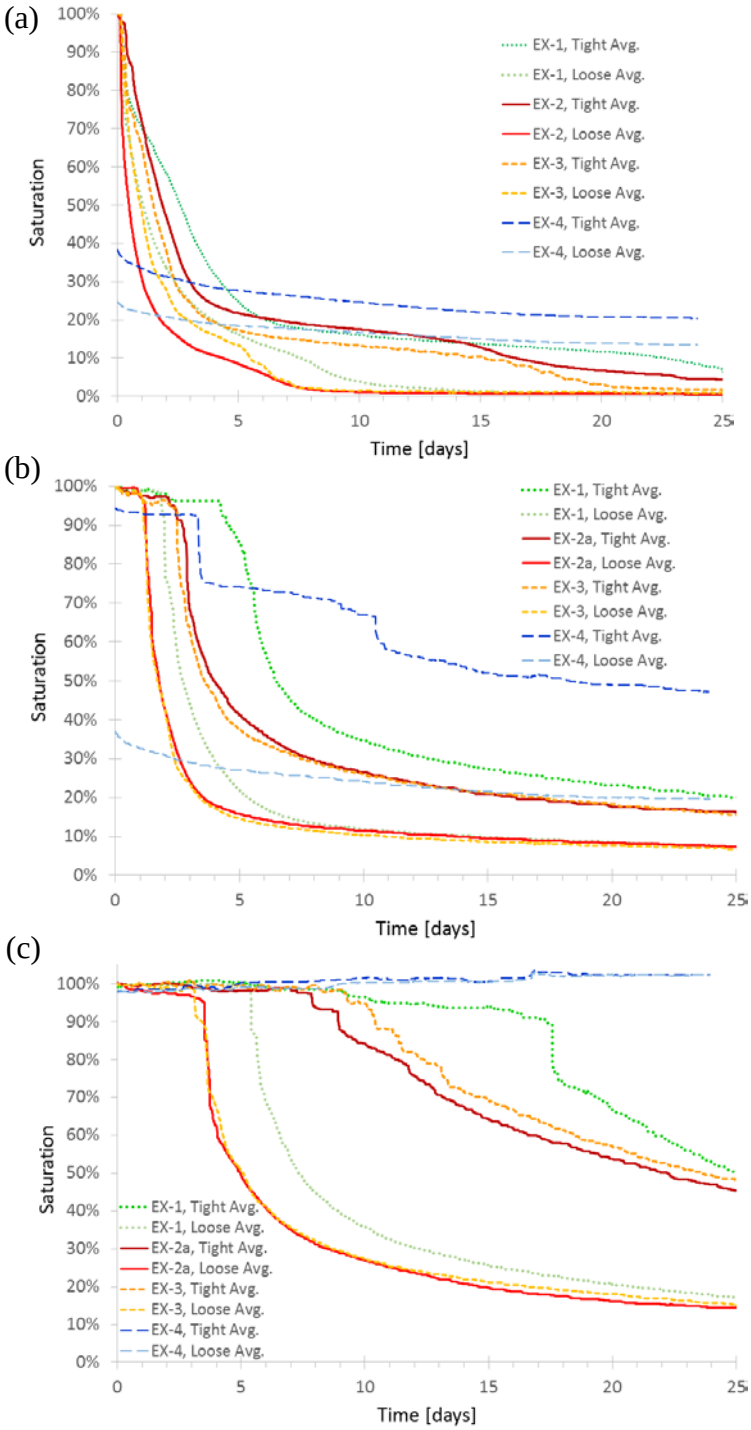

Figure 13. Soil moisture profile comparisons between differently packed regions at varying depths within the heterogeneous packing region at (a) 2.5-cm bgs (b) 7.5-cm bgs (c) 12.5-cm bgs.

Out of the first three experiments, EX-1 exhibited a more gradual decline in saturation with less dramatic transition between stages of evaporation due to the ambient conditions associated with the experiment. EX-3 displayed a reduction in saturation for both tight and packed regions at 2.5-cm bgs in much closer agreement than with other experiments. The diurnal conditions resulting in heating and cooling of the surface caused subsurface fluctuations in water flow to more closely balance flow from loose to tight packed regions and condensation in the subsurface due to change in temperature during cooling. However, these conditions extended only to the first layer of sensors. The saturation conditions between EX-2 and EX-3 were almost identical for both packing regions as shown in Figure 13b and 13c.

Under the constant water table condition, EX-4 started at a lower saturation for the top 7.5-cm bgs. The overall difference between initial and final saturation compared to all other experiments was much smaller for both the tight and loose packed regions. This was a result of maintaining a constant water head at 20.6 cm bgs. The capillary rise based upon air entry pressure was maintained at 4.5 cm bgs in the tight packed region and 11 cm bgs in the loose region. *Lu and Likos* [2004] state that the capillary rise in soil describes the upward movement of water above the water table resulting from the gradient in water potential across the air-water interface at the wetting front. The constant head device was lowered to maintain a constant water table. As a result, there was water remaining below the surface and above the capillary fringe associated with the air entry head for the various packed regions. This is evident as the level of saturation decreased at a quicker rate during the first 5 days of the experiment as compared to after. The tight packed saturation at 2.5-cm bgs matched almost exactly the loose packed saturation at 7.5-cm bgs. This correlation matches the difference in air-entry pressure as well as further supports the concept that water flows from the loose to the tight packed region due to difference in capillarity. The same level of saturation in the differently packed regions at different depths is possible because of the water flow balancing the energy across the heterogeneous boundaries. In Figure 13c, the upward movement of water and the resulting fully saturated conditions regardless of region of packing beyond 11-cm bgs explains why the saturation remained at 100%.

4.4.2.4. Subsurface temperature comparison

Subsurface temperature profiles across the length and throughout the depth of the sand tank were obtained and compared with those presented in Figure 8. Regardless of

type of packed region and depth, the subsurface temperatures remained similar until the saturation as measured at 2.5 cm bgs in the tight packed region, $S_{2.5(T)}$, decreased to the point where the constant rate of steep decrease began to change denoting transition to stage 2a evaporation. As with the surface, the subsurface temperatures at all depths increased at a quick rate (rate of increase decreased with depth) between periods of constant rate of decrease in $S_{2.5(T)}$. The correlations between the first three experiments cannot be made with EX-4 due to the lack of full saturation and RH profiles as a function of the constant water table conditions.

4.4.2.5. Summary of integrated observations applicable to multiple experiments

The comparison between the four experiments in relation to the variety of measurements taken yielded a number of observations that held true regardless of the environmental conditions associated with each experiment and are summarized. Many of these observations resulted from comparing the level of saturation with other parameters discussed above. All experiments showed a relatively significant decrease in front propagation during stage 1 evaporation. Front propagation continued to decrease at a much slower rate to the time associated with saturation reaching residual saturation in the tight packed region at 2.5 cm bgs. After that point, the front was essentially constant. The time period is the same during stage 2a evaporation where the point of inflection for cumulative water loss matches the point of inflection for $S_{2.5(T)}$ in Figure 13a.

Measured temperatures across the surface remain relatively constant during stage 1 evaporation. The temperatures then rise at an increased rate during stage 2a. This transition period is bounded by the relatively constant slope of steep decrease and constant slope of gradual decrease in saturation of the tight packed regions for EX-1, EX-2, and EX-3. The fact that RH and saturation changed minimally during all of EX-4 as shown in Figures 12 and 13a provides additional reason for the relatively constant surface temperatures discussed in Section 4.2.4.

For EX-1, EX-2 and EX-3, the time associated with the decrease in RH of the loose regions occurred during stage 2a evaporation for tight regions based upon soil moisture as shown in Figure 13a. RH in the loose packed region transitioned to a more gradual decrease at the point where saturation in the loose region reached the residual saturation. The RH in both the loose and tight packed regions stabilized at a residual RH once the saturation in the tight regions decreased to residual saturation. This phenomenon is indicative of the subsurface flow from loose to tight regions. Once the tight packed regions

soil moisture levels were significantly reduced, the RH levels decreased. EX-4, which had minimal change in soil moisture as compared to the other experiments, maintained a relatively constant RH level as expected due to maintaining a constant water table.

The principle discrepancy in the research conducted related to evaporation analysis. The discrepancy between the observed and simulated evaporation rates in the latter three experiments may be a function of the method presented by *Shahraeeni and Or* [2010]. The method may not apply as their experiment was conducted under ambient conditions and using a constant thermal conductivity for both soils. In the experiments associated with this work, the thermal conductivity was evaluated continuously and used to calculate the evaporation rate. The largest discrepancy between observed and simulated evaporation rates occurred with EX-4. The existence of a constant water table may negate the use of *Shahraeeni and Or's* method under these conditions as well.

5. Laboratory scale investigation of evaporation and condensation in bare soil for testing models based on non-equilibrium-based phase change approaches under different boundary and initial conditions

ABSTRACT

Evaporation and condensation in bare soils govern water and energy fluxes between the land and atmosphere. Phase change between liquid water and water vapor (i.e. evaporation and condensation) is commonly evaluated in soil hydrology using an assumption of instantaneous phase change (i.e. chemical equilibrium). Nevertheless, finite volatilization and condensation times have been observed experimentally under certain conditions, questioning the validity of this approach. To mathematically describe non-equilibrium phase change, many formulations, derived from irreversible thermodynamics and the kinetic theory of gases, exist. The purpose of this investigation was to perform a comparison of the various formulations using a fully coupled non-isothermal heat and mass transfer model that simulates the processes of evaporation and condensation from soils. Non-equilibrium phase change formulations were compared with experimental data, generated under a series of initial and boundary conditions. The numerical model accounted for three common non-equilibrium phase change formulations applied in the literature in addition to a fourth formulation, a modified Hertz-Knudsen formulation proposed here within. This formulation, based on kinetic theory of gases, simulates simultaneous evaporation and condensation, the results of which were in good agreement with experimental data under all environmental conditions analyzed. This formulation was capable of preserving the magnitude and shape of evaporation curves. Simulation results showed that the two non-equilibrium formulations that applied non-isothermal approaches generally better predict evaporation than isothermal approaches. Analysis of local dimensionless Damkohler numbers showed that the vapor concentrations within the porous media were not at equilibrium under the experimental conditions tested.

5.1. INTRODUCTION

Approximately one-third of the Earth's surface is covered by land [*Kottek et al.*, 2006] of which 15.2% is bare soil. An additional 12.6% of the land surface is devoted to cropland which in some cases can remain fallow up to half the year [*Latham et al.*, 2014]. Bare soil evaporation and its counterpart, condensation, are therefore integral components of the hydrogeologic balance in terms of mass and energy exchanges between the land and atmosphere [*Berge*, 1990]. These phenomena have been extensively studied at various scales in porous media – from pore to global – in a number of different scientific and industry contexts including but not limited to: climate modeling [*Walker and Rowntree*, 1977; *Shukla and Mintz*, 1982], water resources management [*Penman*, 1948; *Fereres et al.*, 2003], vapor intrusion and air-sparging/vapor extraction technologies [*Armstrong et al.*, 1994; *Ho et al.*, 1994], waste storage [*Waugh et al.*, 1994; *Scanlon et al.*, 2005], food preservation and cooking [*Halder et al.*, 2011; *Dhall et al.*, 2012], textile production [*Farnworth*, 1986; *Li and Zhu*, 2003], and cosmetics [*Wissing and Müller*, 2003; *Souto and Müller*, 2008].

Despite decades of study, our understanding and theoretical characterization of evaporation and condensation phenomena in soil remains incomplete. This is in part due to complex transport mechanisms that comprise evaporation and condensation (e.g. phase change, capillary flow, film flow and vapor diffusion) [*Prat*, 2002; *Zhang*, 2010, *Zeng et al.*, 2011] and strongly coupled interactions between the soil surface and atmospheric forcings (e.g. humidity, air temperature, turbulent wind flow, thermal radiation) [*Ishihara et al.*, 1992; *van de Griend and Owe*, 1994, *Prat*, 2002]. In modeling these highly dynamic and strongly coupled systems, simplifying assumptions are often made that reduce complexity of the actual physical and chemical processes occurring in the soil and at the soil-atmosphere interface. However, many of these mechanisms are crudely parameterized and inconsistent with current physical understanding due to the complexity of the problem in field scenarios and the scarcity of field or laboratory data capable of testing and refining energy and mass transfer theories. One common simplification is the assumption of local chemical equilibrium with respect to mass concentration at the representative elementary volume (REV) scale. By definition, phase change between liquid water and water vapor is driven by a difference in chemical potential between phases; a higher liquid water chemical potential will lead to evaporation just as a higher water vapor chemical potential will result

in water condensation [*Tsuruta et al.*, 1999; *Chammari et al.*, 2003]. The difference between the vapor concentration/pressure and equilibrium vapor concentration/pressure is a common REV scale analog for chemical potential. The chemical potential gradient between the two phases or vapor concentration difference determines how far the system is from chemical equilibrium, thereby directly controlling the evaporation or condensation rate (i.e. the greater the chemical potential/vapor concentration difference, the higher the mass flux). The assumption of local chemical equilibrium assumes that the water vapor concentration in the air is always equal to its equilibrium value (i.e. vaporization and condensation occur instantaneously); this is hereinafter referred to as the equilibrium phase change approach. In models based on the equilibrium phase change approach, the vapor and capillary pressures are coupled through the use of Kelvin's equation [*Thomson*, 1870], and the mass balance equations for liquid water and water vapor are combined into a unified governing equation. Chemical equilibrium is implicitly attained by assuming that the water vapor concentration, or partial pressure of the water vapor, is always equal to its equilibrium vapor concentration/pressure (described by Kelvin's equation) [*Halder et al.*, 2011]. Kelvin's equation, used to describe the impacts of a curved liquid/vapor interface on vapor pressure [*Skinner and Sambles*, 1972], has been verified in small capillary tube experiments. In many cases, researchers have found that long times, on the order of a year (e.g. *Bacon*, 1905), are often required to reach equilibrium. It is important to note that the applicability of Kelvin's equation has never been experimentally tested in macroscopic porous media [*Schünder*, 2004].

The equilibrium phase change approach is often implemented in soil hydrology (e.g. *Whitaker*, 1977; *Parlange et al.*, 1998; *Grifoll et al.*, 2005; *Zhang et al.*, 2005; *Bittelli et al.*, 2008; *Sakai et al.*, 2009; *Novak*, 2010) because the characteristic time required for phase change is believed to be several orders of magnitude smaller than the diffusion time [*Halder et al.*, 2011]. *Smits et al.* [2012a] explain that the Damkohler number (Da) can be used to determine whether the assumption of local chemical equilibrium is justified. The Da number relates the characteristic reaction (phase change) time to the characteristic transport time [*Bahr and Rubin*, 1987; *Lichtner*, 1998; *Niessner and Hassanizadeh*, 2009]:

$$Da = \frac{k_{eff} l^2}{D_R \phi} \tag{1}$$

where k_{eff} (s^{-1}) is the effective mass transfer coefficient, l (m) is a characteristic length, D_R ($m^2\ s^{-1}$) is a reference water vapor diffusivity in soil, and ϕ ($m^3\ m^{-3}$) is the porosity of the

soil. Generally, if the Da number >> 1, the phase change dominates and it is justifiable to apply the equilibrium phase change approach. As part of their analysis, *Smits et al.* [2012a] performed a Da number calculation (Equation 1) using values of k_{eff}, D_R, and ϕ obtained in a previous study and a characteristic length equal to the diameter of a soil grain. The authors calculated a maximum Da number equal to 0.04 within a temperature range of 22-70 °C, mathematically demonstrating that the equilibrium phase change approach may not pertinently reflect the actual conditions present in the pore.

Equilibrium phase change is called into question by numerous experimental studies that have observed measureable volatilization and condensation retardation or response times on the same order of magnitude as the characteristic vapor diffusion time due to environmental conditions that drive vapor densities in the pore space away from equilibrium values (e.g. *Bénet and Jouanna*, 1982; *Armstrong et al.*, 1994; *Minkowycz et al.*, 1999; *Ruiz and Bénet*, 2001; *Chammari et al.*, 2003; *Chammari et al.*, 2008; *Lozano et al*., 2008; *Bénet et al.*, 2009; *Lozano et al*., 2009; *Assouline et al.*, 2010; *Ouedraogo et al.*, 2013). Experiments investigating drying kinetics carried out on macroscopic (clay rich) soil samples have shown that the assumption of equilibrium phase change is unrealistic in hygroscopic soils, (i.e adhesion force dominated soil moisture domains) because evaporation must compete with water sorption to the soil grains [*Bénet and Jouanna*, 1982; *Chammari et al.*, 2003; *Lozano et al*., 2008; *Ouegraogo et al.*, 2013].

There are many environmental conditions that have been shown to commonly lead to non-equilibrium conditions. Shallow air flow in the soil near the land-atmosphere interface due to turbulence in the free flow domain or deeper air flow due to vapor extraction technologies can lead to non-equilibrium vapor conditions [*Armstrong et al.*, 1994]. During diurnal cycles, evaporation and condensation rates respond directly, however with slight time delays, to changes in atmospheric parameters. For example, increasing temperatures during the day leads to a corresponding increase in evaporation and decreased condensation which become reversed as temperatures decrease at night [*Assouline et al.*, 2010; *Assouline et al.*, 2013]. Studies such as *Benét et al.* [2009], *Lozano et al.* [2009], and *Ruiz and Bénet* [2009] found that hygroscopic soils (i.e. soils with high clay content) and a variety of fluids (e.g. water, heptane) also influence equilibrium conditions in porous media.

The volatilization time identified in the above examples is accounted for in the liquid water and water vapor mass balance equations by explicitly describing a finite

liquid-gas phase change rate (hereinafter referred to as the non-equilibrium phase change approach). Several empirical or semi-empirical formulations have been derived in the literature to represent non-equilibrium phase change in modeling efforts. Each formulation depends on a variable, referred to as a phenomenological coefficient [*Bénet et al.*, 2009], equilibrium time coefficient [*Le et al.*, 1995; *Scarpa and Milano*, 2002], or constant of proportionality [*Bixler*, 1985; *Zhang and Datta*, 2004]. These coefficients are a function of the interfacial area per volume between the liquid water and gas phases and would ideally be described in terms of simplified menisci geometries [*Shahraeeni and Or*, 2010], non-dimensional expressions [*Geller and Hunt*, 1993], or experimental data (e.g. *Lozano et al*., 2008; *Bénet et al.*, 2009; *Lozano et al.*, 2009), however, many lack physical meaning. Due to the difficulty of incorporating the first two methodologies and a dearth of experimental data, the coefficients are often used as fitting parameters.

The equilibrium and non-equilibrium phase change approaches' ability to accurately capture evaporation and the associated soil moisture redistribution under strictly drying conditions has been compared numerically under non-isothermal and under isothermal conditions in *Smits et al.* [2011, 2012b] and *Ouedraogo et al.* [2013], respectively. These studies showed that both phase change approaches are able to provide accurate predictions during the relatively constant-rate atmospheric driven Stage I evaporation (Figure 1). The evaporation and soil moisture simulation results predicted using the equilibrium phase change approach rapidly deviated from measured experimental data as the drying front quickly retreated below the soil surface during the falling-rate Stage IIa evaporation (Figure 1). During vapor diffusion-limited Stage IIb evaporation (Figure 1) when the soil moisture regime becomes hygroscopic, the equilibrium phase change approach led to significant overestimations of evaporation [*Smits et al.*, 2011]; the assumption of equilibrium phase change leads to an artificial enhancement of the vapor flux. Unrealistically large negative pressure jumps, which in turn cause numerical problems with the soil-water retention and relative permeability functions, were also shown to occur. The non-equilibrium phase change approaches, on the other hand, were able to more accurately capture evaporation rate and soil moisture distributions during stages IIa and IIb. *Ouegraogo et al.* [2013] also point out that the equilibrium phase change approach ignores the existence of other factors competing for soil moisture such as moisture sorption to the soil grains in organic rich or clay rich soils [*Ouegraogo et al*., 2013].

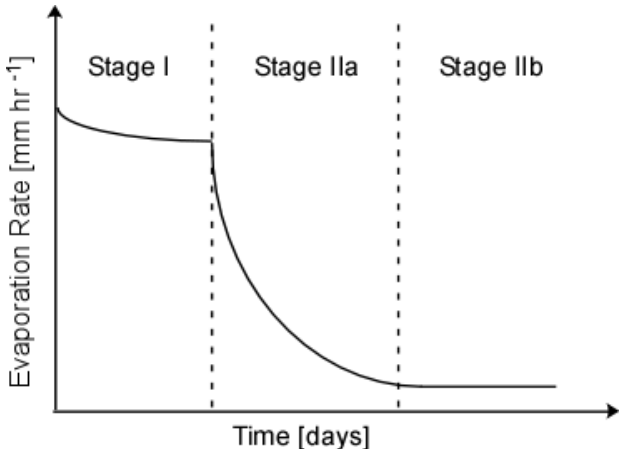

Figure 1. Example evaporation rate curve showing the two stages of evaporation. Capillary flow dominated atmospheric demand influenced Stage I evaporation displays a high approximately constant evaporation rate. Transitory Stage IIa evaporation corresponds to a falling evaporation rate. Diffusion-limited Stage IIb evaporation has a low approximately constant evaporation rate.

The purpose of this paper, is to use laboratory data obtained under different environmental and boundary conditions to test the applicability of existing non-equilibrium phase change formulations as well as present a new approach based on the Hertz-Knudsen equation, incorporated into ,a non-isothermal multiphase numerical model that simulates evaporation and condensation in soil. Numerical results were compared with experimental data to evaluate each formulation's ability to accurately predict evaporation and condensation, soil moisture distributions, temperature profiles, and water vapor concentration under various boundary conditions. Experimental data used in the model testing were generated in a series of four experiments that differed in terms of environmental conditions (e.g. surface temperature, humidity and wind speed) and initial conditions (e.g. depth to water table, temperature).

5.2. THEORY

In this section, we first examine microscopic phase change (Section 2.1) to provide important background needed for macroscopic scale phase change implementation. This is in turn followed by a discussion of the multiphase heat and mass transfer model (Section 2.2) originally developed by *Smits et al.* [2011, 2012a, 2012b] and modified for the present study. This includes a detailed discourse on the governing and supplementary equations, as well as the non-equilibrium phase change formulations being tested as part of the present

study. In Section 2.3 the modeling procedure, including the prescribed initial and boundary conditions are discussed.

5.2.1 Microscopic-continuum scale phase change

Phase change at the microscopic scale has been an area of intense research for over a century; see *Marek and Straub* [2001] and *Eames et al.* [1997] for in depth reviews. In response to the chemical potential gradient between liquid water and water vapor phases, phase change occurs according to several simultaneously occurring mechanisms (i.e. release/absorption, reflection, replacement) at the liquid-gas interfacial boundary as depicted in Figure 2. During evaporation, a liquid water molecule experiences phase change and is vaporized or released from the bulk liquid. The vaporized molecule can remain as water vapor, be reflected back to and reabsorbed by the bulk fluid, or replace another water vapor molecule which in turn condenses to become a liquid water molecule (i.e. condensation) [*Marek and Straub*, 2001]. The mass flux of water molecules evaporating or condensing is often described at the microscopic scale using statistical rate theory, irreversible thermodynamics, or kinetic theory [*Bond*, 2000] within a thin region separating the liquid surface and bulk gas called the Knudsen layer [*Rose*, 1998]. There are several different mathematical approaches used to describe the rate of phase change in terms of kinetic theory (e.g. *Knudsen*, 1915; *Schrage*, 1953; *Labunstov*, 1967; *Ytrehus*, 1997; *Bond and Struchtrup*, 2004). One of the most commonly used continuum scale (averaged from a microscopic scale representation) phase change formulations is the Hertz-Knudsen equation [*Hertz*, 1882; *Knudsen*, 1915] which calculates the rate of phase change or net evaporation rate ($\dot{m}$, kg m^{-2} s^{-1}) at a liquid-gas interface by assuming a Maxwellian velocity distribution with zero mean velocity in the bulk gas phase yielding:

$$\dot{m} = \sqrt{\frac{M_w}{2\pi R}}\left(\frac{p_l}{\sqrt{T_l}} - \frac{p_v}{\sqrt{T_v}}\right) \tag{2}$$

where M_w (kg mol^{-1}) is the molecular weight of water, R (Pa m^3 K^{-1} mol^{-1}) is the universal gas constant, p (Pa) is pressure, and T (K) is temperature. The subscripts v and l denote the water vapor and liquid water phases, respectively. Equation 2 implicitly assumes that all molecules hitting the liquid surface sorb to the liquid without returning back to the gas phase during condensation, and all molecules vaporizing into the gas phase are never reflected back to the liquid phase during evaporation. This is an oversimplification given

that reflection, absorption, and replacement can all occur (Figure 2) [*Marek and Straub*, 2001].

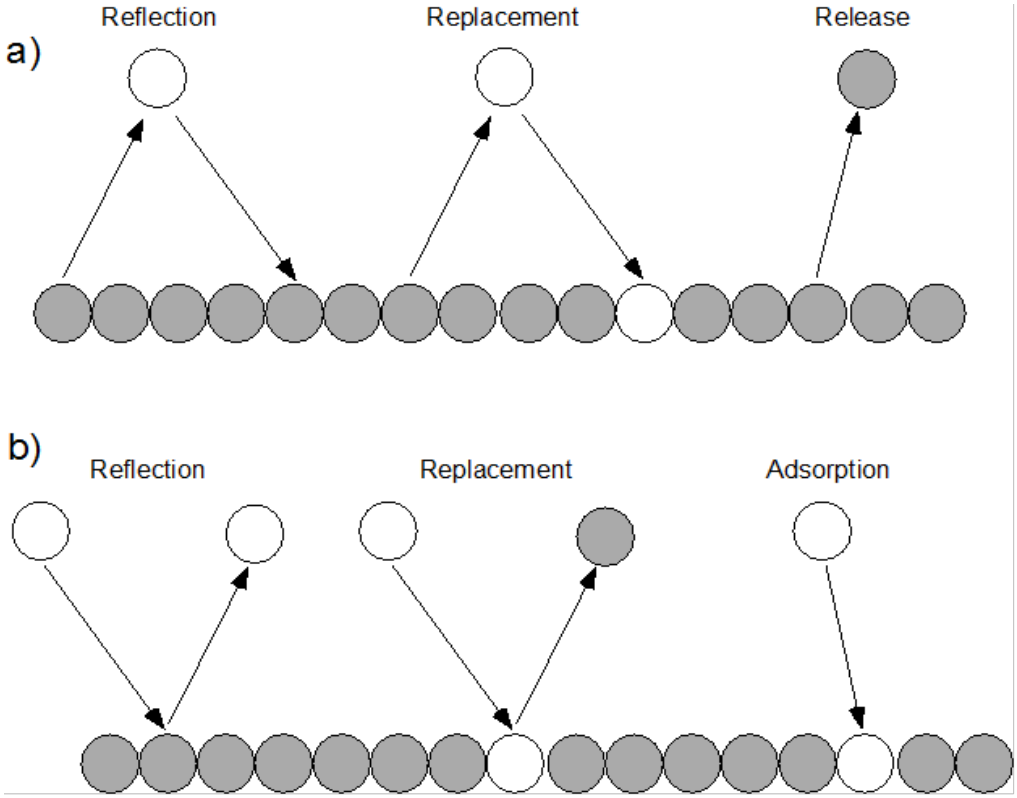

Figure 2. Mechanisms of (a) evaporation and (b) condensation at the microscopic scale. Adapted from Marek and Straub [2001].White circles represent water vapor molecules and grey circles represent liquid water molecules

Early experimental studies showed that measured evaporation rates of some liquids, water included, are substantially less than the maximum values predicted using Equation (2) [*Burrows*, 1957; *Maa*, 1967]. Therefore, terms referred to as evaporation (f_e, –) and condensation (f_c, –) coefficients are commonly applied to Equation (2) to correct for the disagreement between measured and predicted evaporation rates. These coefficients, often treated as a single term (i.e. $f_e = f_c$), allow for relaxing the assumption that all molecules absorb to or volatilize from the liquid-gas interface [*Eames et al.*, 1997; *Tsuruta et al.*, 1999]. *Knudesn* [1915] defined f_e as the ratio of the number of molecules entering the vapor phase to the number of molecules leaving the liquid phase. A ratio of $f_e = 1$ corresponds to all liquid water molecules being transferred to the vapor phase with none being reflected or replaced [*Eames et al.*, 1997; *Marek and Straub*, 2001]. Similarly, f_c is defined as the ratio of molecules sorbed to the liquid phase to the number of molecules hitting the liquid surface [*Prüger*, 1940]. When $f_c = 1$, all incident molecules sorb to the surface [*Rose*, 1998; *Bond*, 2000]. f_e and f_c have been theoretically and experimentally

shown to range between 10^{-4} and 1 within pressure and temperature ranges of 0.1 to 100 kPa and -16.1 to 105°C, respectively; see *Eames et al.* [1997] and *Marek and Straub* [2001] for in depth reviews. Using η_e and η_c defined above and a non-Maxwellian velocity distribution during the derivation process, Equation (2) can be written as [*Schrage*, 1953; *Kucherov and Rikenglaz*, 1960]:

$$\dot{m} = \frac{2}{2-\eta_c}\sqrt{\frac{M_w}{2\pi R}}\left(\eta_e \frac{p_l}{\sqrt{T_l}} - \eta_c \frac{p_v}{\sqrt{T_v}}\right) \tag{3}$$

5.2.2. Macroscopic scale non-equilibrium phase change in porous media

This section briefly discusses the four governing equations used to describe spatial and temporal changes in mass of the liquid, gas (air and water vapor mixture), and water vapor phases, as well as the energy of the overall system. The rate of phase change, $\dot{m}$ (kg m^{-3} s^{-1}) represents mass transfer between the phases in the governing equations that follow.

5.2.2.1. Liquid water phase mass balance

The mass balance for the liquid water phase is written as [*Bear*, 1972]:

$$\frac{\partial(\rho_w \theta_w)}{\partial t} + \nabla \cdot (\rho_w q_w) = -\dot{m} \tag{4}$$

where ρ_w (kg m^{-3}) is the density of water which varies with temperature (Table 1), θ_w (m^3 m^{-3}) is volumetric soil moisture, p_c (Pa) is capillary pressure ($p_c = p_g - p_w$), where p_g is the gas pressure (Pa) and p_w (Pa) is the liquid water pressure), t (s) is time, and q_w (m s^{-1}) is the Darcy velocity expressed as [*Bear*, 1972]:

$$q_w = -\frac{k_{\text{int}} k_{r,w}}{\mu_w} \cdot (\nabla p_w + \rho_w g \nabla z) \tag{5}$$

k_{int} (m^2) is the intrinsic permeability tensor, $k_{r,w}$ (–) is the relative permeability of the wetting fluid, μ_w (Pa s) is the temperature dependent dynamic viscosity of water (Table 1), g (m s^{-2}) is gravitational acceleration, and z (m) is the vertical elevation relative to a prescribed datum. The water retention characteristic curve (p_c-θ_w) is corrected for changes of surface tension with temperature (σ, N m^{-1}) [*Assouline*, 2006; *Assouline et al.*, 2010]:

$$p_c(T) = p_c(T_{ref}) \frac{\sigma(T)}{\sigma(T_{ref})} \tag{6}$$

In Equation (3), $\dot{m}$ is used as a loss or gain term that allows mass to be transferred to or from the liquid water phase; a positive value of $\dot{m}$ denotes evaporation. Dissolution of the gas phase into the liquid water phase was not included in the model due to its negligible impact.

5.2.2.2. Total gas phase mass balance

Similar to the mass balance for liquid water, the dry air mass balance is given by [*Bear*, 1972]:

$$\frac{\partial(\rho_g w_a \theta_g)}{\partial t} + \nabla \cdot \left(\rho_g w_a q_g - D_{av} \rho_g \theta_g \nabla w_a\right) = 0 \tag{7}$$

where θ_g ($m^3\ m^{-3}$) is the gas content, w_a (–) is the mass fraction of dry air in the gas phase, D_{av} ($m^2\ s^{-1}$) is the effective binary diffusion coefficient of air in air-water vapor mixture [*Smits et al.*, 2011], and ρ_g ($kg\ m^{-3}$) is the gas density [*Lide*, 2001], and u_g ($m\ s^{-1}$) is the Darcy velocity of the gas expressed by [*Bear*, 1972]:

$$q_g = -\frac{k_{\text{int}} k_{r,g}}{\mu_g} \cdot (\nabla p_g + \rho_g g \nabla z) \tag{8}$$

where $k_{r,g}$ is the relative gas permeability of the water vapor-air mixture, μ_g (Pa s) is the dynamic viscosity of moist air, and p_g (Pa) is the total gas pressure. The mass balance for the water vapor in the gas phase is expressed similarly to Equation (7):

$$\frac{\partial(\rho_g w_v \theta_g)}{\partial t} + \nabla \cdot \left(\rho_g w_v q_g - D_{av} \rho_g \theta_g \nabla w_v\right) = \dot{m} \tag{9}$$

where w_v (–) is the mass fraction of water vapor in the gas phase. Equations (7) and (9) can be combined while keeping in mind that $w_a + w_v = 1$ and $\nabla \cdot (w_a + w_v) = 0$ to yield the total gas mass balance [*Lide*, 2001]:

$$\frac{\partial(\rho_g \theta_g)}{\partial t} + \nabla \cdot \left[\rho_g q_g\right] = \dot{m} \tag{10}$$

A positive value of $\dot{m}$ denotes that mass is being transferred into the gas phase, or evaporation is occurring.

Equations (7-10) are all dependent on the density of the gas which varies with temperature, gas pressure and the mass fraction of water vapor present in the gas phase. By assuming that a moist air mixture behaves like an ideal gas, the density of the gas can be expressed as:

$$\rho_g = \frac{p_g}{RT}\left[w_v \left(\frac{M_a - M_w}{M_w M_a} \right) + \frac{1}{M_a} \right]^{-1} \tag{11}$$

where M_a and M_w (kg mol^{-1}) are the molar masses of dry air and water respectively. The effective water binary vapor diffusion coefficient that appears in Equation (7) and (9) is defined as the product of the binary diffusion coefficient of water vapor-dry air (Table 1) and tortuosity (τ,–). The *Penman* [1940] model ($\tau = 0.66\theta_g$) is used to estimate the tortuosity and was selected for its better performance in our modeling efforts compared to other tortuosity formulations (e.g. *Millington and Quark*, 1961; *Moldrup et al.*, 1997). In many studies (e.g. *Childs and Malstaff*, 1982; *Cass et al*, 1984; *Campbell*, 1985; *Bear et al.*, 1991; *Smits et al.*, 2011; *Smits et al.*, 2012a; *Davarzani et al.*, 2014) the effective diffusion coefficient is also multiplied by an empirical vapor enhancement factor. The vapor enhancement factor is commonly used to address the underestimation of vapor fluxes by Fick's law of diffusion at intermediate to high soil moisture [*Philip and de Vries*, 1957]. The vapor enhancement factor however, is not employed in the present so as to reduce the number of fitting parameters and to allow the applicability of the non-equilibrium phase change formulations to be directly compared. An effective dispersion coefficient does not need to be included because of the slow flow velocities and large magnitude of the diffusion coefficient [*Davarzani et al.*, 2014].

5.2.2.3. Soil water retention, relative permeability, hydraulic conductivity

Equations (4) and (10) can be solved simultaneously for both the liquid water and total gas pressures, two of the primary unknowns in the model. These two parameters are combined to calculate p_c, which in turn is used to determine the soil saturation at any given location and time within the model domain. In the present study, we applied the van Genuchten-Mualem analytical model [*Mualem*, 1976; *van Genuchten* 1980], corrected for water vapor sorption to the soil grains [*Fayer and Simmons*, 1995] to define the $p_c - S_{ew}$ relationship:

$$\frac{S_w - S_{rw}}{1 - S_{rw}} = \frac{\chi\theta_a}{\phi} + \frac{(\phi - \chi\theta_a)}{\phi} \begin{cases} \left[1 + \left(\alpha \left| \frac{p_c}{\rho_w g} \right| \right)^n \right]^{-m} & \frac{p_c}{\rho_w g} > 0 \\ 1 & \frac{p_c}{\rho_w g} \le 0 \end{cases} \tag{12}$$

where S_w (–) is the water saturation, S_{rw} (–) is the residual water saturation resulting from entrapped water in the pore space, $\chi\theta_a$ (m^3 m^{-3}) is the adsorption of water vapor to the soil grain with θ_a (m^3 m^{-3}) being the soil moisture value at p_c = 1, ϕ (m^3 m^{-3}) is the soil porosity, and α (–), n (–) and m (–) are the van Genuchten soil parameters; m is defined as $m = 1 - 1/n$. The values of α and n of the test soil used in the present study were determined previously from experimental data. The term χ is itself a function of capillary pressure and can be expressed as [*Fayer and Simmons*, 1995]:

$$\chi(p_c) = 1 - \frac{\ln[p_c/(\rho_w g)]}{\ln[p_{cm}/(\rho_w g)]} \tag{13}$$

in which p_{cm} (Pa) is defined as the capillary pressure of water as the water content approaches zero. *Fayer and Simmons* [1995] explain that the ratio of $p_{cm}/(\rho_w g)$ is commonly taken to be 10^7 cm for fine textured soils. This correction allows the model to simulate soil moisture values below the prescribed residual water content as is observed during experimentation. The relative permeability relationship for water is also expressed in terms of the van Genuchten-Mualem analytical model [*Mualem*, 1976; *van Genuchten* 1980]:

$$k_{r,w} = S_{ew}^{1/2}\left[1 - \left(1 - S_{ew}^{1/m}\right)^m\right]^2 \tag{14}$$

and the van Genuchten-Mualem analytical model for the total gas phase as [*Parker et al.*, 1987]:

$$k_{r,g} = (1 - S_{ew})^{1/2}(1 - S_{ew}^{1/m})^{2m} \tag{15}$$

To better represent flow conditions across the full range of saturations or capillary pressures, film flow (dominant under unsaturated/dry conditions) is also taken into account. The effects of both flow regimes are incorporated into the model through the summation of their respective hydraulic conductivities [*Zhang*, 2010]:

$$K(p_c) = K^c(p_c) + K^f(p_c) \tag{16}$$

where K^c (m s^{-1}) and K^f (m s^{-1}) are the hydraulic conductivities due to capillary flow and film flow respectively. The hydraulic conductivity of the capillary flow was expressed as the product of the relative permeability function for the water phase (Equation 14) with the known saturated hydraulic conductivity of the soil. The hydraulic conductivity of the film flow is described using the *Tokunaga* [2009] model. This model was chosen for its lack of empirical fitting parameters as well as its ability to capture film flow behavior, refer to *Smits et al.* [2012a] for an in depth discussion.

5.2.2.4. Energy conservation

Energy conservation at the REV scale for the system consisting of liquid water, gas (air and water vapor), and soil analyzed in the present study is also coupled to Equations (4) and (10) in part by phase change and can be expressed as [*Whitaker,* 1977]:

$$\frac{\partial(\rho_b C_b T)}{\partial T} + \nabla \cdot (C_g \rho_g q_g T + C_w \rho_w q_w T - \lambda_T \nabla T) = -L\dot{m} - Q_s \quad (17)$$

where T (K) is temperature, ρ_b (kg m^{-3}) is the bulk density of the soil, C_g and C_w (J kg^{-1} K^{-1}) are the specific heat capacities of gas and water respectively, λ_T (W m^{-1} K^{-1}) is the effective thermal conductivity of the soil, Q_s (J) is a heat loss/gain due to convection, and L (J m^{-3}) is the latent heat of vaporization which varies as a function of temperature (Table 1). The term $-L\dot{m}$ in the above equation represents heat losses or gains due to evaporation or condensation respectively. At the microscopic scale, temperature differences between the liquid water and water vapor phases can be measured immediately on either side of the liquid-gas interface – experimental studies have reported temperature differences as large as 7.8 °C [*Fang and Ward*, 1999; *Ward and Stanga*, 2001]. This is not possible however at the REV scale; the location of the evaporative front is constantly moving, prohibiting accurate measurement. For this reason, we assume local thermal equilibrium between liquid water, water vapor, and soil ($T_w = T_g = T_s$), as commonly done in the literature. The C_b term in Equation (17) is the effective heat capacity per unit volume of the soil and is estimated as the average of the gas, water, and soil specific heat capacities weighted according to density and soil moisture. The *Campbell et al.* [1994] model is used to calculate the effective conductivity which is given by:

$$\lambda_T = \frac{\omega_w \theta_w \lambda_w + \omega_g \theta_g \lambda_g + \omega_s (1-\phi)\lambda_s}{\omega_w \theta_w + \omega_g \theta_g + \omega_s (1-\phi)} \quad (18)$$

where λ_w (W m^{-1} K^{-1}), λ_g (W m^{-1} K^{-1}), and λ_s (W m^{-1} K^{-1}) are the thermal conductivities of water, gas (air and water vapor) and the soil as defined in *Campbell et al.* [1994]. ω_w (–),ω_g (–), and ω_s (–) are calculated weighting factors for water, gas, and the soil [*Campbell et al.*, 1994]. The heat loss term, Q_s, is calculated according to Newton's law of cooling [*Bird et al.*, 2002] for a thermal gradient across the walls of the tank.

5.2.2.5. Non-equilibrium phase change formulations

As previously discussed, phase change at the macroscopic scale is caused by the vapor concentration (c_v, kg m^{-3}) in the air not being equal to its equilibrium vapor concentration (c_{veq}, kg m^{-3}). The equilibrium vapor concentration is defined as the product of Kelvin's equation for relative humidity [*Thomson*, 1870] and the saturated vapor concentration in the air (c_{vs}, kg m^{-3}) [*Campbell*, 1985]:

$$c_{veq} = c_{vs} \exp\left(\frac{H_c M_w g}{RT}\right) \tag{19}$$

where H_c (m) is capillary pressure head. The saturated vapor concentration is also a function of temperature and can in turn be defined as [*Campbell*, 1985]:

$$c_{vs} = \frac{1}{T} \exp\left(31.3716 - \frac{6014.79}{T} - 0.007924T\right) x10^{-3} \tag{20}$$

The temperature variables in Equation (20) are expressed in degrees Kelvin.

In non-equilibrium thermodynamics, the state of a natural system is constantly evolving with respect to its entropy. Irreversible processes such as non-equilibrium phase change increase the overall entropy of a system. *Bénet and Jouanna* [1982], based on irreversible thermodynamics, proposed to describe non-equilibrium phase change, on the basis of liquid water and water vapor not being in equilibrium with respect to their molar chemical potentials, as:

$$\dot{m} = \frac{L_p}{T}(\mu_w - \mu_v) \tag{21}$$

where L_p (kg K s m^{-5}) is the phenomenological coefficient, T (K) is temperature, and μ_w and μ_v (m^2 s^{-2}) are the chemical potentials of the liquid water and water vapor phases respectively. If one assumes that water vapor behaves as an ideal gas the chemical potentials for liquid water and water vapor can be defined as [*Bénet and Jouanna*, 1982]:

$$\mu_w = \frac{RT}{M_w} \ln\left(\frac{p_{veq}}{p_0}\right) + \eta(p_0, T) \tag{22}$$

and

$$\mu_v = \frac{RT}{M_w} \ln\left(\frac{p_v}{p_0}\right) + \eta(p_0, T) \tag{23}$$

where p_0 (Pa) is the reference pressure, p_{veq} (Pa) is the equilibrium pressure, and p_v (Pa) is the partial vapor pressure, and $\eta(p_o, T)$ is a temperature function. Substituting Equations (22-23) into Equation (21) yields the final phase change formulation derived by *Bénet et al.* [2009] written here in terms of vapor concentration:

$$\dot{m} = -\frac{L_p R}{M_w} \ln\left(\frac{c_v}{c_{veq}}\right) \tag{24}$$

It is important to note that Equation (24) is an isothermal non-equilibrium phase change formulation, an important fact that will be revisited in the discussion of the modeling results in Section 4.1.1. Preliminary modeling efforts using Equation (24) in the present study failed to properly reproduce evaporation rate and cumulative evaporation. We therefore introduced a correction by multiplying Equation (24) by the soil moisture (θ_w, m^3 m^{-3}) in order to take into account the distribution of the liquid-gas interfaces. The final modified version of Equation (24), referred to as Formulation 1 from hereon, is given as:

$$\dot{m} = -\frac{\theta_w L_p R}{M_w} \ln\left(\frac{c_v}{c_{veq}}\right) \tag{25}$$

L_p can be viewed as a fitting parameter. The temperature and soil moisture dependency of L_p has been investigated in a number of different experimental studies (e.g. *Bénet and Jouanna*, 1982; *Ruiz and Bénet*, 2001; *Chammari et al.*, 2003; *Lozano et al.*, 2008; *Bénet et al.*, 2009; *Lozano et al.*, 2009). For the temperature and total gas regime specific to their study, *Bénet et al.* [2009] found that L_p is equal to:

$$L_p = \begin{cases} L_{eq} & r < \dfrac{p_v}{p_{veq}} \le 1 \\ L_{eq} + k\left(r - \dfrac{p_v}{p_{veq}}\right) & 0 < \dfrac{p_v}{p_{veq}} \le r \end{cases} \tag{26}$$

where L_{eq}, k, and r, are experimentally determined coefficients.

The next two non-equilibrium formulations are very similar to the first-order kinetic mass transfer relationships used in organic and inorganic solute vaporization studies (e.g. *Cho and Jaffe*, 1990, *Gierke et al.*, 1992; *Armstrong et al.*, 1994). The second commonly used non-equilibrium phase change formulation (referred from this point on as Formulation 2) tested in the present study relies an equilibrium time parameter as shown in [*Le et al.*, 1995; *Scarpa and Milano*, 2002]:

$$\dot{m} = \frac{\theta_w}{t_{eq}}(c_v - c_{veq}) \tag{27}$$

where t_{eq} (s) is referred to as the equilibrium time coefficient. According to *Scarpa and Milano* [2002], the equilibrium time coefficient is a function of both the evaporation surface area per unit volume and the liquid water velocity. t_{eq} can be estimated as the characteristic time of effective binary water vapor-dry air diffusion coefficient (D_{av}, $m^2\ s^{-1}$) in a cylindrical pore with characteristic length (l_{por}, m) [*Ward and Fang*, 1999; *Halder et al.*, 2011]:

$$t_{eq} = \frac{l_{por}^2}{D_v} \tag{28}$$

Small values of t_{eq} represent near instantaneous phase change or equilibrium conditions. A similar phase change formulation (referred from this point on as Formulation 3) was introduced by *Bixler* [1985] and applied in *Zhang and Datta* [2004] and *Smits et al.* [2011, 2012a, 2012b, 2013]:

$$\dot{m} = \frac{b\theta_w RT}{M_w}(c_v - c_{veq}) \tag{29}$$

where b ($s\ m^{-2}$) is the constant of proportionality. One of the most important distinctions between Formulation 2 and 3 is the presence of a temperature term in Equation (29), again revisited later in terms of the modeling results and discussion in Section 4.1.1. Large values of b means phase change is nearly instantaneous. The terms outside the parentheses containing the vapor concentration terms in Equations (27 and 29) are occasionally combined into a single lumped term [*Prat,* 2002]. Due to the inaccuracy of combining so many terms, this lumping approach is not analyzed as part of this study.

None of the REV scale phase change formulations presented above allow for both evaporation and condensation to be scaled simultaneously. The use of an up-scaled Hertz-Knudsen equation (referred from this point on as Formulation 4) addresses this issue through the employment of dimensionless evaporation f_e (–) and condensation f_c (–) coefficients:

$$\dot{m} = \frac{2\theta_w}{(2 - f_c)}\sqrt{\frac{RT}{2\pi M_w A}}(f_c c_v - f_e c_{veq}) \tag{30}$$

where A (m^2) is cross-sectional area. As per the discussion regarding energy conservation above, thermal equilibrium is assumed to exist between the liquid water and the water

vapor phases. This allows a single temperature value to be used in the above equation. The evaporation and condensation coefficients in Equation (30) are used as fitting parameters in similar fashion to the other coefficients in Formulations 1-3. Values of $f_c = f_e$ represent equilibrium conditions for the Hertz-Knudsen equation. If f_e is held constant at a value approximately equal to 1 and f_c is allowed to vary, any decrease in f_c can be interpreted as driving the system farther from equilibrium conditions [*Kryukov and Levashov,* 2011]. This leads to greater rate of phase change and as a result greater cumulative evaporation.

5.2.3. Modeling procedure and formulation of boundary and initial conditions

Finite element based COMSOL Multiphysics software was used for the numerical simulation component of this study. The non-equilibrium phase change-based model was defined in terms of a two dimensional domain with identical conditions to that of the experiments discussed in Section 3. The model solves the four coupled balance equations for the liquid phase, gas phase, water vapor, and energy discussed above for the primary variables (Table 2).

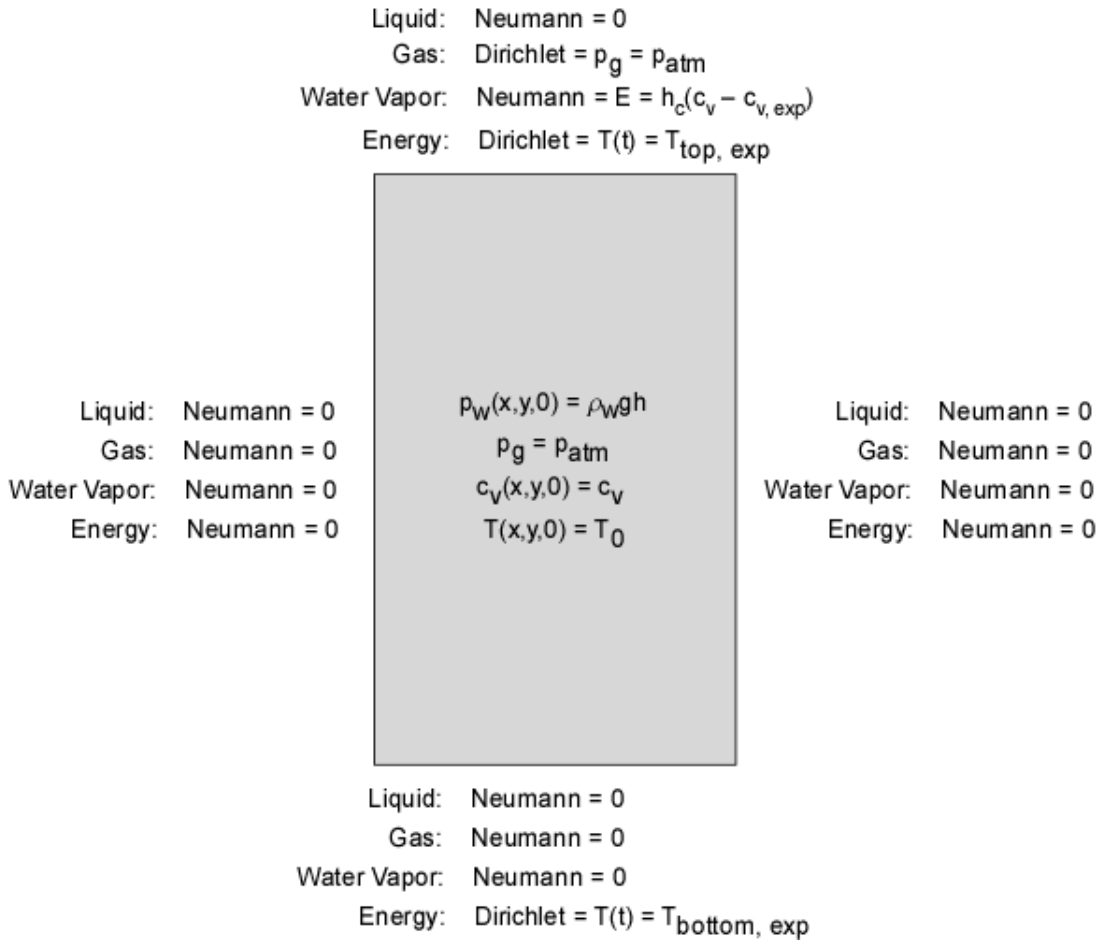

Figure 3. Visual representation of the initial and boundary conditions of the non-equilibrium based model. T (°C) denotes temperature, t (s) time, p_w (Pa) water pressure, p_g (Pa) total gas pressure, p_{atm} (Pa) atmospheric pressure, c_v (kg m^{-3}) vapor concentration, c_{veq} (kg m^{-3}) equilibrium vapor concentration, h_c (m s^{-1}) mass transfer coefficient, and E (kg m^{-2} s^{-1}) evaporative flux. The subscript exp denotes experimental data.

At the beginning of each numerical simulation, the water pressure was assumed to be under hydrostatic conditions, $\rho_w gh$. The total gas pressure was set to atmospheric pressure and the vapor concentration was set to the model's initialized value (zero in the case of full saturation). The temperature within the model domain was set at a constant temperature T_0. The two sides of the model domain were treated as Neumann boundary conditions with mass and energy fluxes equal to zero. Heat loss through the tank walls was taken into account as a sink term within the model domain (Section 2.2.4). The bottom boundary condition was also assigned a Neumann boundary condition of zero with respect to the liquid, total gas, and water vapor phases. A Dirichlet boundary condition set as the experimentally measured temperature was assigned for the energy equation (Figure 3). The top of the model domain was designated as Neumann boundary condition with respect to

the liquid and water vapor phases. A zero flux was provided for the liquid phase and a vapor flux of:

$$E = h(c_v - c_{\exp}) \tag{31}$$

where E (kg m^{-2} s^{-1}) is the evaporative flux and h (m s^{-1}) is a mass transfer coefficient between the soil surface and atmosphere, and c_{exp} (kg m^{-3}) is the experimental vapor concentration determined from relative humidity data. The mass transfer coefficient is defined as the binary diffusion coefficient of water vapor-dry air, D_{av}, divided by a characteristic length, L (m). A length of 2 mm, the approximate thickness of the viscous sublayer, was selected as the characteristic length in similar fashion to *Shahraeeni et al.* [2012], *Haghighi et al.* [2013], and Mosthaf *et al.* [2014]. The total gas phase and energy were treated as Dirichlet boundary conditions; the total gas phase was set equal to atmospheric pressure and energy to experimental temperature data measured at the soil surface.

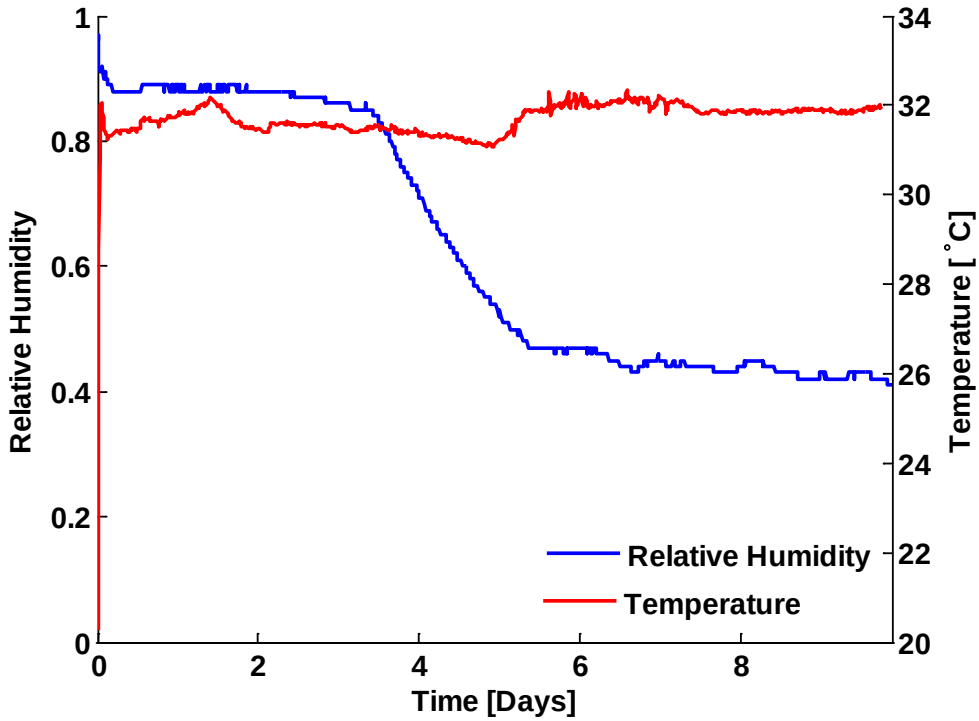

Figure 4. Example of time-dependent experimental surface relative humidity and temperature data provided as inputs to the numerical heat and mass transfer model as boundary conditions at the top boundary of the model domain. Experimental data taken from Experiment 2 (32°C surface temperature, initially fully saturated).

A total of 1973 triangular elements consisting of 1061 mesh points and 16376 number of degrees of freedom were used in the numerical simulation of this study. The

mesh was refined near the top boundary in order to provide greater resolution near the soil surface. Each element represents an area ratio of approximately 0.063. The model was implicitly solved using the UMPACK direct matrix solver that is incorporated in the COMSOL Multiphysics software. Time was advanced using the Backward Euler method with a built-in adaptive time-stepping scheme. In accordance with the experimental datasets, each numerical model ran for the same duration as the experiment it was simulating. The coefficient in each non-equilibrium phase change formulation was the only parameter used to find the best fit to the experimental data collected. A total of 15 to 30 model realizations were run for each coefficient under the four Experimental conditions. The run that best simulated cumulative evaporation, time-dependent soil moisture, and temperature profiles in terms of maximizing the coefficient of determination (r^2 value) was selected as the final run used in Section 4.

5.3. MATERIAL AND METHODS

5.3.1. Soil material

Field soils are often non-uniform heterogeneous mixtures of organic and inorganic materials. This in turn can lead to large local variations of soil physical (e.g. soil moisture adsorption, porosity, density), hydraulic (e.g. soil water retention, hydraulic conductivity) and thermal properties (e.g. thermal conductivity, thermal diffusivity, volumetric heat capacity) which is difficult to capture in numerical modeling efforts. Therefore, a uniform well characterized laboratory test sand was used in the present study to allow us to investigate non-equilibrium phase change without the added complexities introduced through field soils. This allows us to obtain a fundamental understanding of processes and to generate data for model verification. In the following experiments, accusand #30/40 specialty sand (Unimin Corp., Ottawa, Minnesota), identified by its effective sieve size, was used (see Smits et al., 2010, 2012a for sand properties). According to the manufacturer, Accusand #30/40 has a uniformity coefficient of 1.2, a rounded shape, and a composition of 99.8% quartz. A summary of many of the key properties of this test soil under tight packing conditions can be found in Table 3.

5.3.2 Experimental Apparatus

The experimental portion of the present study was performed in a rectangular tank (9.0 cm wide, 25.0 cm long, 55.0 cm tall) constructed out of 1.25 cm thick polycarbonate (Figure 5). The thermal conductivity and specific heat of the polycarbonate was 0.15 W m^{-1} K^{-1} and 1464 J kg^{-1} K^{-1} respectively. The tank was equipped with a sensor network for the continuous and autonomous collection of precision soil and air temperature, relative humidity, soil moisture, thermal properties (i.e. thermal conductivity, thermal diffusivity, volumetric heat capacity), weight, and wind velocity data (Figure 5).

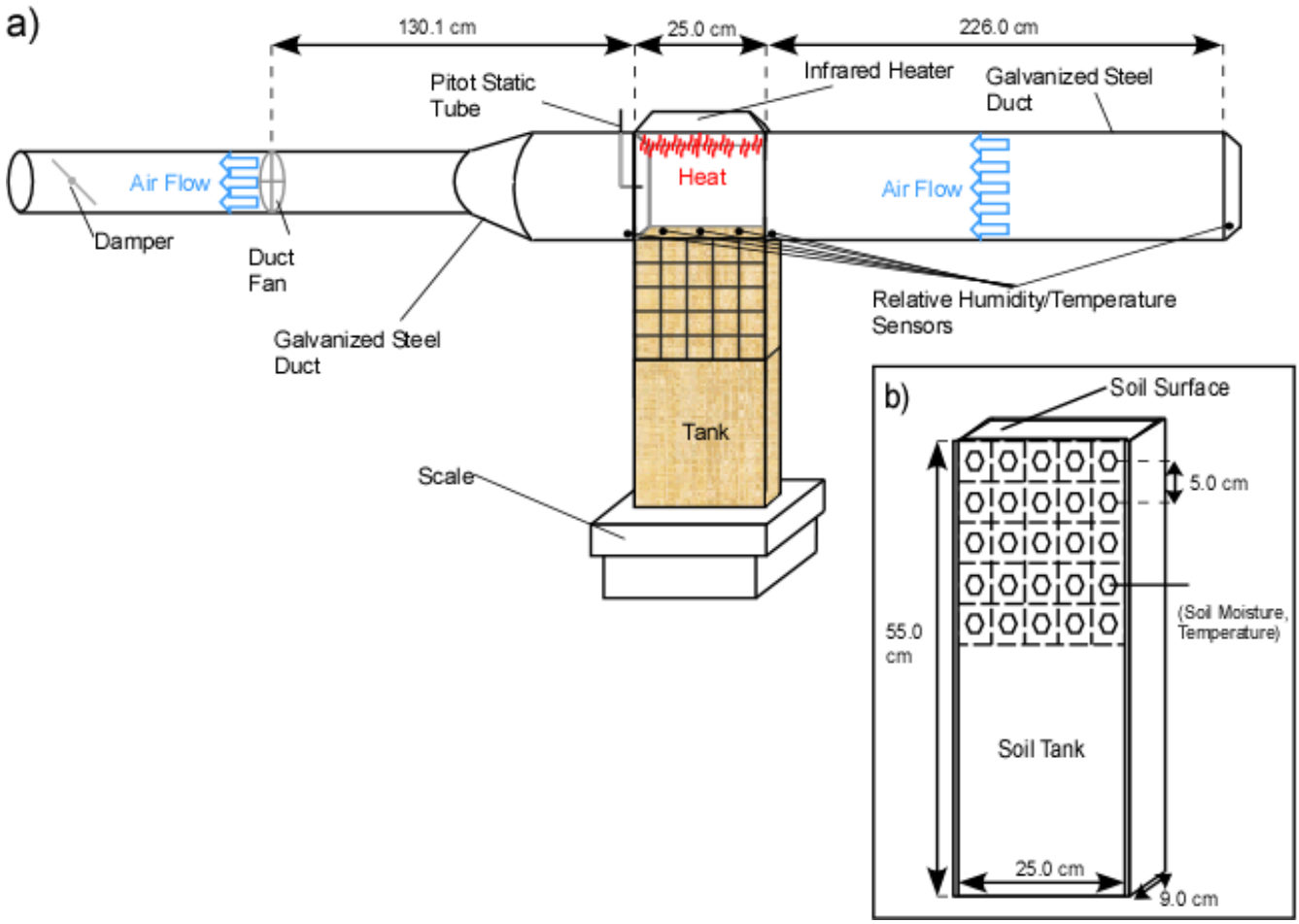

Figure 5. Experimental apparatus used in the experimental portion of this study. Image (a) shows the tank-wind tunnel interface and (b) shows the tank specifications. Figure not drawn to scale.

Soil temperature and moisture distributions were measured along the vertical and horizontal extents of the rectangular tank. The sensors, discussed in detail below, were installed horizontally through the tank walls at 5.0 cm depth increments between the depths of 2.5 cm and 22.5 cm below the soil surface (Figure 5). Temperature was measured using a total of nineteen 5.5 cm long, 70 MHz measurement frequency EC-T

thermistor temperature sensors (Decagon Devices, Inc., Pullman, WA). Twenty-five ECH_2O EC-5 dielectric soil moisture sensors (Decagon Devices, Inc., Pullman, WA) were used to monitor the soil moisture distribution. These 8.9 cm long sensors were calibrated according to the two-point α-mixing model derived in *Sakaki et al.* [2008] which uses the analog-to-digital converter number converted from the measured capacitance due to changes in soil dielectric permittivity. Due to the temperature sensitivity of the dielectric permittivity of the bulk soil [*Assouline et al.,* 2010], a temperature correction as described in *Cobos and Campbell* [2007] was applied to the soil moisture data upon the termination of each experiment. Relative humidity at the soil surface and upstream of the soil tank were measured using a total of four EHT temperature/RH sensors (Decagon Devices, Inc., Pullman, WA; ±2% from 5%-90% relative humidity and ±3% from 90%-100% relative humidity). These sensors, consisting of a film capacitor on a polymer coated ceramic substrate, measure changes in the dielectric constant in response water sorption/desorption. The associated dielectric constant is then correlated to a relative humidity [*Chen and Lu,* 2005]. The EHT sensors located at the soil surface were placed in firm contact with the soil so as to best capture relative humidity conditions directly at the soil-atmosphere interface. Data from the three aforementioned sensors were collected every 10 minutes and stored using ECH_2O EM-50 (Decagon Devices, Inc., Pullman, WA) data loggers.

The tank was placed on a precision 65 kg ± 1 g weighting scale (Sartorius Corporation, Bohemia, NY, Model 11209-95) to measure water loss throughout the duration of the experiment. Weight measurements were used to calculate cumulative evaporation and evaporation rate using a mass balance approach. Weight measurements were collected every 10 minutes. The experimental apparatus was interfaced along the tank's centerline to a miniature open-ended wind tunnel constructed out of galvanized steel ductwork (26.0 cm tall by 8.0 cm wide), Figure 5. The upstream ductwork length is 226 cm in length and a 15.2 cm diameter Pro DB6GTP in-line duct fan (Suncourt, Inc., Durant, IA) with a VS200 variable speed controller (Suncourt, Inc., Durant, IA) was installed 130.1 cm downstream from the tank to pull air through the wind tunnel. Wind velocity was measured every 5 minutes using a pitot-static tube (Dwyer Instruments, Inc., Michigan City, IN; ±5% accuracy) connected to a USB-6218 datalogger (National Instruments Corporation, Austin, TX). The temperature of the soil surface was controlled using an infrared Salamander Model FTE 500-240 ceramic heater (Mor Electric Heating Assoc., Inc., Comstock Park, MI) placed within a reflector above the tank (Figure 4). The heater

output was controlled using a temperature control system (Chromalox, Pittsburgh, PA; Model, 2104) regulated by an infrared temperature sensor (Exergen Corporation, Watertown, MA; Model IRt/C.03) directed at the soil surface.

5.3.3 Experimental procedure and data acquisition

A series of four experiments were run to generate the necessary data to test the non-equilibrium phase change formulations discussed in Section 2.2.5 under different constant and transitory thermal, concentration, and wind velocity boundary conditions and initial saturations. The experiments differed in terms of the boundary and initial conditions (Table 4). Experiments 1-3 started with the soil tank at full saturation so as to capture Stage I and Stage IIa-IIb evaporation. Experiment 4 was partially saturated from the beginning of the experiment to ensure that only Stage IIb evaporation (defined below) occurred. This was accomplished by lowering the water table below the characteristic length of the soil (i.e. the maximum film region thickness that maintains liquid water flow; *Lehmann et al.,* 2008). The average wind velocity applied across the soil surface during each experiment ranged between 0.55 and 0.76 m s^{-1} (Table 4). The temperature of the soil surface was held constant throughout the duration of Experiments 2 and 4 using the ceramic heater discussed above. Experiment 3 simulated diurnal conditions by applying two different surface temperature conditions on 12 hour cycles with the purpose of capturing transient environmental conditions [*Assouline et al.*, 2013]. During each 12 hour period, the temperature was held constant using the ceramic heater. Experiment 1 differed from the others in that it was allowed to run under ambient laboratory conditions in which temperatures varied by approximately ± 1.5 ℃, providing a baseline for the elevated temperature studies.

Prior to the start of each experiment, the tank was wet packed with #30/40 Accusand to approximately the same porosity (Table 4) using dionized water. A common soil packing procedure was used for each experiment. This involved adding sand in 1 cm lift increments while maintaining 5 cm of water above the soil surface. After the addition of each sand layer, the sand surface was tamped and the tank walls repeatedly tapped with a rubber mallet to compact the sand; see *Sakaki and Illangasekare* [2007] for a detailed description of the packing process. *Sakaki and Illangasekare* [2007] found that the approach outlined in their study yielded greater and more uniform packing densities than the standard American Society for Testing and Materials (ASTM) method D 4253–00

[*Youd*, 1973]. Upon termination of each experiment, the tank was cleaned out and the sand was oven dried before the packing process was begun anew. In the case of the partially saturated experiment (Experiment 4), the soil tank was connected to a constant head device. The constant head device, initially set at the soil surface, was lowered to a height corresponding to a depth of 25 cm below the soil surface (the final water table depth). This initiated a drainage process that allowed residual soil moisture to be retained within the unsaturated soil above the water table. A water table depth of 25 cm was selected so as to exceed the characteristic length of the soil [*Lehmann et al.*, 2008], thus ensuring the severance of the hydraulic connection between the water table and soil surface, as discussed above.

5.4. RESULTS AND DISCUSSION

In this section, we compare experimentally measured data (Experiments 1-4, Table 4) with simulation results of the three non-equilibrium phase change formulations found in the literature and the modified Hertz-Knudsen formulation (Formulation 4). Section 4.1 discusses the behavior of the evaporation rate and cumulative evaporation curves for each experiment. A detailed analysis of the ability of the four non-equilibrium phase change formulation's ability to accurately capture evaporation under the various environmental boundary and initial conditions is presented in Section 4.2. This comparison allows us to determine under what boundary and initial conditions specific formulations perform better as well as further investigate under what boundary and initial conditions accounting for non-equilibrium phase change is potentially important. Model outputs include cumulative evaporation, time-dependent evaporation rate, time-dependent soil moisture distributions, soil temperature profiles, vapor densities at the soil surface, and simulated rate of phase change. This is in turn followed by a discussion of the adjustment of and impact of the five fitting coefficients (Formulations 1-4) on evaporation in Section 4.3. Finally, we look at the significance of non-equilibrium phase change with respect to evaporation in Section 4.4 by comparing the Damkohler number (Da) of each experiment and analyzing the concentration profiles.

5.4.1. Experimental evaporation rate and cumulative evaporation

Figure 6 presents cumulative evaporation and evaporation rate curves for the four experiments performed for the present study. The initial and boundary conditions of each experiment significantly affect the evaporation behavior. As seen in the evaporation rate behavior for experiment 1 (Figure 6b), during Stage I evaporation, also referred to as the "constant-rate" stage [*Fisher*, 1923; *Hide*, 1954; *Lemon*, 1956], the evaporation rate is high and relatively constant. For experiments 2-3, although the evaporation rate is initially high, it is not constant. The non-constant Stage I evaporation observed in Experiments 2-3 is due, in part, to the uniformity of the test soil used in the experiments. Pore size distribution and wind velocity have been shown to play key roles in determining the consistency of evaporation during Stage I; poorly graded or uniform soils exposed to high wind velocities will commonly display a rapidly decreasing evaporation rate and short Stage I duration [*Prat*, 2002; *Metzger and Tsotsas*, 2005; *Shahraeeni et al.*, 2012; *Haghighi and Or*, 2013; *Haghighi et al.*, 2013; *Davarzani et al.*, 2014]. Experiment 4 did not experience Stage I (atmospheric dominated) evaporation due to the initial conditions. As discussed previously, the water table for Experiment 4 was hydraulically disconnected from the soil surface (i.e. 25 cm below soil surface). Thus, Experiment 4 only underwent Stage II evaporation which will be explained in detail below.

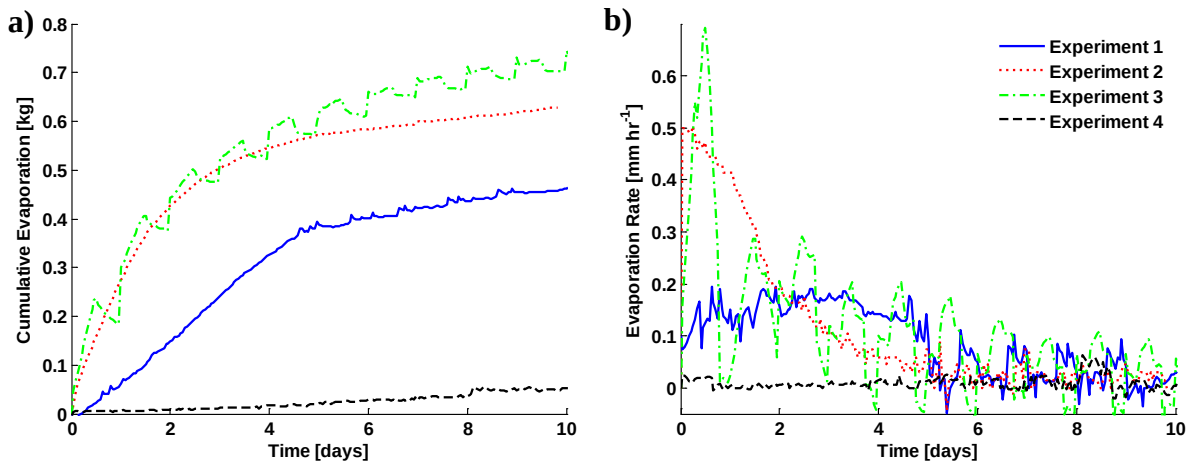

Figure 6. Experimentally measured (a) cumulative evaporation and (b) evaporation rate over time for the four experiments.

The observed differences in evaporation behavior for each experiment are also due to the differences in temperature at the soil surface. Figure 6 and Table 5 show that evaporation increases with increasing surface temperature. Experiments 2-3 which

imposed elevated surface temperature boundary conditions, display both higher evaporation rates (Figure 6a) which is also reflected by the steeper slope of cumulative evaporation curves (Figure 6b) and overall shorter Stage I duration. This is an expected observation given that atmospheric demand increases with increasing surface temperature and decreasing relative humidity. Stage I evaporation, driven primarily by atmospheric demand, is maintained until the capillary driven hydraulic connection between the water table and soil surface is severed [*Lehmann et al.*, 2008].This explains why Stage I evaporation is not truly observed in the cumulative evaporation and evaporation rate curves (Figure 6a and b) for Experiment 4. As previously discussed, a constant water table was maintained at a depth of 25 cm below the soil surface – a value specifically chosen so as to be greater than the characteristic length of the sand used in the present study, thereby hydraulically disconnecting the water table from the soil surface. To reach this final water table depth, the tank had to be drained using the constant head device which explains the elevated initial evaporation rate between Days 0-1 as the water table was still equilibrating with the constant head device. The slight drainage of water during this time period contributed to the overall water loss and the over exaggerated evaporation rate. Experiment 3 differs from the other three experiments in that a diurnally fluctuating temperature boundary condition was imposed. This is seen in the saw-tooth shape of both the cumulative evaporation and evaporation rate curves (Figure 6). During each 24 hour cycle, the soil surface was heated from above for 12 hours at a temperature of 50°C and then allowed to cool to an ambient temperature of approximately 22°C. This led to the observed evaporation during heating periods and condensation during the cooling periods.

As atmospheric demand exceeds the amount of water that can be supplied to the surface, the hydraulic connection is severed and the “falling-rate” or Stage IIa evaporation is initiated; refer to Figure 1 for a classical depiction. This transitory period is identified in Figure 6a by the sudden drop in evaporation rate and the rounded part of the cumulative evaporation curves (Figure 6b). This change in evaporation rate is due to the drying front, the interface between the partially saturated and completely dry zones, retreating below the soil surface and the evaporation becoming diffusion limited. At this time, the soil saturation at and below the soil surface approaches zero and the overall surface temperature increases as the evaporative cooling effect due to phase change is no longer felt [*Yiotis et al.*, 2007; *Lehmann and Or*, 2009]. The surface boundary conditions are still important, albeit reduced compared to Stage I evaporation, in determining the duration of

Stage IIa evaporation and the rate at which the evaporation rate decreases (i.e. slope of evaporation rate curve). The hotter surface temperatures (Experiments 2-3) yield the fastest decrease in evaporation (Figure 6a) within the shortest period of time. This shows that atmospheric demand still plays an important role in the drying process during this transition period. The evaporation rate will continue to fall during Stage IIa evaporation until it eventually levels off at an approximately constant value (Figure 6a, Table 5) which signifies the onset of Stage IIb evaporation. Evaporation (i.e. phase change) occurs at the drying front and any thin liquid films and the resulting water vapor diffuses through the soil body to the surface [*Lehmann et al.*, 2008; *Lehmann and Or*, 2009]. Stage IIb can also be identified as the section of the cumulative evaporation curve where the water loss again becomes linear with a very small slope. At this point in time, the evaporative front is located sufficiently deep in the soil column that the atmospheric boundary conditions play a less vital role. This is seen by the similar Stage IIb evaporation rates for Experiments 1-4 (Figure 6a, Table 5) which remain relatively constant until each experiment's termination. The observed fluctuations in evaporation rate of Experiment 1 and Experiment 3 during Stage II is the result of temperature fluctuations around the tank, i.e. laboratory climate system cycling and infrared heater cycling respectively. Experiments 2 and 4 maintained a constant temperature around the tank from the overhead heater.

5.4.2. Comparison of model outputs with experimental results

Figure 7 offers a visual comparison of the simulated cumulative evaporation and evaporation rate over time compared to experimental data for experiments 1-4. This figure will be discussed below in unison with Table 5, which provides a more quantitative comparison of the phase change coefficients (L_p, t_{eq}, b, f_e, from Equations 25, 27, 29, 30) and the r^2 values for the simulated cumulative evaporation curves. The fitting and sensitivity of these coefficients is discussed in Section 4.3. Figure 7 and Table 6 show that although all formulations are able to capture the overall trend of evaporation, certain formulations outperform others in their ability to capture the transitions and stages of evaporation. In every experimental condition tested, the four non-equilibrium phase change formulations are capable of capturing the correct trends of both cumulative evaporation and evaporation rate. However, Formulation 4 and to a lesser degree Formulation 3, consistently provide the best reproduction of curve shape and total water loss. Formulation 4 is able to better simulate cumulative evaporation similar to those

measured experimentally because it predicts the highest evaporation rates during Stage I evaporation when the majority of water loss takes place. This observation is further validated by the r^2 values provided in Table 6.The results presented in both Figure 7 and Table 6 are unfortunately the best possible fits; increasing or decreasing the mass transfer coefficients in Formulations 1-3 beyond the maximum or minimum values presented in Table 6 would not lead to any improvement of Stage I estimation. Further improvements to the simulation results could only be attained by including the empirical vapor enhancement factor discussed earlier in Section 2.2.2.

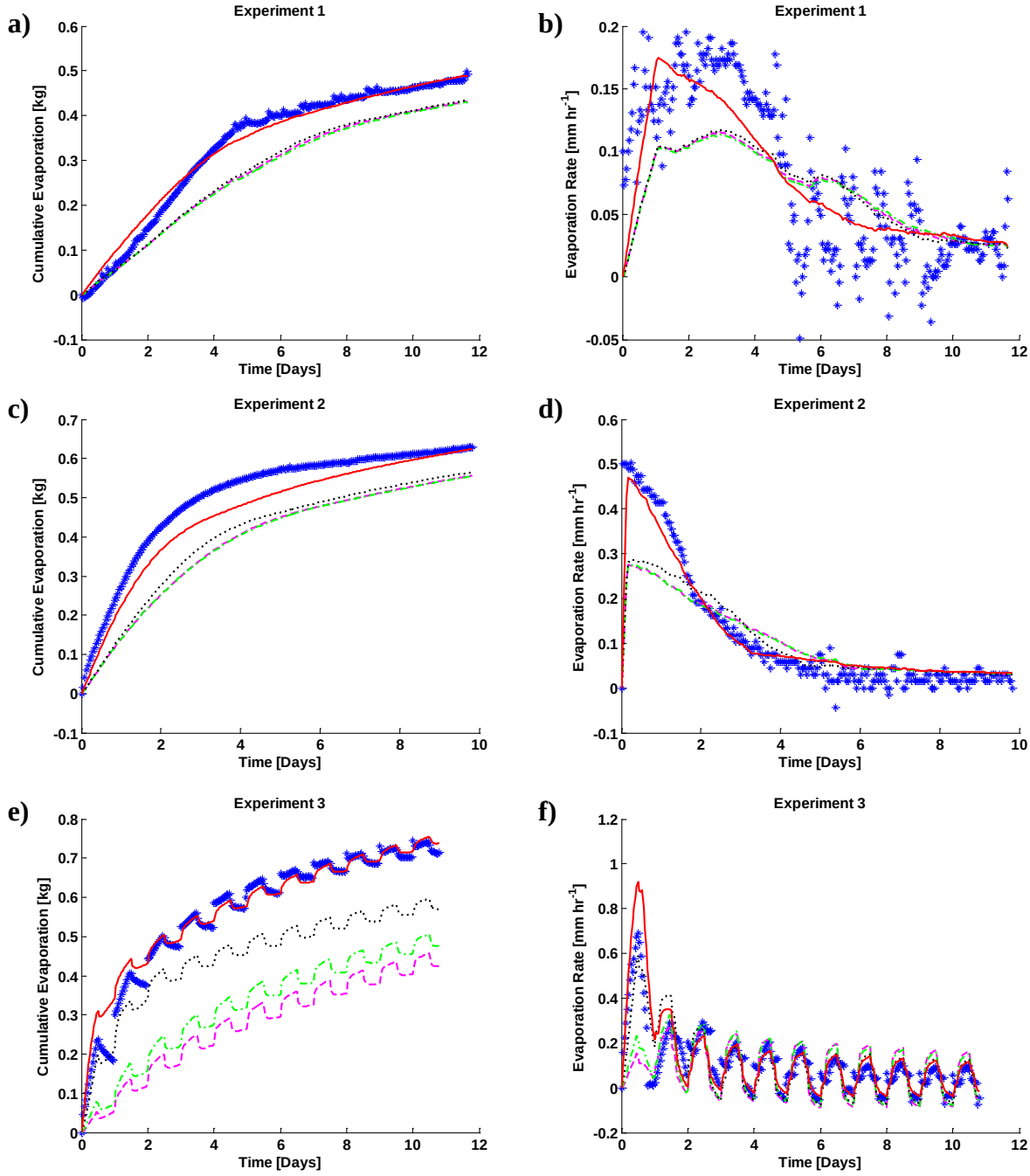
a)
Experiment 1
Cumulative Evaporation [kg]
Time [Days]
b)
Experiment 1
Evaporation Rate [mm hr-1]
Time [Days]
c)
Experiment 2
Cumulative Evaporation [kg]
Time [Days]
d)
Experiment 2
Evaporation Rate [mm hr-1]
Time [Days]
e)
Experiment 3
Cumulative Evaporation [kg]
Time [Days]
f)
Experiment 3
Evaporation Rate [mm hr-1]
Time [Days]

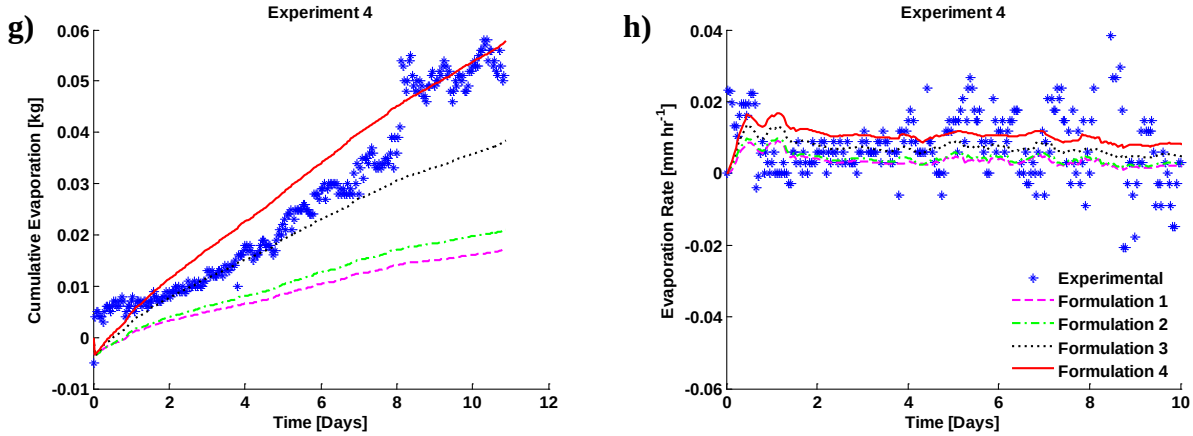

Figure 7. Observed and simulated cumulative evaporation and evaporation rate curves using the four non-equilibrium phase change formulations. (a-b) Experiment 1 boundary and initial conditions, (c-d) Experiment 2 boundary and initial conditions, (e-f) Experiment 3 boundary and initial conditions, and (g-h) Experiment 4 boundary and initial conditions.

Despite the poor estimations of Formulations 1-3 during Stage I evaporation, they are able to reproduce the transitory Stage IIa and diffusion-limited Stage IIb (Figure 7). This is reflected in both the magnitude of the evaporation rates and similar slopes of the cumulative evaporation curves during the latter part of the simulations when compared with the experimental data. During these latter evaporative stages, Formulation 4 actually performs worse than Formulations 1-3. Figure 7 shows that Formulation 4 overestimates the slope of the cumulative evaporation curve during Stage IIb evaporation in addition to the total cumulative water loss at Day 10 in Experiments 1-3, an observation that becomes more apparent at times greater than 10 days. This over prediction is due to the evaporation rates simulated by Formulation 4 being slightly larger than that measured experimentally during Stage IIb. This issue could be addressed by simply reducing the difference between the evaporation and condensation coefficients (Equation 30). However, doing so would lead to a reduction of the evaporation rate during Stage I evaporation.

Figure 7 and the above analysis of the simulation results raises the question of why Formulations 3 and 4 yield better results, especially in the case of Experiments 2-4 (Figure 7c-h) which imposed constant elevated temperature boundary conditions at the soil surface. Formulations 1 and 2 are isothermal representations of phase change whereas Formulations 3 and 4 are non-isothermal. Because phase change with respect to evaporation and condensation involves heat transfer in addition to mass transfer, the isothermal assumption limits the ability of Formulations 1 and 2 to capture evaporative behavior, especially under elevated temperatures. This is further supported by Experiment

1 (Figure 7a-b) which was performed under ambient conditions similar to those in which Formulations 1 and 2 were derived. In this case, temperature plays a less pronounced role as seen in the similarity of Formulations 1-3, Formulation 4 being the notable exception for reasons that will be expanded upon later. As mentioned above, Formulations 3 and 4 both take temperature into account. They differ however in that Formulation 4 applies the square root of the temperature whereas Formulation 3 does not. This leads to the more angular shaped cumulative evaporation curves (Figure 7) predicted using Formulation 3 compared to those predicted using Formulation 4.

The poor performance of Formulation 1 compared to the other Formulations tested may also be due to the use of the natural log of the difference of the vapor concentration and equilibrium vapor concentration (Equation 25). The natural log of a difference of two numbers is generally much smaller than the difference between the same two numbers. If one further compares Formulation 3 (Equation 29) with Formulation 4 (Equation 30) under equilibrium conditions (i.e. $f_e = f_c$), the two formulations look very similar, with the $2/(2-f_c)$ and square root terms in Formulation 4 being the main differences. Nonetheless, as discoursed earlier in Section 2.2, the evaporation and condensation coefficients are not necessarily equal. Different evaporation and condensation coefficients, in turn, offer more flexibility and potentially represent more realistic conditions, assuming the coefficients are known. This will be discussed in detail in Section 4.3.

Analyzing the temperature, soil moisture, and surface relative humidity model outputs in addition to cumulative evaporation and evaporation rate are important to determine if the numerical model accurately captures the physical processes occurring in the soil body. Although all model simulations were analyzed, this section only presents results from Experiment 2. Figure 8 shows simulated and observed temperature profiles at 1 hr, 1 day and 10 days for Experiment 2. The nonlinearity of the experimental and simulated temperature profiles is caused by the nonlinear response of soil thermal properties (i.e. thermal diffusivity, thermal conductivity, volumetric heat capacity) to the redistribution of soil moisture [*Prunty and Horton*, 1994]. As shown in Figure 8, the temperature profiles become more curvilinear as time progresses and the soil dries (the evaporative front moves downward into the soil), an indicator of the transition of evaporation from Stage I to Stages IIa and IIb [*Yiotis et al.*, 2007; *Lehmann and Or*, 2009]. This is a result of a temperature increase immediately below the soil surface due to air having a much lower heat absorbing, or "temperature buffering", capacity than liquid

water. The decrease in surface temperature between Day 1 and Day 10 (Figure 8b and 8c) is the result of slight fluctuations in heater output throughout the entire experiment. Figure 8 shows that the model does a good job of reproducing the temperature profiles, especially after the first day. The difference in simulated temperatures between the four non-equilibrium phase change formulations is less than 0.1°C. As discussed earlier, the isothermal behavior of Formulations 1 and 2 contributed to the overall poor predictions of evaporation. However, as shown in Figure 8, there appears to be appreciable impact of isothermal vs. non-isothermal behavior on temperature.

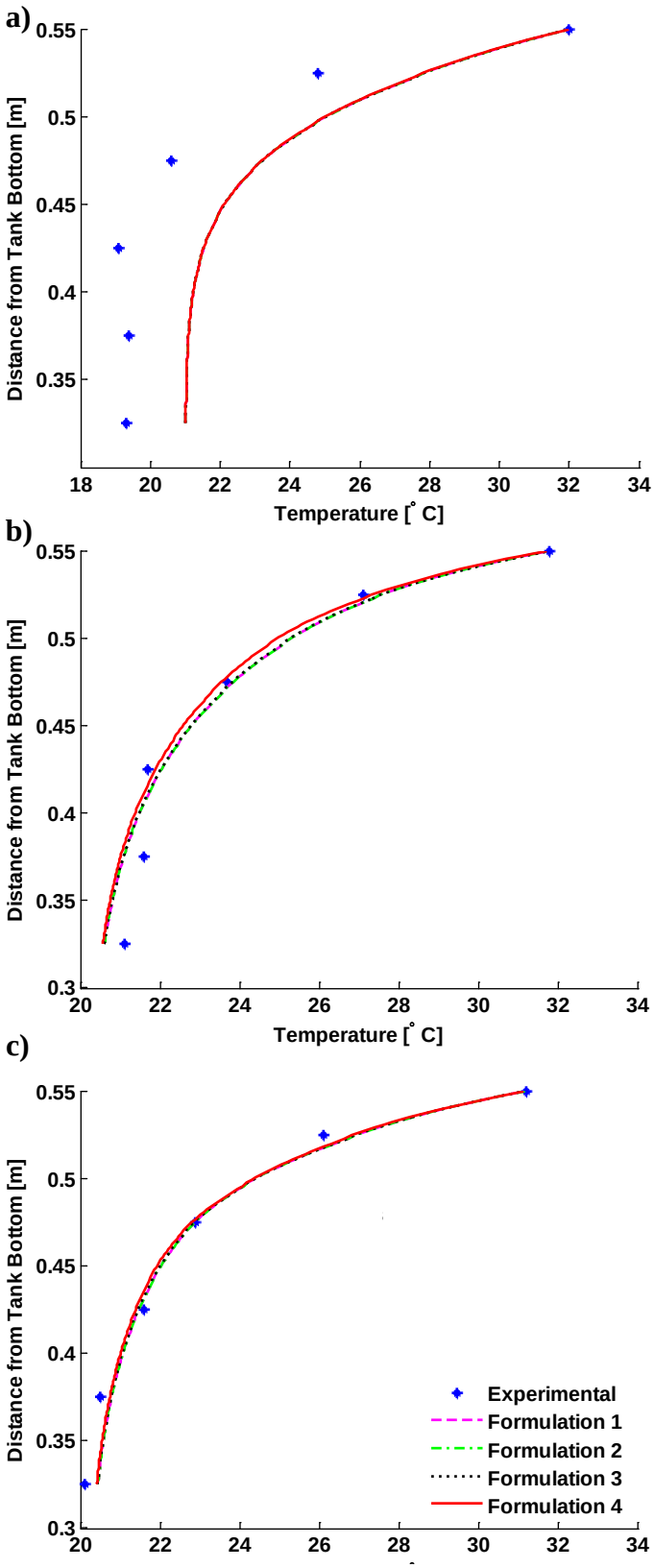

Figure 8. Observed and simulated temperature profiles at time (a) 1 hr, (b) 1 day, and (c) 10 days for Experiment 2.

The time distributed experimental soil moisture at depths of 2.5 cm and 7.5 cm below the soil surface are shown in Figure 9 in conjunction with the simulation results for the four non-equilibrium phase change formulations under the boundary and initial conditions as Experiment 2. Soil moisture at depths greater than 7.5 cm below the soil surface are not shown because the soil at these depths remained fully saturated. The simulated soil moisture curves do not reach the same residual soil moisture value as that experimentally measured (0.005 m^3 m^{-3}). This is due in part to the value of the residual soil moisture in the model being set to a constant value of 0.028 m^3 m^{-3} and then corrected for temperature via *Fayer and Simmons* [1995] (Section 2.2.3). This suggests the need for additional corrections that can effectively take into account temperature effects (e.g. *She and Sleep*, 1998) and changes in soil water retention properties resulting from changes in bulk density with depth (e.g. *Assouline*, 2006). The greatest deviation between observed and simulated soil saturation occurs at a depth of 7.5 cm. A large portion of this discrepancy is the result of Stage I-IIb not being properly captured by the model. In the case of Formulations 1-3, including the vapor enhancement factor would undoubtedly help improve model results as discussed in *Smits et al.* [2012a].

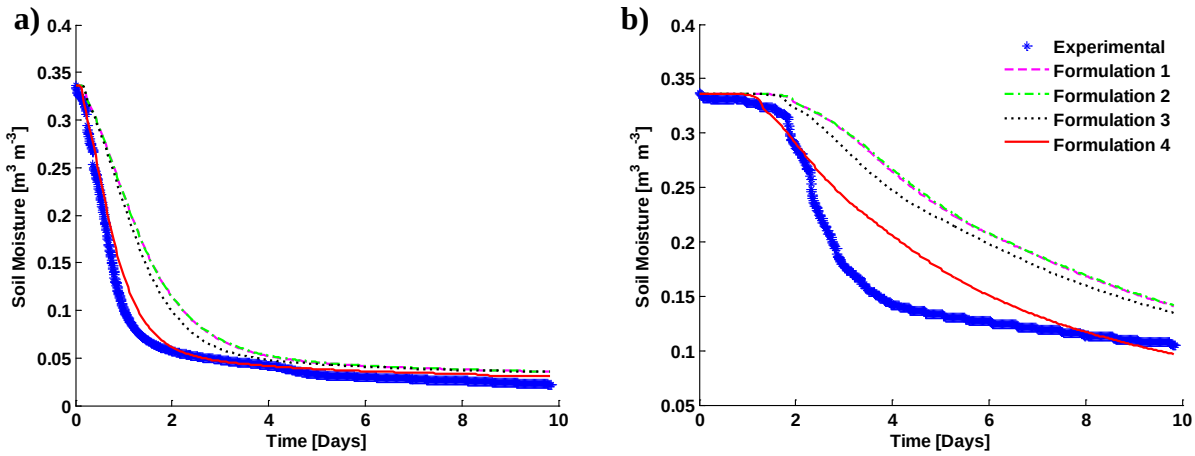

Figure 9. Observed and simulated time-dependent soil moisture distributions at depths of (a) 2.5 and (b) 7.5 cm below the soil surface for Experiment 2.

As in the case of the cumulative evaporation and evaporation rate curves, Formulation 4, followed by Formulation 3, best reproduces the soil saturation at the two depths shown throughout the model simulation (Figure 9). This is the result of Formulation 4 predicting the greatest evaporation rates, thereby allowing the soil to dry out the fastest. The importance of properly simulating Stage IIa and Stage IIb evaporation in terms of both behavior (i.e. shape) and magnitude become especially clear in Figure 9b. The inability of

any formulation to predict the same evaporation rate during this period leads to slower drying and retreat of the drying front. This is seen by the overall overestimation of the soil moisture and the near linear response at later times. Again, this issue could be resolved through the introduction of the vapor enhancement factor which would increase the rate of vapor transport at these depths.

Simulated and observed vapor concentrations at the soil surface are plotted in Figure 10. Experimentally measured relative humidity and temperature were used to calculate the vapor concentration ($c_v = c_{vs}$RH) at the soil surface (Figure 10a) and at a depth of 2.5 cm (Figure 10b). Figure 10a shows that the simulated vapor concentrations are lower than the measured concentrations. This is partly explained by the EHT/RH sensors used to measure the temperature and relative humidity. In an attempt to attain measurements that reflect the soil surface, i.e. gas in the pores directly at the interface, and not the surrounding air, the sensors were placed in good contact with the soil surface. This was done by firmly pressing the sensors into the soil which may therefore better reflect the vapor concentration of the soil pores immediately below the soil surface rather than the vapor concentration at the soil surface itself. This observation is consistent with that of *Davarazani et al.* [2014]. Comparing the formulations themselves, Figure 10a shows that all four formulations produce similar concentration profiles (i.e. the shape is the same). Nonetheless, Formulation 4 predicts vapor concentrations that are lower than Formulations 1-3. This is expected given the use of the condensation coefficient in the modified Hertz-Knudsen equation (Equation 30) which scales the amount of vapor present in the pore space. At a depth of 2.5 cm (Figure 10b), the model is able to better simulate the vapor concentration within the soil profile than at the soil surface. Formulation 4 closely fits the experimentally measured vapor concentration, especially at early times. At later times, the evaporation rate predicted using Formulation 4 is greater than that measured, leading to the observed increase in vapor concentration from approximately Day 5 to the end of the simulation. Formulation 1 underestimates the vapor concentration throughout the entire duration of the experiment simulated because it predicts the lowest rate of phase change as demonstrated by the evaporation curves (Figure 7). Formulations 2-3 similarly under predict the vapor concentration at early times but overestimate the vapor concentration at late times for the same reasoning behind Formulation 4. Despite the differences between the measured and simulated results, the model is capable of capturing the kinetics of vapor

concentration at the soil surface as seen in the general trends of the curves when applying any of the non-equilibrium phase change formulations

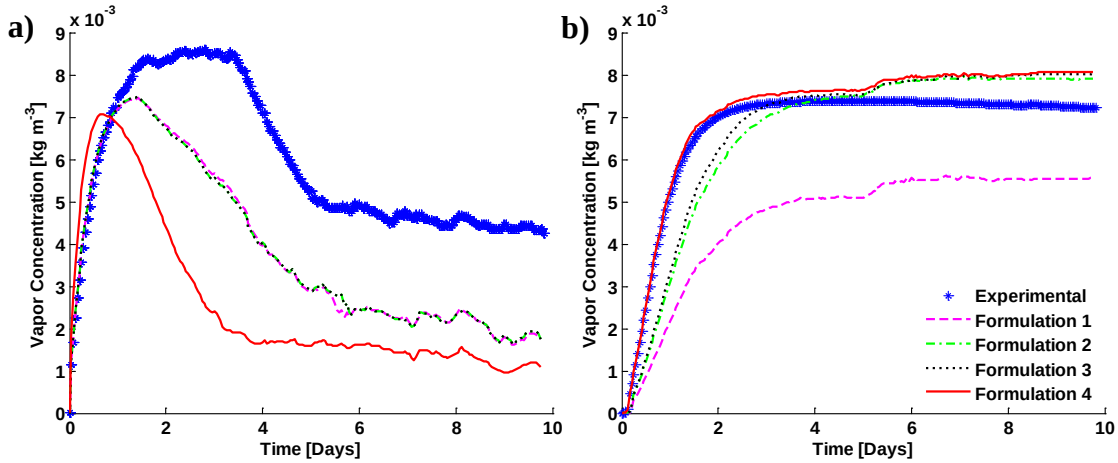

Figure 10. Observed and simulated vapor concentrations at (a) the soil surface and (b) a depth of 2.5 cm for Experiment 2.

5.4.3. Effect of mass transfer coefficients on evaporation

Figure 11 shows the sensitivity of the five mass transfer coefficients (i.e. L_p, t_{eq}, b, f_e, and f_c) used in the four non-equilibrium phase change formulations (Equations 25, 27, 29, 30) compared to Experiment 2. Adjustment of the coefficients affects the magnitude of the phase change rate which in turn alters the slope of cumulative evaporation curve during Stage I and IIb evaporation (Figure 11). This is especially noticeable at initial time periods or during initial evaporation. For example, increasing L_p or b, or decreasing t_{eq} (Formulations 1-3) increases the overall cumulative evaporation. In the case of L_p and b, larger values correspond to a faster rate of phase change (i.e. steeper slope during Stage I and Stage IIb evaporation), approaching equilibrium conditions. Similarly, decreasing t_{eq} towards teq = 0, also leads to equilibrium conditions or instantaneous phase change [*Halder et al.*, 2007].

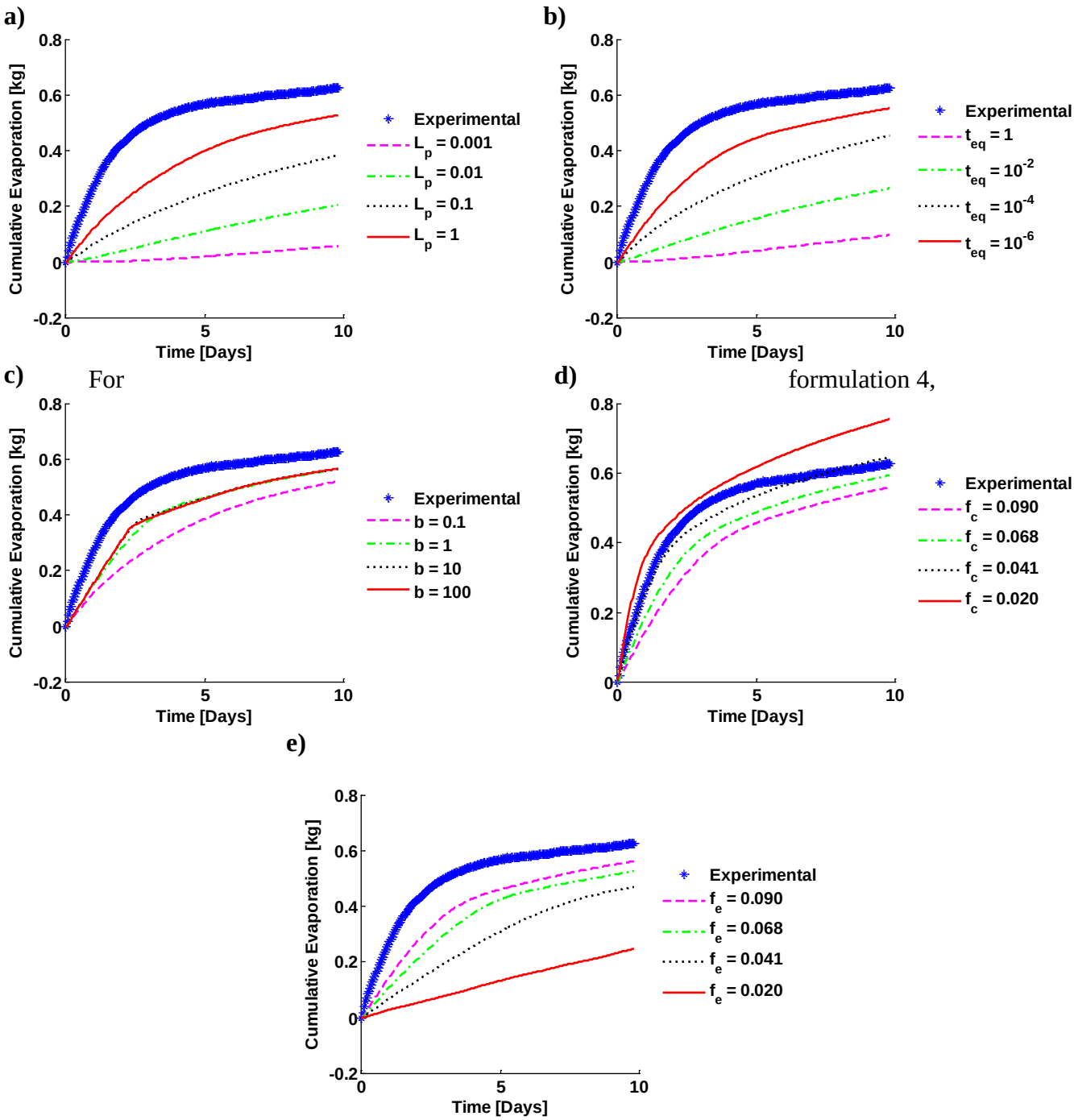

For formulation 4,

Figure 11. Sensitivity analysis of the mass transfer coefficients contained in (a) Formulation 1, (b) Formulation 2, (c) Formulation 3, and (d-e) Formulation 4 as shown for the simulation of Experiment 2. Cumulative evaporation increases by increasing the mass transfer coefficients in Formulations 1-3. Decreasing the value of the condensation coefficient in Formulation 4 similarly increases overall cumulative evaporation. Decreasing the value of the evaporation coefficient in Formulation 4 leads to a decrease in total cumulative evaporation.

decreasing f_c while holding f_e = 0.09, leads to increases in cumulative evaporation (Figure 11d). $f_{c,}$ directly scales the vapor concentration, c_v, in Equation (30); decreasing the value of f_c therefore drives phase change farther away from equilibrium conditions. Figure 11e shows that when f_c is held constant at 0.09 and f_e is decreased, the total cumulative evaporation decreases; c_v is greater than c_{veq} which in turn drives condensation, thereby limiting total cumulative evaporation. Increasing the difference between f_e and f_c drives the system farther away from equilibrium conditions which in turn creates a greater phase change demand (Figure 12). When f_e is greater than f_c, evaporative demand increases because the vapor concentration in the pore space is less than the equilibrium value. Similarly when f_e is less than f_c, the air in pore space is oversaturated with respect to water vapor, causing condensation to occur; this seen by the reduction of cumulative evaporation in Figure 12 in the case where f_e = 0.036 and f_c = 0.072.When $f_e = f_c$ (in this case 0.09), it is the same as assuming that all molecules are volatilized (evaporation) or sorbed (condensation) without any being reflected or replaced. As discussed earlier in Section 2.1, this is an unrealistic assumption [*Marek and Straub*, 2001]. An evaporation coefficient value less than 1 is also expected because water is dipolar and the water surface is therefore given dipolar interactions with other molecules [*Alty*, 1931; *Alty and Nicoll*, 1931; *Tschudin*, 1946; *Marek and Straub*, 2001].

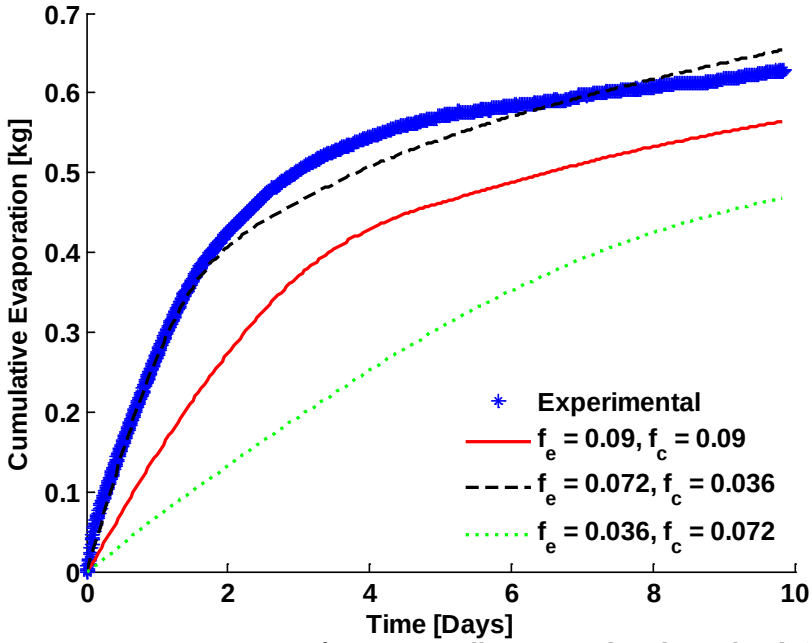

Figure 12. Comparison of experimentally measured and simulated (using Formulation 4) cumulative evaporation for Experiment 2. Equilibrium conditions is simulated by $f_e = f_c$. Evaporation conditions is simulated by $f_e > f_c$. Similarly, condensation conditions is simulated by $f_e < f_c$.

Figure 11 also provides the maximum and minimum bounds in which the fitting coefficients in Formulations 1-4 were found to lie for the experimental conditions of the present study. These extrema represent the limits beyond which any further increase or decrease will lead to no significant improvement in evaporation prediction, i.e. the change in total cumulative evaporation becomes less than 0.0001 kg with any increase or decrease of the transfer coefficients. For example, increasing the value of L_p beyond the maximum value of 1 in Figure 11a does not improve cumulative evaporation estimates. Similarly, decreasing t_{eq} beyond 10^{-6} (Figure 11b) does not improve results. In some cases, increasing or decreasing the mass transfer coefficient beyond its maximum or minimum value can change the shape of the predicted cumulative evaporation. This is best seen by Formulation 3 (Figure 11c); increasing the value of b leads to an abrupt cumulative evaporation curve that does not display a smooth transition from Stage I to IIb.

As mentioned earlier, the final values of L_p, t_{eq}, b, f_e and f_c (Table 6) were determined by minimizing the error (determined using the coefficient of determination) between the experimental and simulated cumulative evaporation curves. This raises the question of how the final values of these coefficients in this study compare to those used in other studies. Table 7 shows that the values of L_p used to produce the cumulative

evaporation curves shown in Figure 6 are approximately 7 to 8 orders of magnitude larger than in *Bénet et al.* [2009]. The discrepancy of the L_p values may be the result of differences in the experimental conditions applied. For example, the work of *Bénet et al.* [2009] was performed under static (no air flow) conditions and isothermal temperature regimes. In similar fashion to L_p, the value of b is 4 to 7 orders of magnitude larger than the values found in *Smits et al.* [2011]. This may be again due to a difference in experimental design and due to the dependency of the *Smits et al.* [2011] model on a vapor enhancement factor. This enhancement factor contributes in terms of increasing vapor diffusion and therefore evaporation, thereby allowing a smaller value of b to be used. Further need for vapor enhancement is discernable with respect to t_{eq} which falls within the range provided by *Halder et al.* [2011] (Table 7) but still significantly underestimates evaporation. This is no longer an issue on the other hand, when Formulation 4 is used. The final values of f_e and f_c used in the present study fall within the ranges identified in *Eames et al.* [1997] and *Marek and Straub* [2001]. The only possible discrepancy that appears in these values (Table 6) is the magnitude of f_e relative to f_c. Some microscopic scale studies have found that f_c is often up to 1.2 times greater than f_e [*Rubel and Gentry,* 1984; *Marek and Straub,* 2001]. One possible explanation for this observation may be that the temperatures and pressures of past studies being below atmospheric conditions and interfacial surface areas on the order of 1 cm^2 [*Bonacci et al.,* 1976; *Marek and Strab,* 2001].

The five coefficients identified in the non-equilibrium phase change formulations (i.e. L_p, t_{eq}, b, f_e, and f_c) are treated as constant parameters as commonly done in many numerical studies simulating evaporation (e.g. *Zhang and Data,* 2004; *Halder et al.,* 2011; *Smits et al.,* 2011; *Smits et al.,* 2012a; *Smits et al.,* 2012b; *Smits et al.,* 2013; *Davarazani et al.,* 2014). Extensive experimental testing in *Bénet and Jouanna* [1982], *Ruiz and Bénet* [2001], *Chammari et al.* [2003], *Bénet et al.* [2009], and *Lozano et al.* [2009] have shown a dependency of L_p on temperature, pressure, and soil moisture. They show that as pressure and temperature increase, L_p similarly increases. L_p was also shown to have a bell-shaped relation to soil moisture [*Ruiz and Bénet;* 2001; *Bénet et al.,* 2009; *Lozano et al.,* 2009]. At high saturations, the liquid water in the pores is in a funicular state and the gas is almost or completely occluded from the system, thereby preventing phase change from occurring. As soil dries and more gas is allowed to invade the pore spaces above the evaporative front (i.e. pendular regime), the liquid-gas interfacial area increases, allowing

for greater rates of phase change. The rate of phase change will increase within the pendular regime until soil saturation reaches 25%-35%. As the soil continues to dry, becoming hygroscopic, the rate of phase change decreases, decreasing the liquid-water interfacial area because there is less and less liquid water retained in the pore spaces.

Ideally, the five coefficients identified in the non-equilibrium phase change formulations would be modeled as functions of the variables discussed above (i.e. T, p, θ_w). This would mean constantly changing the values of the coefficients in response to changes in soil moisture redistribution during Stage I, IIa, and IIb evaporation. Doing this, however, would require prior knowledge of the $\dot{m}$–θ_w relationship at various temperatures and pressures; a valuable area of future research on the subject of non-equilibrium phase change in porous media. The $\dot{m}$–θ_w relationship would need to be determined by generating precision experimental datasets modeled after those of *Lozano et al.* [2008], *Bénet et al.* [2009] and *Lozano et al.* [2009]. These datasets would need to be produced under carefully controlled temperature, total gas pressure, vapor concentrations (i.e. relative humidity), soil moisture, and evaporation rates. This data would in turn be used to inverse model the phase change coefficients L_p, t_{eq}, b, f_e, and f_c using Equations 25, 27, 29, and 30.

5.4.4. Significance of non-equilibrium conditions

As discussed in Section 1, the Damkohler number (Equation 1) can be used to determine how close a system is to equilibrium conditions. A value of Da >> 1 signifies that phase change is instantaneous or the liquid water and water vapor phases are in equilibrium with each other. Figure 13 displays a local Da number at a depth of 2.5 cm and 7.5 for Experiments 1-4 as a function of time using experimental data. A depth of 2.5 cm (Figure 13a) was chosen because it allows analysis over a full range of soil moisture and represents near surface conditions. Similarly, a depth of 7.5 cm allows conditions close to the evaporation front to be analyzed without the effects of atmospheric demand dominating. A characteristic length, l, of $5\text{x}10^{-4}$ m (the average pore length of #30/40 Accusand) and a reference vapor diffusivity of 10^{-6} m^2 s^{-1} were selected for the calculations. The effective mass transfer coefficient was determined from the modified Hertz-Knudsen Formulation (Equation 30):

$$k_{eff} = \frac{2\theta_w f_c}{(2 - f_c)} \sqrt{\frac{RT}{2\pi M_w A}} \tag{32}$$

in similar fashion to the analysis performed in *Smits et al.* [2012b]. As seen in Figure 13, the values of Da do not exceed 1 under any of the four experimental boundary and initial conditions applied in the present study at either a depth of 2.5 or 7.5 cm. This signifies that experimentally, the system is never close to equilibrium with respect to vapor concentrations. This provides a basis of comparison for the type of vapor concentration conditions that should be expected; i.e. the model should not predict equilibrium conditions.

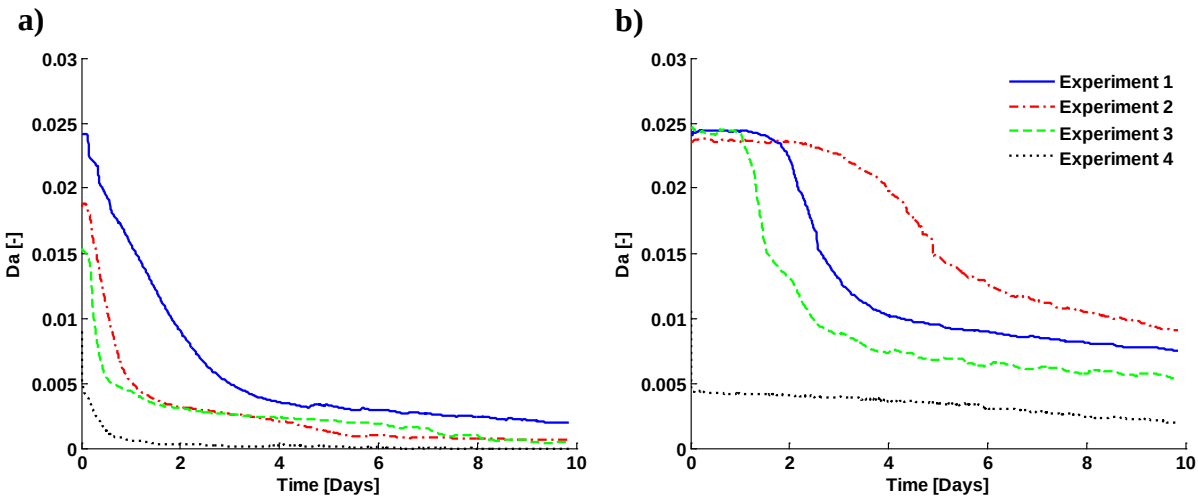

Figure 13. Damkohler number (Da) calculated plotted as a function of time for the four experimental conditions performed for the present study using experimental data for the effective mass transfer coefficient in Formulation 4 at a depth of (a) 2.5 cm and (b) 7.5 cm.

Figure 14 presents the simulated vapor concentration profiles normalized to the calculated equilibrium vapor concentration (Equation 19) for Experiments 1-4 at the times of 1 hour, 1 day, and 5 days. A ratio of 1 would signify that the vapor concentration in the pore space is equal to equilibrium vapor concentration whereas a value of zero indicates no water vapor is present (i.e. the pore space is fully saturated with liquid water). The vapor concentration-equilibrium vapor concentration ratio is not equal to zero at the soil surface due to the boundary conditions applied, see Section 2.3. As Figure 14 shows, the vapor concentration in the soil is never equal to the equilibrium vapor concentration, supporting the Damkohler number analysis above. This suggests that the assumption of equilibrium based phase change may not be the most representative approach to apply when modeling evaporation in porous media. The continuous downward movement of the evaporation

front in Experiments 1-3 causes the location in the soil tank with the highest vapor concentration to similarly retreat downward. This phenomenon is not observed in Experiment 4 (Figure 14d) because the water table, and therefore evaporation front, were held constant. The overall increase in the maximum vapor concentration ratios observed in Figures 14a-c over time are also the result of evaporation becoming vapor diffusion limited, i.e. Stage IIa and IIb. Concentrations are able to build up because vapor diffusion coefficient in the porous medium is scaled by the tortuosity of the sand (Section 2.2.2).

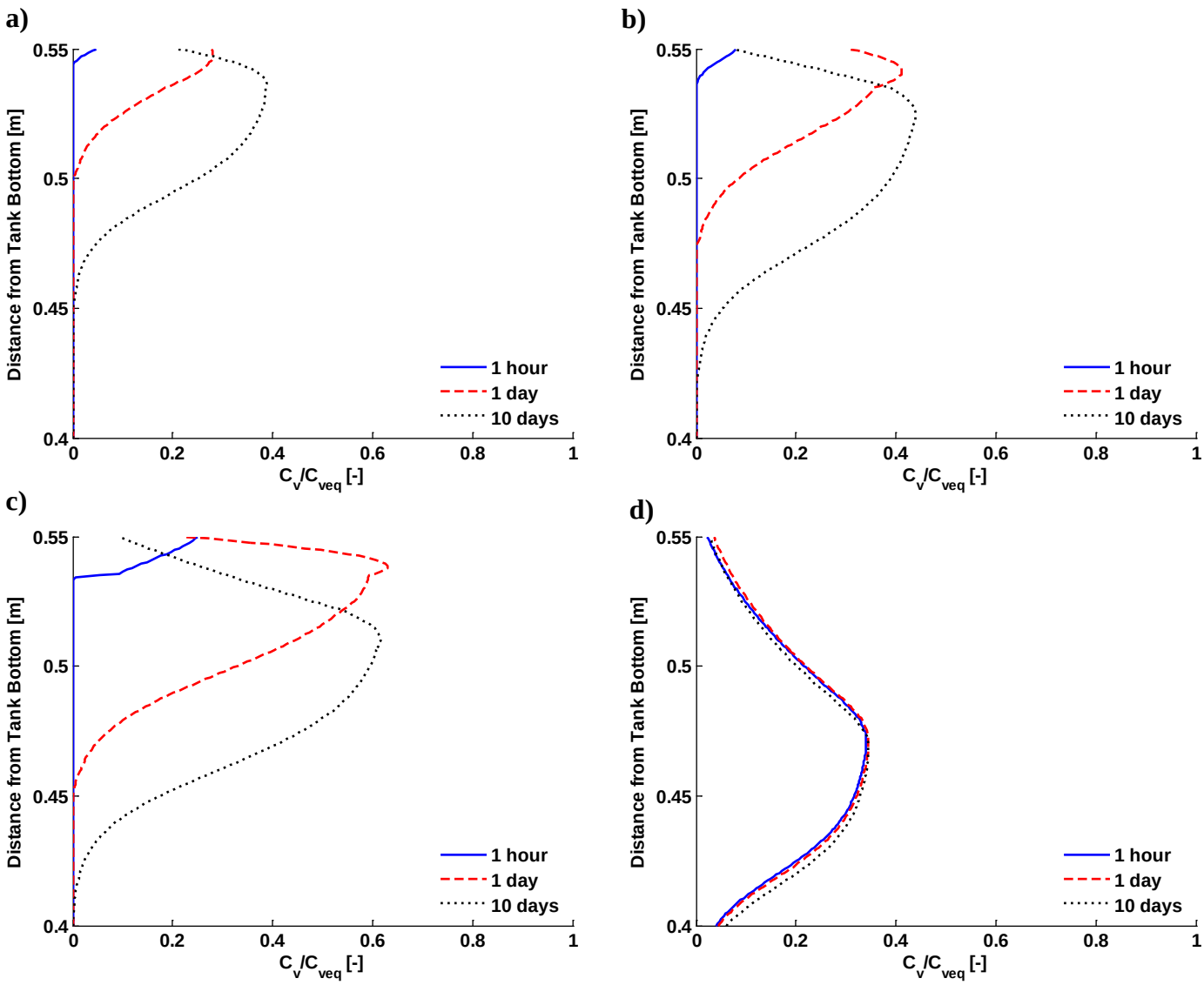

Figure 14. Vapor concentration-equilibrium vapor concentration ratio profiles plotted as a function of time for (a) Experiment 1, (b) Experiment 2, (c) Experiment 3, and (d) Experiment 4.

Figure 15 shows the simulated vapor concentrations for the four phase change formulations under the conditions of Experiment 2. Figure 15 demonstrates that Formulations 1-3 predict lower vapor concentrations than Formulation 4, often by a factor of 2. This is due to Formulation 4 being able to simulate larger rates of phase change than the other non-equilibrium phase change formulations as shown earlier in the cumulative evaporation and evaporation curves (Figure 7). The vapor concentrations profiles of Formulations 1-3 could have been increased to those of Formulation 4 through the use of a vapor enhancement factor. Again, curve fitting was not the objective of this study; addition of the vapor enhancement factor would have actually helped to hide the overall merits of using Formulation 4.

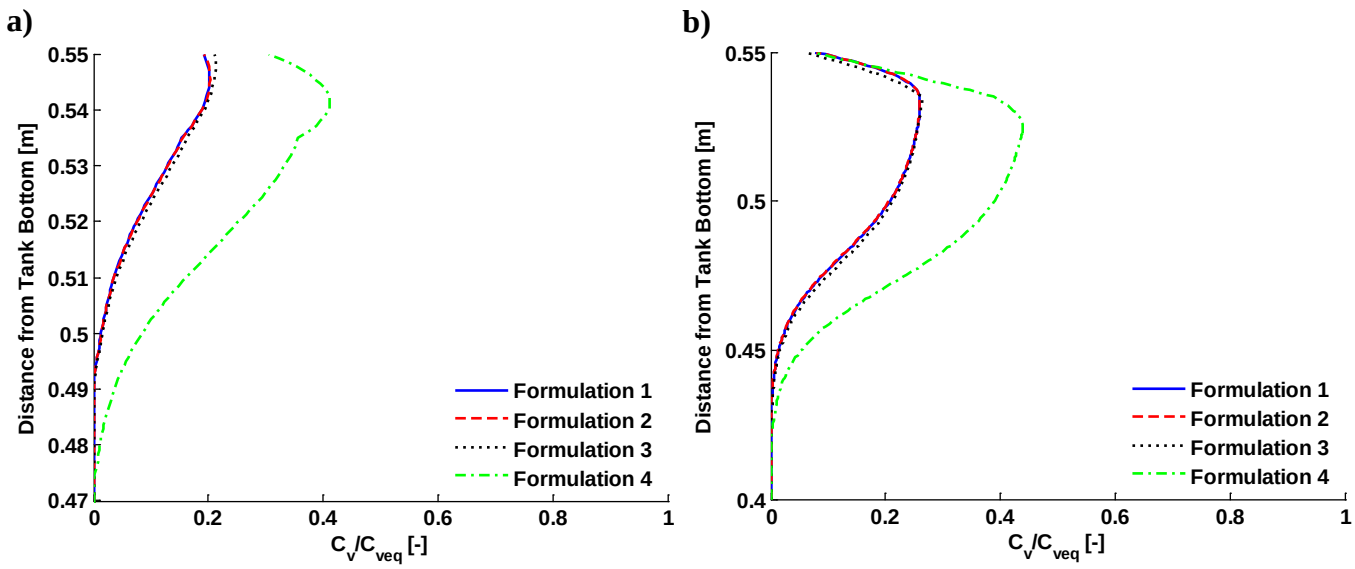

Figure 15. Vapor concentration-equilibrium vapor concentration ratio for the four non-equilibrium phase change formulations tested under the initial and boundary conditions of Experiment 2 at (a) 1 day and (b) 10 days.

5. **5. CONCLUSIONS**

The purpose of this work was to test four non-equilibrium phase change formulations (three existing in the literature and one proposed by the authors in the present study) under a variety of carefully controlled boundary (soil surface temperature, wind velocity) and initial conditions (i.e. depth to water table). This was accomplished through the use of a heat and mass transfer model that incorporates non-equilibrium phase change. Modeling results for each non-equilibrium phase change formulation were compared with precision laboratory data generated under the same conditions in a unique soil tank outfitted with a sensor network capable of measuring soil and air temperature, soil moisture, relative humidity, wind velocity, and weight loss. All numerical modeling was performed without the use of an enhancement factor, a commonly used empirical fitting parameter, in order to provide a better basis of comparison between formulations. Results showed that the newly proposed REV scale Hertz-Knudsen non-equilibrium phase change formulation is able to best capture evaporation and associated phenomena, i.e. soil temperature, soil moisture, vapor densities under most conditions.

Accounting for phase change is applicable to current hydrologic and environmental problems including land-atmospheric modeling and understanding contaminant volatilization and transport in the shallow subsurface. The comparisons and analyses of the non-equilibrium models in this study show the importance of taking non-equilibrium phase change into account. Non-equilibrium phase change better captures and more realistically describes the different processes and behavioral aspects associated with evaporation and condensation phenomena. Furthermore, comparisons of the non-equilibrium phase change formulations show the importance of making the proper selection to best reproduce observed cumulative evaporation and evaporation rate, soil moisture distributions, etc. under various environmental conditions. Choosing the proper phase change formulation allows commonly used empirical fitting parameters to be neglected, greatly simplifying model calibration and allowing evaporation to be simulated in terms of known or understood processes. Stage IIa evaporation, the most difficult and transitory evaporation stage, is still not fully captured correctly using the non-equilibrium phase change approach, suggesting further fundamental research on understanding the nature of

evaporation and condensation in pore-space and theoretically representing these processes at macroscopic-scale numerical models of heat and mass transfer in porous media.

5.6. REFERENCES

Alty, T. (1931), The reflection of vapour molecules at a liquid surface, *Proc. Royal Soc. London*, 131, 554-564.

Alty, T. and F.H. Nicoll (1931), The interchange of molecules between a liquid and its vapor, *Can. J. Res.*, 4, 547-558.

Armstrong, J.E., E.O. Frind, and R.D. McClellan (1994), Nonequilibrium mass transfer between the vapor, aqueous, and soil-phases in unsaturated soils during vapor extraction, *Water Resour. Res.*, 30, 355-368.

Assouline, S. (2006), Modeling the relationship between soil bulk density and the water retention curve, *Vadose Zone J*., 5, 554–563.

Assouline, S., K. Narkis, S. W. Tyler, I. Lunati, M. B. Parlange, and J. S. Selker (2010), On the diurnal soil water content dynamics during evaporation using dielectric methods, *Vadose Zone J*., 9, 709–718.

Assouline, S., S.W. Tyler, J.S. Selker, I. Lunati, C.W. Higgins, and M.B. Parlangee (2013), Evaporation from a shallow water table: Diurnal dynamics of water and heat at the surface of drying sand, *Water Resour. Res*., 49, 4022-4034.

Bacon, A.A. (1905), The equilibrium pressure of a vapor at a curved surface, *Phys. Rev.*, *20*, 1-9.

Bahr, J.M., and J. Rubin (1987), Direct comparison of kinetic and local equilibrium formulations for solute transport affected by surface reactions, *Water Resour. Res.*, 23(3),438-452.

Bear, J. (1972), *Dynamics of Fluids in Porous Media*. Dover, Mineola, N. Y.

Bear, J., J. Bensabat, and A. Nir (1991), Heat and mass transfer in unsaturated porous-media at a hot boundary. 1. One-dimensional analytical model, *Transp. Porous Media*, 6, 281–298.

Bénet, J., and P. Jouanna (1982), Phenomenological relation of phase change of water in a porous medium: experimental verification and measurement of the phenomenological coefficient, *Int. J. Heat Mass Transf*., 25, 1747–1754.

Bénet, J., A.L. Lozano, F. Cherblanc, and B. Cousin (2009), Phase change of water in a hygroscopic porous medium. Phenomenological relation and experimental analysis for water in soil, *J. Non-Equil. Thermodyn*., 34, 133-153.

Berge, H.F.M. (1990), Heat Transfer in Bare Topsoil and the Lower Atmosphere, *Cent. for Agric. Publ. and Doc*., Wageningen, Netherlands.

Bird, R. B., W. E. Stewart, and E. N. Lightfoot (2002), Transport Phenomena, 2nd ed., John Wiley, New York.

Bittelli, M., F. Ventura, G. S. Campbell, R. L. Snyder, F. Gallegati, and P.R. Pisa (2008), Coupling of heat, water vapor, and liquid water fluxes to compute evaporation in bare soils, *J. Hydrol*., 362, 191–205.

Bixler, N.E. (1985), NORIA: A finite element computer program for analyzing water, vapor, air, and energy transport in porous media, Sandia Natl. Lab., Albuquerque, N. M.

Blasius, H. (1908), Grenzschichten in Flüssigkeiten mit kleiner Reibung, *Z. Math Phys.*, 56, 1-37.

Bonacci, J.C., A.L. Myers, G. Nongbri, and L.C. Eagleton (1976), The evaporation and condensation coefficient of water, ice and carbon tetrachloride, *Chem. Eng. Sci.*, 31, 609-617.

Bond, M. (2000), Non-equilibrium evaporation and condensation modeled with irreversible thermodynamics, kinetic theory, and statistical rate theory, Thesis B. Eng., University of Victoria. 1-194.

Bond, M. and H. Struchtrup (2004), Mean evaporation and condensation coefficients based on energy dependent condensation probability, *Phys. Rev. E*., 70, 1-21.

Burrows, G. (1957), Evaporation at low pressure, *J. App. Chem*., 7, 375-384.

Campbell, G.S. 1985. Soil Physics with BASIC. Elsevier, New York.

Campbell, G. S., J. D. Jungbauer, W. R. Bidlake, and R. D. Hungerford (1994), Predicting the effect of temperature on soil thermal-conductivity, *Soil Sci*., 158, 307–313.

Cass, A., G. S. Campbell, and T. L. Jones (1984), Enhancement of thermal water-vapor diffusion in soil, *Soil Sci. Soc. Am. J*., 48, 25–32.

Chammari, A., B. Naon, F. Cherblanc, and J. Bénet (2003), Transfert d'eau en sol aride avec changement de phase – Water transport with phase change at low water content, *Comptes Rendus de Mécanique*, 331, 759-765.

Chammari, A., B. Naon, F. Cherblanc, B. Cousin, and J. Bénet (2008), Interpreting the drying kinetics of a soil using a macroscopic thermodynamic non-equilibrium of water between the liquid and vapour phase, *Dry.Technol*., 26, 836–843.

Childs, S. W., and C. Malstaff (1982), Heat and mass transfer in unsaturated porous media, *Final Rep. PNL-4036*. Batelle Pacific Northwest Lab. Richland, Wash.

Cho, H.J., and P.R. Jaffe (1990), The volatilization of organic compounds in unsaturated porous media during infiltration, *J. Cont. Hydrol.*, 6, 387-410.

Cobos, D. and C. Campbell (2007), Correcting temperature sensitivity of ECH2O soil moisture sensors. *Application Note, Decagon Devices, Pullman, WA*.

Culligan, K. A., D. Wildenschild, B. S. B. Christensen, W. G. Gray, and A. F. B. Tompson (2004), Interfacial area measurements for unsaturated flow through a porous medium, *Water Resour. Res. 40,* W12413.

Davarzani, H., K. Smits, R. M. Tolene, and T. Illangasekare (2014), Study of the effect of wind speed on evaporation from soil through integrated modeling of the atmospheric boundary layer and shallow subsurface, Water Resour. Res., 50, doi:10.1002/2013WR013952.

Dhall, A., A. Halder, and A.K. Datta (2012), Multiphase and multicomponent transport with phase change during meat cooking, *J. Food Eng*., 113, 299-309.

Eames, I. (1997), The evaporation coefficient of water: a review, *Int. J. Heat Mass Transf*., 42, 2963–2973.

Fang, G. and C.A. Ward (1999), Examination of the statistical rate theory expression for liquid evaporation rates, *Phys. Rev. E.*, 59, 441-453.

Farnworth, B. (1986), A numerical model of the combined diffusion of heat and water vapor through clothing, *Textile Res. J.*, 56, 653-665.

Fayer, M. J., and C.S. Simmons (1995), Modified soil water retention functions for all matric suctions, *Water Resour. Res*., 31, 1233–1238.

Fereres, E., D.A. Goldhamer, and L.R. Parsons (2003), Irrigation water management of horticultural crops, *Hort. Sci.*, 38, 1036-1042.

Fisher, R.A. (1923), Some factors affecting the evaporation of water from soil, *J. Agron. Sci*., 13, 121-143.

Geller, J.T., and J.R. Hunt (1993), Mass transfer from nonaqueous phase organic liquids in water-saturated porous media, *Water Resour. Res.*, 29(4), 833-845, doi:10.1029/92WR02581.

Gierke, J.S., N.J. Hutzler, and D.B. McKenzie (1992), Vapor transport in columns of unsaturated soil and implications for vapor extraction, *Water Resour. Res.*, 28, 323-335.

Grant, S.A., and A. Salehzadeh (1996), Calculation of temperature effects on wetting coefficients of porous solids and their capillary pressure functions, *Water Resour. Res.*, *32*(2), 261-270.

Grifoll, J., J.M. Gasto, and Y. Cohen (2005), Non-isothermal soil water transport and evaporation, *Advances in Water Res*., 28, 1254-1266.

Haghighi, E., and D. Or (2013), Evaporation from porous surfaces into turbulent airflows: Coupling eddy characteristics with pore scale vapor diffusion, *Water Resour. Res.*, 49, 1-11.

Haghighi, E., E. Shahraeeni, P. Lehmann, and D. Or (2013), Evaporation rates across a convective air boundary layer are dominated by diffusion, *Water Resour. Res*., 49, 1602–1610.

Halder, A. A. Dhall, and A.K. Datta (2011), Modeling transport in porous media with phase change: Applications to food processing, *J. Heat Transf*., 133, 031010-1.

Hertz, H. (1882), Uber die verdunstung der flüssigkeiten insbescondere des quecksilbers, im lufteeren raume, *Ann. Phys. Und Chemie*, 17, 177-200.

Hide, J.C. (1954), Observations on factors influencing the evaporation of soil moisture, *Soil Sci. Soc. Amer. Proc.*, 18, 234-239.

Hillel, D. (1980), *Fundamental of Soil Physics*, Academic, San Diego, Calif.

Ho, C.K., S.W. Liu, and K.S. Udell (1994), Propagation of evaporation and condensation fronts during multicomponent soil vapor extraction, *J. Contam. Hydro.*, 16, 381-401.

Ishihara, Y., E. Shumojima, and H. Harada (1992), Water vapor transfer beneath bare soil where evaporation is influenced by a turbulent surface wind, *J. Hydrol.*, 131, 63-104.

Katata, G., H. Nagai, H. Ueda, N. Agam, and T.J. Sauer (2008), Development of a land surface model including evaporation and adsorption processes in the soil for the land-air exchange in arid regions, *J. Hydrometeorol.*, *8*, 1307-1324.

Knudsen, M. (1915), Die maximale verdampfungsgeschwindigkeit des quecksilbers, *Ann. Phys. Und Chemie*., 47, 697-708.

Kottek, M., J. Grieser, C. Beck, B. Rudolf, and F. Rubel (2006), World map of the Koppen-Geiger climate classification updated, *Meteorologische Zeitschrift*., 15, 259-264.

Kryukov, A.P. and V.Yu. Levashov (2011), About evaporation–condensation coefficients on the vapor–liquid interface of high thermal conductivity matters, *Int. J. Heat Mass Transf*., 54, 2042-3048.

Labunstov, D.A. (1967), An analysis of evaporation and condensation processes, *Tepiofiz. Vysok. Temp*., 5, 647-653.

Latham, J., R. Cumani, I. Rosati, and M. Bloise (2014), Global land cover SHARE (GLC-SHARE) database beta-release version 1.0-2014, Food and Agriculture Organization of the United Nations (FAO).

Le, C., N. Ly, and R. Postle (1995), Heat and mass transfer in the condensing flow of steam through an absorbing fibrous medium, *Int. J. of Heat Mass Transf.*, 38, 81 – 89.

Lehmann, P. and D. Or (2009), Preferential evaporation and capillary coupling in porous media with textural contrasts, *Phys. Rev. E*, 80, 046318.

Lehmann, P., S. Assouline, and D. Or (2008), Characteristic lengths affecting evaporative drying of porous media, *Phys. Rev. E.*, 77, 56309.

Lemon, E.R. (1956), The potentialities for decreasing soil moisture evaporation loss. *Soil Sci. Soc. Am. J.*, 20, 120-125.

Li, Y., and Q. Zhu (2003), Simultaneous heat and moisture transfer with moisture sorption, condensation, and capillary liquid diffusion in porous textiles, *Textile Res. J*., 73, 515-524.

Lichtner, P.C. (1998), Modeling reactive flow and transport in natural systems, in *Proceedings of the Rome Seminar on Environmental Geochemistry,* edited by L. Martini and G. Ottonello, pp. 5-72, Dip. Di Sci. dell Terra, Univ. di Genova, Genoa, Italy.

Lide, D. R. (Ed.) (2001), *Handbook of Chemistry and Physics*, CRC Press, Boca Raton, Fla.

Lozano, A., F. Cherblanc, B. Cousinand, and J. Bénet (2008), Experimental study and modeling of the water phase change kinetics in soils, *Eur. J. Soil Sci*., 59, 939–949.

Lozano, A.L., F. Cherblanc, and J.C. Bénet (2009), Water evaporation versus condensation in a hygroscopic soil, *Transp. Porous Med*., 80, 209-222.

Maa, J.R. (1967), Evaporation coefficient of liquids, *Indust. Eng. Chem. Fund*., 6, 104-116.

Marek, R., and J. Straub (2001), Analysis of the evaporation coefficient and the condensation coefficient of water, *Int. J. Heat Mass Transf.*, 44, 39–53.

Metzger, T., and E. Tsotsas (2005), Influence of pore size distribution on drying kinetics: A simple capillary model, Drying Technol., 23, 1797–1809,

Millington, R. J., and J. M. Quirk (1961), Permeability of porous solids, *Trans. Faraday Soc*., 57, 1200–1207.

Minkowycz, W.J., A. Haji-Sheikh, and K. Vafai (1999), On departure from local thermal equilibrium in porous media due to a rapidly changing heat source: the Sparrow number, *Int. J. Heat Mass Transf.*, 42, 3373-3385.

Moldrup, P., T. Olesen, D. E. Rolston, and T. Yamaguchi (1997), Modeling diffusion and reaction in soils: VII. Predicting gas and ion diffusivity in undisturbed and sieved soils, *Soil Sci*., 162, 632–640.

Monteith, J.L. and M.H. Unsworth (1990), *Principles of Environmental Physics*, Routledge Chapman and Hall, New York.

Mosthaf, K., R. Helmig, and D. Or (2014), Modeling and analysis of evaporation processes from porous media on the REV scale, *Water Resour. Res.*, 50, doi:10.1002/2013WR014442.

Mualem, Y. (1976), A new model for predicting the hydraulic conductivity of unsaturated porous media, *Water Resour. Res., 12*, 513–522.

Niessner, J., and S.M. Hassanizadeh (2009), Modeling kinetic interphase mass transfer for two-phase flow in porous media including fluid-fluid interfacial area, *Trans. Porous Media*, 80, 329-344, doi:10.1007/s11242-009-9358-5

Novak, M.D. (2010), Dynamics of near-surface evaporation zone and corresponding effects on the surface energy balance of a drying bare soil, *Agr. and Forest Meteor*., 150, 135-1365.

Ouedraogo, F., F. Cherblanc, B. Naon, and J.C. Bénet (2013), Water transfer in soil at low water content. Is the local equilibrium assumption still appropriate?, *J. Hydrol.*, 492, 117-127.

Parker, J. C., Lenhard, R. J. and T. Kuppusamy (1987), A parametric model for constitutive properties governing multiphase flow in porous media, *Water Resour. Res.*, 23, 618-624.

Parlange, M.B., A.T. Cahill, D.R. Nielsen, J.W. Hopmans, and O. Wendroth (1998), Review of heat and water movement in field soils, *Soil Tillage Res.*, 47, 5-10.

Penman, H.L. (1940), Gas and vapor movements in soil: I. The diffusion of vapors through porous solids, *J. Agric. Sci*., 30, 437-462.

Penman, H.L. (1948), Natural evaporation from open water, bare soil and grass, *Proc. Royal Soc. London*, 193, 120-145.

Philip, J. R., and D. A. de Vries (1957), Moisture movement in porous materials under temperature gradients, *Eos Trans. AGU*. 38, 222–232.

Prat, M. (2002), Recent advances in pore-scale models for drying of porous media, *Chem. Eng. J.*, 86, 153-164.

Prunty, L., and R. Horton (1994), Steady-state temperature distribution in nonisothermal unsaturated closed soil cells, *Soil Sci. Soc. Am. J*., 58, 1358–1363.

Rose, J.W. (1998) Interphase matter transfer, the condensation coefficient and dropwise condensation, *Proc. of 11th IHTC*., 1, 89-104.

Rubel, G.O., J.W. Gentry (1984), Measurement of the kinetics of solution droplets in the presence of adsorbed monolayers: determination of water accommodation coefficients, *J. Phys. Chem.*, 14, 3142-3148.

Ruiz, T., and J. C. Bénet (2001), Phase change in a heterogeneous medium: Comparison between the vaporization of water and heptanes in an unsaturated soil at two temperatures, *Transp. Porous Media*, 44, 337–353.

Sakai, M., N. Toride, and J. Simůnek, (2009), Water and vapor movement with condensation and evaporation in a sandy column, *Soil Sci. Soc. Am. J*., 73, 707–717.

Sakaki, T., and T.H. Illangasekare (2007), Comparison of height-averaged and point-measured capillary pressure-saturation relations for sands using a modified Tempe cell, *Water Resour. Res*., 43, W12502.

Sakaki, T., A. Limsuwat, K.M. Smits, and T.H. Illangasekare (2008), Empirical two-point -mixing model for calibrating the ECH2O EC-5 soil moisture sensor in sands, Water Resour. Res. 44:W00D08.

Scanlon, B.R., R.C. Reedy, K.E. Keese, and S.F. Dwyer (2005), Evaluation of evapotranspirative covers for waste containment in arid and semiarid regions in the southwestern USA, *Vadose Zone J*., 4, 55–71.

Scarpa. F. and G. Milano (2002), The role of adsorption and phase change phenomena in the thermophysical characterization of moist porous materials, *Int. J. Thermophys*., 23, 1033-1046.

Schrage. R.W. (1953), *A Theoretical Study of Interphase Mass Transfer*, Columbia University Press, New York.

Schünder, E.U. (2004), Drying of porous material during the constant and the falling rate period: A critical review of existing hypotheses, *Drying Technol*., 22, 1517-1532.

Shahraeeni, E., and D. Or (2010), Pore-scale analysis of evaporation and condensation dynamics in porous media, *Langmuir*, *26*(17), 13, 924-13,936.

Shahraeeni, E., P. Lehmann, and D. Or (2012), Coupling of evaporative fluxes from drying porous surfaces with air boundary layer-Characteristics of evaporation from discrete pores, *Water Resour. Res*., 48, W09525. doi:10.1029/2012WR011857.

She, H. Y., and B. E. Sleep (1998), Effect of temperature on capillary pressure-saturation relationships for air-water and perchloroethylene-water systems, *Water Resour. Res*., 34, 2587–2597.

Shukla, J., and Y. Mintz (1982), Influence of land–surface evapotranspiration on the earth's climate. *Science*, 215, 1498–1501.

Smits, K.M., T. Sakaki, A. Limsuwat, and T.H. Illangasekare (2010), Thermal conductivity of sands under varying moisture and porosity in drainage-wetting cycles, *Vadose Zone J*., 9,172-180.

Smits, K.M., A. Cihan, T. Sakaki, and T.H. Illangasekare (2011), Evaporation from soils under thermal boundary conditions: Experimental and modeling investigation to compare equilibrium- and nonequilibrium-based approaches, *Water Resour. Res*., 47, W05540.

Smits, K. M., V. V. Ngo, A. Cihan, T. Sakaki, and T. H. Illangasekare (2012a), An evaluation of models of bare soil evaporation formulated with different land surface boundary conditions and assumptions. Water Resour. Res. 48:W12526, doi:10.1029/2012WR012113.

Smits, K.M., A. Cihan, V.Ngo, and T.H. Illangasekare (2012b), Reply to comment by Michael D. Novak on ''Evaporation from soils under thermal boundary conditions: Experimental and modeling investigation to compare equilibrium and nonequilibrium based approaches.", *Water Resour. Res*., doi:10.1029/2011WR011609.

Smits, K.M., A. Cihan, T. Sakaki, S.E. Howington, J.F. Peters, and T. H. Illangasekare (2013), Experimental and modeling investigation of soil moisture and thermal

behavior in the vicinity of buried objects, *IEEE Trans. in Geosci. Remote Sens*., 10.1109/TGRS.2012.2214485

Souto, E.B. and R.H. Müller (2008), Cosmetic features and applications of lipid nanoparticles (SLN®, NLC®), *Int. J. Cosmetic Sci*., 30, 157-165.

Thomson, W. (1870), On the equilibrium of vapour at a curved surface of liquid, *Proc. R. Soc. Edinburgh* **7**:63−68.

Tokunaga, T. K. (2009), Hydraulic properties of adsorbed water films in unsaturated porous media, Water Resour. Res., 45, W06415.

Tschudin, K. (1946), Die verdampfungsgeschwindikeit von eis, *Helvetica Physica Acta*, 19, 91-102.

Tsuruta, T. H. Tanaka., and T. Masuoka (1999), Condensation/evaporation coefficient and velocity distributions at the liquid-vapor interface, *Int. J. Heat Mass Transf*., 42, 4107-4116.

van Bavel, C.H.M. and D.I. Hillel (1976), Calculating potential and actual evaporation from a bare soil surface by simulation of concurrent flow of water and heat, *Agric. Meteorol.*, 17, 453-476.

van de Griend, A.A., and M. Owe (1994), Bare soil surface resistance to evaporation by vapor diffusion under semiarid conditions, *Water Resour. Res*., 30, 181-188.

van Genuchten, M. T. (1980), A closed-form equation for predicting the hydraulic conductivity of unsaturated soils, *Soil Sci. Soc. Am. J.*, 44, 892–898.

Walker, J., and P. R. Rowntree (1977), The effect of soil moisture on circulation and rainfall in a tropical model, *Quart. J. Roy. Meteor.Soc.,* 103, 29–46

Ward, C.A., and G. Fang (1999), Temperature measured close to the interface of an evaporating liquid, *Phys. Rev*., 59, 417-428.

Ward, C. A. and D. Stanga (2001), Interfacial conditions during evaporation or condensation of water, *Phys. Rev. E.*, 64, 051509.

Waugh, W.J., M.E. Thiede, D.J. Bates, L.L. Caldwell, G.W. Gee and C.J. Kemp (1994), Plant cover and water balance in gravel admixtures at an arid waste-burial site, *J. Enivron. Qual*., 23, 676-685.

Whitaker, S. (1977), Simultaneous heat, mass, and momentum transfer in porous media. A theory of drying, *Adv. Heat Transf*., 13, 119-203.

Wissing, S.A. and R.H. Müller (2003), Cosmetic applications for solid lipid nanoparticles (SLN), *Int J. Pharm*., 254, 65-68.

Yiotis, A. G., I. N. Tsimpanogiannis, A. K. Stubos, and Y. C. Yortsos (2007), Coupling between external and internal mass transfer during drying of a porous medium, *Water Resour. Res.*, 43, W06403

Youd, T.L. (1973), Factors controlling maximum and minimum densities of sands, p. 98–112, *In*, E.T. Selig and R.S. Ladd (eds.) Evaluation of Relative Density and its Role in Geotechnical Projects Involving Cohesionless Soils, *Am. Soc. for Testing and Mater. Int*., West Consho-hocken, Pa.

Ytrehus, T. and S. Østmo (1996), Theory approach to interphase processes, *Int. J. Multiphase Flow*, 22, 133-155.

Zeng, Y., Z. Su, L. Wan, J. Wen (2011), Numerical analysis of air-water-heat flow in unsaturated soil: Is it necessary to consider airflow in land surface models?, *J. Geophys. Res.*, 116, D20107.

Zhang, F. (2010), Soil water retention and relative permeability for full range of saturation, Rep. PNNL-19800. Pacific Northwest Natl. Lab. Richland, Wash.

Zhang, J., and A.K. Datta (2004), Some considerations in modeling of moisture transport in heating of hygroscopic materials, *Drying Tech*., 22, 1983–2008.

Zhang, J., A.K. Datta, and S. Mukherjee (2005), Transport processes and large deformation during baking of bread, *Aiche J*., 51, 2569-2580.

6. Study of the effect of wind speed on evaporation from soil through integrated modeling of the atmospheric boundary layer and shallow subsurface

Abstract:

In an effort to develop methods based on integrating the subsurface to the atmospheric boundary layer to estimate evaporation, we developed a model based on the coupling of Navier-Stokes free flow and Darcy flow in porous medium. The model was tested using experimental data to study the effect of wind speed on evaporation. The model consists of the coupled equations of mass conservation for two-phase flow in porous medium with single-phase flow in the free flow domain under non-isothermal, non-equilibrium phase change conditions. In this model, the evaporation rate and soil surface temperature and relative humidity at the interface come directly from the integrated model output. To experimentally validate numerical results, we developed a unique test system consisting of a wind tunnel interfaced with a soil tank instrumented with a network of sensors to measure soil-water variables. Results demonstrated that, by using this coupling approach, it is possible to predict the different stages of the drying process with good accuracy. Increasing the wind speed increases the first stage evaporation rate and decreases the transition time between two evaporative stages (soil water flow to vapor diffusion controlled) at low velocity values; then, at high wind speeds the evaporation rate becomes less dependent on the wind speed. On the contrary, the impact of wind speed on second stage evaporation (diffusion-dominant stage) is not significant. We found that the thermal and solute dispersion in free flow systems has a significant influence on drying processes from porous media and should be taken into account.

6.1 Introduction

A critical component of the water cycle at local, regional and global scales is evaporation. Many researchers focus on evapotranspiration (ET), to include both bare soil evaporation and the vegetative portion (transpiration). Nonetheless, what is fundamental to the process of mass transfer across soil/atmospheric interfaces happens in bare soil; vegetation is a medium that cuts across the soil (roots) and atmosphere (air). Bare soil evaporation in arid or semiarid settings can account for more than half of ET and is therefore critical to its understanding [Huxman et al., 2005] and has been found to be very difficult to project in modeling studies [Seager et al., 2007]. Even though decades of research have improved our understanding of bare soil evaporation, many knowledge gaps still exist in the current science on how the soil water in the shallow subsurface close to the land surface interacts with the air in the atmosphere. Understanding this interaction is paramount to our understanding of many emerging problems to include climate change, water and food supply, leaking of geologically-sequestered CO_2 from soil [Oldenburg and Unger, 2004], the accurate detection of buried objects such as landmines [Das et al., 2001], and the remediation of contaminated soil in the shallow subsurface [Weaver and Tillman, 2005].

The rate of soil evaporation is affected by atmospheric conditions (e.g. humidity, temperature, thermal radiation and wind velocity), and thermal, and hydraulic properties of soil (thermal and hydraulic conductivity, porosity), all of which are strongly coupled. This strong coupling between processes leads to highly dynamic interactions between the atmosphere and soil resulting in dynamic evaporative behaviors [Sakai et al., 2011]. However, the atmospheric coupling to the soil at the land-atmospheric interface is rarely considered in most current models or practical application. This is due to the complexity of the problem in field settings and the scarcity of field or laboratory data capable of testing and refining energy and mass transfer theories. In most efforts to compute evaporation from soil, only indirect coupling is provided to characterize the interaction between multiphase flow in soil under realistic atmospheric conditions even though heat and mass flux are controlled by the coupled dynamics of the land and the atmospheric boundary layer. It is recognized that the most important process that determines the coupling between the soil water and heat is the transport of latent heat (the result of phase change) by vapor flux in the unsaturated soil pores and at the interface between the soil and the atmosphere [Bittelli et al., 2008]. Models that incorporate these processes have been

developed, e.g., [Jassal et al., 2003]; however, as *Bittelli et al.* [2008] note, a detailed experimental verification of vapor movement above the soil surface (i.e., atmospheric boundary layer) has not been conducted. *Bittelli et al.* [2008] suggest that the errors introduced in the vapor flow calculations are due to a number of factors that include lack of proper coupling of the thermal and mass flux processes, deficiencies in the constitutive relationships (e.g. thermal and hydraulic conductivities and soil water content) and difficulty in determining the resistance parameters at the land (soil)-atmospheric interface. For example, a prevalent modeling approach is to derive the aerodynamic and soil surface resistance terms based on semi-empirical or empirical approaches and to adjust the predicted evaporation based on true conditions that depend on ambient conditions such as soil moisture, roughness, wind speed, etc. Traditionally, the influences of atmospheric conditions are applied at the soil surface and aerodynamic resistance is applied on the border between the air flow and permeable media [e.g. [Bittelli et al., 2008; Camillo and Gurney, 1986; Novak, 2010; van de Griend and Owe, 1994]. In these cases, evaporation rate (*E*) can be determined by:

$$E = \frac{1}{r_s + r_v}\left(\left(\rho_v\right)_{pm} - \left(\rho_v\right)_{ff}\right) \qquad (2)$$

where r_s is the soil surface resistance for water vapor transport, r_v is the aerodynamic resistance for water vapor, $\left(\rho_v\right)_{pm}$ is the vapor density immediately below the soil surface (in porous medium) and $\left(\rho_v\right)_{ff}$ is the vapor density immediately above the soil surface (in free medium). The vapor density above the soil surface is calculated based on the measurement of relative humidity on the surface of the porous medium in the free flow medium.

In equation 1, the aerodynamic resistance for vapor transport depends on surface roughness properties and wind speed [Bittelli et al., 2008; Campbell, 1977]. The soil surface resistance depends on soil surface water content. The relationship between aerodynamic resistance to vapor transport and soil water content is typically an exponential form; there are many exponential empirical functions used to describe this relationship [Camillo and Gurney, 1986; van de Griend and Owe, 1994]. Although this approach is widely used, modeling comparison studies have shown significant variation between model parameterizations and evaporative fluxes [Desborough et al., 1996; Schmid, 1997; Smits et al., 2012; Villagarcia et al., 2007]. Recently, with the goal of addressing the issue of coupling the land to the atmosphere,

Smits et al. [2012] evaluated three different modeling approaches of bare soil evaporation formulated with different land surface boundary conditions and compared modeling results to laboratory generated experimental data. Results demonstrated that no one approach could be deemed most appropriate for every situation, demonstrating that further work focusing on the land/atmospheric interface, properly incorporating the complex interactions between the land and the atmospheric boundary layer is needed to increase the understanding of the processes that control shallow subsurface soil moisture flow that controls bare soil evaporation.

The modeling of non-isothermal single-phase (two-component) transfer in the atmosphere and two-phase (two-component) transfer in porous media have been separately investigated by many authors (e.g. [Chao-Yang and Beckermann, 1993; Niessner and Hassanizadeh, 2011; Wang and Cheng, 1997]). Recently, numerical advances have been made in the coupling of free flow (Navier-Stokes) with porous media flow (Darcy flow) [Baber et al., 2012; Chidyagwai and Riviere, 2011; Mosthaf et al., 2011; Nield, 2009; Shavit, 2009], however, these models were not adequately validated with experimental data. Mosthaf et al. (2011) extended the classical single-phase coupling to two-phase flow in porous media and one phase in the free flow. Their model is based on the continuity of fluxes at the porous medium-free medium interface and use of the Beavers-Joseph boundary condition [Mosthaf et al., 2011]. Baber et al. (2012) focused on the numerical concept and its implementation into a local modeling toolbox. The numerical parametric study showed that the proposed model can predict the evaporation phenomenology correctly. They concluded that the variation of permeability influences the duration of the capillary-driven evaporation regime whereas the variation of temperature affects the magnitude of the evaporation rate. They also showed that the choice of the Beavers-Joseph coefficient has a negligible influence on the evaporation rate across the interface [Baber et al., 2012]. However, the aforementioned models did not investigate non-equilibrium multi-phase flow under non-isothermal conditions.

The equilibrium assumption (i.e. instantaneous phase change) is called into question in natural evaporation from soil, in which atmospheric conditions induce mass transfer at the surface and tend to shift to equilibrium [e.g. [Chammari et al., 2008]. However, the common approach when modeling the movement of liquid water, water vapor and heat in the soil immediately below the land-atmosphere interface is to assume that water vapor in air is always in equilibrium with liquid water in the pores (e.g., [Prat, 2002; Sakai et al., 2011; Shokri et al.,

2009; Whitaker, 1977]). In an equilibrium formulation hypothesis, a sufficiently rapid mass exchange between the liquid water and its vapor is implied and it is assumed that the vapor pressure is always equal to the saturated vapor pressure. However, experimental studies [Armstrong et al., 1994; Chammari et al., 2005; Chammari et al., 2008; Lozano et al., 2009; Lozano et al., 2008] have observed a volatilization or condensation time. A recent comparison between equilibrium and non-equilibrium phase change modeling concepts using experimental data by Smits et al., [2011] revealed that the non-equilibrium model is able to better predict evaporation in porous media under certain conditions. Another limitation of the previously mentioned modeling efforts is that they do not take into account dispersion in the free flow domain. However, free flow dispersion, which depends on the Péclet number, may be the dominant regime in the free-flow region.

It is well known that a no-slip condition at the free flow and porous domains surface is not satisfactory and indeed a slip boundary condition occurs. The slip boundary condition was first obtained experimentally by Beavers and Joseph [1967]. Beavers and Joseph proposed that the tangential component of the normal stress of the flow at the free flow and porous medium interface is proportional to the jump of the tangential velocity across the interface [Beavers and Joseph, 1967]. The coupling condition was further studied by Saffman [1971] who concluded that the filtration velocity in porous media was much smaller than the free-flow velocity and can be neglected [Saffman, 1971]. There exist several other formulations for a slip boundary condition to include (1) using a shear stress jump condition by means of the non-local form of the volume averaging technique with an experimentally determined fitting parameter [Ochoa-Tapia and Whitaker, 1997], or (2) using the inertia and boundary effects [Vafai and Kim, 1990]. Alazmi and Vafai (2001) compared five different interface conditions between the porous medium and adjacent fluid layer. They concluded that the velocity field is more sensitive to variation in the boundary condition than the temperature field [Alazmi and Vafai, 2001]. They showed similar results for all five interface conditions. Therefore, the Beaver's Joseph formulation was chosen for this work based on simplicity of the implementation to the numerical model.

In this study, in order to better understand the coupling between free flow and porous media flow, we developed a theory for coupling single-phase (gas), two-component (air and water vapor) transfer in the atmosphere and two-phase (gas, liquid), two-component (air and

water vapor) flow in porous media at the REV scale under non-isothermal, non-equilibrium conditions and taking into account the dispersion in free flow medium (**Figure 1**). Mean wind velocity in the free fluid system, the soil thermo-physical properties and the initial conditions in the soil and atmospheric systems are the only input parameters needed for this model. In order to test the numerical formulations and codes, we performed a series of laboratory experiments under varying wind speeds using bench scale physical models and a unique low velocity porous media/wind tunnel, allowing for better control and gathering of accurate data at scales of interest not feasible in the field.

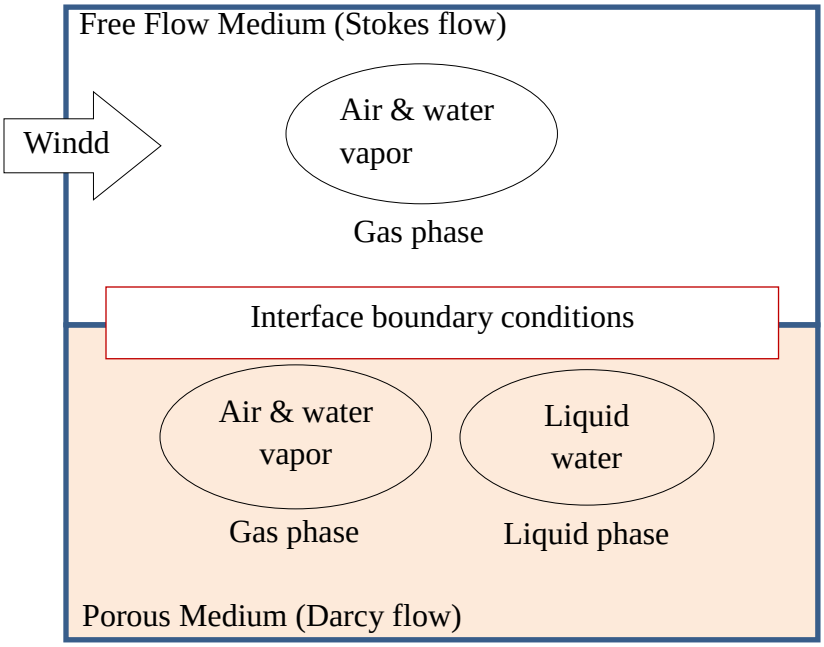

Figure 1. Schematic of the problem configuration for a single phase free fluid that interacts with two fluid phases in porous media.

In addition to bare soil evaporation, the theory developed in this work can also be used for various applications, such as environmental process involving vapor transport across interfaces of porous media and free flow (evaporation and condensation from vadose zone with a surface flows), fuel cells (gas diffusion layers of fuel cells are typically made of fibrous materials is in contact with free gas distributor), biological systems (interaction between blood flow and

surrounding tissues, the dynamics of growing biofilm), and development of food drying process (interaction between air conditions and hygroscopic porous food).

6.2 Numerical Model Formulation

In this section, we present the formulations of macroscopic flow and, mass and energy balance equations for water, air and water vapor in the porous media as well as the gas (air and water vapor) above the porous media (**Figure 2**). The free flow and porous medium flow and transport equations are given in Section 0 and 0, respectively. The different boundary conditions applied on the interface between porous medium and free medium are listed in Section 0.

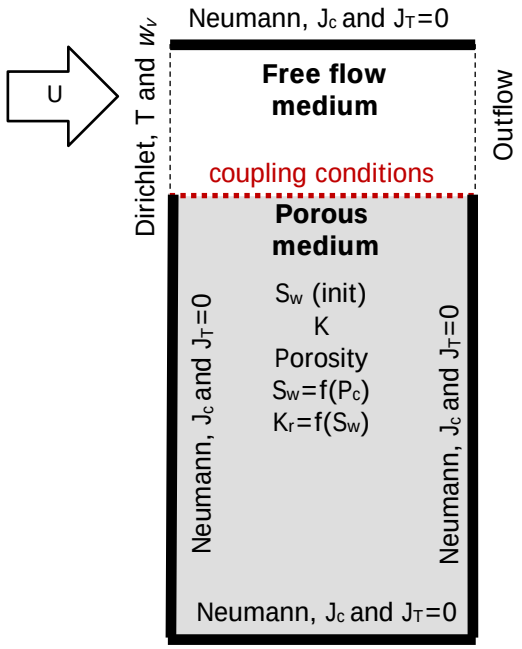

Figure 2. Two dimensional problem configuration (subdomains, boundary and initial conditions) where T is temperature, w_v is water vapor concentration, U is wind speed, S_w is the water phase saturation, J_c and J_T are mass and heat fluxes, P_c is capillary pressure and K is intrinsic permeability.

6.2.1 Governing free flow medium transport equations

We assume non-isothermal, single-phase gas flow in the free-flow domain. The gas phase, identified here with the subscript "g", is composed of two components, water vapor and air. The water vapor component is identified with the subscript "v". We consider in this domain that the density and viscosity of the moist air depends on the temperature and mass fraction of water vapor. The Navier-Stokes equation describes the fluid flow in the free domain. The continuity and Navier-Stokes equations assuming incompressible fluid, with no thermal and solutal expansion, are given respectively by [Bird et al., 2002]

$$\nabla.\mathbf{v}_g = 0\,, \tag{3}$$

$$\rho_g\left(\frac{\partial \mathbf{v}_g}{\partial t} + \mathbf{v}_g.\nabla\mathbf{v}_g\right) = -\nabla p_g + \mu_g\nabla.\left(\nabla\mathbf{v}_g\right) + \rho_g\mathbf{g} \tag{4}$$

The duct flow Reynolds numbers calculated in the range of the wind experimental velocities applied in this study show a laminar flow and transition flow regime. However, the boundary layer Reynolds numbers stay less than the critical value. In this study, we use Stokes equation for the flow motion in free flow region, assuming a laminar, Poiseuille flow between two parallel plates and consequently, negligible vapor transfer by turbulent diffusion is valid. Nevertheless, the surface turbulence can significantly affect the transport just beneath the soil surface [Ishihara et al., 1992] and should be addressed in the future.

The energy transfer in the free flow region is described by the following equation for the gas phase [Kaviany, 2001]

$$\left(\rho c_p\right)_g\frac{\partial T}{\partial t} + \left(\rho c_p\right)_g\nabla.\left(T\,\mathbf{v}_g\right) = \nabla.\left(\mathbf{\Lambda}_g.\nabla T\right), \tag{5}$$

where T is the moist air temperature, and $\mathbf{\Lambda}_g$ is the thermal dispersion tensor of moist air.

The component mass conservation is described by the following equation for the free fluid domain [Bird et al., 2002]

$$\frac{\partial \rho_g w_v}{\partial t} + \nabla.\left(\rho_g w_v\mathbf{v}_g\right) = \nabla.\left(\mathbf{D}_v.\nabla\left(\rho_g w_v\right)\right), \tag{6}$$

where w_v is the mass fraction of water vapor component in the gas-phase in free flow domain and $\mathbf{D}_v$ is the Taylor dispersion tensor of water vapor in air.

We define the thermal and solutal Péclet numbers as

$$\mathrm{P}e_T = \frac{uH}{\lambda_g \big/ \left(\rho c_p\right)_g}, \text{ and } \mathrm{P}e_C = \frac{uH}{\mathscr{D}_v} \tag{7}$$

respectively, where H is the height of free flow region, λ_g is the thermal conductivity of air-vapor binary mixture (or moist air thermal conductivity), u is the velocity field in x-direction and $\mathscr{D}_v$ is the binary diffusion coefficient of water vapor in dry air which is a function of temperature [Campbell, 1985]. The longitudinal Taylor dispersion coefficients of equations (3) and (4) in a stratified media can be calculated as [Wooding, 1960]

$$\frac{\left(\Lambda_g\right)_{xx}}{\lambda_g} = 1 + \frac{Pe_T^2}{210} \tag{8}$$

$$\frac{\left(\mathrm{D}_v\right)_{xx}}{\mathscr{D}_v} = 1 + \frac{Pe_C^2}{210} \tag{9}$$

6.2.2 Governing porous medium transport equations

Natural soil in the unsaturated zone is often represented as a three-phase system, consisting of the solid, liquid and gas phases. In this study, we consider that two components are present in the gas-phase: dry air and water vapor. The solid phase is assumed to be inert and non-deformable. The soil pores are occupied by water as a liquid phase, and a gaseous binary mixture consisting of dry air and water vapor. We consider that the amount of air dissolved in liquid water is negligible; therefore, the liquid phase can be treated as a single component. In this section, we use the same notation as in the free medium. When necessary, the superscripts (*ff*) and (*pm*) are used to denote the free flow and porous medium subdomains, respectively.

Two-phase flow and transport

The flow of two non-compressible immiscible fluids in a rigid porous medium can be described by two coupled pressure-pressure partial differential equations [Bear, 1972]

$$\phi \frac{dS_\ell}{dp_c} \frac{\partial \rho_\ell \left(p_g - p_\ell\right)}{\partial t} + \nabla . \left(\rho_\ell \mathbf{v}_\ell\right) = -\dot{m} \tag{10}$$

$$\phi \frac{dS_g}{dp_c} \frac{\partial \rho_g \left(p_g - p_\ell\right)}{\partial t} + \nabla.\left(\rho_g \mathbf{v}_g\right) = +\dot{m} \tag{11}$$

where the water and gas velocity can be defined on the basis of the extended Darcy's law for multi-phase flow, with definition of relative permeability as

$$\mathbf{v}_\ell = -\frac{k_{r\ell}}{\mu_\ell}\mathbf{K}\left(\nabla p_\ell + \rho_\ell \mathbf{g}\right) \tag{12}$$

$$\mathbf{v}_g = -\frac{k_{rg}}{\mu_g}\mathbf{K}\left(\nabla p_g + \rho_g \mathbf{g}\right) \tag{13}$$

Here, the subscript ℓ and g denote the liquid phase (wetting phase) and gas phase (non-wetting phase), respectively. $\mathbf{v}_\ell$ and $\mathbf{v}_g$ are the velocities within the wetting and non-wetting fluids, S denotes fluid saturation, p pressure, ρ density, $\mathbf{K}$ intrinsic permeability tensor and k_r relative permeability of the phases, μ fluid dynamic viscosity, $\mathbf{g}$ gravitational acceleration, ϕ total porosity of the porous medium and $\dot{m}$ phase change rate between water and its vapor due to evaporation or condensation. The non-equilibrium effect is calculated and implemented to the model through this phase change rate. We will show in Section 0 how it can be calculated from fluid and porous medium properties. The comparison between the equilibrium and non-equilibrium model for a porous medium-free flow coupled system will be investigated in a future study. Nonetheless, the reader can see Smits et al. (2011) for a comparison between equilibrium and non-equilibrium formulations without coupling between free flow and porous medium flow.

Equations (8) and (9) can be solved simultaneously for the main unknown pressures p_g and p_ℓ. Since the medium is incompressible and the two fluids jointly fill the void space,

$$S_g + S_\ell = 1 \tag{14}$$

The normalized wetting saturation (or effective wetting saturation) is defined as

$$S_{e\ell} = \frac{S_\ell - S_{\ell r}}{1 - S_{\ell r}} \tag{15}$$

where $S_{\ell r}$ is the residual saturation related to pore scale trapping. The residual saturation changes linearly as a function of temperature as shown in She and Sleep, 1998 [She and Sleep, 1998] and was implemented in this work. The difference between the non-wetting and wetting pressure is

known as the capillary pressure and can defined as a function of the normalized wetting fluid saturation

$$p_c(S_{e\ell}) = p_g - p_\ell \tag{16}$$

To describe the relations between p_c , $k_{r\ell}$, k_{rg} and S_{el} the analytical models of van Genuchten-Mualem can be used as [Mualem, 1976; van Genuchten, 1980]

$$S_{e\ell} = \begin{cases} \left[1+(\alpha|H_c|)^n\right]^{-m} & H_c > 0 \\ 1 & H_c \le 0 \end{cases} \tag{17}$$

where α and n are the Van Genuchten soil parameter ($m = 1-1/n$). Here, because p_c is large and the changes in other parameters are small, the equivalent height of water or capillary pressure head is used instead of capillary pressure as $H_c = p_c/(\rho_\ell g)$. The relative permeability of the wetting phase are specified according to the van Genuchten–Mualem model [Mualem, 1976; van Genuchten, 1980]

$$k_{r\ell} = S_{e\ell}^{\frac{1}{2}}\left[1-\left(1-S_{e\ell}^{\frac{1}{m}}\right)^m\right]^2 \tag{18}$$

The van Genuchten–Mualem model for relative non-wetting phase permeability can be written as [Parker et al., 1987]

$$k_{rg} = (1-S_{e\ell})^{\frac{1}{2}}\left[1-S_{e\ell}^{\frac{1}{m}}\right]^{2m} \tag{19}$$

The mass balance for water vapor in the gas phase can be expressed as [Bear, 1972]

$$\phi\frac{\partial(\rho_g S_g w_v)}{\partial t} + \nabla.(\rho_g w_v \mathbf{v}_g - \mathrm{D}_v^*\nabla(\rho_g w_v)) = \dot{m} \tag{20}$$

Because of slow flow velocities in porous media and high diffusion coefficients, dispersion can be neglected in the gas phase. Therefore, the effective vapor diffusion in porous medium can be predicted as

$$\mathrm{D}_v^* = \tau\,\phi S_g \mathscr{D}_v \tag{21}$$

The tortuosity τ can be estimated as [Millington and Quirk, 1961]

$$\tau = \frac{\left(\phi S_g\right)^{7/3}}{\phi^2} \tag{22}$$

In order to take into account the water vapor flux enhancement by thermal gradients, the empirical vapor enhancement factor from [Cass et al., 1984] was multiplied in this study by the vapor diffusion coefficient.

Energy balance equation

When the principle of local-scale thermal equilibrium is valid, a one-equation equilibrium model, which consists of a single transfer equation can be written as $T_w = T_g = T_s = T$.

The characteristic time associated with thermal equilibrium is much lower than the characteristic time associated with mass transfer. Therefore, using the local thermal equilibrium assumption is acceptable for this work.

The macroscopic form of the governing equation for T can be then written as [Whitaker, 1977]

$$\left(\rho c_p\right)^* \frac{\partial}{\partial t} T + \nabla.\left(\left(\rho c_p\right)_\ell \mathbf{v}_\ell T + \left(\rho c_p\right)_g \mathbf{v}_g T\right) - \nabla.\left(\Lambda^* \nabla T\right) = -L\dot{m} - Q_s \tag{23}$$

$$\left(\rho c_p\right)^* = \left((1-\phi)\left(\rho c_p\right)_s + \phi S_\ell \left(\rho c_p\right)_\ell + \phi S_g \left(\rho c_p\right)_g\right) \tag{24}$$

where Λ^* is the effective thermal conductivity of the combined three-phases and depends on structure, porosity, the ratio of the thermal properties of the solid phase on the fluid phase, and dispersion in porous media. Q_s is the heat loss term and L is the latent heat of water vaporization which is function of temperature [Monteith and Unsworth, 1990]. The model proposed by Campbell et al. (1994) was used to determine the effective soil thermal conductivity [Campbell et al., 1994]. It is based on the assumption that thermal conductivity of any mixture can be expressed as the weighted sum of the thermal conductivities of the individual components of the mixture. The effective thermal conductivity Λ^* is given by

$$\Lambda^* = \frac{\omega_\ell \phi S_\ell \lambda_\ell + \omega_g \phi S_g \lambda_g + \omega_s (1-\phi)\lambda_s}{\omega_\ell \phi S_\ell + \omega_g \phi S_g + \omega_s (1-\phi)} \tag{25}$$

where λ_ℓ, λ_g, λ_s are the thermal conductivities of water, gas and soil matrix and ω_ℓ, ω_g and ω_s are the respective weighting factors for each phase calculated according to [Campbell et al., 1994].

Non-equilibrium phase change

As mentioned in the introduction, the assumption of equilibrium mass exchange is called into question for many natural drying applications. Bénet et al., [2009] evaluated several experimental studies to understand the thermodynamics of non-equilibrium phase change during soil drying. In their work, a non-equilibrium situation is created experimentally by extracting the gas phase of a small soil sample, and replacing it with dry air under isothermal conditions. Their proposed model involves three coefficients that must be determined experimentally. The volumetric phase change, $\dot{m}$, can be calculated based on the framework of linear thermodynamics of irreversible processes where fluxes are expressed as a linear function of forces

$$\dot{m} = -L_P \frac{R}{M} \ln\left(\frac{P_v}{P_{veq}}\right) \tag{26}$$

where P_v is the partial pressure of vapor, and P_{veq} is the partial pressure of vapor in equilibrium [Bénet et al., 2009], M is the molar mass of water and L_P is a phenomenological coefficient that depends on water saturation and the temperature. The phenomenological coefficient is characterized by three coefficients through the following expressions:

$$L_P = L_{eq}, \text{ when } r < \frac{P_v}{P_{veq}} \le 1 \tag{27}$$

$$L_P = L_{eq} + k\left(r - \frac{P_v}{P_{veq}}\right), \text{ when } 0 < \frac{P_v}{P_{veq}} \le r \tag{28}$$

where L_{eq}, k and r are determined experimentally. Unfortunately, the experimental data for these three coefficients are limited to specific soil, temperatures and total gas pressures and therefore cannot be used in this study. In addition, hygroscopic effects have a significant influence by lowering the phase change velocity [Cherblanc et al., 2007]. In the experimental

part of this study we have used sandy soil; therefore, phase change will be faster compared to the soils used in [Bénet et al., 2009].

An alternative method of representing the term $\dot{m}$ can also be used [Bixler, 1985; Le et al., 1995; Scarpa and Milano, 2002; Zhang and Datta, 2004]. In this study, we assumed that the phase change rate is proportional to the difference between the equilibrium density of vapor and its actual density through an appropriate time delay coefficient t_{eq} (relaxation time to obtain the equilibrium within the pore space). This method also takes into account the water availability for evaporation by including soil water content.

$$\dot{m} = \frac{(S_\ell - S_{\ell r})\phi}{t_{eq}}\left(\rho_{veq} - \rho_v\right) \tag{29}$$

where $\rho_v = \rho_g w_v$ is the vapor density and ρ_{veq} is the equilibrium vapor density. The equilibrium vapor density is calculated by Kelvin's equation which assume equilibrium at a curved air-water interface as

$$\rho_{veq} = \rho_{vs} \exp\left(H_c M_w g / RT\right) \tag{30}$$

where ρ_{vs} is the saturated vapor density in the gas phase that varies with temperature as [Campbell, 1985]

$$\rho_{vs} = \exp(31.37 - 6014.79\mathrm{T}^{-1} - 7.92\times10^{-3}\mathrm{T})\mathrm{T}^{-1}\times10^{-3} \tag{31}$$

High precision in equilibrium time is not expected to significantly improve the model prediction [Halder et al., 2011]. Therefore, we estimate t_{eq} using the characteristic time of pure binary diffusion for a simple cylindrical pore with an averaged pore characteristic length ℓ_{por} that the vapor has to diffuse

$$t_{eq} = \frac{\ell_{por}^2}{\mathrm{D}_v^*} \tag{32}$$

Equation (29) can therefore be rewritten as

$$\dot{m} = \frac{\mathrm{D}_v^*}{\ell_{por}^2}\left(\rho_{vs} \exp\left(H_c M_w g / RT\right) - \rho_g w_v\right)(S_\ell - S_{\ell r})\phi \tag{33}$$

6.2.3 Interface boundary conditions

To couple the two domains, suitable boundary conditions at the free and porous medium interface are needed. The different boundary conditions applied at the interface between porous medium and free medium are listed below (see also [Mosthaf et al., 2011] :

Hydrodynamic interface boundary condition

The continuity of the normal stresses (pressure jump boundary condition in the gas-phase), which is the sum of pressure term and viscous term in free fluid can be introduce as [Whitaker, 1999]

$$\left[\mathbf{n}.\left(p_g\mathbf{I}-\mu_g\nabla\mathbf{v}_g\right)\mathbf{n}\right]_{ff}=\left[p_g\right]_{pm},\ \text{on}\ \Gamma \tag{34}$$

Here, the term p_g in porous medium is defined as the sum of the water pressure and the capillary pressure. In practice, the viscous term may be small compared with the pressure, and in this case the continuity of total normal stress reduces to the continuity of pressure [Nield and Bejan, 2006].The continuity of the normal mass fluxes for the gas-phase can be expressed as

$$\left[\left(\rho_g\mathbf{v}_g\right).\mathbf{n}\right]_{ff}=-\left[\left(\rho_g\mathbf{v}_g\right).\mathbf{n}\right]_{pm},\ \text{on}\ \Gamma \tag{35}$$

where the flux of the liquid phase has been vanished at the interface and

$$\left[\left(\rho_\ell\mathbf{v}_\ell\right).\mathbf{n}\right]_{pm}=0,\ \text{on}\ \Gamma \tag{36}$$

The Beavers-Joseph-Saffman slip boundary condition for the tangential component of the free flow velocity reads

$$\mathbf{v}_g.\mathbf{t}_\mathrm{j}=\frac{\sqrt{\mathrm{K}}}{\alpha_{BJ}}\mathbf{t}_\mathrm{j}.\nabla\mathbf{v}_g,\ \text{on}\ \Gamma \tag{37}$$

where $\mathbf{t}_\mathrm{j}$ (j=1, …, n-1) are linear independent unit tangential vectors to the boundary Γ, and α_{BJ} is a dimensionless slip coefficient. In this study, the surface roughness of the porous medium appears as a coefficient in the surface slip boundary condition. Therefore, the aerodynamic resistance of water vapor and surface resistance are not necessary in this model. As mentioned previously, the related humidity and temperature of the soil surface are outputs of this model. The parameter α_{BJ} is empirical and depends on flow conditions, interface location, surface microstructure and porosity. The slip coefficient can be estimated using an equation proposed by Neale and Nader, [1974]. They imposed conditions of continuity of velocity and its

gradient at the fluid porous medium boundary. By solving the Brinkman equation and comparing the resulting mass flow rate, they proposed that $\alpha_{BJ} = \sqrt{\mu_{eff}/\mu}$, where μ_{eff} is the effective viscosity in Brinkman's model and μ is the fluid viscosity [Neale and Nader, 1974]. Following Whitaker [1999], the effective viscosity is explicitly given by $\mu_{eff}/\mu = 1/\phi$, where ϕ the porous medium porosity. [Kim et al., 1994] The Brinkman equation contains Laplacian terms and is of the same order as Stokes equation. Therefore, through the use of Brinkman equation at the free/porous interface and in the bulk of porous matrix, the boundary conditions in both Stokes and Darcy equations become compatible. An averaging method used by Shavit et al, [2002] to study the free flow problem at the interface of porous medium and free flow region [Shavit et al., 2002]. They used a Cantor configuration representing the porous media. Their results show that the apparent viscosity approach does not produce a satisfactory agreement with experimental. They proposed therefore a modified Brinkman equation which fit better with flow problem. However, theoretical studies by Lundgren [1972] [Lundgren, 1972] and Kim and Russell [1985] [Kim and Russel, 1985] pointed out that the applicability of Brinkman equation is restricted only to the high porosity domain ($\phi > 0.6$) where the curvatures of the streamlines in the bulk porous medium adjacent to the interface are generally greater than the pore diameter. This requirement is highly restrictive since most natural porous media have porosity less than 0.6. It is therefore preferable in most practical situations to use Darcy's law together with the Beavers and Joseph boundary condition [Nield, 2009].

In this study, we used a constant slip coefficient of 0.01 based on the only measurement data available in [Kim et al., 1994] which has similar porous medium properties to our experimental study.

Continuity boundary condition for temperature at the porous medium-free medium interface

In this work, we assume a local thermal equilibrium at the interface, providing a continuity boundary condition for temperature as

$$[T]_{ff} = [T]_{pm}, \text{ on } \Gamma \tag{38}$$

$$\left[\mathbf{n}.\left(\left(\rho c_p\right)_\ell \mathbf{v}_\ell T + \left(\rho c_p\right)_g \mathbf{v}_g T - \Lambda^* \nabla T\right)\right]_{pm} = -\left[\mathbf{n}.\left(\left(\rho c_p\right)_g \left(T_g \mathbf{v}_g\right) - \Lambda_g \nabla T_g\right)\right]_{ff}, \text{ on } \Gamma \tag{39}$$

Continuity boundary condition for concentration at the porous medium-free medium interface

We also assume the continuity of the component mass fluxes across the interface. This equilibrium is considered as

$$\left[w_v\right]_{ff} = \left[w_v\right]_{pm}, \text{ on } \Gamma \tag{40}$$

$$\left[\mathbf{n}.\left(\rho_g w_v \mathbf{v}_g - \mathrm{D}_v^* \nabla\left(\rho_g w_v\right)\right)\right]_{pm} = -\left[\mathbf{n}.\left(\rho_g w_v \mathbf{v}_g - \mathrm{D}_v \nabla\left(\rho_g w_v\right)\right)\right]_{ff}, \text{ on } \Gamma \tag{41}$$

After the implementation of the initial and boundary conditions, the system of partial differential equations for the non-equilibrium model in a two-dimensional domain was simultaneously solved using the COMSOL Multiphysics software that is based on the Finite Element Method. A summary of the equations to be solved and their corresponding primary variables is listed in Table 1.

Table 1. List of model equations and their primary variables

	Equation type	Equation numbers	Primary variables
Free-flow subdomain	Continuity and Navier-Stokes	(1), (2)	$\mathbf{v}_g$, p_g
	Component mass balance	(4)	w_v
	Energy balance	(3)	T
Porous-medium subdomain	Mass balances	(8), (9)	p_g, p_ℓ
	Component mass balance	(20)	w_v
	Energy balance	(23)	T

6.3 Experimental setup

To validate the proposed theoretical model, we developed a test system consisting of a wind tunnel placed above a soil tank equipped with a network of sensors to measure different soil-water variables. A series of experiments under varying boundary conditions were performed, using test sand for which the hydraulic and thermal properties were well characterized. Precision data for soil moisture, soil and air temperature and relative humidity, as well as wind velocity

under well-controlled transient heat and wind boundary conditions was generated. In this section, the experimental material, methods and protocols are discussed.

6.3.1 **Sand Material**

Uniform specialty silica sand, Accusand #30/40 (effective sieve number) was used for this series of experiments. Based on the technical sheet provided by the manufacturer (Unimin Corp., Ottawa, MN), this sand is 99.8% quartz, its grain shape is classified as rounded, the uniformity coefficient is approximately 1.2, and the grain density is 2.66 g/cm^3. Additional important properties of the test sand are summarized in Table 2. The capillary pressure (P_c) – water content (θ) relationship and thermal conductivity (λ) – water content (θ) relationship as a function of temperature for the sand under tight packing conditions were measured using a small tempe cell apparatus with a network of sensors that continuously monitored soil moisture, temperature, capillary pressure and soil thermal properties. A detailed description of the measurements of the P_c-θ and λ–θ relationships is given in *Smits et al*. [2010, 2012].

Table 2. Properties of Accusand #30/40 under tight packing conditions

						van Genuchten Model Parameters (m=1-1/n)****	
	d_{50} [mm] *	**Dry Bulk Density [g cm^{-3}]**	**Porosity**	**Residual water content ****	**Saturated Hydraulic Conductivity, Ks [cm sec^{-1}] *****	**α [m^{-1}]**	**n**
	0.52	1.77	0.334	0.028	0.106	5.7	17.8

* estimated from sieve data provided by the manufacturer
**measured in a separate column test
***measured in a separate hydraulic conductivity test
****van Genuchten model parameters estimated using the computer code RETC

6.3.2 Development of Experimental Apparatus

Laboratory testing was performed using a two-dimensional bench scale tank constructed of acrylic plexiglass (height = 55.0 cm, length = 25.0 cm, width = 9.0 cm, wall thickness = 1.25 cm, specific heat = 1464 Jkg^{-1}K^{-1}, thermal conductivity = 0.2 Wm^{-1}K^{-1}, and density = 1150 kgm^{-3}) as seen in **Figure 3**a (the inside volume of the tank, excluding the sensors, is 12,375 cm^3). Water content and temperature distributions within the tank were continuously monitored using

dielectric soil moisture sensors (Decagon Devices, Inc. ECH$_2$O EC-5, sensor length = 5.5 cm, measurement frequency = 70 MHz, accuracy ±3%) and temperature sensors (Decagon Devices Inc. RT-1, accuracy ±0.5°C from 5-40°C, better than ±1.0°C from 40-50°C), respectively. In addition to the sensors within the tank, relative humidity and temperature was monitored at two locations on the soil surface, three locations 7.5 cm above the soil surface, and ambient conditions outside the tank using relative humidity/temperature sensors (Decagon Devices Inc. EHT RH/Temperature, accuracy ±2% from 5-90% RH, ±3% from 90-100% RH, temperature accuracy ±0.25°C). The relative humidity/temperature sensors at the soil surface were placed in direct contact with the soil grains in order to get an accurate reading directly on the soil surface.

A total of 25 soil moisture sensors and 19 temperature sensors were installed horizontally through the plexiglass walls of the tank. Five relative humidity/temperature sensors were installed on and above the soil surface (**Figure 3**a). Five channel, continuous data loggers (Decagon Devices, Inc. Em50) were used to collect data from all the sensors. During the experiment, the tank was placed on a scale (Sartorius Model 11209-95, Range = 65kg, Resolution = ±1g) in order to continuously monitor the cumulative weight loss of water from the tank.

To better understand the physical processes associated with evaporation in dry, bare soil conditions, heat flux and air flow were induced over the soil surface to simulate an arid/ semi-arid environment. As shown in **Figure 3**b, heat and wind was generated by infrared heaters and a duct fan placed within galvanized steel ductwork (26.0 cm by 8.0 cm rectangular and 15.2 cm round diameter, respectively). The ductwork was aligned along the centerline of the tank to channel heated air across the soil surface. Five ceramic infrared heaters (Mor Electric Heating Assoc., Inc. Infrared Salamander Model FTE 500-240) placed in parallel within a reflector, were used to induce heat over the soil surface. An in-line duct fan (Suncourt Pro Model DB6GTP, 15.2 cm diameter) with variable speed controller (Suncourt Model VS200) was used to induce wind over the soil surface. As shown in **Figure 3**b, the infrared heaters were positioned upstream of the tank while the duct fan was positioned downstream in order to draw heated air from the upstream end over the soil surface and vent the air at the downstream end.

To maintain a constant air temperature over the soil surface, the infrared heaters were connected to a temperature control system (Chromalox Model 2104), which was regulated by an

infrared temperature sensor (Exergen Corporation Model IRt/c.03) placed on the ductwork. The infrared sensor provides input back to the temperature control system to ensure that temperature output from the heaters remained constant. The ambient air temperature gradient at the outer boundaries of the tank was monitored using a relative humidity/temperature sensor (Decagon Devices Inc. EHT RH/Temperature sensor, accuracy as given above) upstream of the tank and an air temperature sensor (Decagon Devices Inc. ECT, sensor length = 3.0 cm, temperature accuracy as given above) downstream of the tank as seen in **Figure 3**b.

To control wind velocity over the soil surface, a variable speed controller, connected to the in-line duct fan, was used in combination with a galvanized steel duct damper (15.2 cm diameter) downstream of the fan and/or electrostatic register vent filters upstream of the fan. Wind velocity was monitored using a stainless steel pitot tube (Dwyer Instruments, Inc. Model 167-12, 0.32 cm diameter, 30.48 cm insertion length, accuracy ±5%) connected to a differential pressure transmitter (Omega Engineering, Inc. Model PX653-0.1D5V, Range = 0-0.1 inches of H_2O, 0-25 Pascals) and an anemometer. The pitot tube and anemometer were suspended in the center of the tank, 10 cm above the soil surface as seen in **Figure 3**a for the entire duration of the experiment. The pressure data from the pitot tube was converted into wind velocity in meters per second by solving Bernoulli's equation and compiled using LabVIEW software (National Instruments Corp.). The wind velocity profile was used to obtain the average velocity over the soil surface.

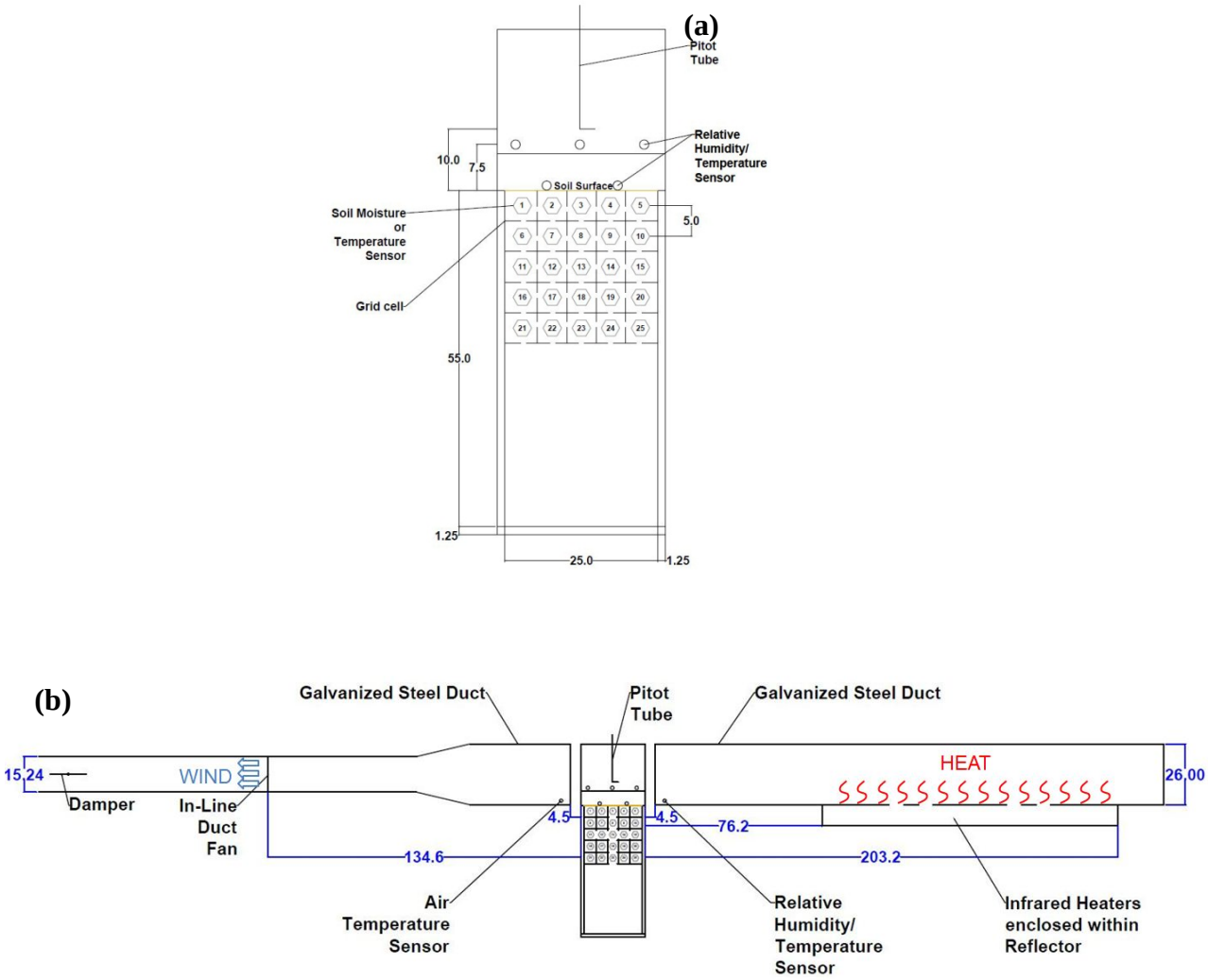

Figure 3. Schematic view of the experimental setup (a) tank and sensors (b) complete setup including tank and ductwork (all dimensions are in centimeters).

6.3.3 Procedure

The tank was first wet-packed with Accusand #30/40 in incremental layers of approximately 1 cm in an effort to achieve uniform bulk density in accordance with the methods outlined in *Sakaki and Illangasekare* [2007]. The water table was initially established at the top surface of the tank. Prior to starting the experiment, the soil surface was covered with plastic wrap in order to prevent evaporation. No flow conditions were maintained along the bottom and side boundaries of the tank.

At the start of the experiment, the plastic wrap was removed from the upper boundary of the tank, to allow for evaporation, while heat and wind were induced at the

soil surface using the infrared heaters and duct fan, respectively. For each experiment, air temperature was kept constant at approximately 35-40°C using the temperature control system (Chromalox Model 2104) regulated by the infrared temperature sensor (Exergen Corporation Model IRt/c.03) placed on the ductwork. Wind velocity varied for each experiment between 0.55 and 3.65 m/s . Water content, temperature, relative humidity, wind velocity and soil tank weight were continuously monitored at ten minute intervals. A total of four experiments were conducted. Each experiment was run for approximately 12 days.

6.4 Results

In this section, we present a demonstration of experimental results (Section 4.1) for a specific wind velocity. Then, the experimental results are compared in Section 0 with those obtained from a numerical simulation for the horizontal temperature gradient setup shown in Figure 2.

6.4.1 Experimental results demonstration and discussion

Results from experiment run number 2 (average wind velocity of 1.22 m/s) are presented below including graphs and summary tables of measured relative humidity and temperature, as well as calculated saturation from measured soil water content. Data from this experiment are used as a base case for comparison with the remaining experimental data. Observed trends as well as differences between experiments are noted.

Wind velocity

Figure 4 shows the wind velocity versus time for experiment run number 2. There is a sinusoidal diurnal fluctuation in wind velocity, which may be due to variability in atmospheric conditions, e.g. barometric pressure changes to constant air density assumption. This diurnal trend was also observed in the other experiments and considered to be minor. Studying the impact of diurnal variation of temperature on evaporation is not the objective of this study; therefore, the wind velocity was averaged over the entire experiment and the mean wind velocity was used in the numerical model. The average measured maximum wind velocity for each experiment is summarized in Table 3.

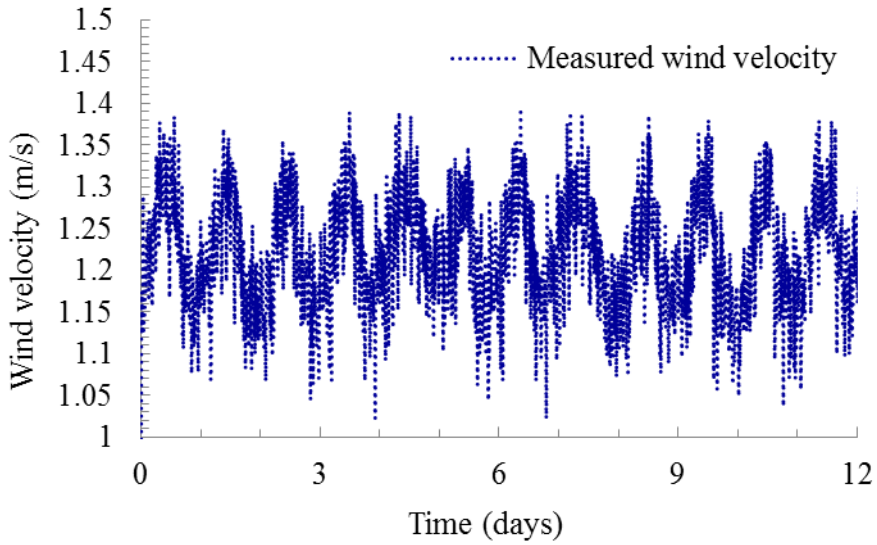

Figure 4. Wind velocity over the soil surface for experiment run number 2.

Table 3. Experimental Wind Velocities

Experiment Run #	Average Maximum Wind Velocity (m/s)
1	0.55
2	1.22
3	3.00
4	3.65

Relative humidity

Figure 5 displays the relative humidity and temperature measured on the soil surface versus time for experiment number 2 (wind velocity = 1.2 m/s). Based on these data, initial relative humidity (RH) on the soil surface remains relatively constant (RH=0.80) for a period of approximately 1.8 days, followed by a steep decrease over approximately 4 days at which point relative humidity stabilizes (RH=0.35). In contrast, initial temperature (T) on the soil surface (T=26°C) increases for a period of approximately 3 days at which point temperature stabilizes (T=33°C). This general trend was observed in all the other experiments. **Table 4** provides a summary of initial and final relative humidity and temperature measurements on the soil surface for each experiment. For the first three days of the experiment, the relative humidity of the downstream air is higher than the upstream

air since the vapor flow to the free air stream moistures it (**Figure 5**). However, after three days, the trend is reversed and the RH of the upstream air is higher. The apparent reversed trend in relative humidity is due to either a difference in wall-soil contact at side of soil tank or a change in sensor contact with the soil (may have changed over time due to heating and flexibility of the sensor cable.

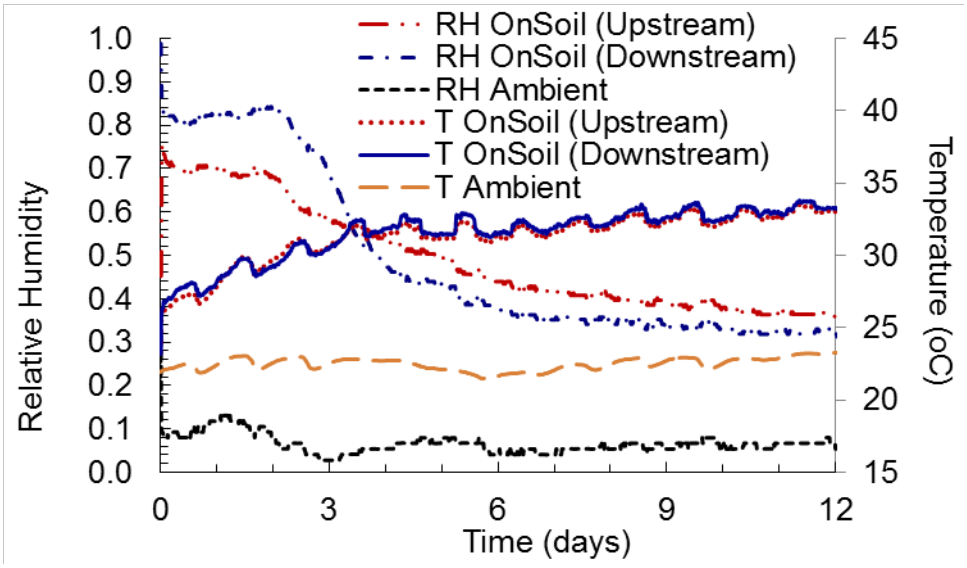

Figure 5. Relative humidity and temperature measured on the soil surface and relative humidity in ambient air upstream of the soil tank.

Table 4. Summary of relative humidity and temperature measured on the soil surface

Experiment Run #	Maximum Wind Velocity (m/s)	Initial RH On Soil	Final RH On Soil	Initial Temperature On Soil (°C)	Final Temperature On Soil (°C)	Change in Temperature On Soil (°C)
1	0.55	0.75	0.35	27	31	+4
2	1.22	0.80	0.35	26	33	+7
3	3.00	0.65	0.25	29	37	+8
4	3.65	0.55	0.20	33	44.5	+11.5

Figure 6 displays relative humidity measured 7.5 cm above the soil surface versus time for experiment number 2. Based on this data, relative humidity above the soil surface is approximately equal to the incoming relative humidity of the ambient air upstream of the tank, which typically varied between 0.05 – 0.10. Thus, no effect from evaporation was observed at this height above the soil surface; water evaporating from the soil surface

was drawn downstream of the tank prior to reaching a height of 7.5 cm above the soil surface. This trend applies to all the experiments.

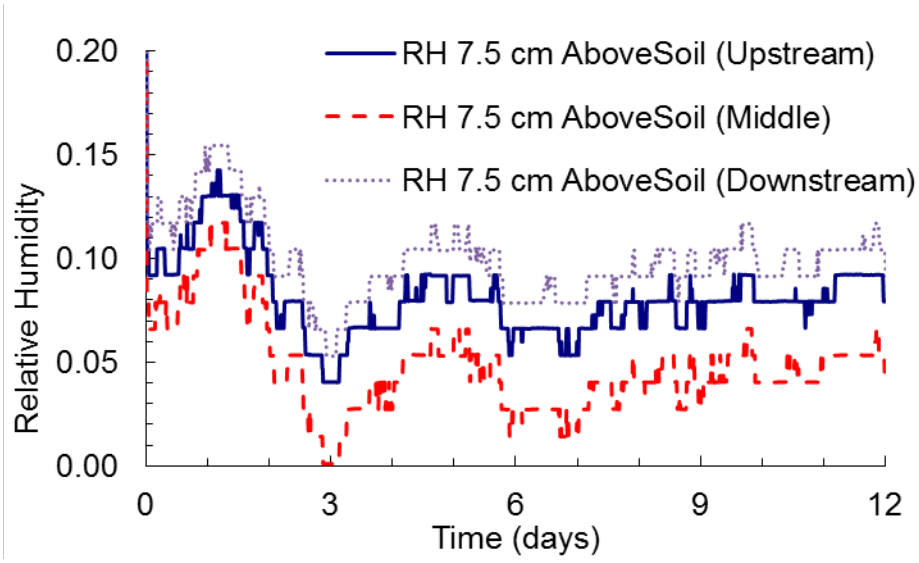

Figure 6. Relative humidity measured 7.5 cm above the soil surface at upstream, middle and downstream of the tank.

Temperature

As previously discussed in Section 3.2 and 3.3, for each experiment, source temperature was kept constant at approximately 40°C using a temperature control system regulated by an infrared temperature sensor placed on the ductwork. **Figure 7** displays the air temperature measured on the soil surface, 7.5 cm above the soil surface, upstream, in the middle and downstream of the tank.

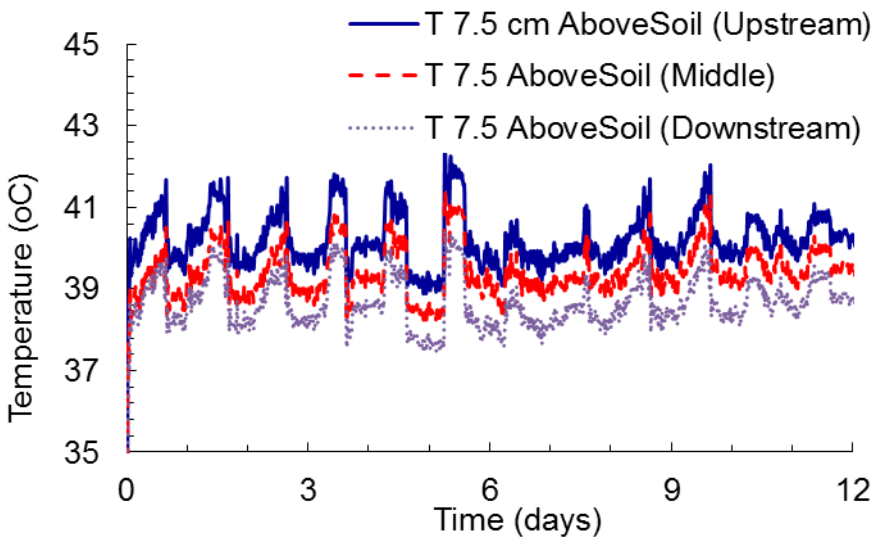

Figure 7. Temperature measured 7.5 cm above the soil surface at upstream, middle and downstream of the tank.

Based on this data, there is an apparent diurnal fluctuation in temperature, which may be due to changes in atmospheric conditions, variability in the temperature control system and/or temperature of the ductwork. There is also incremental heat loss from the upstream boundary to the downstream boundary of the tank. Observed heat loss from the upstream to downstream boundary may be influenced by the presence of the thermal sensors themselves; the thermal sensors have different thermal properties than the atmosphere, which could lead to perturbations of the thermal field. Overall heat loss across the tank was estimated by subtracting the upstream/incoming duct air temperature from the downstream/outgoing duct air temperature. A similar trend was observed in all experiments, as shown in **Table 5**.

Table 5. Summary of Ambient Air Temperature Upstream and Downstream of Tank

Experiment Run #	Wind Velocity (m/s)	Air Temperature Upstream (°C)	Air Temperature Downstream (°C)	Change in Air Temperature (°C)
1	0.55	41	35	-6
2	1.22	41	35	-6
3	3.00	42	38	-4
4	3.65	46	41	-5

Figure 8a shows soil temperature versus time for experiment number 2 for depths of 2.5 cm (Sensors 3), 7.5 cm (Sensors 8), 12.5 cm (Sensors 13), and 17.5 cm (Sensors

18). Sensors are numbered as labeled in **Figure 3**a. As evident in the figure, the deeper the sensor, the less influence the surface temperature and wind velocity have on the local temperature. We observed that soil temperature remained quite unchangeable with time below a depth of 15 cm (Sensors 16-25). **Figure 8**b shows temperature versus time for this experiment for a depth of 2.5 cm (Sensors 1, 3, and 5). We can observe here a difference in temperature for the same depth sensors. Sensor 3 is placed at the middle of the soil tank and, at this location, there is less heat loss compared to Sensor 1 and Sensor 5 located at the left and right side of the tank, respectively. Therefore, we observe a higher temperature for this sensor than two others. Finally, the temperature at the upstream is always higher than the downstream in the wind tunnel; therefore, Sensor 5 shows a higher temperature than Sensor 1. We will see in the next section that these differences create an asymmetrical saturation profile in the soil tank.

(a)

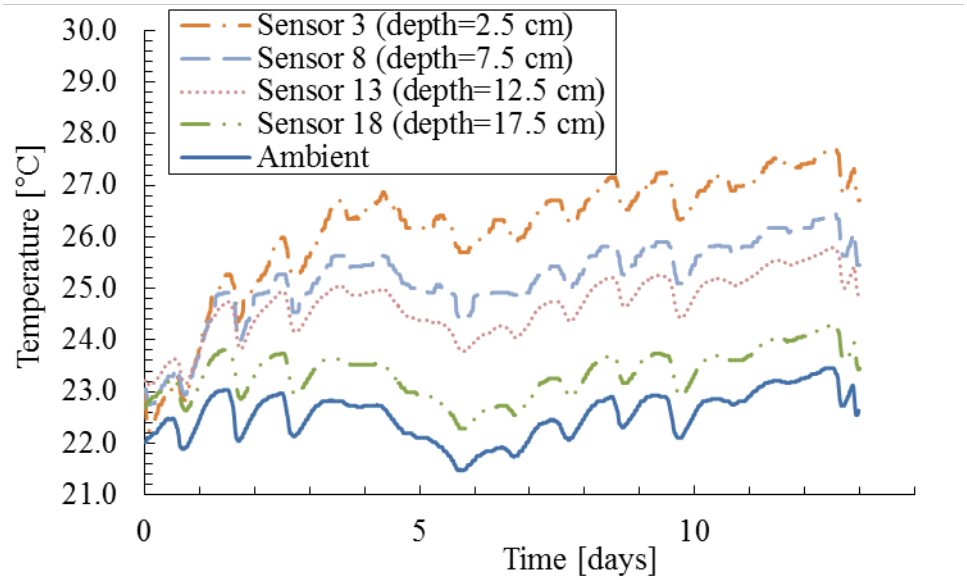

(b)

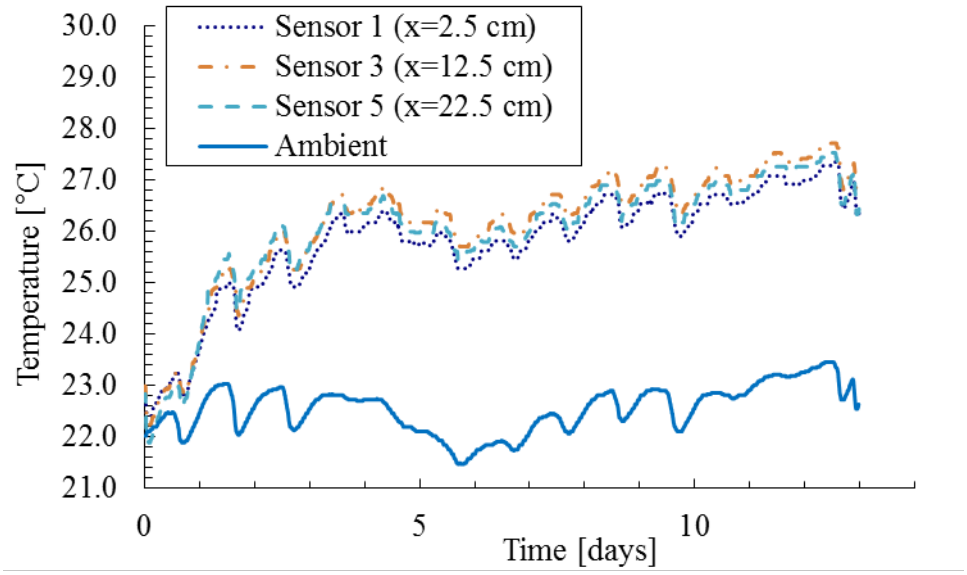

Figure 8. Evolution of soil temperature measured (a) vertically at the middle of soil tank and (b) horizontally at depths of 2.5 cm.

Saturation

Figure 9a shows the soil saturation measured over time for experiment number 2 (U=1.22ms^{-1}) for soil depths of 2.5 cm, 7.5 cm, 12.5 cm, and 17.5 cm. For each experiment, the soil remained saturated below a depth of 15 cm (Sensors 16 to 25). Saturation values were calculated for each experiment using the empirical two-point α-mixing model from [Sakaki et al., 2008]. This method requires knowledge of the water saturated and air dry sensor analog-to digital converter (ADC) counts and soil porosity Although it is known that performance of dielectric permittivity sensors is temperature dependent due to the changes in the electrical characteristics of the soil with temperature (e.g. [Assouline et al., 2010; Bogena et al., 2007; Kizito et al., 2008; Seyfried and Grant, 2007]), the method developed by Sakaki et al. (2008) does not account for temperature dependency. Assouline et al. (2010) concluded that care must be taken in interpreting "subtle" changes in the apparent dielectric permittivity under conditions where temperature fluctuations are significant, for example, close to the soil surface under diurnal temperature conditions. Although the diurnal temperature variations in the experiments reported here were rather small (maximum of 4ºC difference, 2.5 cm below the soil surface), we amended this method to correct for temperature sensitivity using the method outlined in [Cobos and Campbell, 2013]. The maximum temperature sensitivity of the measurements was relatively small (0.002 cm^{3}cm^{-3}) but should be accounted for, as

pointed out by Assouline et al., (2010), especially when analyzing soil water profiles in the shallow subsurface. Bogena et al. (2007) used a two-step calibration method to develop preliminary models for estimating dielectric constant as a function of temperature [Bogena et al., 2007]. According to Bogena et al. (2007), for the soil temperature ranges reported here within (approximately between 23-27^{o}C), the maximum error in soil water content due to temperature effects on the sensor circuitry is 0.4 vol %. Seyfried and Grant (2007) found that for temperatures ranging from 5 to 45^{o}C, the maximum apparent water content change is ± 0.028 cm^3cm^{-3} for saturated soils while the effect of temperature on dry samples was not detectable [Seyfried and Grant, 2007].

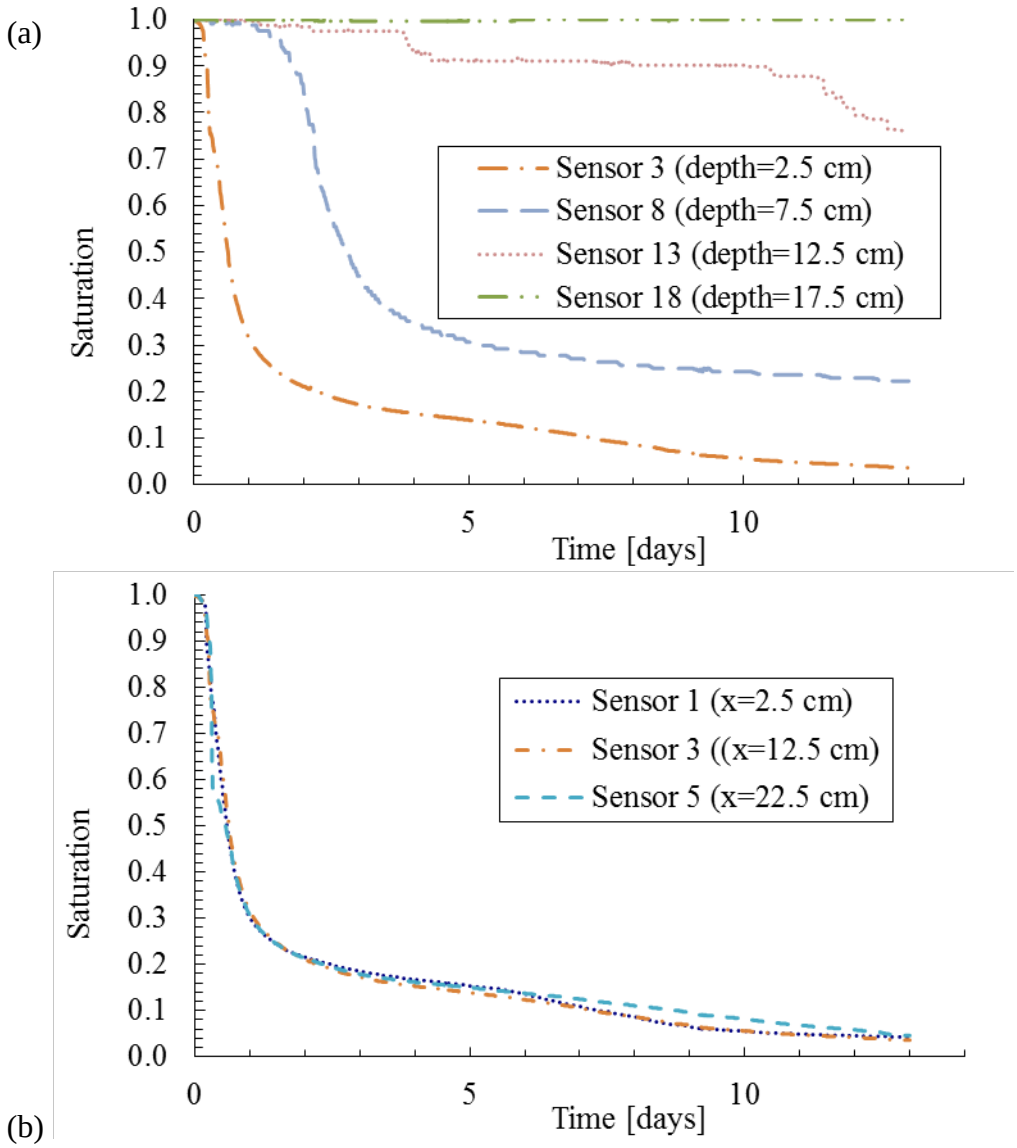

Figure 9. Evolution of soil saturation measured (a) vertically at the middle of soil tank and (b) horizontally at a depth of 2.5 cm.

Based on these saturation curves, (Figure 9a), it appears that the primary, capillary-driven drying front associated with Stage-1 evaporation moves relatively fast through the first row of sensors (i.e. Sensor 3 located 2.5 cm under the soil surface) and reaches the second row, at a depth of 7.5 cm, by the first day. This drying front moves slower through this second row of sensors, i.e. more gently sloping saturation curve for Sensors 6-10 compared to Sensors 1-5, as evaporation appears to transition to Stage-2 evaporation by about the second day. The primary drying front reaches the third row of sensors, at a

depth of 12.5 cm, by the third day. Based on the gentle slope of the saturation curves by the third day, it appears that there is a secondary, diffusion-driven drying front, associated with Stage-2 evaporation, which is slowly transporting water to the soil surface. This general trend was observed in all the experiments; more gently sloping saturation curves were noted for experiments with wind velocity <1.22 m/s and more steeply dipping saturation curves for those experiments with wind velocity >1.22 m/s. Figure 9b shows saturation versus time for experiment #2 for a depth of 2.5 cm (Sensors 1, 3, and 5). We can observe a light asymmetrical distribution of saturation in the soil tank near the soil surface. This asymmetrical behavior may come from the difference in temperature upstream and downstream of the wind tunnel and as discussed above, slightly affect the saturation readings. The kinetic of the cumulative evaporation is plotted in Figure 10 for four different free flow maximum average wind speeds (U) of 0.55, 1.22, 3.00, 3.65 meters per second. This figure shows clearly that the wind speed has a considerable effect on the evaporation processes. Here, increasing the wind speed increases the total evaporation. Increasing wind speed has a great effect on the initial evaporation rate then its influence becomes smaller. These observations are indicative of the two distinct stages of bare soil evaporation. Stage-1 evaporation is an atmosphere-controlled stage in which the evaporation rate is relatively high and relatively constant due to high atmospheric demands (i.e., high temperatures and wind velocity at the soil surface) and predominantly independent of soil water content [Lehmann et al., 2008; Shokri et al., 2010]. A transition regime, evaporation is driven by capillary transport and occurs at or near the rate of free-water evaporation [Bittelli et al., 2008; Dingman, 2002]; Yiotis et al., 2003; Lehmann and Or, 2009]. However, experimental evidence suggests that Stage-1 evaporation may not always be high and constant but rather drop from the onset of the drying process. This drop, as seen in the experimental data presented here, is often associated with high wind velocities with a thin boundary layer and large soil pores [Shahraeeni et al., 2012]. Stage-2 evaporation, also known as the falling rate period, is a soil-controlled stage in which the evaporation rate is relatively low and controlled by the rate at which water can be transmitted to the soil surface in response to potential gradients induced by upward-decreasing soil water contents, rather than atmospheric demands. This evaporation is driven by diffusive transport and is less than the rate of free-water evaporation [Dingman, 2002; Lehmann et al., 2008; Yamanaka et al., 2004]. As anticipated, due to the greater atmospheric demand, i.e. faster wind velocity, experiments with wind velocity 1.22 m/s,

the constant relative humidity (or Stage-1 evaporation) was approximately 2 – 3 days, whereas, experiments with wind velocity >1.22 m/s, Stage-1 evaporation was approximately 1 – 1.5 days.

From the comparison of the slopes of the curves (Figure 10), we can see that the evaporation rate is faster for a higher wind speed for the first stage of the evaporation processes. However, the wind speed has less influence over time in the second stage (diffusion-dominant) evaporation. Increasing wind speed, increases the first stage evaporation rate and decreases the transition time from first stage to second stage evaporation. For high values of wind speed, evaporation becomes less dependent on changes in wind velocity. The evaporation rate in the diffusion-dominant regime seems to decrease for high values of wind speed. The origin of this diffusion flux reduction may be due to the turbulence at the soil surface. In order to prove this phenomenon, further experiments are needed. This issue will be investigated in future work.

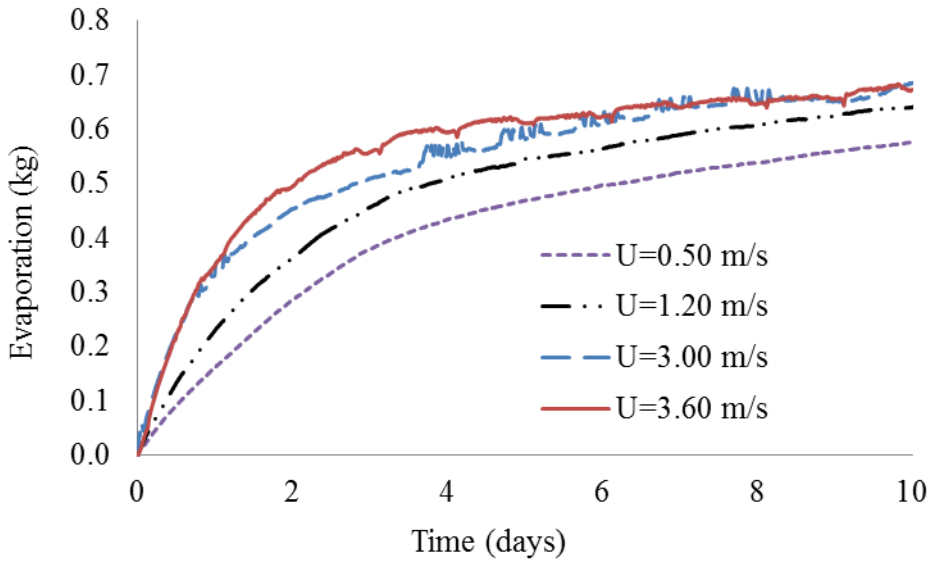

Figure 10. Kinetic of cumulative evaporation for different wind speeds (U= maximum wind speed in free medium).

In the next section, we compare experimental results with our numerical model to better understand any discrepancies between theory and experiments and the validity of the proposed model.

6.4.2 Numerical simulation and comparison with experimental results

To validate the proposed two-dimensional, non-isothermal, non-equilibrium coupled evaporation model, the numerical results for temperature, saturation and evaporation rate are compared with experimental results. The subdomains, porous media properties, boundary conditions and initial values are depicted in **Figure 11**. Here, the heat source is imposed in the same direction as the experimental wind speed (right-hand side of the wind tunnel). In reality, changing wind speed in the experimental setup can change the heat loss rate in the free medium and influence the evaporation rate. Therefore, before comparing the experimental and numerical results, we first show the sensitivity of the model to some parameters e.g. free flow thermal and solutal dispersion, wind speed, wind temperature and vapor concentration, Beavers-Joseph slip coefficient, soil permeability and porosity, and soil residual water content, respectively. In this parametric study, we have neglected the heat loss in the free flow domain. This approach also allows us to use very small wind velocities that are difficult to generate experimentally.

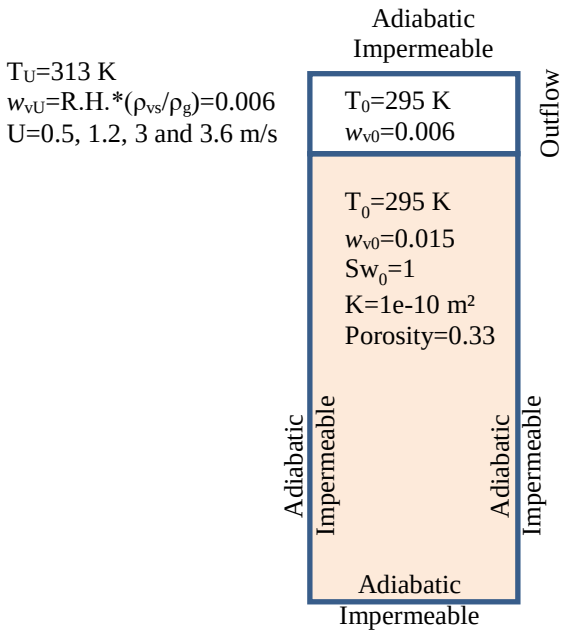

Figure 11. Subdomains, boundary conditions and initial values of experimental case.

Effect of free flow thermal and solutal dispersion

Because the Péclet numbers that correspond to the heat and mass transfer in the free-flow region of our experimentation are high, we cannot ignore thermal and solutal dispersion. An average wind speed of 1 m/s, with free flow height of H=0.21 m (see the experimental configuration of **Figure 3**) results in $Pe_T = 11235$ and $Pe_C = 9975$ from equation (7). From Equations (7) and (5), the ratio of the effective coefficients to the molecular diffusion and conduction coefficients becomes very significant. These high values clearly show the importance of thermal and solutal dispersion in the free medium domain in this study. To show the importance of including solutal and thermal dispersion in the free flow domain on the evaporation processes, simulated cumulative evaporation for U=1 m/s with and without considering disperison are plotted in **Figure 12**. As we can see, there is a significant difference between the two cases, demonstrating the importance of including atmospheric system dispersion in evaporation modeling efforts.

To better understand the effect of dispersion in the free flow regime on the evaporation rate, a comparison was made between the results from two models, with and without dispersion. Surface plots of temperature and concentration at day one are depicted in **Figure 13** for the two models. Comparing the temperature profiles of **Figure 13**a and 13b (with and without considering dispersion) shows that the thermal dispersion causes an increase in temperature with a more uniform heat distribution on the soil surface and therefore, increasing evaporation. Here, the temperature distribution on the soil surface is asymmetric without considering the dispersion (**Figure 13**a). However, temperatures measured on the upstream and downstream soil surface do not show a significant asymmetrical behavior (see Figure 5). Comparing **Figure 13**a and 13b also shows how the dispersion causes the replacement of the humid air on the soil surface with the dry air flowing through the wind tunnel. Therefore, the air demand for evaporation increases and the evaporation process is enhanced.

A vertical profile of temperature and vapor concentration at the middle of the soil tank is plotted in **Figure 14** at one and 11 days, for two cases (with and without considering the dispersion in free flow region). We can see clearly that considering the dispersion in free flow increases the temperature and decreases the vapor concentration on the soil surface, which enhances the evaporation processes.

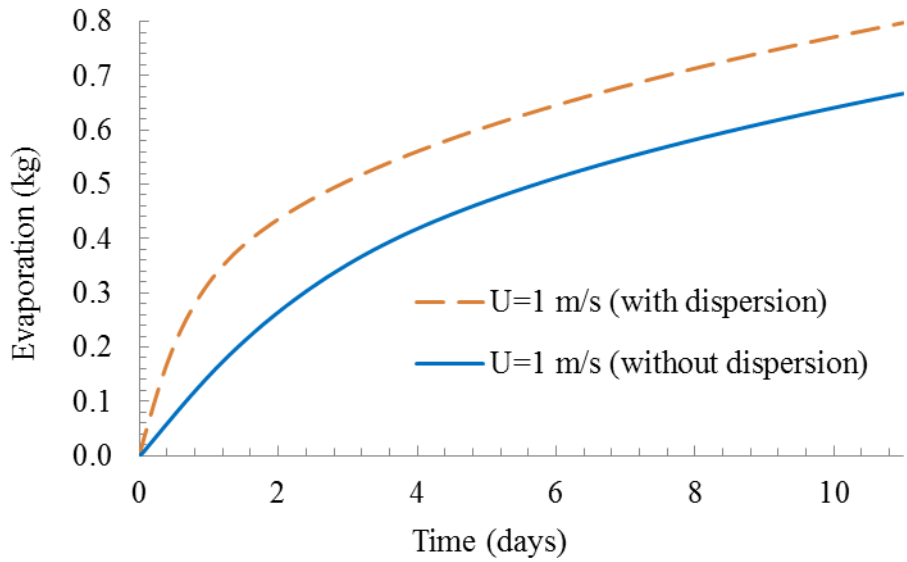

Figure 12. Comparison between evaporation processes with and without taking dispersion in the free flow domain into account ($K=1\times10^{-10}$ m^2, $S_{wr}=0.075$, $U=1$ m/s, $T_U=313$ K, $w_{vU}=0.006$, $\alpha_{BJ}=0.01$, $\phi=0.33$)

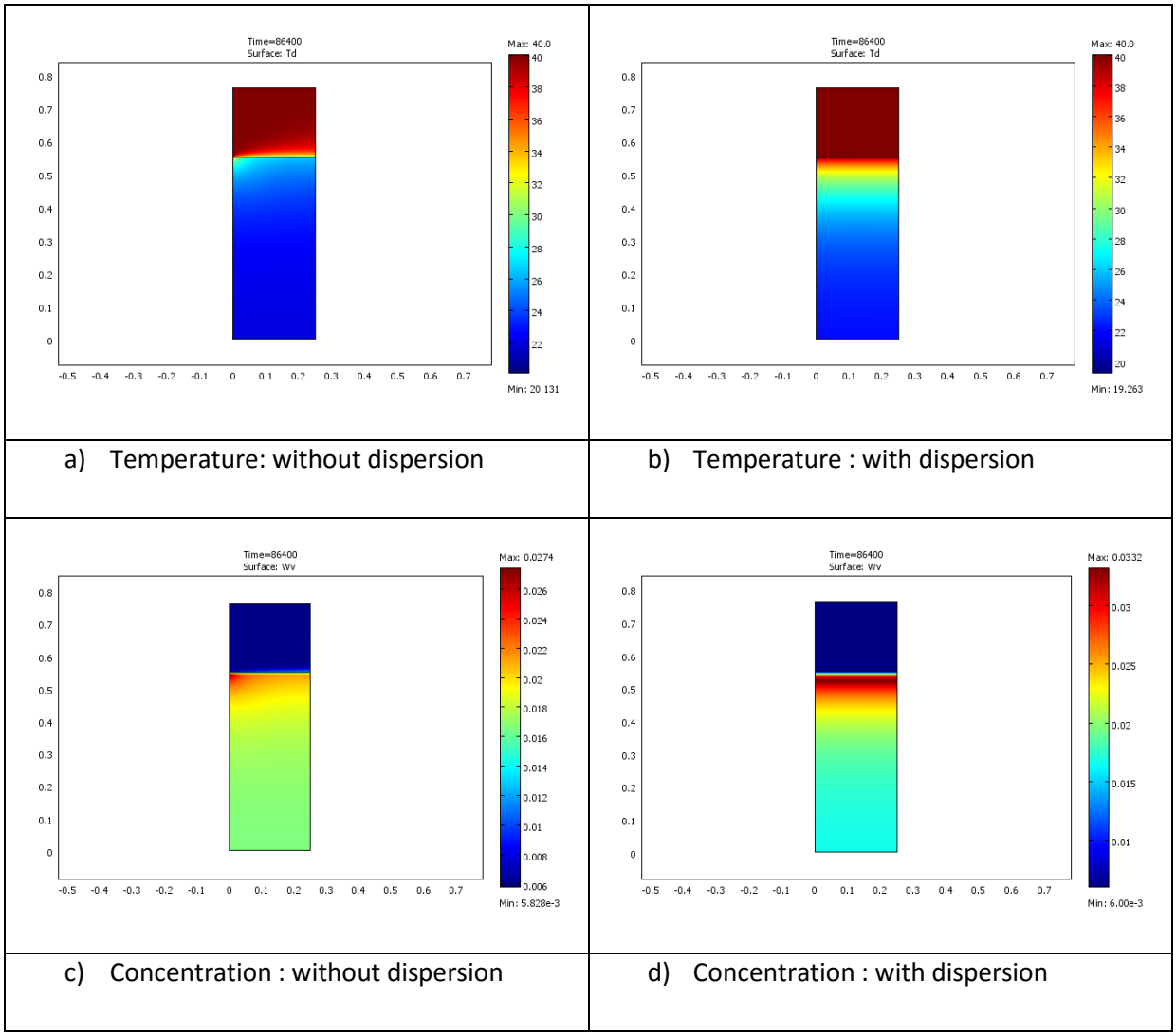

a) Temperature: without dispersion

b) Temperature : with dispersion

c) Concentration : without dispersion

d) Concentration : with dispersion

Figure 13. Temperature and vapor concentration surface plot with and without considering free flow dispersion ($K=1\times10^{-10}$ m^2, $S_{wr}=0.075$, $U=1$ m/s, $T_U=313$ K, $w_{vU}=0.006$, $\alpha_{BJ}=0.01$, $\phi=0.33$).

.

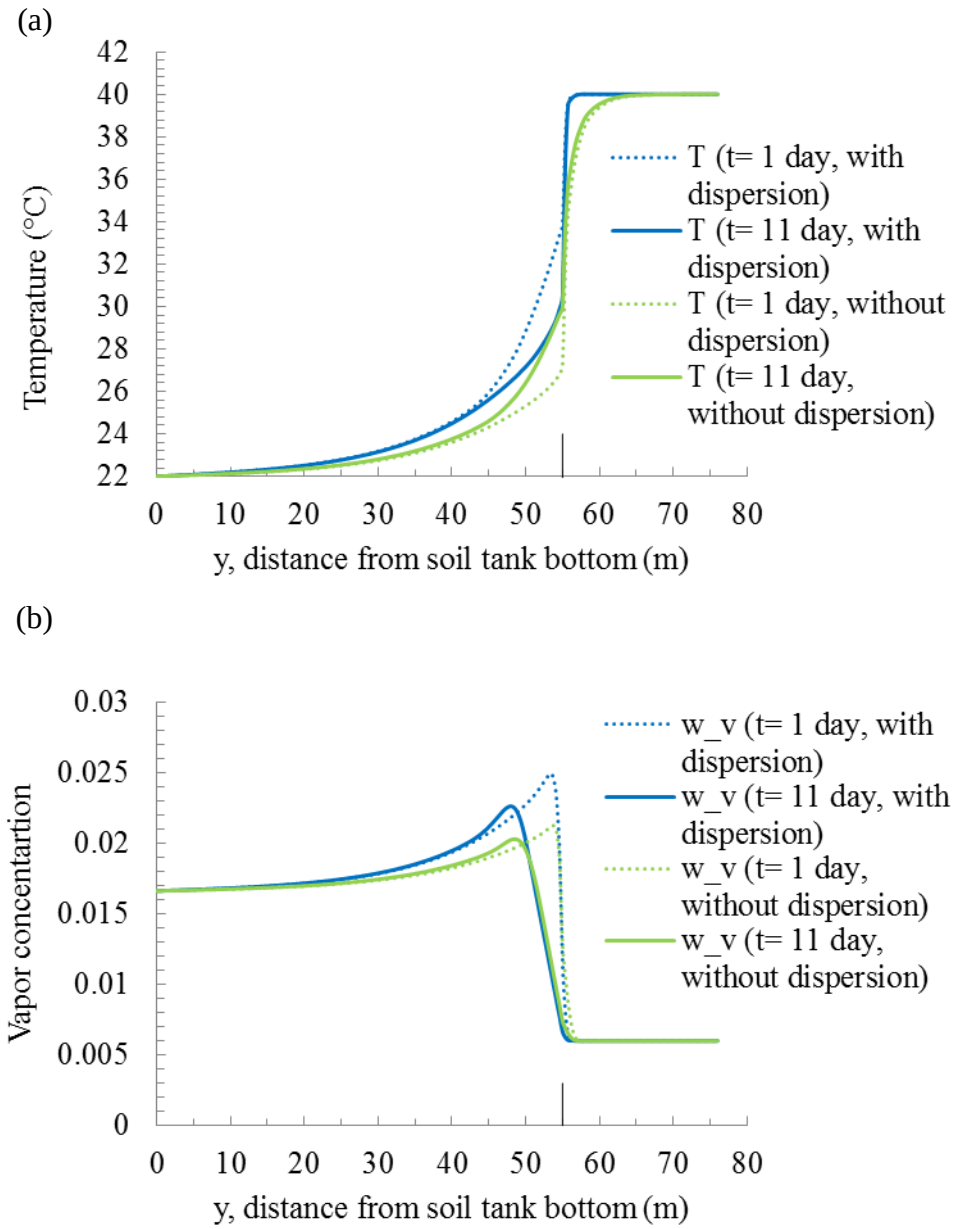

Figure 14. Comparisons of (a) temperature and (b) vapor concentration profile between with and without considering dispersion after t=1 and 11 days for soil profile at tank center ($K=1\times10^{-10}$ m^2, $S_{wr}=0.075$, U=1 m/s, $T_U=313$ K, $w_{vU}=0.006$, $\alpha_{BJ}=0.01$, $\phi=0.33$).

Effect of wind speed

Figure 15 shows simulation results for a range of wind speeds between 0.002 m/s and 6 m/s. This figure clearly shows that the wind speed has a considerable effect on the drying processes in non-isothermal system. Increasing the wind speed increases the first stage evaporation rate and decreases the transition time between two evaporative stages

(soil water flow regime to water vapor diffusion controlled regime) at low velocity values; then, at high values of wind speed the evaporation rate becomes less dependent and finally independent on wind speed. On the contrary, the impact of wind speed on second stage evaporation (diffusion-dominant stage) is not significant.

Increasing the wind speed in a non-isothermal system increases the heat and mass transfer by convection in free flow region. The thermal and solutal dispersion becomes more and more important. Therefore, the temperature is increased and the vapor concentration becomes the same as the wind vapor concentration above the soil surface.

As the experimental results also show in Figure 10, one can distinguish a critical velocity value from which the evaporation is no longer dependent on the wind speed. At the critical wind speed, the temperature rises to the wind temperature and the vapor concentration falls to the wind vapor concentration above the soil surface. Therefore, a higher wind speed cannot change the evaporation processes.

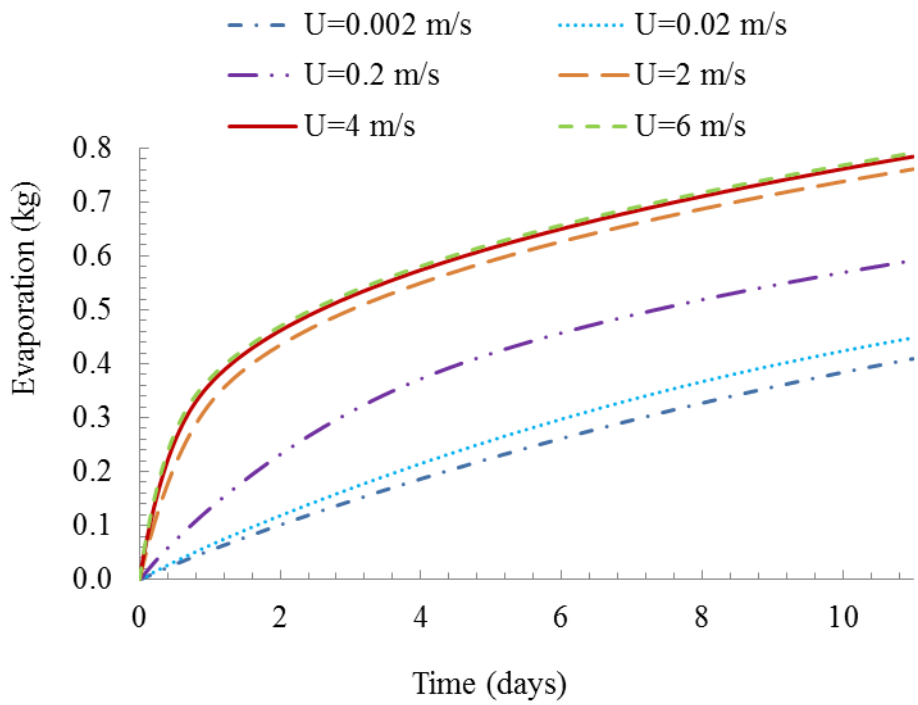

Figure 15. Impact of wind speed on evaporation processes in a non-isothermal system ($K=1\times10^{-10}$ m^2, $S_{wr}=0.075$, $T_U=313$ K, $w_{vU}=0.006$, $\alpha_{BJ}=0.01$, $\phi=0.33$).

Effect of wind temperature and vapor concentration on evaporation

The effect of wind temperature on evaporation processes from the soil was tested by comparing three theoretical models, T_U= 22 °C (isothermal case), 30 °C and 40 °C (experimental reference case). Figure 16 provides a comparison of the cumulative evaporation with these different wind temperature levels. Increasing the wind temperature enhances the evaporation from the soil tank and decreases the transition time from a capillary-dominated evaporation regime to the diffusion-dominated regime. The phase change rate increases with an increase in soil surface temperature. As a consequence, the evaporation increases, the interface dries out faster and the transition happens earlier. However, according to Figure 16, changing the wind temperature does not significantly change the evaporation rate during Stage-2 evaporation.

The variations of the wind water vapor concentration are tested in **Figure 17** for the vapor mass fractions of 0.000, 0.015, and 0.030, respectively. Here, the drier the air blowing across the soil surface, the higher the cumulative evaporation in both stages. Similar to temperature effects, the soil surface dries faster with a lower vapor concentration and therefore transition between the two evaporation phases occurs earlier. The vapor concentration gradient and air capacity for evaporation is higher for the dryer air blowing on the soil surface; therefore, the evaporation process enhanced.

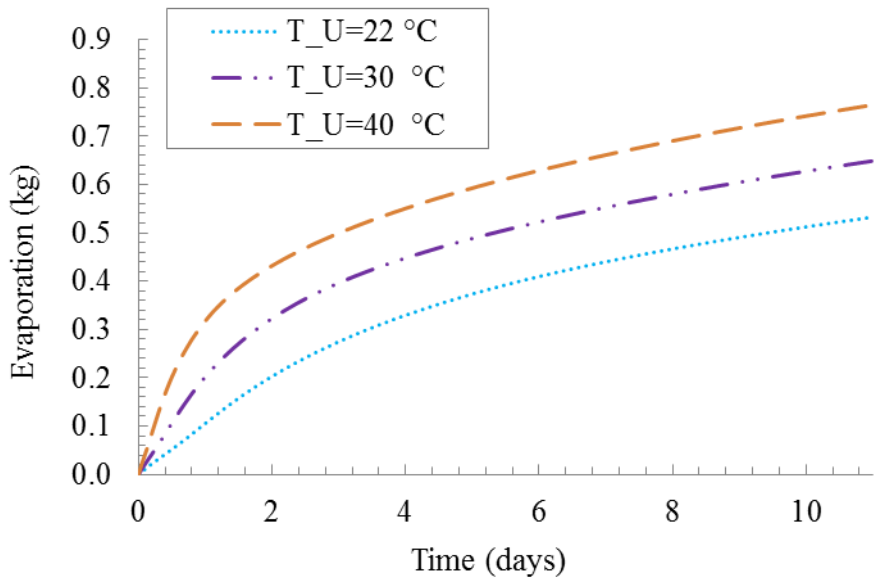

Figure 16. Effect of wind temperature on drying process ($K=1\times10^{-10}$ m^2, $S_{wr}=0.075$, U=1 m/s, $w_{vU}=0.006$, $\alpha_{BJ}=0.01$, $\phi=0.33$).

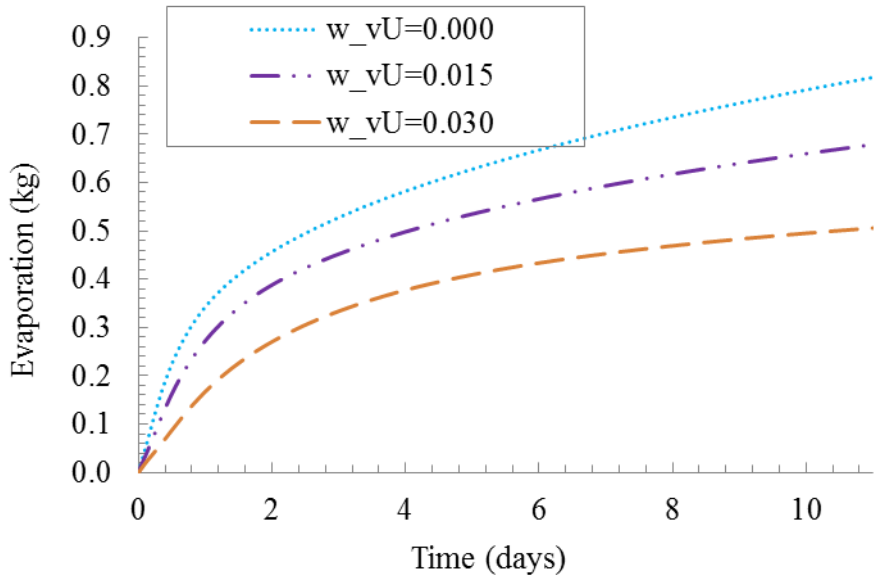

Figure 17. Effect of wind vapor quantity on drying process ($K=1\times10^{-10}$ m^2, $S_{wr}=0.075$, $U=1$ m/s, $T_U=313$ K, $w_{vU}=0.006$, $\alpha_{BJ}=0.01$, $\phi=0.33$).

Effect of slip coefficient (α_{BJ})

The influence of the Beavers-Joseph coefficient on the drying process is examined by varying α_{BJ} in the range of 0.01 to 10. Results for cumulative evaporation versus time (Figure 18) show that the Beavers-Joseph slip coefficient, α_{BJ} , slightly influences the resulting cumulative evaporation but not significantly. This observation is consistent with the results in Baber et al. (2012). Therefore, the choice of the Beavers-Joseph coefficient has a small influence on the evaporation rate across the interface.

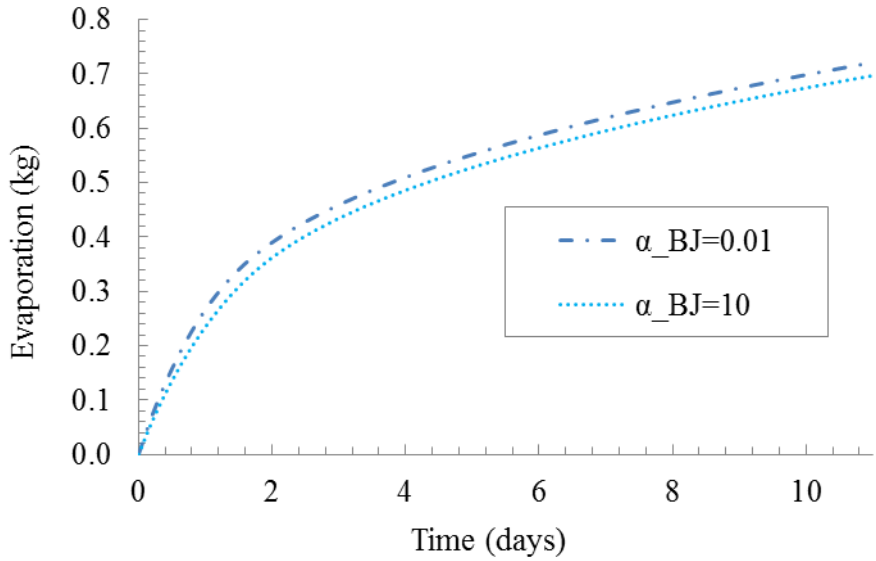

Figure 18. Effect of Beavers-Joseph slip coefficient on drying process ($K=1\times10^{-10}$ m^2, $S_{wr}=0.075$, U=1 m/s, $T_U=313$ K, $w_{vU}=0.006$, $\phi=0.33$).

Effect of porous medium permeability (k)

We tested three different porous media permeabilities: $k=10^{-9}$ m^2, 10^{-10} m^2 and 10^{-11} m^2. As depicted in **Figure 19**, changing the permeability does not change the first stage evaporation rate significantly. However, increasing the permeability increases the transition time between two evaporation stages, which affects the cumulative evaporation.

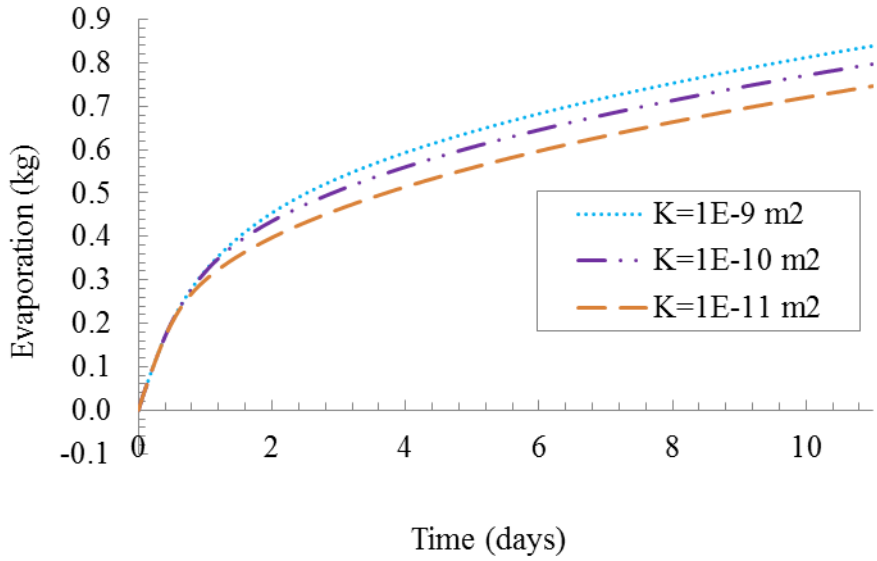

Figure 19. Effect of porous medium permeability on drying process ($S_{wr}=0.075$, U=1 m/s, $T_U=313$ K, $w_{vU}=0.006$, $\alpha_{BJ}=0.01$, $\phi=0.33$)

Effect of porous medium porosity (ϕ)

The cumulative evaporation for different porous medium pore volume fractions (porosity), over 11 days is plotted in **Figure 20**. As these results show, porosity has a great influence on evaporation process in porous media.

Increasing the porous medium pore volume fraction increases considerably the amount of the cumulative water evaporation from the porous medium. It accelerates the evaporation rate in the capillary-driven evaporation regime and enhances the diffusive flux in the diffusion-dominated regime. For example, increasing the porosity of porous medium of 0.10 to 0.33 can increase the amount of the evaporation about four times.

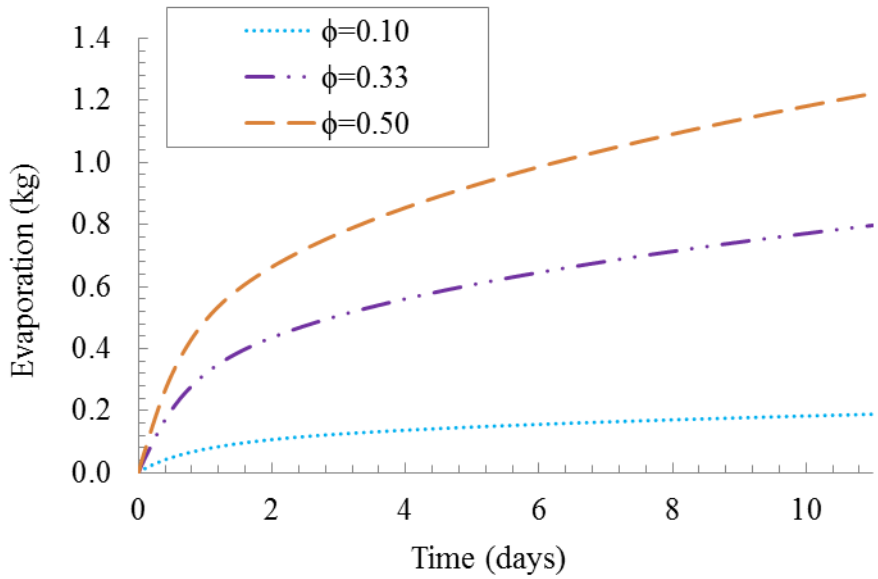

Figure 20. Effect of porous medium porosity on drying process ($K=1\times10^{-10}$ m^2, $S_{wr}=0.075$, U=1 m/s, $T_U=313$ K, $w_{vU}=0.006$, $\alpha_{BJ}=0.01$).

Effect of porous medium residual saturation (S_{wr})

The sensitivity of the model is also examined by varying the water residual saturation (S_{wr}) in the porous medium. The results of evolution of cumulative evaporation are plotted in **Figure 21**, for different S_{wr} values. Here, changing the residual saturation does not change the first stage evaporation rate significantly. The transition time occurs earlier for higher water residual saturation. However, increasing the residual saturation decreases the evaporation rate in the second evaporation stage considerably. Higher soil residual saturation causes a higher tortuosity factor at the diffusion-dominant regime which reduces the diffusion flux to the soil surface and decreases the evaporation rate.

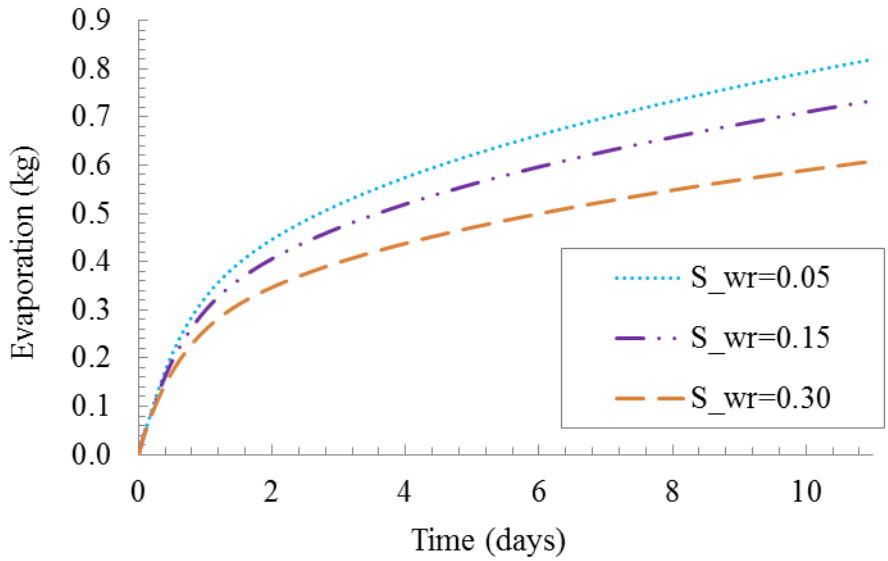

Figure 21. Effect of residual saturation on drying process ($K=1\times10^{-10}$ m^2, U=1 m/s, T_U=313 K, w_{vU}=0.006 , α_{BJ}=0.01, ϕ=0.33).

Impact of the sensors

The sensors themselves have different thermal properties than the porous medium, which could lead to perturbations of the heat and mass transfer in the system. To study the impacts of the sensors on the evaporation process, we simulated the theoretical model with a 2D geometry crossing on the soil temperature sensors. Each sensor was included in the model as a square, 0.075 m of length, corresponding to the sensor diameter. The soil moisture sensors are stainless steel and completely water proof with a thermal conductivity of 16 W/(m.K), density of 798 Kg/m3 and heat capacity of 520 J/(Kg.K). **Figure 22** shows

the results of the cumulative evaporation for the model with and without consideration of the sensors. Results show that the soil sensors increase the first stage evaporation rate by approximately 2%. This is principally due to the sensors improving the thermal conduction in the porous medium. Although the sensors enhance the heat transfer by conduction in the soil, they also favor heat loss from the soil. When considering the sensor in the theoretical model, the evaporation rate decreases about 5% for the second stage evaporation. The sensors decrease the tortuosity of the porous medium and therefore increase the diffusion flux of the water vapor from the soil to the soil surface. The comparison results in the next section come from the model geometry without the sensors. However, the results are modified according to the impact of the sensor percentage calculated in this section.

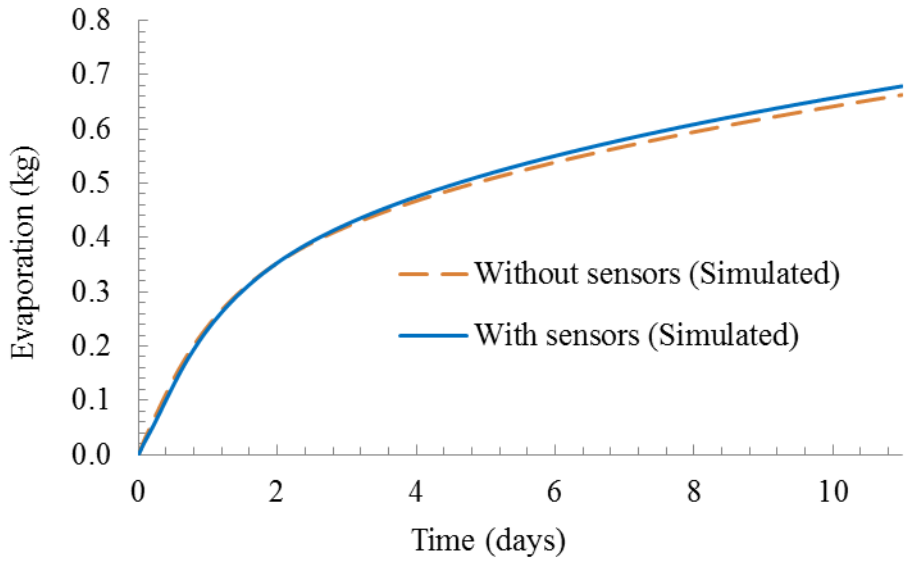

Figure 22. Impact of the sensors on drying process ($K=1\times10^{-10}$ m^2, $S_{wr}=0.075$, U=1.2 m/s, $T_U=313$ K, $w_{vU}=0.006$, $\alpha_{BJ}=0.01$, $\phi=0.33$)

In the next section, comparing these results with experimental results is done to understand the amount of discrepancy between theory and experience and the validity of the proposed model.

6.4.3 Comparison with experimental results

Observed and simulated evaporation rates for wind speeds of 0.55 m/s and 1.2 m/s are plotted in **Figure 23**a and 23b, respectively. We note that the flow regime in the free flow region is lamniar for these two wind speed values. The free flow wind mean temperature and mean concentration are chosen from the experimental data and imposed as a boundary condition in the free flow region upstream. Generally, there is good agreement between

model and experimental results, although in both cases, the model underestimated the evaporation rate for the regime transition period of the experiments. Although not shown, this was seen in the 3.0 and 3.6 m/s test cases as well. In all comparisions, however, the model could capture the transition behavior between Stage-1 and Stage-2 evaporation.

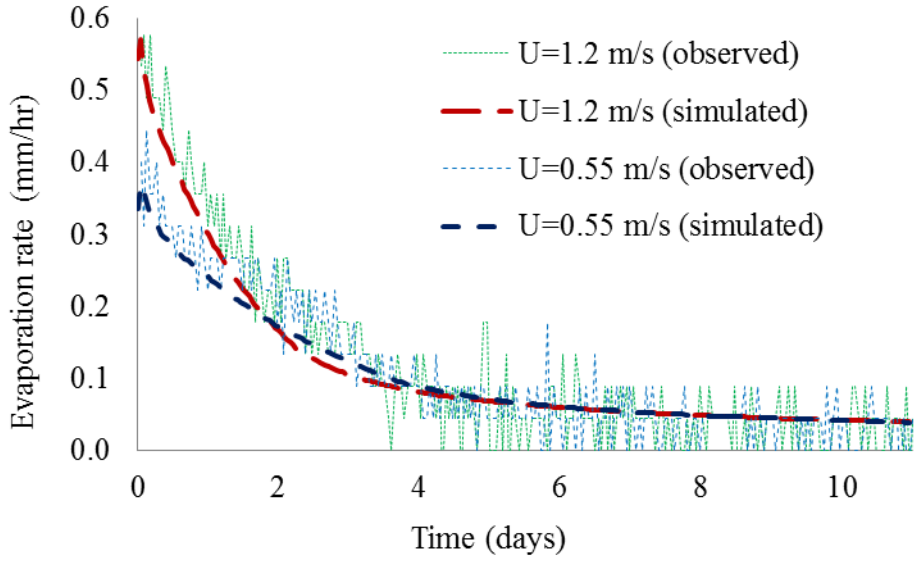

Figure 23. Comparison between experimental and theoretical evaporation rate results for U=0.55 m/s and U=1.2 m/s.

The evolution over time of the observed saturation (shown before in **Figure 9**) is compared with the simulated results in **Figure 24**a and 24b. Comparison between experimental and theoretical saturation results for U=1.2 m/s at x=0.125 m for different depths is plotted in **Figure 24**a. The model can predict the first and second stage evaporation with a good precision at a depth of 2.5 centimeters below the soil surface. However, the results for the second stage evaporation at a depth of 7.5 cm and 12.5 cm are over estimated. The origin of this discrepancy is that the model overestimates the temperature variation in soil at this stage of evaporation.

The simulated and experimental results of the saturation evolution are plotted in **Figure 24**b for U=1.2 m/s at 2.5 centimeter below the soil surface. The numerical results

of the saturation profiles do not show the asymmetric behavior across the soil tank horizontal axis.

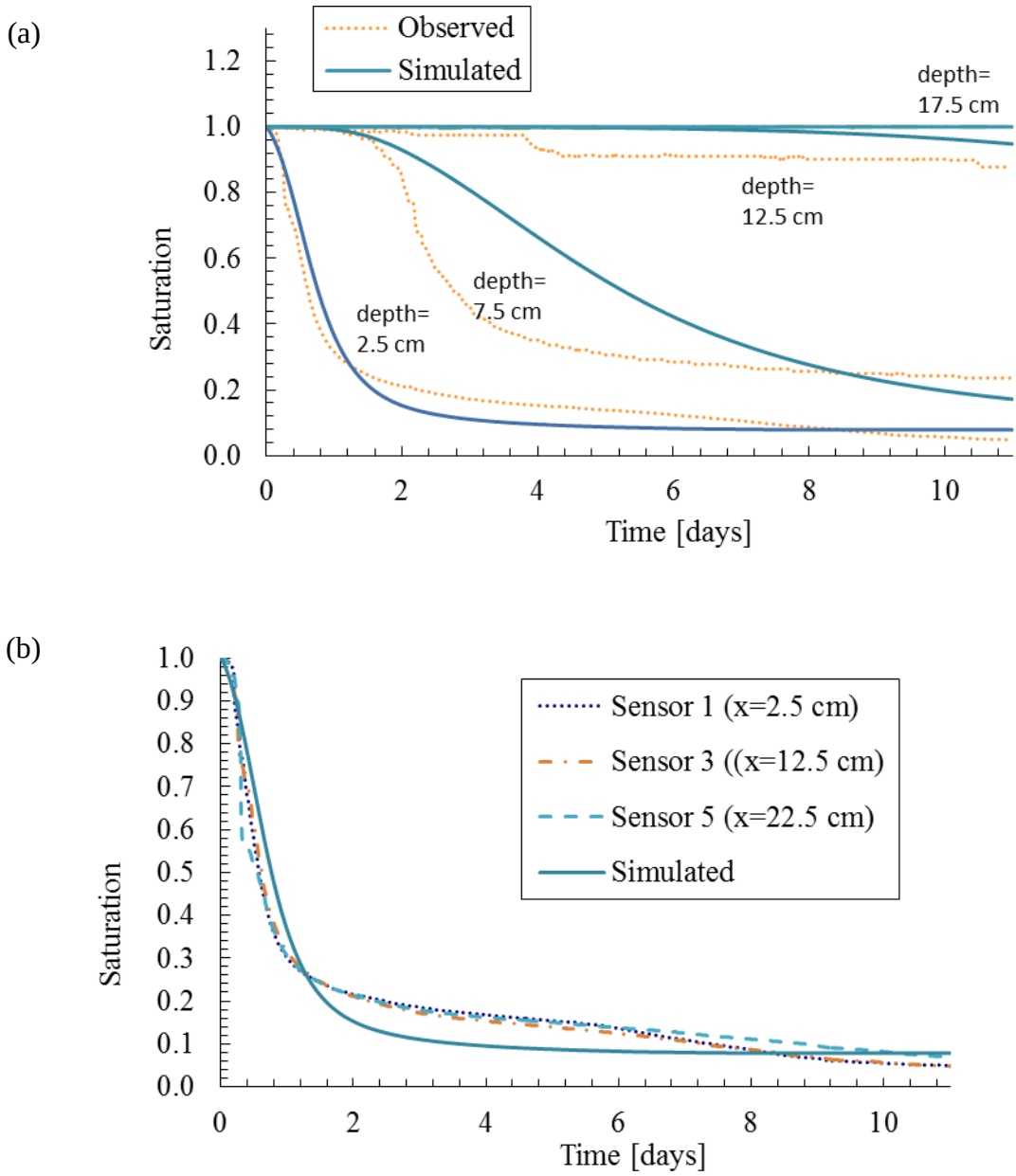

Figure 24. Comparison between experimental and theoretical saturation results for U=1.2 m/s at a) *x*=0.125 m b) depth of 0.025 m.

Figure 25a and 25b show the comparison between predicted and measured temperature and saturation profiles after 6.5 days at different depths, located along the centerline of the test tank. The observed and modeled temperatures and saturations agreed well for all locations over the entire duration of the experiments. This is statistically confirmed with the MIA values (range from 0.923-0.988). The deviations between

simulated and measured soil moistures and temperatures may, in part, be due the accuracy and resolution of the soil moisture sensors and thermistors compared to the model. The last experimental data point in Figure 25a corresponds to the temperature measured on the soil surface (see Figure 5).

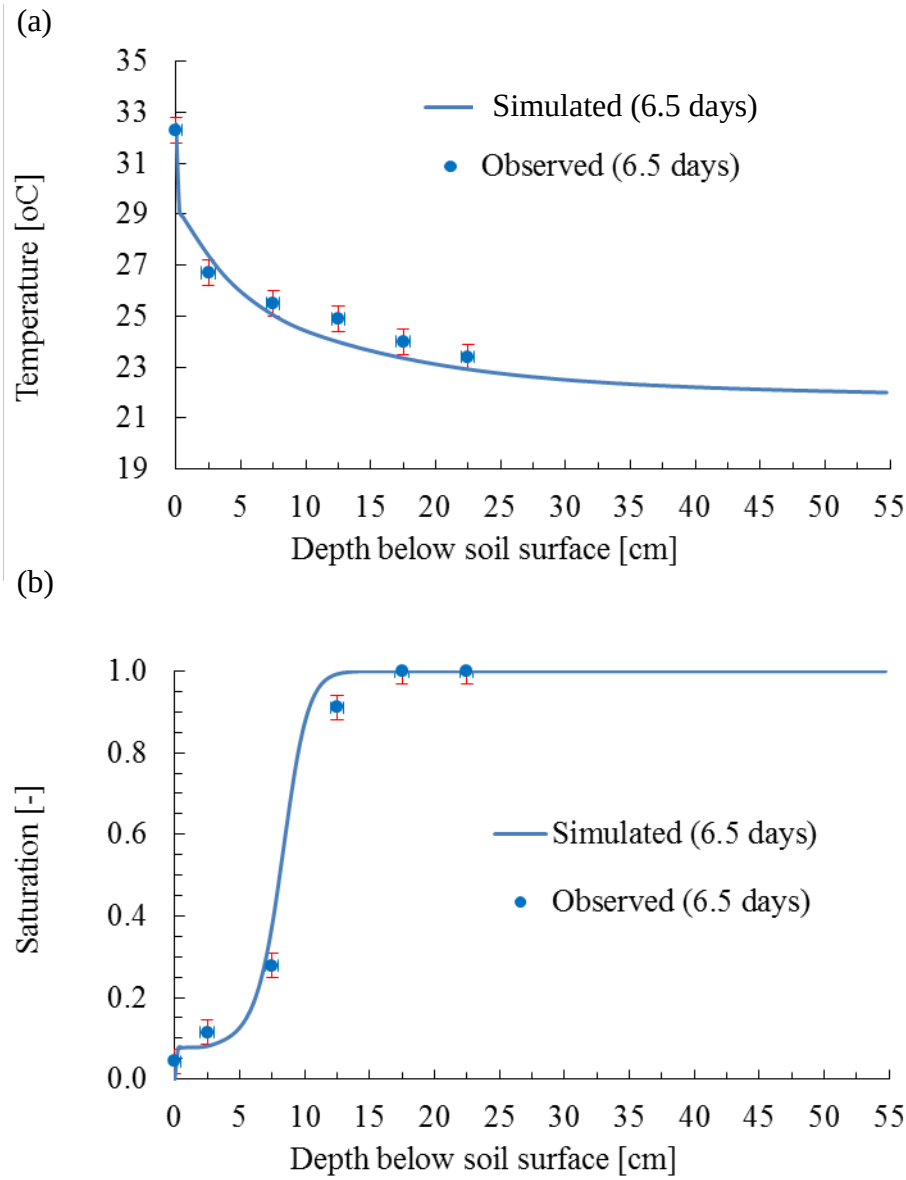

Figure 25. Simulated and observed (a) temperature and (b) saturation at t=6.5 days for soil profile at tank center (arc-length 0.125m).

Using the measured soil surface relative humidity and temperature data, we calculated the water vapor concentrations on the soil surface and compared them with corresponding vapor concentrations from the numerical simulation at differents depths. As seen in **Figure 26**, simulation results one centimeter beneath the soil surface fit the

experimental soil surface results better than than the simulation results from the soil surface. In an attempt to understand the relative humidity directly on the soil surface, the relative humidity sensors require good contact with the the gas phase in the soil pores so that the readings can better reflect that of the soil surface and not the surrounding air. It can be argued that in the process of maintaining good contact, the sensor is not reading the soil surface humidity but rather the relative humidity of some location beneath the soil surface. The model is able to correctly capture the kinetic form of the phemomena; however, there is a small dicrepency between the measured and simulated profiles. We note that, in this model, the evaporation rate and surface relative humidity are a direct outcome of the proposed model concept and not imposed as a boundary condition.

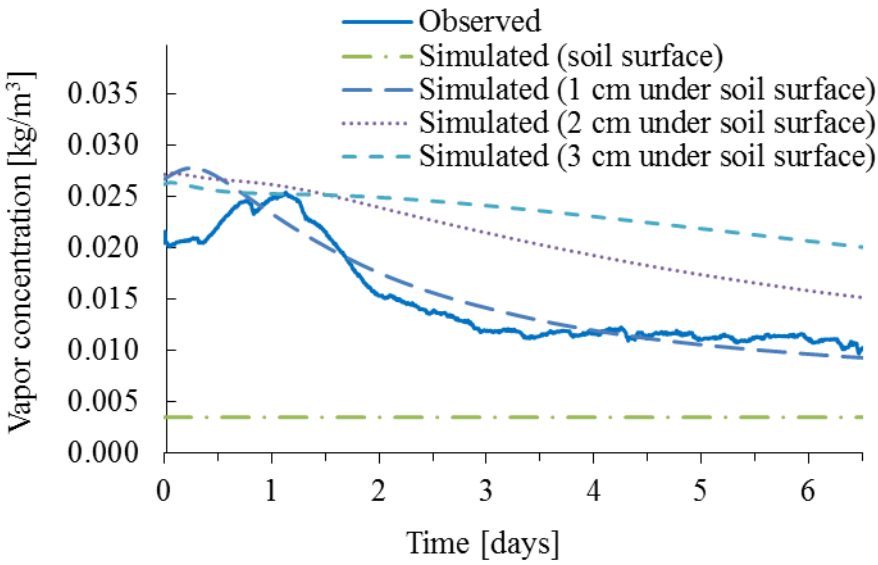

Figure 26. Simulated and observed vapor concentration with time on the soil surface (observed and simulated) and at locations 1,2, and 3cm below the soil surface for U=1.22 m/s.

6.5 Conclusion

With the goal of improving our understanding of the land/atmospheric coupling to predict the important process of bare soil evaporation, we developed a model based on the coupling of Navier-Stokes free flow and Darcy flow in porous medium. The model consists of the coupled equations of mass conservation for the liquid phase (water) and gas phase (water vapor and air) in porous medium with gas phase (water vapor and air) in free

flow domain under non-isothermal, non-equilibrium phase change conditions. The boundary conditions at the porous medium-free flow medium interface include dynamical, thermal and solute equilibriums, and using the Beavers-Joseph slip boundary condition. What is unique about this coupled model is that the evaporation rate and soil surface temperature conditions come directly from the model output. In order to experimentally validate the numerical results, we developed and used a unique two-dimensional test system with a wind tunnel placed above a soil tank equipped with a network of different sensors. The theoretical model sensitivities to the important soil and air properties are discussed. The parameter sensitivity study shows that the drying processes can be physically interpreted and qualitatively match the behavior of the physical experiments. Results from numerical simulations were compared with experimental data.

The comparison results demonstrate that the coupling concept used in the integrated model formulation can predict the different stages of the drying process in porous media with good accuracy. Increasing the wind speed, in a non-isothermal system, increases the first stage evaporation rate and decreases the transition time at low velocity values; then, at high values of wind speed the evaporation rate becomes less dependent of flow in free fluid. In the opposite, the impact of the wind speed on the second stage evaporation rate (diffusion-dominant stage) is not significant. The thermal and solutal dispersion in free flow domain should be taken into account when solving the coupled concept model. The new phase change rate equation leads to good correlation between theoretical and experimental results. The proposed theoretical model can be used to predict the evaporation process where a porous medium flow is coupled to a free flow for different practical applications.

Acknowledgments

This research was funded by the U. S. Army Research Office Award W911NF-04-1-0169 the Engineering Research and Development Center (ERDC), the National Security Science and Engineering Fellowship (NSSEFF) Award No. FA9559-10-1-0139 and National Science Foundation grant EAR-1029069. The authors wish to thank Rainer Helmig and Klaus Mosthaf for contribution during the development of the theoretical model in IWS of University of Stuttgart, Paul Schulte and Stephan Liu from Colorado School of Mines, Russell Harmon from the Army Research Office, and Stacy Howington, John Peters and Matthew Farthing from ERDC for support and technical contributions.

Nomenclature

c_p	Constant pressure heat capacity, J.kg/K	T	Temperature, K
$\mathscr{D}_v$	Binary diffusion coefficient of water vapor in air, m^2/s	T_α	Temperature of the α-phase, K
D_v^*	Effective diffusion coefficient of water vapor in air for porous medium, m^2/s	$\mathbf{v}_\alpha$	Average velocity of the α-phase, m/s
$\mathbf{D}_v$	Dispersion tensor of water vapor in air for free medium, m^2/s	x, y	Cartesian coordinates, m
E	Evaporation rate, $kg/m^2.s$	w_v	Mass fraction of water vapor in the gas phase
$\mathbf{g}$	Gravitational acceleration, m^2/s	*Greek symbols*	
$\mathbf{I}$	Identity tensor	ϕ	Volume fraction of the pore or porosity
$k_{r\alpha}$	Relative permeability of the phase α	μ_{eff}	Effective viscosity, Pa.s
$\mathbf{K}$	Intrinsic permeability tensor, m^2	μ_α	Dynamic viscosity for the α-phase, Pa.s
L	Latent heat of vaporization, J/Kg	ρ_v	Vapor density in gas phase, kg/m^3
L_P	A phenomenological coefficient	ρ_{veq}	Equilibrium vapor density in gas phase, kg/m^3
$L_{eq},\ k,\ r$	Coefficients in Eqs. (27) and (28)	ρ_α	Total mass density for the α-phase, kg/m^3
ℓ_{por}	Pore characteristic length	τ	Tortuosity of porous medium
$\mathbf{n}$	Unit normal vector	α_{BJ}	Beavers-Joseph coefficient
p_c	Capillary pressure, Pa	$\mathbf{\Lambda}_g$	Thermal dispersion tensor for moist air in free medium, W/m.K
Pe_T, Pe_C	Thermal and solutal Péclet numbers	λ_α	Thermal conductivity of the α-phase, W/m.K
P_v	Partial vapor pressure in gas phase, Pa	Λ^*	Effective thermal conductivity coefficient in porous medium, W/m.K

P_{veq}	Equilibrium partial vapor pressure in gas phase, Pa	∇	Del Operator
p_α	Pressure of the α-phase, Pa	Γ	Interface between free flow medium and porous medium
Q_s	Heat loss, J/m^3.s	ω	weighting factor in Eq. (25)
r_v , r_s	Aerodynamic and surface resistances for water vapor, s/m	*Subscripts, superscripts and other symbols*	
$\dot{m}$	Phase change rate, kg/(m^3.s)	α	ℓ (liquid), s (solid) and, g (gas) phases
S_α	Saturation of the phase α	pm	Porous medium
t	Time, s	ff	Free flow medium
t_{eq}	Equilibrium time, s		
$\mathbf{t}_j$	Unit normal tangential vector		

References

[Alazmi and Vafai, 2001]Alazmi, B. and Vafai, K.: 2001, Analysis of fluid flow and heat transfer interfacial conditions between a porous medium and a fluid layer, *International Journal of Heat and Mass Transfer* **44**, 1735–1749.

[Armstrong et al., 1994]Armstrong, J. E., Frind, E. O. and McClellan, R. D.: 1994, Nonequilibrium mass transfer between the vapor, aqueous, and solid phases in unsaturated soils during vapor extraction, *Water Resources Research* **30**(2), 355–368.

[Assouline et al., 2010]Assouline, S., Narkis, K., Tyler, S., Lunati, I., Parlange, M. and Selker, J. S.: 2010, On the diurnal soil water content dynamics during evaporation using dielectric methods, *Vadose Zone Journal* **9**(3), 709–718.

[Baber et al., 2012]Baber, K., Mosthaf, K., Flemisch, B., Helmig, R., MÃ¼thing, S. and Wohlmuth, B.: 2012, Numerical scheme for coupling two-phase compositional porous-media flow and one-phase compositional free flow, *IMA Journal of Applied Mathematics* **77**(6), 887–909.

[Bear, 1972]Bear, J.: 1972, *Dynamics of Fluids in Porous Media*, 764 pp., Dover, Mineola, N. Y.

[Beavers and Joseph, 1967]Beavers, G. S. and Joseph, D. D.: 1967, Boundary conditions at a naturally permeable wall, *Journal of Fluid Mechanics* **30**, 197–207.

[Bénet et al., 2009]Bénet, J.-C., Lozano, A.-L., Cherblanc, F. and Cousin, B.: 2009, Phase change of water in a hygroscopic porous medium. phenomenological relation and experimental analysis for water in soil, *Journal of Non-Equilibrium Thermodynamics* **34**, 133 – 153.

[Bird et al., 2002]Bird, R., Stewart, W. and Lightfoot, E.: 2002, *Transport Phenomena*, 2nd ed. New York: J. Wiley and Sons.

[Bittelli et al., 2008]Bittelli, M., Ventura, F., Campbell, G. S., Snyder, R. L., Gallegati, F. and Pisa, P. R.: 2008, Coupling of heat, water vapor, and liquid water fluxes to compute evaporation in bare soils, *Journal of Hydrology* **362 (3-4)**, 191–205.

[Bixler, 1985]Bixler, N. E.: 1985, Noria – a finite element computer program for analyzing water, vapor, air, and energy transport in porous media,, *Rep. SAND84-2057, UC-70, Sandia Natl. Lab., Albuquerque, N. M* .

[Bogena et al., 2007]Bogena, H., Huisman, J., Oberdörster, C. and Vereecken, H.: 2007, Evaluation of a low-cost soil water content sensor for wireless network applications, *Journal of Hydrology* **344**(1-2), 32–42.

[Camillo and Gurney, 1986]Camillo, P. and Gurney, R. J.: 1986, A resistance parameter for bare-soil evaporation models, *Soil science* **141 (2)**, 95–105.

[Campbell, 1977]Campbell, G. S.: 1977, *An Introduction to Environmental Biophysics*, Springer-Verlag, New York.

[Campbell, 1985]Campbell, G. S.: 1985, *Soil physics with BASIC : transport models for soil-plant systems / Gaylon S. Campbell*, Elsevier, Amsterdam ; New York :.

[Campbell et al., 1994]Campbell, G. S., Jungbauer, J. D., Bidlake, W. R. and Hungerford, R. D.: 1994, Predicting the effect of temperature on soil thermal-conductivity, *Soil Science* **158**, 307–313.

[Cass et al., 1984]Cass, A., Campbell, G. S. and Jones, T. L.: 1984, Enhancement of thermal water-vapor diffusion in soil, *Soil Science Society of America Journal* **48**(1), 25–32.

[Chammari et al., 2005]Chammari, A., Naon, B., Cherblanc, F., Cousin, B. and Bénet, J.: 2005, Water transport in soil with phase change, *in* M. Frémond and F. Maceri (eds), *Mechanical Modelling and Computational Issues in Civil Engineering*, Vol. 23 of *Lecture Notes in Applied and Computational Mechanics*, Springer Berlin Heidelberg, pp. 135–142.

[Chammari et al., 2008]Chammari, A., Naon, B., Cherblanc, F., Cousin, B. and Bénet, J.: 2008, Interpreting the drying kinetics of a soil using a macroscopic thermodynamic non-equilibrium of water between the liquid and vapour phase, *Drying Technology* **26 (7)**, 836–843.

[Chao-Yang and Beckermann, 1993]Chao-Yang, W. and Beckermann, C.: 1993, A two-phase mixture model of liquid-gas flow and heat transfer in capillary porous media- i. formulation, *International Journal of Heat and Mass Transfer* **36**(11), 2747 – 2758.

[Cherblanc et al., 2007]Cherblanc, F., Lozano, A.-L., Ouedraogo, F. and Bénet, J.-C.: 2007, Non-equilibrium liquid-gas phase change in hygroscopic porous media, *European Drying Conference* p. Biarritz : France.

[Chidyagwai and Riviere, 2011]Chidyagwai, P. and Riviere, B.: 2011, A two-grid method for coupled free flow with porous media flow, *Adv. Water Resour.* **34**(9), 1113–1123.

[Cobos and Campbell, 2013]Cobos, D. and Campbell, C.: 2013, Correcting temperature sensitivity of ech2o soil moisture sensors, *Decagon Devices, Application Note* .

[Das et al., 2001]Das, B., Hendrickx, J. and Borchers, B.: 2001, Modeling transient water distributions around landmines in bare soils, *Soil Science* **166(3)**, 163–173.

[Desborough et al., 1996]Desborough, C. E., Pitman, A. J. and Irannejad, P.: 1996, Analysis of the relationship between bare soil evaporation and soil moisture simulated by 13 land surface schemes for a simple non-vegetated site, *Glob. Planet. Change* **13**(1-4), 47–56.

[Dingman, 2002] Dingman, S. L.: 2002, *Physical hydrology*, Prentice Hall.

[Halder et al., 2011]Halder, A., Dhall, A. and Datta, A. K.: 2011, Modeling transport in porous media with phase change: Applications to food processing, *Journal of Heat Transfer* **133**(3), 031010.

[Huxman et al., 2005]Huxman, T. E., Wilcox, B. P., Breshears, D. D., Scott, R. L., Snyder, K. A., Small, E. E., Hultine, K., Pockman, W. T. and Jackson, R. B.: 2005, Ecohydrological implications of woody plant encroachment, *Ecology* **86**(2), 308–319.

[Ishihara et al., 1992]Ishihara, Y., Shimojima, E. and Harada, H.: 1992, Water vapor transfer beneath bare soil where evaporation is influenced by a turbulent surface wind, *Journal of Hydrology* **131**(1-4), 63 – 104.

[Jassal et al., 2003]Jassal, R. S., Novak, M. D. and Black, T. A.: 2003, Effect of surface layer thickness on simultaneous transport of heat and water in a bare soil and its implications for land surface schemes, *Atmos.-Ocean* **41**(4), 259–272.

[Kaviany, 2001] Kaviany, M.: 2001, *Principles of Heat Transfer*, Wiley, New York.

[Kim et al., 1994]Kim, D. S., Cho, E. S. and Choi, C. K.: 1994, An experimental study on fluid flow characteristics of superposed porous and fluid layers, *Korean Journal of Chemical Engineering* **11**, 190–197.

[Kim and Russel, 1985]Kim, S. and Russel, W. B.: 1985, Modelling of porous media by renormalization of the stokes equations, *Journal of Fluid Mechanics* **154**, 269–286.

[Kizito et al., 2008]Kizito, F., Campbell, C., Campbell, G., Cobos, D., Teare, B., Carter, B. and Hopmans, J.: 2008, Frequency, electrical conductivity and temperature analysis of a low-cost capacitance soil moisture sensor, *Journal of Hydrology* **352**(3-4), 367 – 378.

[Le et al., 1995]Le, C., Ly, N. and Postle, R.: 1995, Heat and mass transfer in the condensing flow of steam through an absorbing fibrous medium, *International Journal of Heat and Mass Transfer* **38**(1), 81 – 89.

[Lehmann et al., 2008]Lehmann, P., Assouline, S. and Or, D.: 2008, Characteristic lengths affecting evaporative drying of porous media., *Phys Rev E Stat Nonlin Soft Matter Phys* **77**(5 Pt 2), 056309–. http://europepmc.org/abstract/MED/18643163

[Lozano et al., 2009]Lozano, A., Cherblanc, F. and Bénet, J.-C.: 2009, Water evaporation versus condensation in a hygroscopic soil, *Transport in Porous Media* **80**(2), 209–222.

[Lozano et al., 2008]Lozano, A.-L., Cherblanc, F., Cousin, B. and Bénet, J.-C.: 2008, Experimental study and modelling of the water phase change kinetics in soils, *European Journal of Soil Science* **59**(5), 939–949.

[Lundgren, 1972]Lundgren, T. S.: 1972, Slow flow through stationary random beds and suspensions of spheres, *Journal of Fluid Mechanics* **51**(02), 273–299.

[Millington and Quirk, 1961]Millington, R. J. and Quirk, J. P.: 1961, Permeability of porous solids, *Transactions of the Faraday Society* **57**, 1200–1207.

[Monteith and Unsworth, 1990]Monteith, J. L. and Unsworth, M. H.: 1990, *Principles of Environmental Physics*, Routledge Chapman and Hall, New York.

[Mosthaf et al., 2011]Mosthaf, K., Baber, K., Flemisch, B., Helmig, R., Leijnse, A., Rybak, I. and Wohlmuth, B.: 2011, A coupling concept for two-phase compositional porous-medium and single-phase compositional free flow, *Water Resour. Res.* **47**(10), W10522–.

[Mualem, 1976]Mualem, Y.: 1976, A new model for predicting the hydraulic conductivity of unsaturated porous media, *WATER RESOURCES RESEARCH* **12**, 513–522.

[Neale and Nader, 1974]Neale, G. and Nader, W.: 1974, Practical significance of brinkman's extension of darcy's law: Coupled parallel flows within a channel and a bounding porous medium, *The Canadian Journal of Chemical Engineering* **52**(4), 475–478.

[Nield, 2009]Nield, D.: 2009, The beavers-joseph boundary condition and related matters: A historical and critical note, *Transport in Porous Media* **78**, 537–540.

[Nield and Bejan, 2006]Nield, D. A. and Bejan, A.: 2006, *Convection in Porous Media*, Third Edition, Springer-Verlag, New York.

[Niessner and Hassanizadeh, 2011]Niessner, J. and Hassanizadeh, S. M.: 2011, *Mass and Heat Transfer During Two-Phase Flow in Porous Media - Theory and Modeling*, InTechOpen.

[Novak, 2010]Novak, M. D.: 2010, Dynamics of the near-surface evaporation zone and corresponding effects on the surface energy balance of a drying bare soil, *Agricultural and Forest Meteorology* **150**(10), 1358 – 1365.

[Ochoa-Tapia and Whitaker, 1997]Ochoa-Tapia, J. and Whitaker, S.: 1997, Heat transfer at the boundary between a porous medium and a homogeneous fluid, *International Journal of Heat and Mass Transfer* **40**(11), 2691 – 2707.

[Oldenburg and Unger, 2004]Oldenburg, C. and Unger, A.: 2004, Coupled vadose zone and atmospheric surface-layer transport of co2 from geologic carbon sequestration sites, *Vadose Zone Journal* **3**, 848–857.

[Parker et al., 1987]Parker, J. C., Lenhard, R. J. and Kuppusamy, T.: 1987, A parametric model for constitutive properties governing multiphase flow in porous media, *Water Resources Research* **23**(4), 618–624.

[Prat, 2002]Prat, M.: 2002, Recent advances in pore-scale models for drying of porous media, *Chemical Engineering Journal* **86**(1-2), 153 – 164.

[Saffman, 1971]Saffman, R.: 1971, On the boundary condition at the surface of a porous medium, *Studies in Applied Mathematics* **50**, 93–101.

[Sakai et al., 2011]Sakai, M., Jones, S. B. and Tuller, M.: 2011, Numerical evaluation of subsurface soil water evaporation derived from sensible heat balance, *Water Resour. Res.* **47**, 17.

[Sakaki et al., 2008]Sakaki, T., Limsuwat, A., Smits, K. M. and Illangasekare, T. H.: 2008, Empirical two-point Î±-mixing model for calibrating the ech2o ec-5 soil moisture sensor in sands, *Water Resources Research* **44**(4), 1–8.

[Scarpa and Milano, 2002]Scarpa, F. and Milano, G.: 2002, The role of adsorption and phase change phenomena in the thermophysical characterization of moist porous materials, *International Journal of Thermophysics* **23**, 1033–1046.

[Schmid, 1997]Schmid, H.: 1997, Experimental design for flux measurements: matching scales of observations and fluxes, *Agricultural and Forest Meteorology* **87**(2-3), 179 – 200.

[Seager et al., 2007]Seager, R., Ting, M. F., Held, I., Kushnir, Y., Lu, J., Vecchi, G., Huang, H. P., Harnik, N., Leetmaa, A., Lau, N. C., Li, C. H., Velez, J. and Naik, N.: 2007, Model projections of an imminent transition to a more arid climate in southwestern north america, *Science* **316**(5828), 1181–1184.

[Seyfried and Grant, 2007]Seyfried, M. S. and Grant, L. E.: 2007, Temperature effects on soil dielectric properties measured at 50 mhz, *Vadose Zone Journal* **6**(4), 759–765.

[Shahraeeni et al., 2012]Shahraeeni, E., Lehmann, P. and Or, D.: 2012, Coupling of evaporative fluxes from drying porous surfaces with air boundary layer: Characteristics of evaporation from discrete pores, *Water Resources Research* **48**(9), W09525.

[Shavit, 2009]Shavit, U.: 2009, Special issue on "transport phenomena at the interface between fluid and porous domains", *Transp. Porous Media* **78**(3), 327–330.

[Shavit et al., 2002]Shavit, U., Bar-Yosef, G., Rosenzweig, R. and Assouline, S.: 2002, Modified brinkman equation for a free flow problem at the interface of porous surfaces: The cantor-taylor brush configuration case, *Water Resources Research* **38**(12), 56–1–56–13.

[She and Sleep, 1998]She, H. Y. and Sleep, B. E.: 1998, The effect of temperature on capillary pressure-saturation relationships for air-water and perchloroethylene-water systems, *Water Resources Research* **34**(10), 2587–2597.

[Shokri et al., 2009]Shokri, N., Lehmann, P. and Or, D.: 2009, Characteristics of evaporation from partially wettable porous media, *Water Resources Research* **45**(2), W02415.

[Smits et al., 2012]Smits, K. M., Ngo, V. V., Cihan, A., Sakaki, T. and Illangasekare, T. H.: 2012, An evaluation of models of bare soil evaporation formulated with different land surface boundary conditions and assumptions, *Water Resour. Res.* **48**, 15.

[Vafai and Kim, 1990]Vafai, K. and Kim, S.: 1990, Fluid mechanics of the interface region between a porous medium and a fuid layer - an exact solution, *International Journal of Heat and Fluid Flow* **11**, 254–256.

[van de Griend and Owe, 1994]van de Griend, A. A. and Owe, M.: 1994, Bare soil surface resistance to evaporation by vapor diffusion under semiarid conditions, *WATER RESOURCES RESEARCH* **30 (2)**, 181–188.

[van Genuchten, 1980]van Genuchten, M. T.: 1980, A closed-form equation for predicting the hydraulic conductivity of unsaturated soils, *Soil Science Society of America Journal* **44**, 892–898.

[Villagarcia et al., 2007]Villagarcia, L., Were, A., Domingo, F., Garcia, M. and Alados-Arbotedas, L.: 2007, Estimation of soil boundary-layer resistance in sparse semiarid stands for evapotranspiration modelling, *J. Hydrol.* **342**(1-2), 173–183.

[Wang and Cheng, 1997]Wang, C. and Cheng, P.: 1997, Multiphase flow and heat transfer in porous media, *Advances in Heat Transfer* **30**, 93–182, 182a, 183–196.

[Weaver and Tillman, 2005]Weaver, J. and Tillman, F.: 2005, Uncertainty and the johnson-ettinger model for vapor intrusion calculations:, *U.S. Environmental Protection Agency Publication* **EPA/600/R-05/110**, 43.

[Whitaker, 1977]Whitaker, S.: 1977, Simultaneous heat, mass, and momentum transfer in porous media: A theory of drying, Vol. 13 of *Advances in Heat Transfer*, Elsevier, pp. 119 – 203.

[Whitaker, 1999]Whitaker, S.: 1999, *The method of Volume Averaging*, Kluwer Academic Publishers,Dordrecht, The Netherlands.

[Wooding, 1960]Wooding, R. A.: 1960, Instability of a viscous liquid of variable density in a vertical hele-shaw cell, *Journal of Fluid Mechanics* **7**, 501–515.

[Yamanaka et al., 2004]Yamanaka, T., Inoue, M. and Kaihotsu, I.: 2004, Effects of gravel mulch on water vapor transfer above and below the soil surface, *Agricultural Water Management* **67**(2), 145 – 155.

[Zhang and Datta, 2004]Zhang, J. and Datta, A. K.: 2004, Some considerations in modeling of moisture transport in heating of hygroscopic materials, *Drying Technology* **22**, 1983–2008.